Open Access Dissertations   Electronic Theses and Dissertations

2017-05-01

Extended Charge Carrier Lifetimes in Hierarchical Donor-Acceptor Supramolecular Polymer Films

Carmen X. Guzman
University of Miami, c.guzman6@umiami.edu

UNIVERSITY OF MIAMI

EXTENDED CHARGE CARRIER LIFETIMES IN HIERARCHICAL DONOR-
ACCEPTOR SUPRAMOLECULAR POLYMER FILMS

By

Carmen Xenia Guzman

A DISSERTATION

Submitted to the Faculty
of the University of Miami
in partial fulfillment of the requirements for
the degree of Doctor of Philosophy

Coral Gables, Florida

May 2017

UNIVERSITY OF MIAMI

A dissertation submitted in partial fulfillment of
the requirements for the degree of
Doctor of Philosophy

EXTENDED CHARGE CARRIER LIFETIMES IN HIERARCHICAL DONOR-
ACCEPTOR SUPRAMOLECULAR POLYMER FILMS

Carmen Xenia Guzman

Approved:

_____
Françisco M. Raymo, Ph.D.
Professor of Chemistry

_____
Jamie D. Walls, Ph.D.
Associate Professor of
Chemistry

_____
Burjor Captain, Ph.D.
Associate Professor of Chemistry

_____
Guillermo Prado, Ph.D.
Dean of the Graduate School

_____
Joshua Cohn, Ph.D.
Professor of Physics

GUZMAN, CARMEN XENIA   (Ph.D., Chemistry)

Extended Charge Carrier Lifetimes in Hierarchical   (May 2017)
Donor–Acceptor Supramolecular Polymer Films

Abstract of a dissertation at the University of Miami.

Dissertation supervised by Professor Françisco M. Raymo.
No. of pages in text. (236)

With an impending surge in the global demand for energy, there is a need for disruptive solar energy harvesting approaches. Supramolecular donor-acceptor polymers that undergo long-distance, photo-induced charge separation, are one solution to this challenge. We report that supramolecular polymer films composed of a 2:1 mixture of mono-diamidopyridine diketopyrrolopyrrole (DPP) electron donors and perylene derived bisdiimide (PDI) electron acceptors, undergo photo-induced charge transfer in the solid-state. The two monomers form 2:1 helical heteroaggregate supramolecular polymers as a result of triple H-bonding and $\pi \cdots \pi$ stacking orthogonal to the H-bonding axis. Using ultrafast transient absorption spectroscopy, we demonstrate that recombination lifetimes increase a thousand-fold compared to solution. Supramolecular donor-acceptor polymer films were designed by considering structure and electron transfer dynamics synergistically. This route towards functional hierarchical superstructures could lead to new materials for artificial photosynthesis and organic electronics.

To my loving family and amazing friends

ACKNOWLEDGEMENTS

First and foremost, I would like to thank my research advisor, Professor Adam Braunschweig, for his patience, motivation, and immense knowledge throughout my graduate career. Without his guidance and persistent help, this dissertation would not have been possible.

I thank the members of my committee, Professor Françisco M. Raymo, Professor Jamie D. Walls, Professor Burjor Captain and Professor Joshua Cohn for their valuable time, support, advice, and encouragement throughout this whole process. Additionally, I would also like to thank my undergraduate advisor Professor Jose Cerda, for encouraging me to pursue my doctorate degree.

I extend my gratitude for all of my group members and the undergrads that worked with me and my colleagues for all of their support, love, and advice throughout the years. An additional thank you goes to the National Science Foundation for their financial support in my graduate career.

Lastly, I would like to thank my family and friends for their love and aid. To my father, Edwin, who inspired me to pursue science; to my mother, Bennie, that is my biggest cheerleader in whatever I do; to my sister Xianelly who helped me survive the stress and never let me give up; to my amazing boyfriend Heath Lacy, for his words of encouragement which helped me every day; And to my best friends Ashley Santana, Alana Vagnozzi, Mattie Aguero, Mary Black, and Amanda Candileri whom I can always count on for continuous laughs and endless loyalty. It is because of these amazing people that I was able to pursue my passion of science.

TABLE OF CONTENTS

LIST OF FIGURES

LIST OF TABLES

CHAPTER 1

DESIGNING SUPRAMOLECULAR POLYMERS

1.1 Introduction

Living systems produce materials with complex structures and advantageous optoelectronic properties by bringing together simple organic components such that the resulting nanoscale organization triggers new interactions with electromagnetic fields, ions, and charges. Some particularly elegant examples include green fluorescent protein,[1] rhodopsin,[2] and the bacterial reaction center [3-5] that possess order on the molecular and nanometer scale and whose responses to external stimuli include switchable fluorescence, signaling, and light conversion to chemical energy, respectively. Two noteworthy attributes that these materials share are that they are composed almost entirely of organic matter and possess the characteristic of emergence-upon-assembly – in which new properties are only observed upon the formation of hierarchical order, whose structure across the molecular-to-macroscopic continuum is dictated by noncovalent interactions programmed into the individual molecular components. As a result of this spatial arrangement, new electronic interactions arise that enable remarkable functionality, such as the conversion of light to chemical energy in photosynthesis (Fig. 1.1). In the reaction center, a series of chromophores with systematically decreasing energy levels are positioned precisely in space to enable a cascade of electron and energy transfer events that rapidly move photogenerated charge from one side of the complex to the other.[3-5] Current synthetic routes are unable to reproduce such multi-lengthscale order and advanced
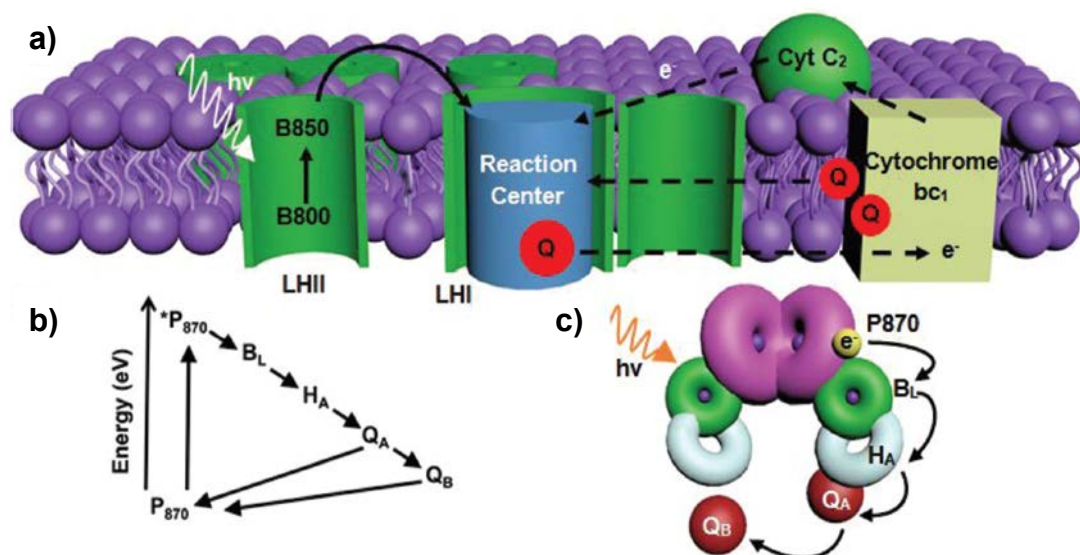
Fig. 1.1 Photosynthesis in *Rhodobacter sphaeroides* light harvesting bacteria. (a) Photosynthesis, the biological process by which incident light is converted to chemical energy, occurs through a complex process involving several optically and electronically active components operating in concert. (b) Directional and fast energy transfer occurs along the chromophores in the reaction center because each step from the special pair to the quinone in the process is energetically favorable. (c) Light for photosynthesis is collected in the reaction center, where energy is passed through a series of precisely positioned chromophores. Incident light (orange) is absorbed by neighboring antenna pigments (purple). Separated charge migrates through the chromophores to a strongly attached quinone (red, Q_A) where it can be abstracted by a neighboring loosely bound quinone (red, Q_B) which diffuses through the membrane to the cytochrome unit where it undergoes oxidation to complete charge separation and transfer.

function with artificial materials because the large sizes and the complex assembly processes involved exceed the limits of modern manufacturing capabilities. Despite the prevalence of the elegant and functional optoelectronically active structures found in Nature, the materials that continue to dominate the optics and electronics industries are crystalline and inorganic,[6-9] and are not competitive with natural systems in terms of cost, toxicity, and weight. However, the drawback of using biomaterials as replacements is that their lack of stability and poor processiblity has precluded their device integration. So for both industrial applications and to gain fundamental insight into the complex machinery of life, it is important to continue developing organic materials that possess hierarchical order and stimuli-responsive optical and electronic behavior.

By adopting a biomimetic design approach[10-12] where hierarchical assembly and emergent behavior are equally important goals of molecular design, researchers have successfully developed organic materials with impressive optical,[13] mechanical,[14-15] and electronic properties.[16] Building blocks of both biological[17-20] and synthetic origin[10-12] have been leveraged to achieve diverse molecular architectures and functions, and the common element among all these components is that reversible, noncovalent bonding directs superstructure formation. A particularly noteworthy subset of these bioinspired materials, and the subject of this introduction, are the supramolecular polymers,[21-23] which are macromolecules whose monomers are held together principally by noncovalent bonding through either H-bonding, $\pi\cdots\pi$ stacking, metal coordination, or mechanical bonding (Fig. 1.2).[24-27] Similar to oligonucleotides and oligopeptides, they combine the benefits of Poly. Chem.and supramolecular chemistry to achieve properties that are absent in the individual components. The benefits of supramolecular polymers include their ease-of-preparation from simple building blocks, dynamic macromolecular composition, and hierarchical structure. The remarkable new emergent properties can include the ability to embed information within molecular scaffolds,[28-29] impressive mechanical performance,[4, 15] structural changes in response to biological stimuli,[30-32] and beneficial interactions with electromagnetic fields.[13] Thus, many compelling reasons exist to continue developing new supramolecular polymer-based solutions to address pressing research challenges.
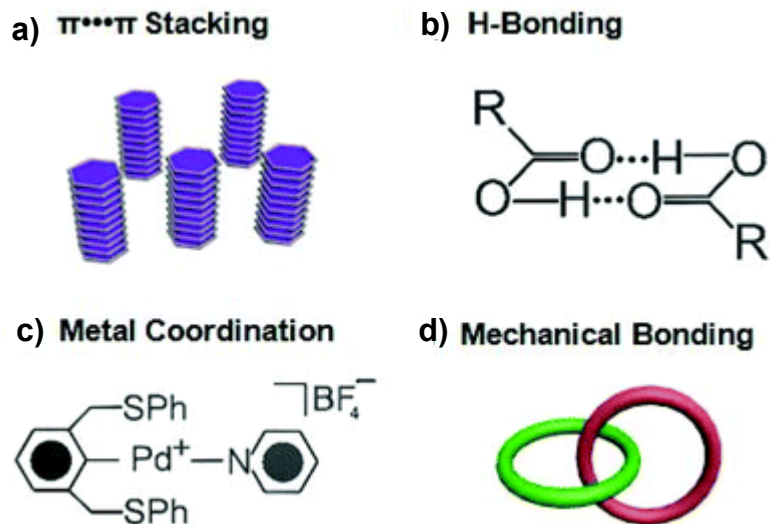
Fig. 1.2 Commonly utilized noncovalent bonding interactions in supramolecular polymer chemistry include (a) $\pi \cdots \pi$ stacking, (b) H-bonding, (c) metal coordination, and (d) mechanical bonding.

Supramolecular polymers have been explored in the context of medical, electronic, energy, and environmental applications, and several excellent reviews exist already related to this rapidly growing research field.[16, 21-23, 31] Rather than providing another comprehensive article, our aim is to highlight a few exemplary supramolecular polymers and related systems that achieve one particularly important photophysical property, namely photoinduced charge separation, which is a critical step in artificial photosynthesis.[33] By highlighting their commonalities, we hope to derive design principles for creating new organic materials for energy harvesting, signaling, and sensing. Supramolecular polymers with emergent optoelectronic properties are achieved when considerable attention is given to the three pillars of photoactive supramolecular polymer design: topology, noncovalent assembly, and electron and spin dynamics. This introduction will discuss the design of artificial supramolecular polymers with emergent optoelectronic properties, where the three aforementioned criteria have been successfully employed to create materials that

collect photons and convert them to charges that can be subsequently collected. Particular attention is devoted towards a multicomponent supramolecular polymer prepared in our group composed of a diketopyrrolopyrrole (DPP) electron donor and a perylene derived bisdiimide (PDI) electron acceptor that, following assembly into superstructures with a 2 : 1 donor–acceptor ratio, produces long-lived charge carriers following irradiation with visible light.[34-35]

1.2 Polymer Topology

Macromolecules are distinct from their small molecule counterparts in that their structures are defined not so much by the relative positions of a few atoms in space, but by the sequence and arrangement of molecular repeating units, termed monomers. Thus a major advantage of Poly. Chem.is that vast topological diversity is accessible from a few easy-to-prepare building blocks, and that important rheological, mechanical, and electronic properties are dependent on the topology that can be varied by changing reaction conditions during the polymer synthesis. In the context of macromolecular science, the term topology refers to the size, shape, and connectedness as the chief elements of topology. This includes the monomer sequence of polymer segments, and the accessibility of different polymer topologies is related intimately to the types of bonding that link together monomeric units within a given chain. As such, we suggest that macromolecular topologies can be broadly classified in terms of the bonding types that they employ, which include the covalent polymers, supramolecular polymers, and hybrid polymers, the latter of which use a combination of covalent and noncovalent bonds to arrange monomers spatially.
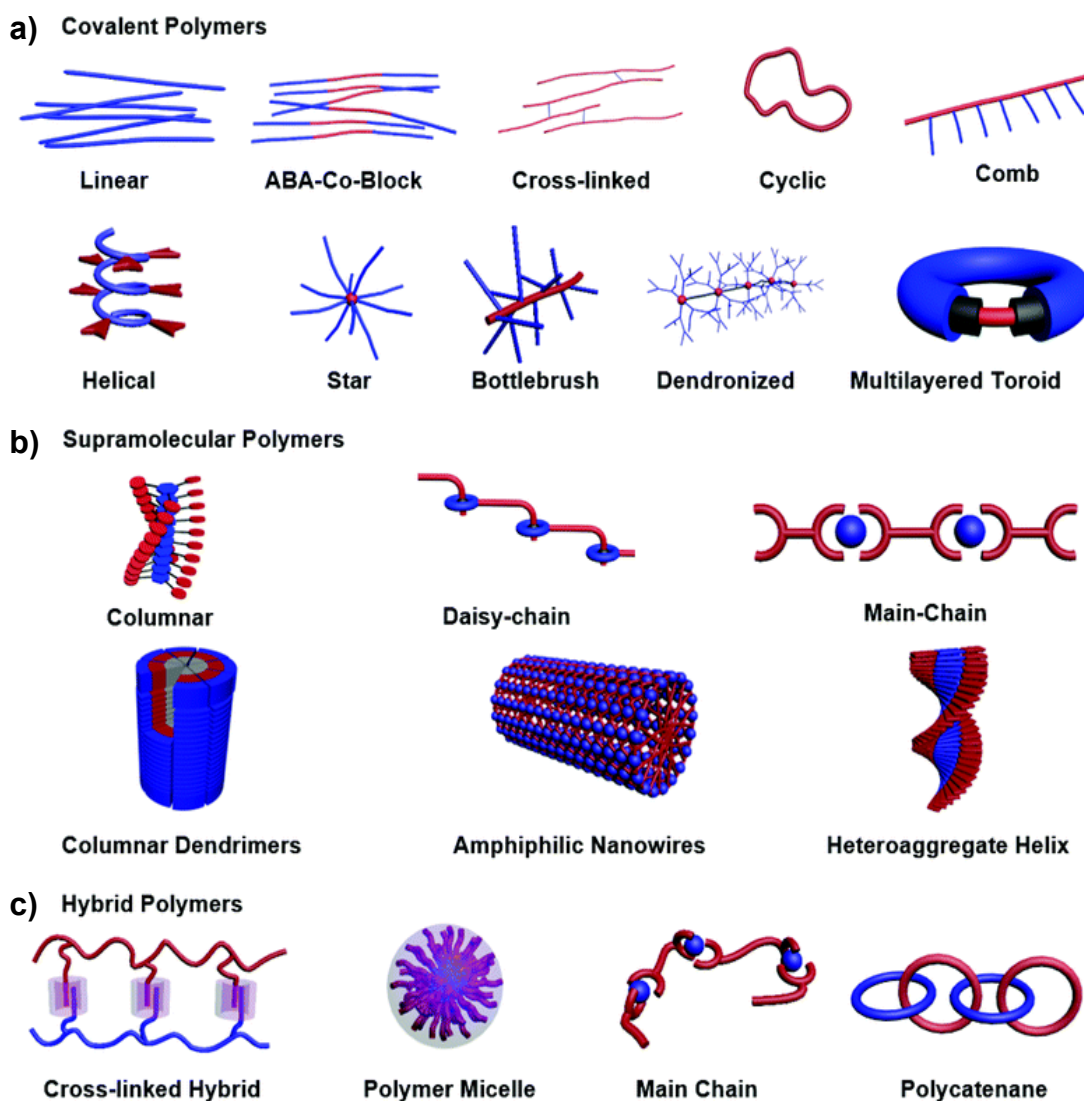
Fig. 1.3 Polymer topology. Polymers derive their properties from the monomer composition, sequence, and arrangement in space (topology). Polymers can be classified in terms of the types of bonding that hold the monomers together, which include covalent, noncovalent, or a hybrid of both. (a) Covalent polymer topologies, where monomers are held together by covalent bonds, are broadly studied in the following categories:cyclic,[36] helical,[37-38] star,[39] bottlebrush,[40-42] dendronized,[43] and multilayered toroid.[44](b) Supramolecular polymer topologies, where monomers are brought together by noncovalent bonds, are broadly studied in the following categories: columnar,[45] daisy-chain,[46] main chain,[47-48] columnar dendrimers,[49-50] amphiphilic nanowires[51] and heteroaggregate helices.[35, 52-53] (c) Supramolecular-covalent hybrid polymers possess functional groups capable of noncovalent recognition appended to covalent polymers, and are studied in the following categories: cross-linked hybrids,[28, 54] polymer micelles,[55] linear hybrids,[47] and polycatenanes.[56]

Polymers whose chains are held together solely by covalent bonds constitute the largest class of synthetic macromolecules, and in covalent polymers (Fig. 1.3 a) topology is dictated by the monomer sequence, the structure of the initiator, and the monomer type. Generally, the covalent polymers are composed of sections of linear chains, whose monomers can be identical or varied, and in the latter case can be arranged along the strand in blocks or as a random arrangement of monomers in the chain. By using initiators with multiple reactive sites, other topologies with different connectivities, such as star polymers,[39, 57] can be obtained, and when more than one polymerizable group is incorporated into the monomers, cross-linking between chains occurs. The creative combination of these three elements can lead to more exotic topologies, such as comb,[58-59] dendronized,[43, 60] and bottle-brush polymers,[61-62] where initiators themselves can be macromolecules. While there have been significant recent developments related to self-immolative polymers[63-65] and polymers with mechanically labile bonds,[66-67] the bonds within covalent polymers are generally considered to be kinetically and thermodynamically stable under normal laboratory temperatures and pressures. Thus to predict the structure that will be formed during a covalent polymerization, the rate constant k of the reaction employed to make the polymer is the single most useful parameter for predicting chain length, monomer sequence, and even connectivity.

The defining characteristic of supramolecular polymers that distinguishes them from covalent polymers is that the monomers in supramolecular polymers are held together by dynamic bonds. These include H-bonding,[68] $\pi \cdots \pi$ stacking,[69] host–guest encapsulation,[25] and any additional interactions where an equilibrium can be established between bound and unbound states. This fluctuation endows supramolecular polymers with a high degree of internal order and adaptability, where shape and chain length can be altered

in response to environmental changes. As a result, supramolecular polymers have been explored in the context of shape memory materials,[70] degradable plastics,[71] drug delivery,[28, 72] and artificial photosynthetic systems.[73] Use of supramolecular polymers for artificial photosynthesis will be discussed in detail in following sections. The dynamic properties of supramolecular polymers, including degree of polymerization, connectivity, and assembly mechanism, can be understood through the equilibrium constant, K, between bound and unbound states, which captures simultaneously bond strength and equilibrium position. Thus one helpful way to distinguish covalent and supramolecular polymers is that the structure of the former is predicted using k, whereas the behaviors of the latter are conceptualized through K.

The topologies accessible with supramolecular polymers are closely dependent upon the types of interactions bringing the monomers together and are distinct from those common to covalent polymers (Fig. 1.3 b). Most, but certainly not all, supramolecular polymers employ only a single type of noncovalent interaction to bring the monomers together into repeating chains. For example, monomers where $\pi\cdots\pi$ interactions are dominant form one dimensional stacks,[69] where the polymer chain propagates orthogonally to the plane formed by the aromatic monomer. An alternate architecture is the main-chain or daisy-chain, where propagation is along the long-axis of the monomer, and these polymers typically use H-bonding, metal-coordination, or pseudocatenation to create the polymers.[47] Biological systems rarely use only a single noncovalent interaction, and more sophisticated supramolecular polymer topologies can be obtained when monomers are designed such that multiple noncovalent interactions operate in concert to control the architecture. Although such systems are challenging to design and understand, they often display impressive functionality and can also be used to understand the subtleties of

assembly in complex natural materials. An early example is the amphiphilic nanowire system of Stupp *et al.*,[51] which uses combinations of H-bonding and van der Waals forces to form multifunctional nanotubes that have been used for numerous applications, such as spinal cord lesion repair in paralyzed animals.[74] Another system uses both H-bonding and π···π stacking to form supramolecular polymers composed of electron donors and perylene bisdiimide electron acceptors to create multicomponent homochiral donor–acceptor helices that undergo photoinduced charge separation only after the donors and acceptors arrange into a precisely defined topology dictated by the multiple noncovalent interactions acting together.[35, 52] Thus researchers are increasingly incorporating lessons from Nature to create supramolecular polymers with progressively more complex topologies, which are making macromolecules with emergent properties more widely available.

A particularly interesting and underexplored class of synthetic materials are the hybrid polymers[75] that possess elements of both covalent polymer and supramolecular polymer within a single macromolecular structure (Fig. 1.3 c). A biological example of such a hybrid polymer system is DNA, which possesses a covalent poly(deoxyribophosphate) backbone and uses the H-bonding and π···π stacking between purines and pyrimidines orthogonal to the backbone long-axis to cross-link the covalent chains.[76] This synergistic combination of covalent and supramolecular segments is the hallmark of biopolymers, and endows oligonucleotides, oligopeptides, and oligosaccharides with their information-carrying potential. Several groups have attempted to reproduce this hybrid topology – in which supramolecular interactions are used to cross-link covalent chains of non-natural origin – using H-bonding,[77-78] metal coordination,[79-80] donor–acceptor,[81-83] and host–guest interactions.[25, 84-85] Some particularly elegant examples have used this cross-linked hybrid architecture to append noncovalent

recognition units into a sequence along the polymer backbone as a demonstration of biomimetic chemical information storage.[28] Another noteworthy hybrid architecture involves linear covalent segments with noncovalent recognition units appended to the chain termini, so the hybrid polymers form when these supramolecular macromonomers are brought together, and the resulting polymers make excellent stimuli responsive and degradable materials.[86] Another class of unique topologies that demonstrates the potential of combining covalent and supramolecular polymers is the mechanically bonded polymers – polymers whose monomers are interlocked, thereby preventing dissociation without cleavage of an internal covalent bond. These can include polycatenanes[56, 87] and polyrotaxanes,[88-90] whose formation is first templated by noncovalent interactions that bring the monomeric components into a defined conformation followed by the formation of a covalent bond that irreversibly links the components into the chain-link structure. New hybrid topologies are being developed constantly, and what is most interesting about these materials is how they leverage both k and K to produce structures that respond to external stimuli.

1.3 Supramolecular Polymer Assembly

In the context of supramolecular polymers, the term "assembly" refers to the step-by-step process by which the monomers come together to form higher order aggregates, and this process is analogous to the polymerization mechanism for the formation for covalent polymers.[91-94] In contrast to covalent polymers, however, supramolecular polymers are held together by dynamic bonds that are constantly traversing the energy landscape between bound and unbound states.[95] As such, important parameters like polymer size and stability at thermodynamic equilibrium are multivariable functions dependent upon concentration, temperature, bond strength, mechanical actuation, and other reaction

conditions,[93] so emergent properties and structural changes in response to external stimuli are dictated by the assembly pathway, the strength of bonds that are in continuous flux, and changes to the external environment. While there are many different pathways by which the monomeric building blocks can come together to form higher order structure, three assembly paradigms, namely isodesmic,[94] cooperative,[96-97] and sergeants-and-soldiers[98-99] assembly will be discussed, with particular emphasis placed upon how each contributes to the emergence of chirality – which is the spontaneous formation of axial, helical, or planar chirality that arises from the relative arrangement of the monomers within the supramolecular polymers in the presence of some enantiomeric excess. Emergent chirality is not necessarily present in supramolecular polymers, even if the monomers possess stereogenic units, and as such, monitoring for the emergence of chirality is a powerful technique for assigning the structure, tracking the assembly mechanism, and determining how bond-strength changes as a function of polymerization conditions.[22]

Isodesmic assembly implies that binding strength between monomers is independent of the supramolecular polymer's degree of polymerization,[93-94] and that even in the presence of enantiomerically pure monomers, emergent chirality does not arise.[34] The central assumption behind isodesmic assembly is $K_n = K_{n-1}$, where n is the number of monomers in the supramolecular polymer and K_n is the binding constant for the addition of another monomer to the chain. Thermodynamic parameters including K_n, $\Delta G°$, $\Delta S°$, and $\Delta H°$ can be determined quantitatively by fitting titration data to well-known isodesmic binding models.[97] The main implication of isodesmic assembly is that no additional information is communicated between the monomer and polymer that is not communicated by the individual monomers, or in other words the polymer structure does not possess any additional order that is not present in the simplest unit (Fig. 1.4 a). The increase in size of

isodesmic polymers with increasing concentrations is similar conceptually to the increase in degree of polymerization over time in condensation polymerizations because large isodesmic polymers are obtained from small nuclei combining to form longer chains.[92] As a result, in isodesmically assembling supramolecular polymers, emergent chirality does not occur because this requires communication between monomers in the growing chain, which would imply that the binding constant changes as the chain grows because new interactions occur in the chain that are not present in simple dimers. In the example of $\pi\cdots\pi$ stacked linear supramolecular polymers composed of an enantiomerically pure solution of monomers, the resulting chain will be disordered with no preferred orientation of the monomers with respect to the propagation axis of the chain. It should be noted that the majority of supramolecular polymers grow according to an isodesmic model.

In cooperative assembly structural information is communicated through the polymer, affecting both the structure of the growing polymer and the strength of binding of each additional monomer.[93, 96-97] The defining characteristic of cooperative assembly is that $K_n \neq K_{n-1}$, in other words the size of the stack affects the binding affinity.[34, 92-93] Cooperative interactions can be both positive and negative, where the former increases the binding strength of each additional monomer to growing the chain ($K_n > K_{n-1}$), and the latter occurs when each additional monomer binds less strongly to the growing chain ($K_n < K_{n-1}$). Many different types of cooperative pathways have been proposed to accommodate for the different origins of cooperativity, so no standard model exists for determining thermodynamic parameters for binding in cooperative supramolecular polymers. However most positively cooperative supramolecular polymer assembly pathways share common attributes: firstly, the relationship between chain size and concentration is termed "nucleation growth" and is almost the exact opposite to the growth

of chains over time in a living polymerization. Unlike living polymerizations, the oligomerization of the monomers, termed nucleation, is initially slow, but once initiation occurs, polymerization proceeds rapidly. Nuclei form until the number of monomers reaches a threshold value, after which they propagate into long chains through a pathway referred to as elongation (Fig. 1.4 b).[92] A second common attribute of positively cooperative polymer assembly is the emergence of higher order chirality when a chiral monomer is present in excess. One example of this phenomenon has been observed in $\pi\cdots\pi$ stacked heteroaggregates composed of achiral PDI electron acceptors and chiral DPP electron donors, whose individual components form π-stacked homoaggregates without emergent chirality.[35] When both components are mixed, they form 2 : 1 donor : acceptor heteroaggregates as a result of $\pi\cdots\pi$ stacking and complementary triple H-bonds between the donor and acceptor. What is remarkable about these systems is that, in isolation, the chiral donors do not display emergent chirality, but when the chiral donor is mixed with the achiral acceptor, homochiral helices form because of the cooperative interactions of the donors and acceptors in the growing stacks, and as the stack grows, so too does K for the binding of additional monomers.[34] An important consequence of this cooperative assembly is that the association of the monomers into supramolecular polymers can be observed by simply monitoring the emergence of chirality as degree of polymerization increases, a phenomenon that is absent in the supramolecular polymers formed from either of the individual components.
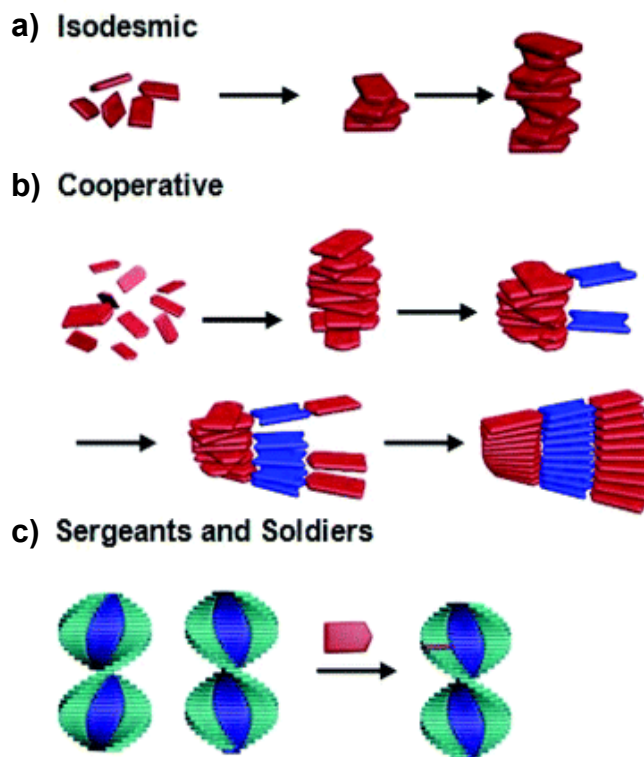
Fig. 1.4 Supramolecular polymer assembly pathways. (a) An isodesmic model assumes equal binding energy independent of stack size, and does not produce emergent chirality. The red shapes indicate chiral monomers. (b) When positively cooperative assembly occurs, the binding strength of new components to the polymer chain increases with increasing stack size as a result of multiple noncovalent interactions operating in concert.[35] Red shapes are chiral monomers that bind to the achiral blue monomers to form a helically chiral superstructure. (c) Sergeants-and-soldiers assembly occurs when a small percentage of chiral component dictates the chirality of a supramolecular polymer.[99] Both green and blue shapes represent achiral monomers, and a small amount of chiral (red) monomer changes the solution from a racemic mixture of M and P helices to a homochiral solution composed of only P helices.

A final use of emergent chirality to understand assembly and structure in supramolecular polymers involves the sergeants-and-soldiers principle. In the sergeants-and-soldiers assembly pathway, a small percentage of chiral monomers impose chirality onto an achiral supramolecular polymer.[98-99] This small enantiomeric excess directs the rest of the otherwise racemic mixture of chains to follow the directionality imposed by the chiral building block (Fig. 1.4 c). In terms of understanding structure and assembly, there are several important implications of the sergeants-and-soldiers principle: firstly, the resulting chiral structures are easily studied by a variety of accessible analytical tools. Secondly, the revelation of emergent chirality confirms that cooperative interactions are

driving assembly, and this would be difficult to confirm in the absence of emergent chirality. Finally, the ability of a small stimulus, in this case nominal enantiomeric excess, to control structure and emergent properties suggests many opportunities remain to use supramolecular polymers as sensors and reconfigurable materials.

1.4 Emergent Optoelectronic Properties

Photosynthesis is an inspiring natural model for the design of artificial materials to convert light directly to charge and thereby source infinitely renewable energy to meet increasing global demand.[100] The components of photosynthesis are remarkable in that they are organic, they organize into complex arrangements as a result of multiple noncovalent interactions operating in concert, and the directional flow of energy and electrons occurs as a result of the synergistic combination of structural and orbital effects. Increasingly, researchers are attempting to create organic systems for artificial photosynthesis,[33] where successful materials achieve long-lived charge-separated states by bringing together electron donor and electron acceptor components into structures that possess the precise spatial arrangement, orbital energies, and electronic coupling to facilitate photoinduced electron transfer with long-lived charge separated states. Supramolecular systems, and particularly supramolecular polymers, are ideal for artificial photosynthesis because they can achieve complex topologies with the requisite long-distance order from easy-to-prepare and modular components that come together as a result of noncovalent assembly. By appropriately designing topology, assembly, and spin and orbital interactions, a number of artificial systems have been prepared that successfully produce long-lived charge separated states following photoinduced charge separation.
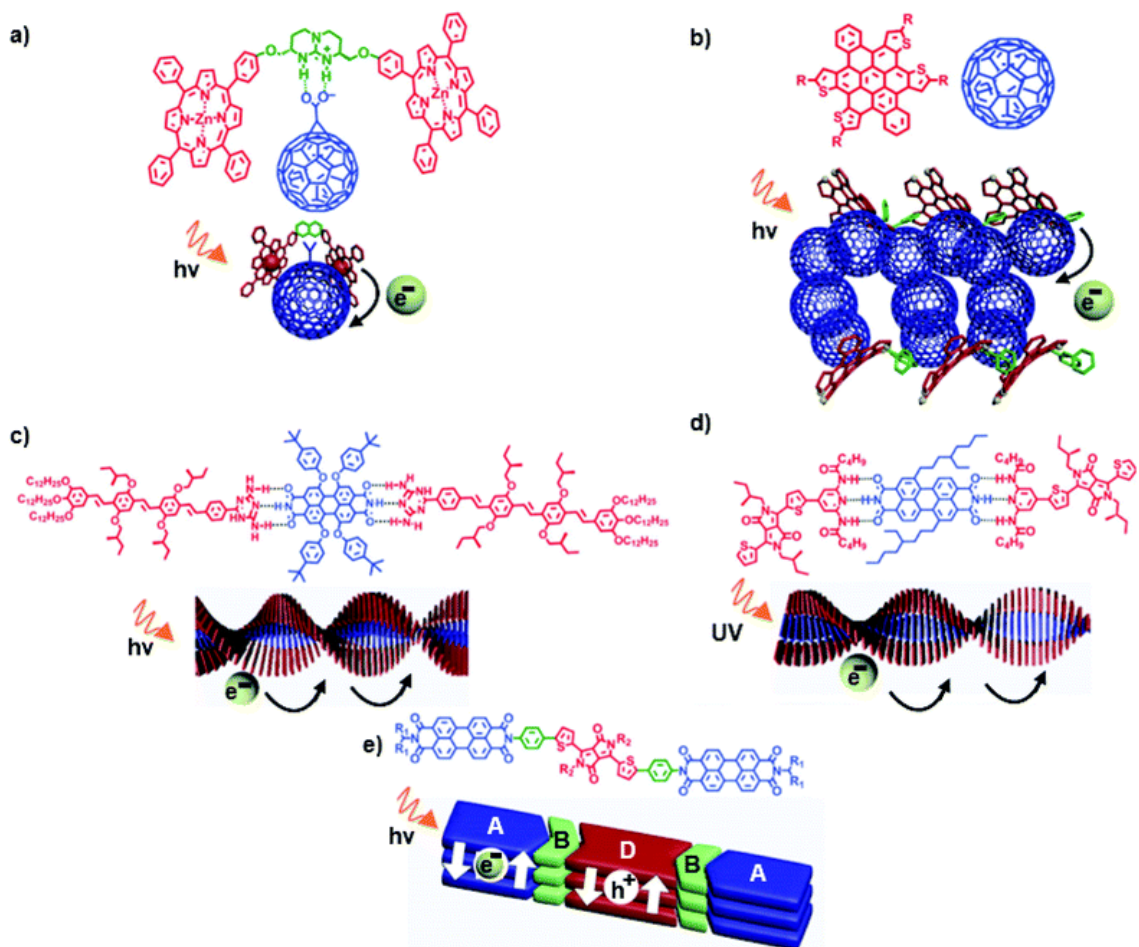
Fig. 1.5 Photoactive supramolecular systems. (a) Porphyrin electron donors and fullerene electron acceptors assemble as a result of cooperative H-bonding and van der Waals interactions, resulting in a complex that achieves a photoinduced charge separated state. (b) Dibenzotetrathienecoronenes (DBTCCs) envelop the much larger C_{60} crystals to bring about a binary donor–acceptor motif capable of electron transfer.[40, 101] The supramolecular structure comes about as a result of sulfur–sulfur interactions and the molecular conformations of the DBTCC molecules. (c) An oligophenylene vinylene-PDI donor–acceptor system that assembles into helical superstructures as a result of orthogonal π···π stacking, H-bonding interactions, and chiral side-chains appended to the donor. Charge separation is observed upon irradiation.[52, 101] (d) A DPP-PDI donor–acceptor supramolecular polymer that forms helical supramolecular polymers as a result of cooperative H-bonding and π···π stacking, and undergoes photoinduced charge separation in solution and in the solid-state.[35] (e) Donor–bridge–acceptor composed of PDI donors and DPP acceptors that stacks in the solid-state, resulting in a long-lived charge separated state following irradiation.[102]

The benefits of synergistically designing supramolecular assembly and orbital interactions to achieve photoinduced electron transfer in solution are elegantly demonstrated in a system designed by Guldi *et al*. composed of guanidinium bis-porphyrin donors and fullerene carboxylate acceptors that form a donor–acceptor hybrid (Fig. 1.5 a)

through the cooperation of H-bonding and $\pi\cdots\pi$ stacking.[103] The combination of fullerenes and porphyrins for artificial photosynthesis is an attractive one because of their large abundance and relatively low productions costs, and the charge separation and charge recombination of this pair has many similarities to natural photosynthetic systems, including the ultrafast formation of a long-lived radical pair state. As such both have been explored in the context of bulk heterojunction organic photovoltaics, which consist of blended films of the two components, but the phase segregation has been cited as one of the reasons why device efficiency remains low. Alternatively, covalently linked donor–acceptor systems for artificial photosynthesis with the same two components had been demonstrated previously,[104] but their preparation is cumbersome, which precludes optimization because of the challenges of modifying their structure. In the supramolecular porphyrin-fullerene system, the H-bonding, $\pi\cdots\pi$ stacking and electrostatic interaction work cooperatively to bring the donor and acceptor together in the requisite proximity for electron transfer. The energy level of the donor is positioned such that the singlet excited state undergoes rapid-electron transfer to the donor, and as a consequence, the donor and acceptor undergo efficient photoinduced electron transfer following supramolecular assembly. Although it does not form a supramolecular polymer, this system demonstrates how cooperative noncovalent assembly and appropriate orbital design can be combined to achieve long-lived charge separated states as an emergent property. A binary donor–acceptor co-crystal composed of dibenzotetrathienocoronenes (DBTCCs) and fullerene molecules developed in the Nuckolls group (Fig. 1.5 b) forms sandwich-like supramolecular polymer topologies[101] and has been reported to achieve a long charge separated lifetime with high power conversion efficiency.[40] This system makes extensive use of the contorted conformations of DBTCC molecules to envelop the much larger C_{60}

molecules in a tight shell. While not supramolecular polymers, the Guldi and Nuckolls systems elegantly demonstrate how energy levels and supramolecular interactions can be designed synergistically. By understanding how these supramolecular systems achieve photoinduced charge separation in solution and in the solid state, respectively, researchers can create supramolecular polymers that combine emergent photophysics with the benefits of macromolecular science.

To this end, a multicomponent helical supramolecular polymer designed by Würthner *et al.* (Fig. 1.5 c) demonstrates how advanced principles of macromolecular topology and orbital design can be combined to create materials for artificial photosynthesis.[52] In their "coassembled p–n junction" electron donating chiral oligomeric phenylene vinylene (OPV) and PDI electron acceptors are brought into proximity by triple H-bonding between diaminotriazine groups on the OPVs and the diimide groups on the PDIs, forming supramolecular polymers with a 2 : 1 donor : acceptor ratio. Orthogonal to the H-bonding, homo $\pi\cdots\pi$ stacking between the separate chromophores resulted in a right-handed helix. Upon aggregation followed by photoexcitation with 455 nm light, this system undergoes ultrafast photoinduced charge separation because, like the aforementioned system, the frontier molecular orbital levels are situated appropriately to enable electron transfer from the donor to the acceptor. In an effort to explore a similar multicomponent supramolecular polymer motif, the Braunschweig group developed a system composed of DPP electron donors and PDI electron acceptors (Fig. 1.5 d), whose superstructure formation is driven by triple H-bonding between a diamidopyridine group on the DPP and the diimide groups on the PDI, as well as homoaggregation from $\pi\cdots\pi$ stacking along the helical axis.[34-35] The advantage of this system is that DPP has been heralded as a promising chromophore for OPVs because its absorption has broad overlap with the solar spectrum,[105] so it has greater

potential for energy harvesting, and as a result of strong homo $\pi\cdots\pi$ interactions, forms well-ordered aggregates. In addition, the DPP frontier molecular orbital levels are positioned to enable LUMO to LUMO electron transfer or HOMO to HOMO hole transfer to the PDI acceptors, and as expected, upon excitation with 435 nm light, rapid charge separation (<0.2 ps) occurs followed by slower (32 ps) recombination to the ground state. Both these systems demonstrate how supramolecular polymer assembly in combination with appropriate orbital design can be used to achieve photoinduced charge separation. These two examples by Würthner and Braunschweig demonstrate the potential of combining the benefits of organic chromophores and supramolecular architectures to achieve charge separation wherein order and electronic structure can be maintained over large distances.

The Wasielewski group has investigated numerous covalent and supramolecular systems to understand how orbital energies and spin dynamics can be leveraged to increase charge separation efficiency,[73] and in particular have pioneered the use of PDIs as both chromophores and as supramolecular building blocks in artificial photosynthetic systems. Using the same DPP-PDI donor–acceptor pair that was shown to undergo efficient charge separation by Braunschweig *et al*.,[35] they recently demonstrated [102] microsecond charge carrier lifetimes in a covalently linked DPP-PDI donor–bridge–acceptor molecule (Fig. 1.5 e). Photoexcitation in solution results in quantitative charge separation with a recombination lifetime of 340 ps. However upon forming films, the charge recombination lifetime increases to 4 μs as a result of $\pi\cdots\pi$ stacking in the solid-state. The authors attribute this increase to diffusion of the free charge carriers through the film, and stipulate that these remarkably long lifetimes could lead to efficient charge collection. The Wasielewski

system is a unique addition to the donor–acceptor supramolecular systems discussed previously.

Certainly, many more interesting examples exist where supramolecular aggregation and photophysics contribute to the ability to convert light-to-charge, but these examples have been selected to show the evolution of ideas and how the interplay of concepts from supramolecular Poly. Chem.and photophysics are leading to new solutions for addressing the challenge of harnessing solar energy. It is critical to emphasize that the emergent optoelectronic behavior discussed in this article is a direct product of careful design that considers the three pillars of supramolecular polymer assembly. Such behavior is readily obtainable after defining a desired topological model, choosing the proper assembly model to yield the target architecture, and matching electronic and spin dynamics of the monomers.

1.5 Summary

In seeking to develop new materials for optical and electronic applications, researchers are increasingly looking to Nature for inspiration, and in doing so have found that new and useful properties often emerge when multiple components come together into sophisticated macromolecular architectures as a result of distinct noncovalent interactions operating in concert. The exploration of these new materials has led to the realization that molecular topology and optoelectronic properties are intimately related, and that the topologies accessible are dependent upon the types of bonding that bring the components together. These lessons have been applied to prepare a series of supramolecular systems whose purpose is the conversion of light to charge – the first step in artificial photosynthesis – and the results are supramolecular polymers with ever increasing light conversion efficiency and longer lived charge carriers. These successes point towards the continuing need to

investigate supramolecular macromolecules, and particularly in the context of developing

materials with exotic and useful optoelectronic properties.

CHAPTER 2

SUPERSTRUCTURES OF DIKETOPYRROLOPYRROLE DONORS AND PERYLENEDIIMIDE ACCEPTORS

2.1 Background

Small molecules that self-assemble into well-ordered hierarchical superstructures as a result of multiple noncovalent interactions direct the most complex tasks in biology, and supramolecular chemists seek to emulate this design approach to create synthetic systems with comparable functionality.[24, 93, 106-114] To organize chromophores into superstructures, which could be used to probe fundamental aspects of charge generation in organic systems as well as understand assembly in complex supramolecular systems,[115-117] hydrogen-bonding (H-bonding) and $\pi\cdots\pi$ interactions are commonly combined.[45, 52, 77, 96, 118-131] Often, these chromophores display unique spectroscopic signatures corresponding to aggregated states that can be used to track assembly. Examples include homoaggregates of oligo(*p*-phenylenevinylenes) (OPVs) [45, 77, 96, 125, 130] or substituted perylenediimides (PDI),[123, 127-128] where H-bonding precedes π-aggregate formation, and heteroaggregates such as a system consisting of either melamine or OPVs whose H-bonding with PDIs initiates the assembly of π-stacked superstructures. [52, 118-121, 129]

Models that describe homoaggregation of a monomer into a supramolecular polymer provide association constants (K_a's), thermodynamic parameters ($\Delta H°$ and $\Delta S°$), and degrees of polymerization.[94, 132-134] Alternatively, models that consider two or more noncovalent interactions are rare, and most simplify their description of assembly by considering only a single interaction.[135-138] This failure to account for different
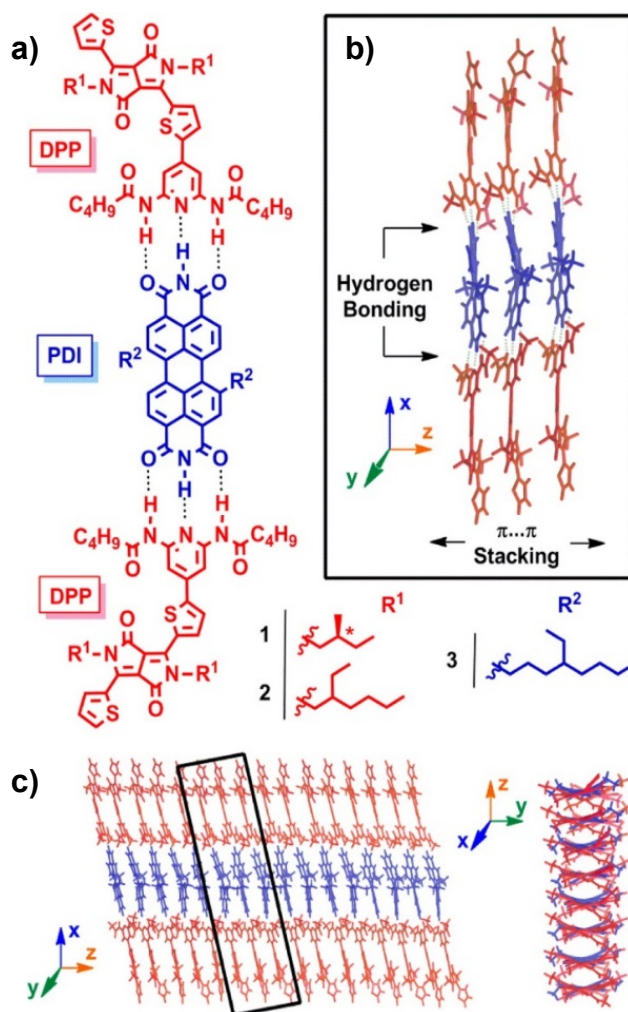
Fig. 2.1 (a) DPP donor (red) and PDI acceptor (blue) molecules 1-3 are capable of (b) heteroaggregation through a combination of H-bonding and $\pi\cdots\pi$ stacking, resulting in (c) well-ordered superstructures.

supramolecular recognition events working in concert limits the ability of scientists to create systems with the functional complexity comparable to natural hierarchical structures, in particular when different components come together to form heteroaggregates.

To address this challenge, we studied the aggregation of chiral and achiral monodiamidopyridine diketopyrrolopyrrole-based (mDPP) donors with a 1,7-substituted PDI acceptor (Fig. 2.1 a). Upon mixing in solution, the PDI and DPPs assemble into well-ordered superstructures (Fig. 2.1 c) because of (1) complementary triple H-bonds along

one spatial axis (x), (2) large aromatic surfaces that drive aggregation via $\pi\cdots\pi$ stacking along an orthogonal axis (z), and (3) solubilizing alkyl chains appended to each aromatic core that can interact along the third orthogonal axis (y) (Fig. 2.1 b). Chiral side chains have been introduced onto the DPP donor **1** so that distinct Cotton effects arising as a result of the formation of chiral superstructures can provide additional information on the emergence of order.[139] Variable-temperature (VT) UV-Vis and circular dichroism (CD) spectroscopic measurements revealed that the PDIs associate to disordered DPP aggregates, which subsequently reorganize into helical heteroaggregates of a single chirality. A new thermodynamic model was developed that quantifies the binding parameters (ΔH° and ΔS°) associated with each interaction (H-bonding and $\pi\cdots\pi$ stacking) and, with the aid of electronic structure theory calculations, elucidates the subtle supramolecular cues that induce the transition from disordered aggregates into well-defined helices.

2.2 Theoretical Equations

DFT Calculations of geometries, energies, and structural properties were performed with *Gaussian 09*, Revision B.01.[140] Donor and acceptor geometries were optimized using Becke's three-parameter exchange functional[141] combined with the Lee–Yang–Parr correlation functional[142] (B3LYP), and the 6-31G(d,p) basis set[143] on an ultrafine grid using tight convergence criteria. Minimization of structure was confirmed via frequency calculations, and all were found to be minimum energy structures. Enthalpies of H-bonding and $\pi\cdots\pi$ stacking were calculated from converged fragments at the B3LYP/6-31G(d,p) level of theory with identical grid and convergence criteria. The carbon lengths of the alkyl chains within **1** and **3** were reduced to one or two to increase the speed of the calculations.

2.2.1 Aggregate Modeling

Changes in the UV-Vis or CD spectra of DPPs, PDIs, or mixtures thereof were induced by changing the sample temperature or concentration. This is the result of the formation or disassembly of aggregates of varying size composed of DPPs and/or PDIs in differing local environments with differing propensity to absorb light at various wavelengths. Accordingly, equilibrium constants, K_a's, can be quantified by first defining a model that includes the appropriate set of equilibria, calculating the hypothetical concentrations of equilibrium species at each temperature or concentration, and finally fitting the resulting data to the spectra and their changes. Fittings were conducted in Microsoft Excel 2010 using the Evolutionary Solving method within the Solver feature by minimizing the total sum of squared residuals (SSR, eq 1), where w_i are the weights assigned to each absorbance.

$$SSR = \sum_i w_i (A_i^{exp} - A_i^{calc})^2 \tag{1}$$

When appropriate, two or more experiments (e.g., VT UV-Vis and CD) are fit simultaneously to the same enthalpy/entropy parameters to minimize the resulting error.

2.2.2 Aggregation of 1 into Homoaggregates (Isodesmic Model)

To model the homoaggregation of **1**, we assume a two-state system, where the fully monomeric **1** and fully aggregated **1** each have a unique temperature-independent extinction coefficient. The observed absorbance changes in a VT UV-Vis experiment were found to fit well to the simplest infinite association model, the isodesmic model, which assumes the association by $\pi \cdots \pi$ stacking between aromatic moieties are equivalent regardless of length of the stack:

$$K = \frac{[(DPP)_{n+1}]}{[(DPP)_n][DPP]} \tag{2}$$

A commonly overlooked aspect is that the value of K_a derived from the fitting process is typically a macroscopic K_a that does not take into account that there are two faces to which each **1** molecule can associate. While a technicality in terms of reporting K_a's within the literature, it is of crucial importance when comparing the experimentally derived thermodynamic parameters to those obtained via computational chemistry, which describe the *microscopic* association process. Assuming the H-bonding moieties of **1** do not participate in $\pi\cdots\pi$ stacking, there are four identical pathways by which two DPP molecules can preferentially associate, the microscopic association constant, K_1, can be defined as:

$$K = 4K_1 = \frac{[(DPP)_{n+1}]}{[(DPP)_n][DPP]} \tag{3}$$

$$[DPP]_t = DPP + 2[DPP]_2 + 3[DPP]_3 + 4[DPP]_4 \ldots \tag{4}$$

It should be noted that due to the flexibility of **1**, K_1 itself includes all possible binding configurations between two faces of **1**. This assumption is necessary as there are likely several different configurations occurring simultaneously in the experiments. Equations 3 and 4 can be combined to give:

$$[DPP]_t = [DPP] + 2(4K_1)[DPP]^2 + 3(4K_1)^2[DPP]^3 +$$

$$4(4K_1)^3[DPP]^4 \ldots \tag{5}$$

$$[DPP]_t = DPP \sum_{n=1}^{\infty} n(4K_1[DPP])^{n-1} \tag{6}$$

Equation 5 can be re-expressed as an infinite series to give:

$$\sum_{n=1}^{\infty} nx^{n-1} = \frac{1}{(1-x)^2} \tag{7}$$

$$[DPP]_t = \frac{[DPP]}{(1-4K_1[DPP])^2} \tag{8}$$

Solving for [DPP] gives eq 9:

$$[DPP] = \frac{8K_3[DPP]_t + 1 - \sqrt{16K_1[DPP]_t + 1}}{32K_1{}^2[DPP]_t} \tag{9}$$

To fit the VT UV-Vis spectrum, K_a's are generated from the van't Hoff equation (eq 10) and are then used to calculate the hypothetical absorbance at each temperature (eq 11). The theoretical data is then fit to the experimental spectroscopic data by minimizing the SSR (eq 1) using the themodynamic parameters ($\Delta H°$ and $\Delta S°$) and the extinction coefficients as fitting parameters.

$$K = e^{-\Delta H^0/RT + \Delta S^0/R} \tag{10}$$

$$A = ([DPP]_t - [DPP])\varepsilon_{aggregate} + [DPP]\varepsilon_{monomer} \tag{11}$$

2.2.3 Assembly of 1 and 3 into Heteroaggregates

Because the ratio of **1:3** in solution (2:1) and the higher number of H-bonds resulting from complementary imides and diamidopyridines, we assume homoaggregation of **3** does not occur to an appreciable extent under the experimental conditions because **3** will preferentially form heteroaggregates, and homoaggregation is thus not included in our model. This assumption is fully supported by UV-Vis and CD evidence in Figure 3. Since strong homoaggregation of **3** occurs without a resulting signal in the CD spectra, our model presumes the **1** molecules are present in a broad distribution of chain lengths as a result of isodesmic stacking as dictated by a macroscopic K_a ($4K_1$) determined previously. The binding of **3** to each of these stacks can be described by two K_a's: K_2 and K_3. The former describes the strength of association of one **3** molecule to a **1** stack of any length that does not already contain **3**. As there are two points by which H-bonding takes place in **3** and n points on a stack of **1** (where n denotes the number of residues), the macroscopic K_a describing this event is $2nK_2$. K_3 describes the binding strength of

additional **3** molecules to **1** stacks already containing **3** molecules and includes (1) the additional binding energy yielded as a result of $\pi\cdots\pi$ stacking between two PDI moieties and (2) the benefit of chelate cooperativity. Because of these additional interactions, we assume that $K_2 \neq K_3$. For the VT experiments of a solution containing both **1** and **3** (a) and b) of Fig. 2.3), precipitation of heteroaggregates occurred below 10 °C, which prevented the assessment of any new bands at low temperatures.

$$K = 4K_1 = \frac{[(DPP)_{n+1}]}{[(DPP)_n][DPP]} \tag{3}$$

$$2nK_2 = \frac{[(DPP)_n(PDI)]}{[(DPP)_n][(PDI)]} \tag{12}$$

$$K_2K_3 = \frac{[(DPP)_n(PDI)_m]}{[(DPP)_n][(PDI)_{m-1}][(PDI)]} n \geq m \tag{13}$$

In eq 13, m is an arbitrary positive integer that is less than n. The components included in the mass balance equation that defines the total concentration of DPP ([DPP]$_t$) for this particular system consist of a series of equations defined by the length of the DPP chain, n:

For $(DPP)_t$

$$n = 1 \quad [DPP] + [(DPP)(PDI)]$$

$$n = 2 \quad 2[DPP_2] + 2[(DPP)_2(PDI)] + 2[(DPP)_2(PDI)_2]$$

$$n = 3 \quad 3[DPP_3] + 3[(DPP)_3(PDI)] + 3[(DPP)_3(PDI)_2] +$$

$$3[(DPP)_3(PDI)_3]$$

$$\downarrow$$

$$n = \infty$$

Substituting in eqs 3, 12, and 13 give:

For $(DPP)_t$

$n = 1$ $[DPP] + (2K_2)[DPP][PDI]$

$n = 2$ $2(4K_1)[DPP]^2 + 2(4K_1)(4K_2)[DPP]^2[PDI] +$

$2(4K_1)(4K_2)(K_2K_3)[DPP]^2[DPP]^2[PDI]^2$

$n = 2$ $3(4K_1)^2[DPP]^3 + 3(4K_1)^2(6K_2)[DPP]^3[PDI] +$

$3(4K_1)^2(6K_2)(K_2K_3)[DPP]^3[PDI]^2 +$

$3(4K_1)^2(6K_2)(K_2K_3)^2[DPP]^3[PDI]^3$

$\downarrow$

$n = \infty$

From the equations above, the mass balance equation can be rewritten as:

$[DPP]_t = [DPP] \sum_{n=1}^{\infty}((\text{n}(4K_1[DPP])^{n-1})$

$(1 + 2nK_2[PDI] \sum_{i=0}^{n-1}(K_2K_3[PDI])^i))$ (14)

Using relationship 15, eq. 14 can be rewritten as eq 16.

$\sum_{i=0}^{n-1} x^i = \frac{1-x^n}{1-x}$ (15)

$[DPP]_t = [DPP] \sum_{n=1}^{\infty}((\text{n}(4K_1[DPP])^{n-1})(1 +$

$\frac{2nK_2[PDI] - 2nK_2^{n+1}K_3^{n}[PDI]^{n+1}}{1-K_2K_3[PDI]}))$ (16)

Expanding eq 16 gives eq 17, which can be solved using eqs 7 and eq 18 to give eq 19.

$$[DPP]_t = [DPP] \sum_{n=1}^{\infty} \text{n}(4K_1[DPP])^{n-1} + \frac{2K_2[PDI][DPP]}{1 - K_2K_3[PDI]}$$

$$\sum_{n=1}^{\infty} \text{n}^2(4K_1[DPP])^{n-1} - \frac{2K_2{}^2K_3[PDI]^2[DPP]}{1-K_2K_3[PDI]}$$

$$\sum_{n=1}^{\infty} \text{n}^2(4K_1K_2K_3[PDI][DPP])^{n-1} \tag{17}$$

$$\sum_{n=1}^{\infty} \text{n}^2 x^{n-1} = \frac{1+x}{(1-x)^3} \tag{18}$$

$$0 = -[DPP]_t + \frac{[DPP]}{(1-4K_1[DPP])^2} + \frac{2K_2[PDI][DPP]+8K_1K_2[PDI][DPP]^2}{(1-K_2K_3[PDI])(1-4K_1[DPP])^3} -$$

$$\frac{2K_2{}^2K_3[PDI]^2[DPP]+8K_1K_2{}^3K_3{}^2[PDI]^3[DPP]^2}{(1-K_2K_3[PDI])(1-4K_1K_2K_3[PDI][DPP])^3} \tag{19}$$

For $(DPP)_t$

$n = 1$ $[(DPP)(PDI)]$

$n = 2$ $[(DPP)_2(PDI)] + 2[(DPP)_2(PDI)_2]$

$n = 3$ $[(DPP)_3(PDI)] + 2[(DPP)_3(PDI)_2] +$

$3[(DPP)_3(PDI)_3]$

$\downarrow$

$n = \infty$

Substituting in eqs 3, 12, and 13 gives:

For $(DPP)_t$

$n = 1$ $(2K_2)[DPP][PDI]$

$n = 2$ $(4K_1)(4K_2)[DPP]^2[PDI] +$

$2(4K_1)(4K_2)(K_2K_3)[DPP]^2[PDI]^2$

$n = 3$ $(4K_1)^2(6K_2)[DPP]^3[PDI] +$

$2(4K_1)^2(6K_2)(K_2K_3)^2[DPP]^3[PDI]^2 +$

$3(4K_1)^2(6K_2)(K_2K_3)^2[DPP]^3[PDI]^3$

$\downarrow$

$n = \infty$

From the equations above, the mass balance equation can be rewritten as:

$$[PDI]_t = [PDI] + 2K_2[PDI][DPP] \sum_{n=1}^{\infty}((\text{n}(4K_1[DPP]^{n-1})$$

$$(\sum_{i=0}^{n-1}((\text{i} + 1)(K_2K_3[PDI])^i)) \tag{20}$$

Using relationship 21, eq 20 can be rewritten as eq 22.

$$\sum_{i=0}^{n-1}(\text{i} + 1)x^i = \frac{1-(n+1)x^n+nx^{n+1}}{(1-x)^2} \tag{21}$$

$$[PDI]_t = [PDI] + \frac{2K_2[PDI][DPP]}{(1-K_2K_3[PDI])^2}$$

$$\sum_{n=1}^{\infty}((\text{n}(4K_1[DPP]^{n-1})\,(1-(n+1)(K_2K_3[PDI])^n +$$

$$n(K_2K_3[PDI])n + 1)) \tag{22}$$

Expanding eq 22 gives eq 23, which can be rearranged to give eq 24 .

$$[PDI]_t = [PDI] + \frac{2K_2[PDI][DPP]}{(1-K_2K_3[PDI])^2}$$

$$\sum_{n=1}^{\infty}((\text{n}(4K_1[DPP]^{n-1} - n^2(4K_1[DPP])^{n-1}\,(K_2K_3[PDI])^n -$$

$$n(4K_1[DPP])^{n-1}\,(K_2K_3[PDI])^n +$$

$$n^2(4K_1[DPP])^{n-1}(K_2K_3[PDI])^{n+1}) \tag{23}$$

$$[PDI]_t = [PDI] + \frac{2K_2[PDI][DPP]}{(1-K_2K_3[PDI])^2}$$

$$\sum_{n=1}^{\infty}((\text{n}(4K_1[DPP]^{n-1} - \left(K_2{}^2K_3{}^2[PDI]\right)^2 -$$

$$(K_2K_3[PDI])n^2(4K_1K_2K_3[DPP][PDI])^{n-1} -$$

$$(K_2K_3[PDI])n(4K_1K_2K_3[DPP][PDI])^{n-1} \tag{24}$$

Equation 24 can be further expanded to give eq 25, which can be solved using eqs 7 and 18 to give eq 26.

$$[PDI]_t = [PDI] + \frac{2K_2[PDI][DPP]}{(1-K_2K_3[PDI])^2} \sum_{n=1}^{\infty} \text{n}(4K_1[DPP]^{n-1} +$$

$$\frac{2K_2{}^3K_3^2[PDI]^3[DPP]- 2K_2{}^2K_3[PDI]^2[DPP]}{(1-K_2K_3[PDI])^2}$$

$$\sum_{n=1}^{\infty} \text{n}^2(4K_1K_2K_3[PDI][DPP]^{n-1} - \frac{2K_2{}^3K_3^2[PDI]^2[DPP]}{(1-K_2K_3[PDI])^2}$$

$$\sum_{n=1}^{\infty} \text{n}^2(4K_1K_2K_3[PDI][DPP]^{n-1} \tag{25}$$

$$0 = -[PDI]_t + [PDI] + \frac{2K_2[PDI][DPP]}{(1-K_2K_3[PDI])^2(1-4K_1[DPP])^2} +$$

$$\frac{\left(2K_2^3K_3^2[PDI]^3[DPP]-2K_2^2K_3[PDI]^2[DPP]\right)\left(1-4K_1K_2K_3[PDI][DPP]\right)}{(1-K_2K_3[PDI])^2(1-4K_1K_2K_3[PDI][DPP])^3} -$$

$$\frac{2K_2^2K_3[PDI]^2[DPP]}{(1-K_2K_3[PDI])^2(1-4K_1K_2K_3[PDI][DPP])^2} \tag{26}$$

Equations 19 and 26 can be expressed as two multivariable functions, 27 and 28:

$$\int ([PDI],[DPP]) = -[DPP]_t + \frac{[DPP]}{(1-4K_1[DPP])^2} +$$

$$\frac{2K_2[PDI][DPP]+8K_1K_2[PDI][DPP]^2}{(1-K_2K_3[PDI])(1-4K_1[DPP])^3} -$$

$$\frac{2K_2^2K_3[PDI]^2[DPP]+8K_1K_2^3K_3^2[PDI]^3[DPP]^2}{(1-K_2K_3[PDI])(1-4K_1K_2K_3[PDI][DPP])^3} \tag{27}$$

$$g([PDI],[DPP]) = -[PDI]_t + [PDI] +$$

$$\frac{2K_2[PDI][DPP]}{(1-K_2K_3[PDI])^2(1-4K_1[DPP])^2} +$$

$$\frac{\left(2K_2^3K_3^2[PDI]^3[DPP]-2K_2^2K_3[PDI]^2[DPP]\right)(4K_1K_2K_3[PDI][DPP])}{(1-K_2K_3[PDI])^2(1-4K_1K_2K_3[PDI][DPP])^3} -$$

$$\frac{2K_2^2K_3[PDI]^2[DPP]}{(1-K_2K_3[PDI])^2(1-4K_1K_2K_3[PDI][DPP])^2} \tag{28}$$

Thus, at any given value of K_1, K_2, K_3, $[DPP]_t$, and $[PDI]_t$, eqs 27 and 28 can be iteratively converged unto $f([PDI],[DPP]) = g([PDI],[DPP]) = 0$, giving [PDI] and [DPP].

Accordingly, Newton's Method was implemented in Microsoft Excel with each two columns corresponding to an iteration:

$$[DPP]_{n+1} = [DPP]_n - \frac{\int ([PDI]_n,[DPP]_n)}{\frac{\partial}{\partial [PDI]_n}\int ([PDI]_n,[DPP]_n)}$$

$$[PDI]_{n+1} = [PDI]_n - \frac{g([PDI]_n,[DPP]_{n+1})}{\frac{\partial}{\partial [PDI]_n}g([PDI]_n,[DPP]_{n+1})}$$

$$[DPP]_{n+2} = [DPP]_{n+1} - \frac{\int ([PDI]_{n+1},[DPP]_{n+1})}{\frac{\partial}{\partial [PDI]_{n+1}}\int ([PDI]_{n+1},[DPP]_{n+1})}$$

$$[PDI]_{n+2} = [PDI]_{n+1} - \frac{g([PDI]_{n+1},[DPP]_{n+2})}{\frac{\partial}{\partial [PDI]_{n+1}}g([PDI]_{n+1},[DPP]_{n+2})}$$

and so forth until convergence is obtained.

To calculate the theoretical UV-Vis and CD data for the fitting, we assume any two or more molecules of **3** in the $\pi\cdots\pi$ stacks will contribute to the absorbance band at 615 nm with each residue exhibiting a temperature-independent extinction coefficient (ε_2). All molecules of **3** in any other state, including monomers and heteroaggregates with only one molecule of **3**, exhibit a different extinction coefficient (ε_1), which is equivalent to the initial absorbance observed at 615 nm prior to the onset of heteroaggregation.

All heteroaggregates with one molecule of **3** can be expressed by eq 29, which can be solved using eq 7 to yield eq 30:

$$\sum_{n=1}^{\infty}[(DPP)_n(PDI)] = 2K_2[DPP][PDI]\sum_{n=1}^{\infty} n(4K_1[DPP])^2 \quad (29)$$

$$\sum_{n=1}^{\infty}[(DPP)_n(PDI)] = \frac{2K_2[DPP][PDI]}{(1-4K_1[DPP])^2} \quad (30)$$

From the Beer–Lambert Law, the theoretical absorbance can then be calculated as:

$$A = \left([PDI] + \frac{2K_2[DPP][PDI]}{(1-4K_1[DPP])^2}\right)\varepsilon_1 + \left([PDI]_t - \right.$$
$$\left. [PDI]\frac{2K_2[DPP][PDI]}{(1-4K_1[DPP])^2}\right)\varepsilon_2 \tag{31}$$

Since the transition temperature—that is the temperature in which the bands corresponding to an intermolecular electronic transition between molecules of **3** arise—for the CD spectrum is significantly less than the transition observed by UV-Vis, we assume that monomers and heteroaggregates containing either one or two molecules of **3** yield no signal. That is, at the very minimum, three molecules of **3** need to be $\pi\cdots\pi$ stacked to obtain an ordered aggregate. The total concentration of all aggregates containing two bound PDI molecules can be expressed as:

$$\sum_{n=1}^{\infty}[(DPP)_n(PDI)_2] =$$
$$2(4K_1)(2K_2)(K_2K_3)[DPP]^2[PDI]^2\sum_{n=1}^{\infty}(n +$$
$$1)(4K_1K_2K_3[DPP])^{n-1} \tag{32}$$

Equation 32 can be solved with eq 33 to give eq 34:

$$\sum_{n=1}^{\infty}(n+1)x^{n-1} = \frac{2-x}{(1-x)^2} \tag{33}$$

$$\sum_{n=1}^{\infty}[(DPP)_n(PDI)_2] =$$
$$\frac{32K_1K_2^2K_3[DPP]^2[PDI]^2-64K_1^2K_2^3K_3^2[DPP]^3[PDI]^2}{(1-4K_1K_2K_3[DPP])^2} \tag{34}$$

Thus, the CD signal can be calculated as:

$$CD = ([PDI]_t - [PDI] - \frac{2K_2[DPP][PDI]}{(1-4K_1[DPP])^2} -$$
$$\frac{32K_1K_2^2K_3[DPP]^2[PDI]^2-64K_1^2K_2^3K_3^2[DPP]^3[PDI]^2}{(1-4K_1K_2K_3[DPP])^2} \tag{35}$$

where X is a proportionality constant.

To fit the VT UV-Vis and CD spectra, K_a's are generated from the van't Hoff equation (eq 10) and are then used to calculate the hypothetical absorbance and CD at each temperature (eqs 31 and 35). The theoretical data is then fitted to the experimental UV-Vis and CD data simultaneously by minimizing the SSR (eq 1) using the thermodynamic parameters ($\Delta H°$ and $\Delta S°$), the extinction coefficients, and CD proportionality constant as fitting parameters.

2.3 Results

DPP donors **1** and **2** have diamidopyridine (DAP) groups, which can form triple H-bonds with the diimide groups of PDI acceptor **3** (Fig. 2.1 a). The donors differ only by their *N*-alkyl chains: **1** possesses homochiral (*S*)-2-methylbutyl side chains, and **2** has racemic 2-ethyloctyl chains. Like complex biological systems, these assemblies form from the combined effects of multiple noncovalent interactions working in unison, and the aim of this study is to derive models that describe how the effects of each individual interaction contribute to the formation of the resulting superstructure. Initially, the homoaggregation of **1** and **3** were analyzed independently by UV-Vis spectroscopy to understand the role homoaggregation plays in the formation and structure of heteroaggregates. The UV-Vis spectrum of **1** in toluene displays absorption maxima at 538 and 580 nm at 25 °C, which are the result of dipole allowed $S_0 - S_1$ electronic transitions.[144] Upon cooling, these bands undergo bathochromic shifts with increasing sharpness, which are spectral signatures of J-type aggregation (Fig. 2.2 a).
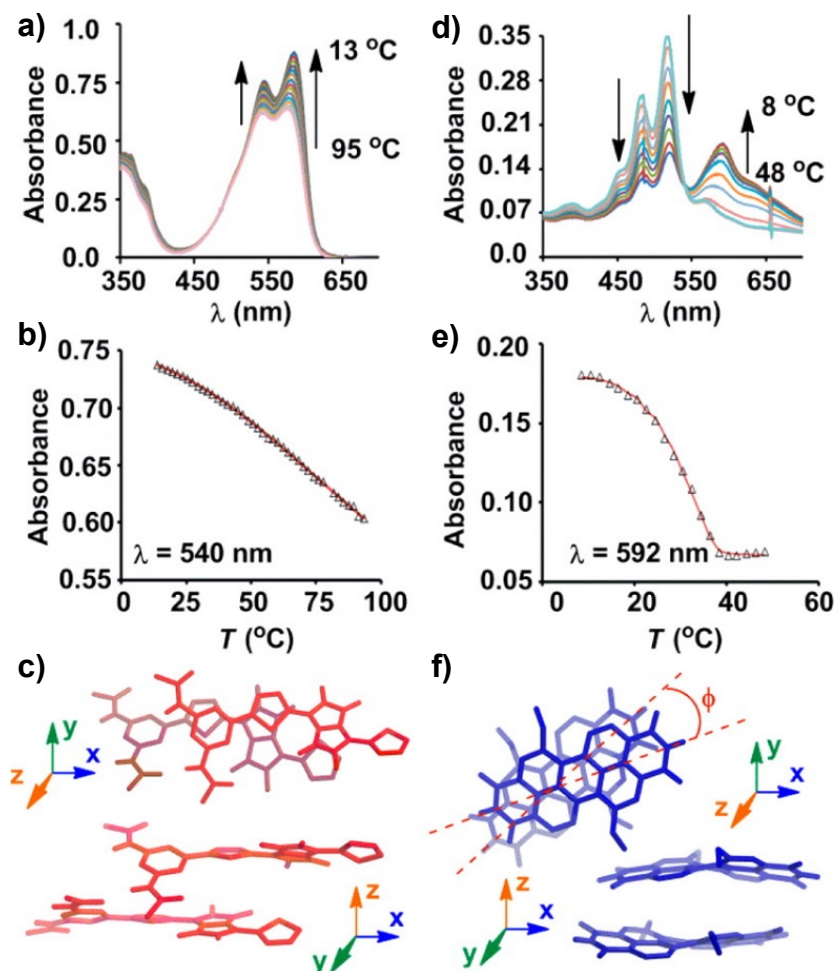
Fig. 2.2 (a) VT UV-Vis spectra of a 20 μM solution of **1** in toluene. (b) The absorption peak at 540 nm in the VT UV-Vis of **1** fit to an isodesmic model. (c) Top and side view of a DFT structure of a $\pi\cdots\pi$ stacked DPP dimer. (d) VT UV-Vis spectra of a 35 μM solution of **3** in toluene. (e) The absorption peak at 592 nm in the VT UV-Vis of **3**. (f) Top and side view of a DFT structure of a $\pi\cdots\pi$ stacked PDI dimer. Dashed lines are run along the N–N′ axis, and are shown to indicate the twist angle, φ, between the stacked PDIs.

Although π-stacked chromophores with chiral side chains often form chiral superstructures,[139] the absorbance intensities of **1** exhibit a sigmoidal dependence with temperature and no signal was observed in VT CD experiments. These observations are characteristic of isodesmic stacking, where the K_a describing the $\pi\cdots\pi$ stacking is constant regardless of aggregate size.[97] By fitting the changes in absorbance of **1** with changes in temperature to an isodesmic model,[133] an excellent fit was obtained to provide $\Delta H°$ and $\Delta S°$ values of -7.4 ± 0.5 kcal mol^{-1} and -3.0 ± 2.0 eu, respectively, indicating the $\pi\cdots\pi$

stacking is enthalpically driven (Fig. 2.2 b). DFT calculations (B3LYP/6-31G(d,p)) on homoaggregates of a DPP that has methyl side chains to simplify the calculation revealed a slipstacked binding geometry with thiophenes overlapping the DPP cores (c and d of Fig. 2). This calculated structure is consistent with the UV-Vis data and a similar slip-stacked geometry observed previously in an X-ray crystal structure of DPP−thiophene oligomers.14 The energy of binding, $\Delta E = -10.5$ kcal mol−1, from the DFT calculations agrees well with the $\Delta H°$ derived from the fitting.

H-bonding is known to affect the supramolecular assembly of 1,7-substituted PDIs, so the homoaggregation of **3** was also investigated by VT UV-Vis spectroscopy. The UV-Vis spectra of 1,7-substituted PDIs typically display characteristic peaks arising from the $S_0 - S_1$ transition[120] that are broadened because of twisting in the perylene ring system[145] that inhibits aggregation beyond π-stacked dimers.[146-147] Previously studied PDIs without *N*-substituents display a sharp peak that are assigned to the J-aggregation of $\pi\cdots\pi$ stacked dimers interconnected by H-bonding.[148-150] Alternatively, mono-*N*-substituted PDIs possessing complementary melamine moieties H-aggregate into helical superstructures as a result of intermolecular H-bonding.[123] For PDI **3**, the UV-Vis spectra revealed a sharp absorbance maximum at 520 nm in toluene with a pronounced vibronic fine structure. Upon cooling, these peaks decrease with a concomitant increase of a broad band with a maximum at 592 nm (Fig. 2.2 e). These spectral changes are similar to non-1,7-substituted PDIs whose $\pi\cdots\pi$ aggregation is intermediate between J- or H-type[147] as a result of rotationally displaced stacked PDIs.[151] DFT calculations of a $\pi\cdots\pi$ stacked dimer of **3** revealed an offset, φ, of 22° between the long axes (Fig. 2.2 f), and thus, we conclude that the new absorption peak corresponds to a similar rotationally displaced stacking geometry. A plot of the absorbance at 592 nm vs temperature reveals negligible

aggregation above 37 °C. Below 37 °C, the absorption increases quickly, suggesting nucleation–growth assembly [97] —where an initial disfavored binding event precludes association until a critical temperature is reached, after which a new thermodynamically favored equilibrium drives the assembly into π-stacked superstructures (Fig. 2.2 f).[92-93, 97, 125] Suspecting intermolecular H-bonding plays a key role in assembly, the VT UV-Vis experiment was repeated with a bis-*N*-cyclohexyl derivative of **3** or in 3% DMSO in toluene, both of which inhibit H-bonding. No spectral changes that indicate π-stacking were observed in either control experiment, confirming that H-bonding promotes the π-stacking of **3**. These investigations into the homoaggregation of **1** and **3** are necessary to understand how the self-assembly of the individual components contributes to the structure and assembly of the multicomponent heteroaggregate assemblies.

Heteroaggregation arising from H-bonding and $\pi \cdots \pi$ stacking was investigated by VT UV-Vis spectroscopy on a 2:1 mixture of **1** and **3**, respectively, in toluene. At 40 °C, the spectrum is a linear composite of the individual spectra (Fig. 2.3 a), indicating that mixed π-heteroaggregates are not present at high temperature. Upon cooling, the absorbance maxima of **3** decrease and two new bands arise at 563 and 615 nm, which are assigned to a $S_0 - S_1$ transition from the $\pi \cdots \pi$ stacking of **3**. Several aspects of the spectrum indicate heteroaggregate formation: (1) the absorbance at 615 nm begins to increase in the mixture at 21 °C, which is a much lower temperature than was observed for the onset of homoaggregation of **3** (39 °C); (2) the new bands at 563 and 615 nm are much sharper than the broad peaks formed by homoaggregates of **3**, suggesting J-type aggregation, meaning
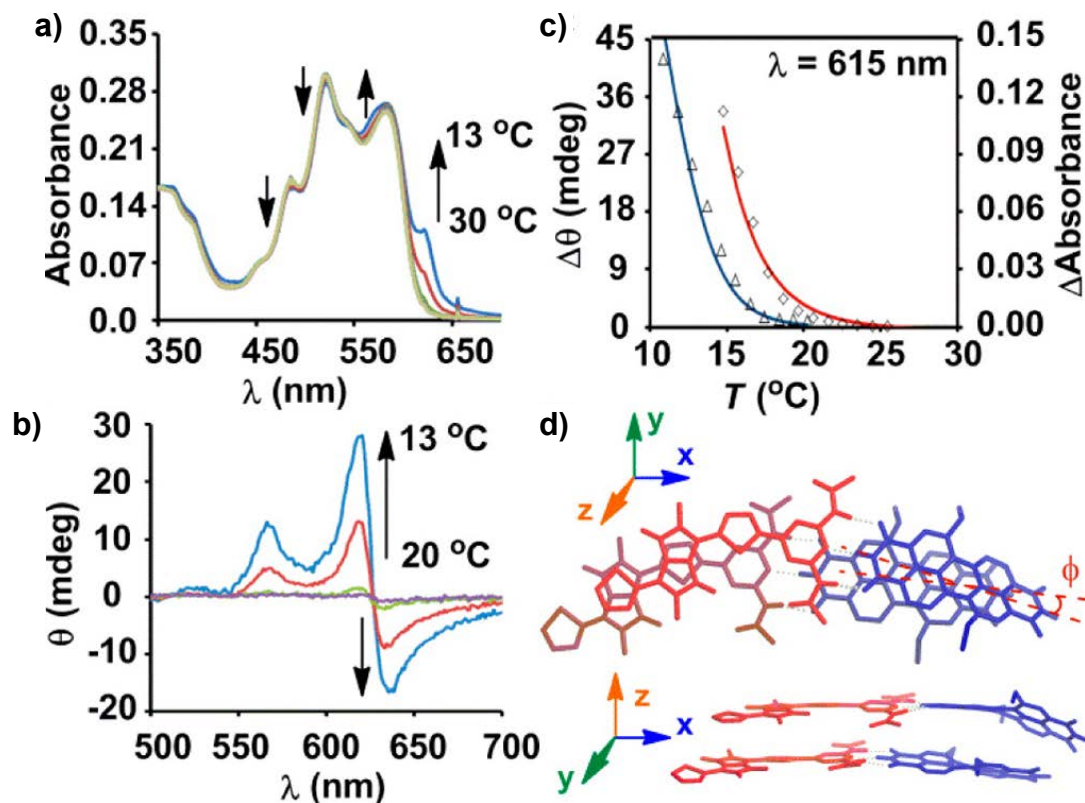
Fig. 2.3 (a) VT UV-Vis and (b) CD spectra of a 70 µM solution of **1** in toluene with 0.5 mol equiv of **3**. (c) The absorbance (◇) and ellipticity (△) at 615 nm obtained by VT UV-Vis and CD respectively fit to a cooperative helix formation model. (d) Top and side view of the DFT structure of the H-bonded and π···π stacked 1:3 dimer. Dashed lines are run along the N–N′ axis, and are shown to indicate the twist angle, φ, between the stacked PDIs.

the π-stacked PDIs adopt a different geometry in the heteroaggregates; and (3) the change in the absorption at 615 nm for the mixture of **1** and **3** is more gradual (Fig. 2.3 c) than for the homoaggregates of **3**, suggesting that homoaggregation pathways are suppressed and a different assembly mechanism is operating that is driven by the triple H-bonding between **1** and **3**.

Prior to the appearance of the PDI π-stacking bands at 563 and 615 nm, the transitions previously assigned to π-stacking of **1** (538 and 580 nm) increase steadily with decreasing temperature, suggesting extensive homoaggregation of **1** precedes heteroaggregate formation. A bisignated Cotton effect, with peaks at 563 and 615 nm, matching the π-stacking peaks of the achiral PDI, appeared in the VT CD spectra. The

bisignated effect is a consequence of electronic coupling between conjugated segments in a helical array (Fig. 2.3 b).[152] Notably, the transition temperature in the VT CD spectrum of the heteroaggregates is 5° lower than in the UV-Vis measurements, suggesting that only after the association of several molecules of **3** onto disordered aggregates of **1** does the rearrangement into chiral heteroaggregate helices occur (Fig. 2.3 c), and the emergent chirality in these superstructures is the direct result of the PDI solubilizing chains interacting along the y-axis. The VT UV-Vis experiments were repeated in a mixture of **2** and **3** (Fig. S5 in SI), and while the same trends were observed in the VT UV-Vis spectra, no Cotton effect arose in the CD spectra of **2** and **3**. The structure of the heteroaggregate of **1** and **3** was modeled by DFT calculations using methyl and ethyl solubilizing chains on DPP and PDI, respectively. While the relative orientations of the DPPs in the heteroaggregates remain relatively unchanged compared to those in the homoaggregates, the π-offset, φ, between PDIs in the heteroaggregates (11°, Fig. 2.3 d) changed significantly compared to PDIs in the homoaggregates (22°), indicating that the preferred conformation of the DPPs dictates the π⋯π stacking angle in the heteroaggregate superstructure. The assessment of PDI J-aggregation from the VT UV-Vis spectrum of the heteroaggregate is supported by the head-to-tail arrangement of the PDIs in the calculated structure (Figure 2.3 d).[153] These observations suggest that a new assembly mechanism that has not been described previously in supramolecular systems is directing the formation of these hierarchical donor–acceptor structures.

The spectroscopic data were used to derive a new quantitative assembly model that describes formation of heteroaggregates that arise from both H-bonding and π⋯π stacking. The corresponding thermodynamic parameters for each interaction were obtained by fitting the changes in absorption with temperature to this model. There exist few quantitative
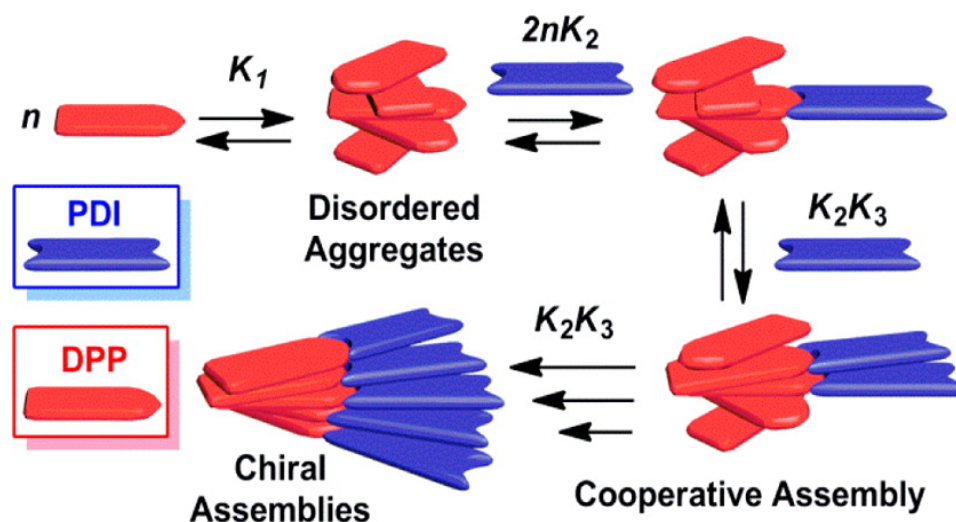
Fig. 2.4 The proposed model for the heteroaggregation of the DPPs (red tiles) and PDIs (blue tiles) into chiral assemblies.

models that describe the formation of heteroaggregates that employ multiple orthogonal interactions.[92, 94, 133-134] The data indicate that PDIs bind to disordered stacks of DPPs to produce chiral superstructures (Fig. 2.4), which leaves an available H-bonding site on each PDI that can potentially be occupied by an additional DPP at higher concentrations. In the model (Fig. 2.4), disordered homoaggregates of **1** assemble isodesmically according to the microscopic binding constant K_1.

Since there are four identical pathways by which this process can occur, K_1 is one-fourth the experimentally observed macroscopic K_a. The initial association event of one molecule of **3** to a stack of **1** of any size is governed by microscopic association constant K_2 (Fig. 2.4). As there are two positions where H-bonding takes place in **3** and n points on a stack of **1**, where n denotes the number of residues, the macroscopic K_a is $2nK_2$. Further association of **3** to the stacks are described by K_2 and K_3, where K_3 is a dimensionless K_a that includes the energy contributions from $\pi \cdots \pi$ stacking and any chelate cooperativity effects[154-155] (Fig. 2.4) associated with the aggregation of **3** within the **1** stacks. The resulting mass balance equations can be written as infinite

series that describe the total concentration of each species, $[PDI]_t$ and $[DPP]_t$, as a function of n (eqs 14 and 20).

Equations 14 and 20 are both convergent and can be solved to obtain $[PDI]$ and $[DPP]$ for any value of K_1, K_2, K_3, $[PDI]_t$, and $[DPP]_t$. $\Delta H°$ and $\Delta S°$ corresponding to K_1 were fixed to the values previously obtained by studying the homoaggregation of **1** and held invariant. This new model can be used to make predictions about the assembly of hierarchical systems that form as a result of multiple orthogonal interactions, in particular when some of these interactions only arise in the heteroaggregate—a hallmark of complexity in biological assembly—and thus cannot be measured by studying the individual components. When both VT UV-Vis and CD measurements were simultaneously fit to the same parameter set, the $\Delta H°$ and $\Delta S°$ for K_2 (-24.1 ± 0.1 kcal mol^{-1} and -70 ± 2 eu) and K_3 (-13.5 ± 0.1 kcal mol^{-1} and -40 ± 1 eu) were obtained. These numbers compare well to the values of ΔE of -17.8 kcal mol^{-1} and -6.3 kcal mol^{-1}, respectively, found by electronic structure theory calculations, although the calculations may underestimate the enthalpy by not accounting fully for cooperative stabilization. These thermodynamic parameters indicate that K_2 is enthalpically driven, which is typical for H-bonded dimers. Interestingly, K_3 is also enthalpically driven, but an entropic penalty is associated with the rearrangement of **3** into J-aggregates, presumably because the contorted perylene rings disfavor this stacking geometry. Nevertheless, the enthalpy associated with π-aggregation overcomes the disfavorable entropy below room temperature, which drives heterosuperstructure formation upon cooling.

2.4 Summary

The self-assembly of heteroaggregates composed of π-conjugated donors and acceptors could lead to synthetic hierarchical structures with functional complexity comparable to their biological counterparts, but models are needed that can describe the complex milieu of interactions involved in superstructure formation. By studying the heteroaggregation of a DPP donor and PDI acceptor, a new model was developed that elucidates the subtle structural cues that induce the transition from a disordered aggregate into a chiral helix. Using this new model, all thermodynamic parameters were quantitatively determined, and both H-bonding and the subsequent helix formation process were found to be enthalpically favored but entropically disfavored. This new model could be used to create ordered superstructures of donors and acceptors, which are increasingly investigated in the context of photovoltaics and for understanding fundamental aspects of charge and energy transport in self-assembled systems. [45, 52, 77, 96, 115-131] It should be noted that, like the system described herein, natural self-assembled systems utilize multiple orthogonal noncovalent interactions that work in unison to form functional hierarchical nanostructures, thereby achieving "complexity out of simplicity", which remains an elusive goal for chemists.[156]

CHAPTER 3

COOPERATIVELY ASSEMBLING DONOR-ACCEPTOR SUPERSTRUCTRES DIRECT ENERGY INTO AN EMERGENT CHARGE SEPARATED STATE

3.1 Background

Natural systems achieve complex optical and electronic properties by employing an "emergence upon assembly" design approach, where new properties that are absent in the individual components arise upon forming hierarchical superstructures composed of pieces with appropriately matched orbital energies.[157-158] An example of such a system is the photosynthetic reaction center because the precise spatial arrangement of electronically complementary chromophores produces long-distance photoinduced charge separation.[5] There is a desire to recreate this bioinspired design strategy for artificial photosynthesis and organic electronics,[159-160] and a common method to prepare these materials is through covalently linking electron donors, acceptors, and light harvesting antenna systems.[73, 161-163] However as the building blocks grow larger and more complex, attempts to covalently link all the pieces confront the limits of synthetic chemistry. As an alternative, supramolecular assembly is increasingly employed to build superstructures that undergo photoinduced charge separation.[52, 73, 116, 122, 164-166] In doing so, scientists harness the inherent error correcting nature of noncovalent assembly and achieve structural complexity through significantly shorter syntheses. Chromophore arrays have been successfully prepared using hydrogen bonding (H-bonding),[108, 167-168] $\pi\cdots\pi$ stacking,[169] and other supramolecular approaches,[170-173] but how the superstructures affect the optoelectronic properties is still an area of investigation because only in a few of these systems have both assembly and charge generation been fully characterized. Thus, there is a need to develop
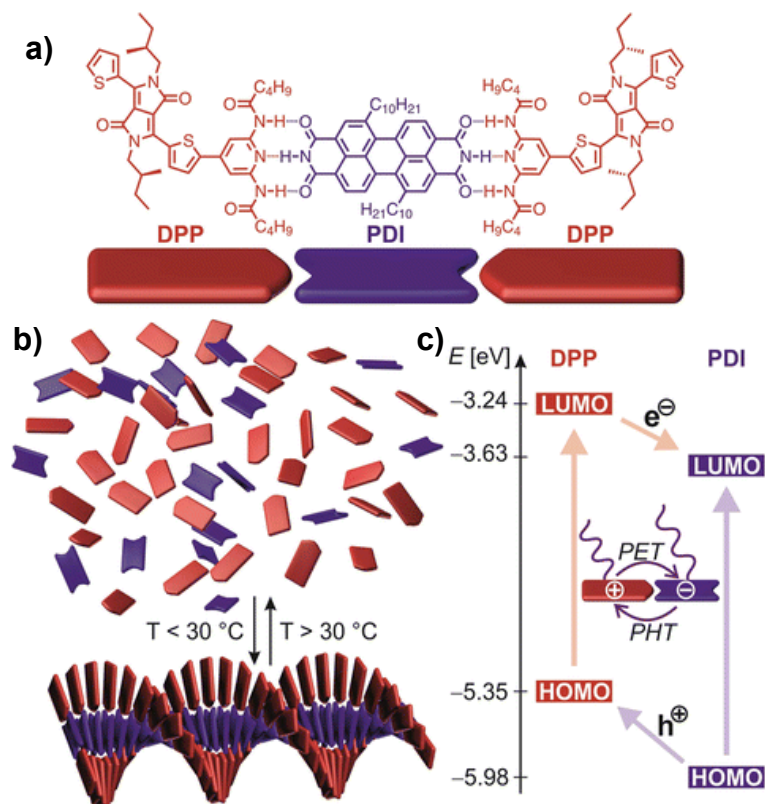
Fig. 3.1 (a) H-bonding brings the DPP donor (red) and the PDI acceptor (blue) together. (b) Upon cooling, superstructures arise from H-bonding and orthogonal π-stacking. (c) FMO scheme indicating possible photoinduced electron and hole transfer via donor or acceptor excitation.

more artificial photosynthetic systems that simultaneously (1) are composed of synthetically modular components, where frontier molecular orbital (FMO) levels, electronic coupling, and absorption can be systematically tuned, (2) assemble into architecturally complex superstructures, and (3) direct photochemical excitation into a charge separated state.

In the chapter 2, we described a supramolecular system composed of the electron-rich organic donor diketopyrrolopyrrole (DPP)[174] and the electron-poor organic acceptor perylene derived bisimide (PDI) (Fig. 3.1 a)[175] that forms 2:1 coassembled helical supramolecular polymers as a result of triple H-bonding between the PDI and the DPP and π–π stacking orthogonal to the H-bonding axis (Fig. 3.1 b).[34] Both donor and acceptor are

prepared in few synthetic steps, where changing the substituents on the DPPs or PDIs modify the bandgap and absorption maxima. Herein, we report the electronic and optical properties of these assemblies and demonstrate that charge transfer is directed by reversible supramolecular interactions. The two chromophores are electronically complementary in that the FMO levels are positioned such that upon photoexcitation, charge transfer can possibly occur by either hole transfer from PDI to DPP or by electron transfer from the DPP to the PDI (Fig. 1 c). Results of our photophysical studies confirm that indeed photoinduced electron transfer is not possible between the disaggregated individual components alone, but only emerges upon superstructure formation. This donor–acceptor system exemplifies how supramolecular assembly and FMOs can be synergistically designed to achieve emergent charge transfer in hierarchical organic superstructures.

3.2 Results

The system assembles into helical superstructures via a cooperative equilibrium that can be switched off or on by varying the temperature or concentration. At high temperature or low concentration, disaggregation is favored, while at low temperature and high concentration, entropically disfavored supramolecular polymerization drives the formation of superstructures with a 2:1 donor:acceptor ratio.

Having demonstrated the biomimetic assembly that uses multiple noncovalent interactions operating in concert, we proceeded to assess the capability of the system to undergo photoinduced charge separation and subsequent charge migration with the aim of creating a long-lived radical pair state that is a prerequisite for harvesting the resulting photochemical energy. The ground-state FMO energy levels of the individual DPP and PDI compounds were investigated by cyclic voltammetry (CV), UV–vis, and fluorescence spectroscopy to determine whether the components were properly designed to undergo

thermodynamically favored charge separation upon assembly. These studies revealed that electron transfer could proceed from the upper SOMO (−3.24 eV) of photoexcited DPP into the PDI LUMO (−3.63 eV) or by respective hole transfer from the lower SOMO (−5.35 eV) of photoexcited PDI into the DPP HOMO (−5.98 eV) with driving forces of −0.39 and −0.63 eV, respectively. (Appendix B, Table B1)   Variable temperature (VT) fluorescence spectroscopy was employed to determine if fluorescence quenching, indicative of charge separation, occurs upon temperature-induced aggregation. A 2:1 solution of DPP (45 μM) to PDI (23 μM) in toluene was prepared, and the fluorescence spectra were measured from 500–800 nm at 12 temperatures ranging from 70 to 20 °C. The solution was photoexcited at 356 nm (Fig. 3.2 a), where the DPP absorbance is three times greater than that of PDI, providing for quasiselective photoexcitation. As controls, individual components as well as a mixture where the PDI was replaced by its *N*,*N*′-dicyclohexyl-substituted derivative that is unable to aggregate were measured under the same conditions (Compound **4**).

3.2.1 Variable Temperature Fluorescence Measurements

The VT fluorescence shows that aggregation driven static quenching occurs as a likely result of charge separation, which we later confirm using femtosecond transient absorption (fs-TA) spectroscopy. As a thermally disaggregated sample (70 °C) is cooled down, the DPP fluorescence intensity initially increases (Fig. 3.2 a) because nonradiative decay of an excited state is typically promoted at higher temperatures (dynamic quenching). The fluorescence intensity reaches a maximum at 40 °C before it drops with decreasing temperatures, as a result of static quenching, and finally stabilizes at 20 °C. Most importantly, the absorbance of the sample at the excitation wavelength 356 nm does not change with temperature, (Appendix B Fig. B10)   and there is no decrease in DPP
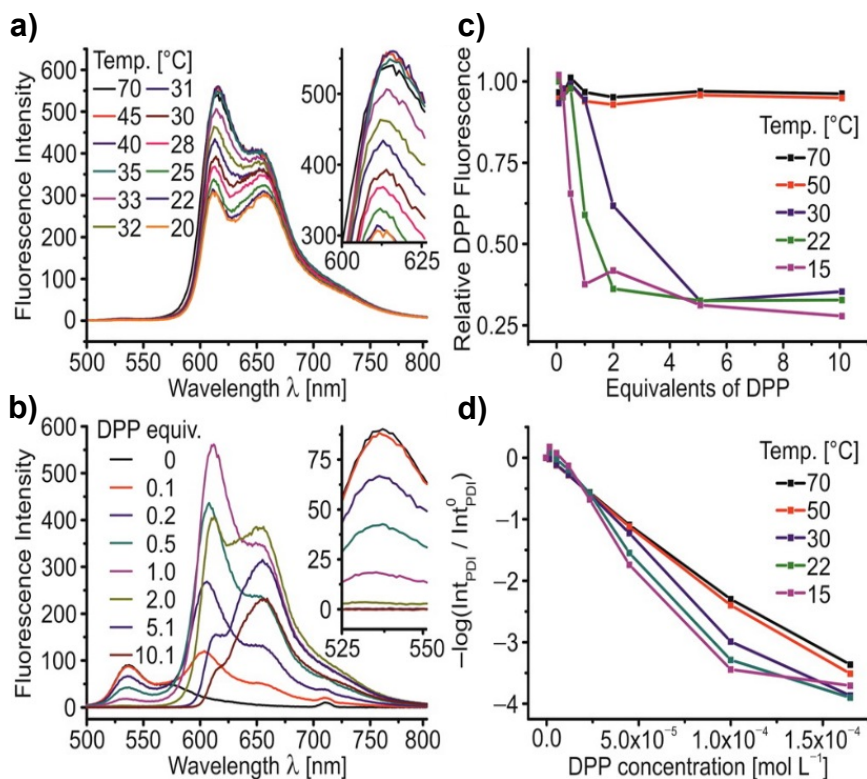
Fig. 3.2 (a) VT fluorescence spectra of a 2:1 DPP:PDI mixture (45 and 23 μM, respectively) in toluene (λEx = 356 nm). (b) Fluorescence titration at 30 °C (λEx = 356 nm), molar equivalents of DPP given based on PDI. (c) Relative DPP fluorescence intensity at various temperatures. (d) Fluorescence quenching of PDI with increasing DPP concentration at various temperatures.

fluorescence in the absence of the PDI, which means that aggregation-induced quenching is not occurring. This indicates that fluorescence quenching is an emergent property that arises with the noncovalent assembly of heterosuperstructures, which begin to form around 30 °C.[34] Further support for this concept comes from dynamic light scattering measurements, (Appendix B Table B4) showing that the formation of large (∼1–2 μm) superstructures occurs concomitantly with fluorescence quenching.

The effects of temperature and concentration on the aggregation induced quenching were further investigated by a VT fluorescence titration (Fig. 3.2 b). To a solution of PDI in toluene (25 μM), a solution of DPP in toluene (481 μM) was added, and the fluorescence spectra were measured at 356 and 483 nm excitation at five temperatures and seven

concentrations. The resulting spectra were compared to that of the individual components, so spectral changes that occur because of aggregation could be unambiguously assigned. The relative fluorescence intensity of the DPP (Fig. 3.2 c) is the ratio of DPP fluorescence in the mixture to that of DPP alone under the same conditions, and this plot depicts the quenching of DPP fluorescence that is induced by temperature and concentration-dependent heteroaggregation. Excess DPP units in the heteroaggregates can act as antennas transferring excitation energy toward the next donor–acceptor pair, thus explaining the observed quenching at DPP:PDI ratios >2:1. A similar analysis for the PDI is not possible since the DPP absorbs fluorescence photons of the PDI. This emission–absorption produces a linear plot at temperatures that disfavor aggregation, and the deviation from this linearity occurring at $T < 30$ °C (Fig. 3.2 d) indicates that the PDI fluorescence is partly quenched by the DPP because temperature-dependent heteroaggregation brings the donor and acceptor close enough for charge separation. Photoexcited PDI could transfer its energy to the DPP via Förster resonance energy transfer, another viable explanation for fluorescence quenching, but this possibility can be ruled out because the DPP would then exhibit a relative fluorescence intensity greater than unity, which was not observed. Terminal H-bonding is crucial for the superstructure formation,[34] and no fluorescence quenching can be observed for the *N,N*-dicyclohexyl protected PDI, which is incapable of H-bonding or superstructure formation (Appendix B).

3.2.2. Femtosecond Transient Absorption Spectroscopy (fs-TA)

To further investigate the photoinduced charge-transfer process, fs-TA experiments were performed at room temperature on the individual compounds and on the 2:1 DPP:PDI mixture in toluene. Photoexcitation of DPP (83 μM) at 485 nm with ~150 fs laser pulses (Appendix B Fig. B45) results in the appearance of ground-state bleaching at (b) 544 and
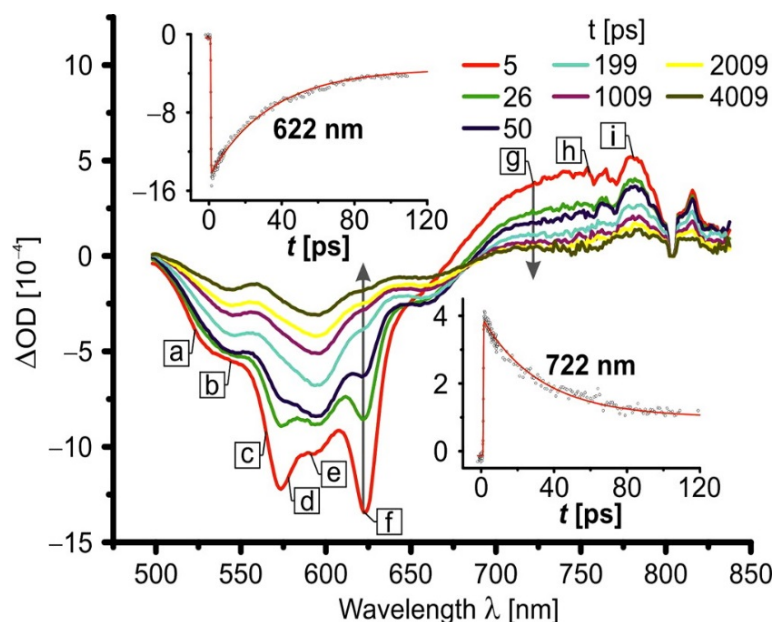
Fig. 3.3 fs-TA spectra of the 2:1 (DPP:PDI) mixture in toluene with absorption vs time profiles of (upper inset) the ground-state absorption band of the supramolecular DPP-PDI aggregate at $\lambda = 622$ nm and (lower inset) the positive feature at $\lambda = 722$ nm. Arrows denote the peaks at 622 and 722 nm. The assignments and lifetimes of each of the labeled peaks (a–i) are provided in Appendix B Table B5.

(e) 594 nm. The ground state recovers monoexponentially with time constants around 5 ns (Appendix B Table B5), which is near the limitation of the detection window. This agrees with fluorescence lifetimes (τ_{FL}, $S_0 \leftarrow S_1$) for comparable structures.[176] Positive transient features between 700 and 800 nm (g–i) decay with longer time constants, indicating that the S_1 state undergoes inefficient singlet triplet crossing[176-177] with a time constant that is approximately two times longer than the fluorescence lifetime, hampering a detailed kinetic analysis in this spectral range. The fs-TA spectrum of the PDI (Appendix B Fig. B46) shows a pronounced ground-state bleaching feature at (a) 523 nm, which is red-shifted compared to the ground-state absorption band at 519 nm because of contributions from stimulated emission. The negative feature at (d) 578 nm arises from stimulated emission alone (Appendix B Fig. B51). The recoveries are dominated by time constants of >6 ns and 4.7 ± 0.1 ns. A broad positive feature (650–785 nm, g) represents the S_1 state of the PDI.[178]

The fs-TA spectrum of a 2:1 mixture (Fig. 3.3) of DPP (83 μM) and PDI (42 μM) contains a pronounced ground-state bleach at (f) 622 nm, which is not present in the spectra of the individual components and corresponds to the supramolecular aggregate, as we have previously shown.[34] This feature displays a fast rise within the 200 fs instrument response time, and the ground state recovers following biexponential kinetics with a fast component of 33.1 ± 0.5 ps (76%) and a slow component of 3.74 ± 0.18 ns (24%). The slow component originates from overlap with the neighboring signals. Concomitant with the recovery of this new ground-state bleach is the decay of the positive feature at 722 nm (31.9 ± 0.7 ps, 71%) from PDI$^{\bullet-}$ (g). These data are in good agreement with the spectral positions of previously reported, similar PDI-based systems,[178-180] and are also in excellent agreement with the absorption maximum of the radical anion of our PDI system, (Appendix B Fig. B47) which we obtained by chemical reduction with F$^-$, (Appendix B Fig. B7) following the method reported by Saha et al.[181-182] The broad PDI$^{\bullet-}$ absorption signal may indicate charge migration through stacked PDIs in the supramolecular aggregate, as it has been previously shown that aggregation-induced migration broadens the absorption of PDI$^{\bullet-}$ and concomitantly lowers its intensity.[122] Following chemically-induced disaggregation with 5% DMSO, which interrupts H-bonding, the TA dynamics within the 2:1 DPP:PDI mixture resemble a linear combination of the individual compounds. While the recoveries of all ground-state bleaches in the 2:1 mixture show a significant amount of a very fast component ($\sim$30 ps, see Appendix B Table B5), upon DMSO-induced disassembly these very fast components vanish, and the intense ground-state bleach at 622 nm disappears entirely.
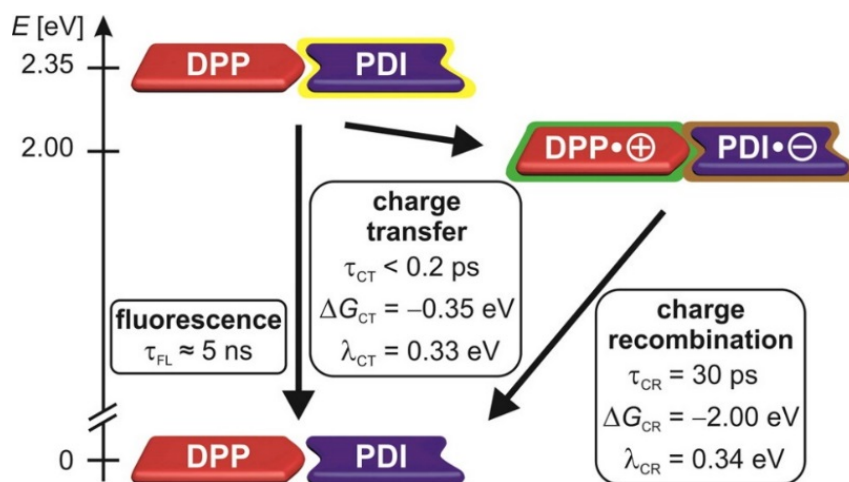
Fig. 3.4 Energy diagram of a DPP-PDI assembly in toluene. Photoexcited DPP (2.07 eV) is not shown, as it is almost isoenergetic with the charge-transfer state (2.0 eV). Band gaps were evaluated using absorption and emission spectroscopy, while the energy of the charge separated state was calculated by performing the Weller correction on the reduction and oxidation potentials.

The absence of fluorescence upon excitation of the aggregate at 622 nm (Appendix B Fig. B9) confirms the ultrafast decay via charge recombination. This hypothesis was further supported by calculating the charge separation energy (ΔGCS) in toluene using the Weller equation (Appendix B, B-E4),[183] which estimates ΔGCS to 2.0 eV (620 nm), indicating that the absorption band of the aggregate corresponds to direct photoexcitation into the charge separated state. Calculation of the static reorganization energy λs by invoking the Marcus relation (Appendix B, B-E6),[184-187] which is based on the dielectric continuum model of the solvent, yields λs = 0.03 eV. As expected for toluene as a low-polarity solvent, this static contribution is insignificant, so that the overall reorganization energy is given by the intrinsic value λi, which we determined by using density functional theory computations employing the ORCA program package.[188] (see SI) The overall reorganization energy λ was calculated to be 0.33 eV, which is very close to the absolute value of ΔG for charge separation from photoexcited PDI (Fig. 3.4). This charge separation (τCS) must therefore occur closely between the normal and the inverted Marcus regime

and is very fast. Owing to the much larger free enthalpy of the charge recombination ($\Delta GCR = -2.0$ eV), the lifetime of this process (τCR) is 30 ps, indicating that it occurs in the Marcus inverted regime.[187] However, τCR is also sensitive to the electronic coupling[189-190] which may contribute greatly to the fast τCR.[191]

3.3 Summary

In conclusion, we have used fluorescence and transient absorption spectroscopy to show that photoexcitation of donor–acceptor superstructures with visible light directs the system into a charge separated state. Importantly cooperative noncovalent bonding and FMO levels were synergistically designed to achieve new photophysical properties that emerge only upon assembly. The presence of the charge-transfer band at 622 nm indicates a more subtle electronic interaction between donors and acceptors upon self-assembly, and the nature of this interaction will be further investigated in the future. We intend to build upon this system that combines easily modified components and convergent supramolecular assembly to increase charge separation lifetimes, explore the influence of superstructure shape upon charge migration, and, ultimately, create new systems for solar energy harvesting and molecular electronics.

CHAPTER 4

EXTENDED CHARGE CARRIER LIFETIMES IN HIERARCHIAL DONOR-ACCEPTOR SUPRAMOLECULAR POLYMER FILMS

4.1 Background

Significant efforts have been devoted toward improving the performance of small molecule organic photovoltaics (OPVs);[117, 192-194] however, challenges still remain with regard to understanding, controlling, and ultimately optimizing the photon-to-current conversion within the photoactive layer. Natural photosynthetic processes that efficiently convert sunlight to fuel rely upon precisely positioned assemblies of photofunctional chromophores for light harvesting, charge separation, and catalysis.[33] Light conversion in the reaction center involves the synergistic combination of superstructure and ultrafast electron transfer to form long-lived radical pairs.[186, 195] The near unity conversion of light to chemical energy in the reaction center is a compelling model for future solar technologies[196] and has inspired the design of organic materials for artificial photosynthesis.[159, 197-198] Similar to the reaction center, the photoactive layers of OPVs require appropriately matched donor and acceptor frontier molecular orbital levels and electronic coupling that enable rapid charge generation, and the resulting films must also possess multilength scale order for charge migration through the films.[199-200] Approaches for designing these materials must consider ease of preparation, solar spectrum absorption, electron transfer dynamics, and film order together to achieve efficient charge generation.

Supramolecular polymers are a promising class of materials that could potentially be used for preparing organized films that undergo photoinduced charge separation. Supramolecular polymers are macromolecules whose monomeric repeat units are held together by noncovalent bonds, and their noteworthy characteristics include assembly from easy-to-prepare small molecules, hierarchical structure, and stimuli responsiveness.[14, 86, 93, 201-203] Several supramolecular polymer systems have been explored in the context of photoinduced charge separation in solution[204-207] and the solid-state,[52, 102, 167, 208] including a system we developed composed of a monodiamidopyridine diketopyrrolopyrrole (mDPP) electron donor and a perylene bisimide (PDI) electron acceptor[34] that assembles into 2:1 mDPP:PDI helical supramolecular polymers (Fig. 4.1 a) as a result of cooperative hierarchical assembly involving $\pi\cdots\pi$ stacking and H-bonding.[35] In solution, this mDPP:PDI supramolecular polymer undergoes ultrafast photoinduced charge separation into mDPP$^{\bullet+}$:PDI$^{\bullet-}$ followed by a recombination $\tau_{CR} = 33$ ps. Thus, we sought to investigate whether this emergent photophysical property–photoinduced charge separation–observed when the donor–acceptor superstructures formed in solution could be translated to the solid state. The challenge however is that the structures of supramolecular polymers that arise in solution and that produce the desirable emergent properties are not always maintained in thin films, and the effect of the condensed phase on photophysical properties are difficult to anticipate. Herein we report how mDPP:PDI supramolecular polymer structure is maintained in the solid state with order at the molecular and micrometer length scales, leading to photoinduced charge separated states that persist 1000-fold longer in the solid-state than in solution. This finding is significant because charge carrier lifetime is directly related to the ability to collect and use the resulting
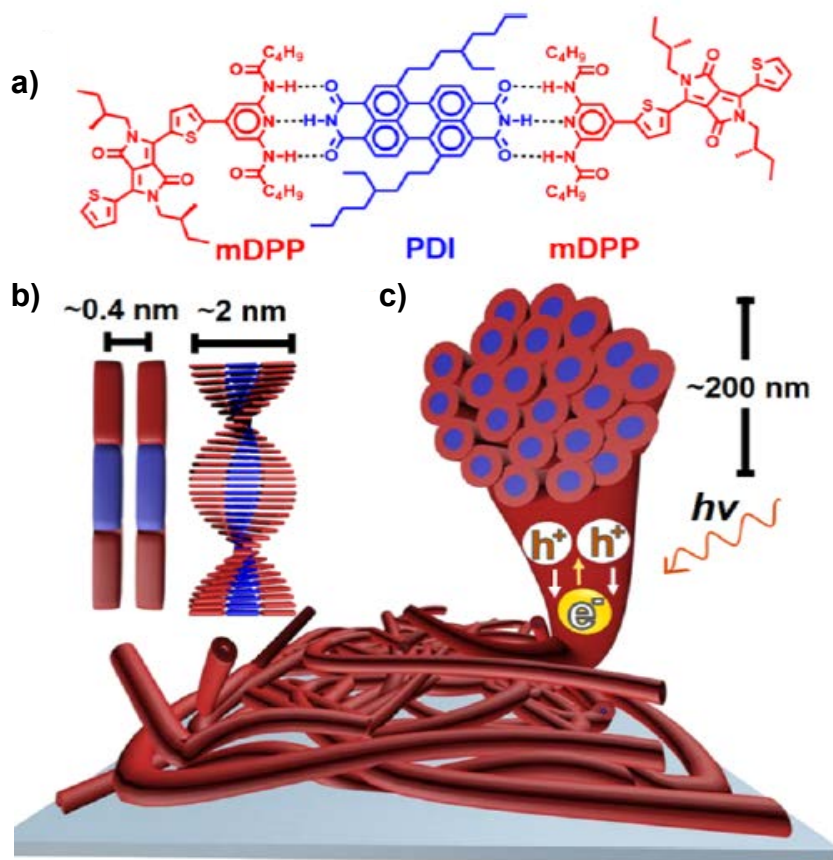
Fig. 4.1 (a) Chiral mDPP donor (red) and the PDI acceptor (blue) forming 2:1 aggregates as a result of H-bonding. (b) π-Stacking orthogonal to the H-bonding creates donor–acceptor supramolecular polymers with helical chirality. (c) Drop-casting of a 2:1 mDPP:PDI solution results in films composed of hierarchical ropes whose fibers are the chiral supramolecular polymers that contain π-channels for transport following photoinduced charge separation.

charges. In this communication we report how mDPP:PDI films were prepared, how their solid-state structures were characterized, and the electron transfer kinetics that dominate upon ordered-thin film formation to produce remarkably long-lived charge carriers.

4.2 Film Characterization

The aim was to prepare films of the supramolecular polymers and determine whether the noncovalent bonding and helical structure observed in solution persisted in the solid-state, and extensive details of the structural characterization of the thin films are provided in the Appendix C. Films of the donor, acceptor, and supramolecular polymer were formed by drop-casting from hot toluene solutions, and upon solvent evaporation the mDPP

formed microcrystals, the PDI formed powders, and the 2:1 mDPP:PDI solution formed hierarchical films with order across the molecular-to-micrometer continuum. Previous studies have shown the need to aggregate data from multiple characterization methods to arrive at accurate film structures for noncovalently organized donor–acceptor films,[34-35, 52, 167, 209] so we combined data from multiple solid-state analytical techniques that probe structure at the supramolecular, nanometer, and micrometer scales and compared them with solution data to arrive at a structure for the 2:1 film that consists of a dense matte of ropes that are bundles of 2:1 mDPP:PDI chiral helices, each of which has three parallel π-channels that propagate along the helical axis (Fig. 4.1b).

4.2.1 Attenuated Total Reflectance Infrared (ATR-IR) and Nuclear-Magnetic Resonance (ssNMR)

Attenuated total reflectance infrared (ATR-IR) and multidimensional ^{13}C solid-state nuclear-magnetic resonance (ssNMR) spectroscopies confirmed the triple H-bonding between the diamidopyridine (DAP) group on the mDPP and the diimide group on the PDI. The ATR-IR spectrum of the mDPP film (Fig. 4.2 a) displays two distinct N–H stretch peaks, a sharp peak at 3392 cm^{-1}, and a broad peak at 3276 cm^{-1}, which are attributed to amide protons that are not and are involved in H-bonding with the carbonyls of DAP groups on adjacent mDPPs, respectively, suggesting the mDPP adopts similar supramolecular H-bonding in the films as in the crystal structure of the previously reported[34] achiral mDPP (Fig. 4.2 b). The ATR-IR spectrum of the 2:1 mDPP:PDI film has only a single broad peak at 3281 cm^{-1} in the N–H stretch region, which suggests that all DAP amide protons in the film are involved in H-bonding, and the simplest explanation consistent with this data is that both DAP amides H-bond with the PDI carbonyls. This analysis is further supported by ssNMR. The ^{1}H resonance at 11.7 ppm that appears in the 2:1 mDPP:PDI mixture is
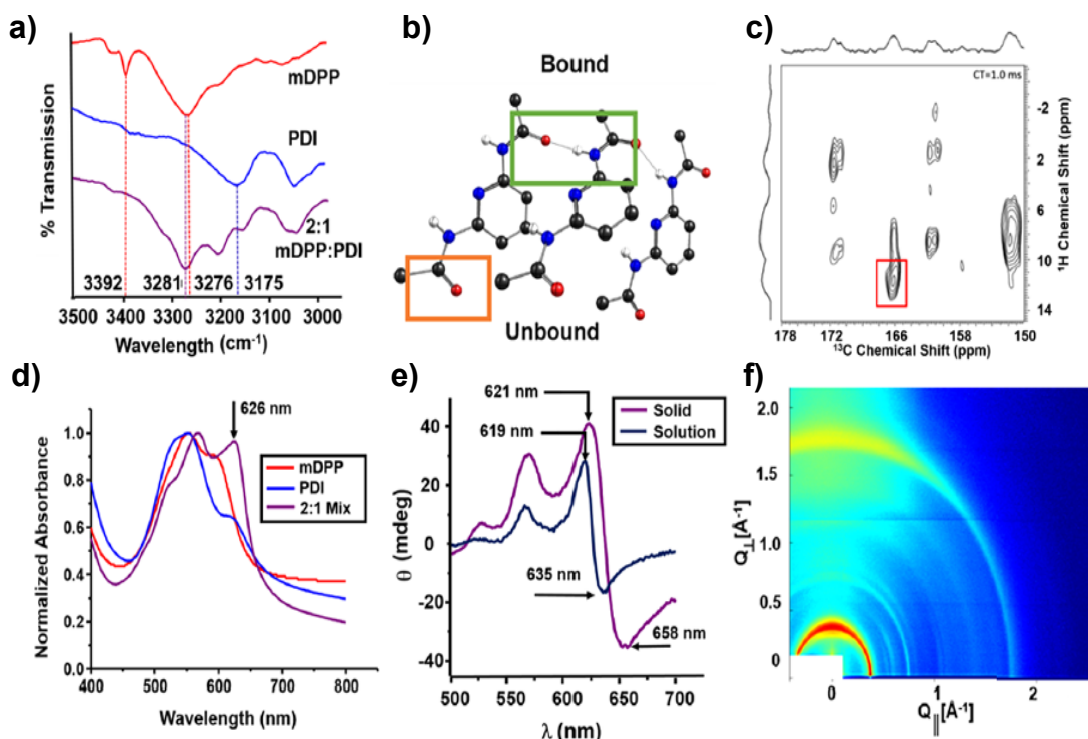
Fig. 4.2 (a) ATR-IR spectra of films of mDPP (red), PDI (blue), and 2:1 mixture (purple). (b) Diamidopyridine regions taken from the crystal structure of achiral mDPP. Orange and green squares highlight the amide protons that are not and are participating in H-bonds, respectively. Color of atoms: Carbon, black; nitrogen, blue; oxygen, red; and hydrogen, white. Highlighted are the unbound and bound amines of the DAP group. (c) HETCOR solid-state ^{13}C NMR of the 2:1 mDPP:PDI mixture. The box indicates the amide proton of mDPP involved in H-bonding with the PDI. (d) Film UV–vis spectra of mDPP (red), PDI (blue), and 2:1 mixture (purple). Highlighted is the charge transfer peak at 626 nm that emerges upon superstructure formation. (e) Overlaid CD spectrum of the 2:1 mixture in solution (navy blue) and in the film (purple). (f) GIWAXS of the 2:1 mDPP:PDI mixture.

assigned to amide protons of PDI forming strong H-bonding with the pyridyl functional group of mDPP (Appendix C Fig. C3). The ^{1}H–^{1}H dipolar DQ/SQ NMR spectra (Appendix C Fig. C6) show that the strong H-bonding resonance at 11.7 ppm correlates to the amide protons of mDPP. The amide proton of PDI correlates to the DAP amide protons of mDPP, which is consistent with the two types of H-bonding that are expected in the superstructure. The ^{1}H → ^{13}C two-dimensional (2D) heteronuclear correlation (HETCOR) (Fig. 4.2 c) shows a correlation between the strong H-bonding site ^{1}H resonance in the 2:1 mDPP:PDI and a ^{13}C resonance in the carbonyl region at 166 ppm.

4.2.2 Circular Dichroism (CD) Spectroscopy and UV-Vis Spectroscopy

The $\pi\cdots\pi$ stacking and chirality of the films was interrogated by UV–vis and circular dichroism (CD) spectroscopies, and taken together these data confirm that the emergent helical chirality observed previously [34-35] in 2:1 mDPP:PDI solutions is maintained in the drop-cast films. The UV–vis spectrum of the 2:1 mDPP:PDI film shows considerable vibronic sharpening compared to the individual components, and in similar systems[52, 102] this phenomenon has been ascribed to ordering resulting from $\pi\cdots\pi$ stacking. In the 2:1 film, a characteristic charge transfer peak appears at 626 nm (Fig. 4.2 d and Appendix C Fig. C1), and this peak is similar to the charge transfer peak at 622 nm that appears in solution[34-35] following formation of donor–acceptor supramolecular polymers composed of parallel channels of mDPP and PDI. This self-stacking of PDI[173, 210-211] and mDPP[174] in the solid-state is consistent with previous literature reports, and the self-segregation likely arises because self-stacking maximizes the π-surface overlap. Further evidence for this helical structure is provided by similarities between the CD spectrum of the 2:1 mDPP:PDI superstructures in solution and the solid-state, which both display bisignated Cotton effects (the signature of helical dyes)[96, 139, 152] with nearly identical shapes and peak positions (Fig. 4.2e). Importantly, the CD spectra of the chiral mDPP present no significant Cotton effect either in solution or in films;[34] rather helical chirality only emerges upon cooperative assembly of the donor–acceptor supramolecular polymers. Thus, on the nanometer scale, these spectroscopic data are consistent with a film structure composed of helical 2:1 mDPP:PDI helices held together by homo $\pi\cdots\pi$ stacking along the helix axis and orthogonal triple H-bonding.
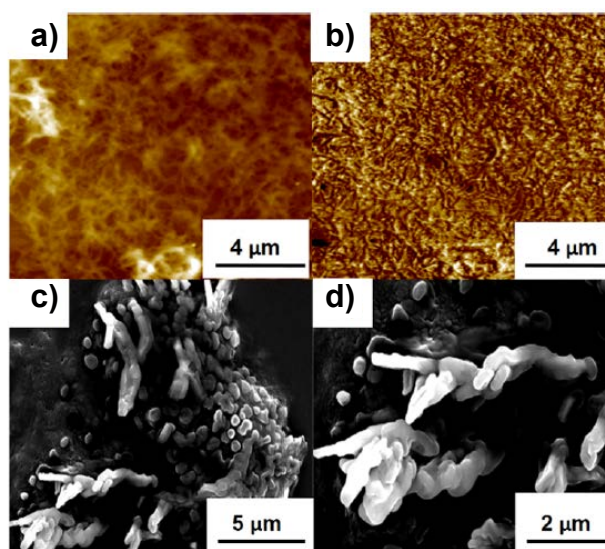
Fig. 4.3 (a) AFM topography image of 2:1 mDPP:PDI mixture on glass. (b) AFM phase image of 2:1 mDPP:PDI mixture on film. (c, d) SEM images at different magnifications of a bundle of supramolecular polymer wires.

4.2.3. Polarized Optical Microscopy (POM) and Atomic Force Microscopy (AFM)

Order on different length scales is the hallmark of biological materials,[212-214] and in the context of light harvesting in photosynthetic systems, order on the nanometer scale directs charge generation, and long-distance order prevents charge recombination. To investigate whether hierarchical order was present in the 2:1 mDPP:PDI supramolecularpolymer films, the micrometer-scale structure of the different films was investigated by polarized optical microscopy (POM), atomic force microscopy (AFM), scanning electron microscopy (SEM), and grazing-incidence wide-angle X-ray scattering (GIWAXS), AFM topographical imaging (Fig. 4.3 a,b), and SEM (Fig. 4.3 c,d) of the 2:1 mDPP:PDI film. These studies revealed a dense tangle of wires that are each several micrometers in length, and the height of the film was 0.32 ± 0.054 μm with individual wires ranging in diameter from ~50 to ~200 nm. POM images (Appendix C Fig. C23 and Fig. C24) confirmed that the mDPP formed crystals with lengths of ~100 μm, the PDI formed powders, and the 2:1 mDPP:PDI mixture formed a relatively homogeneous film without evidence of grain structure or microdomains. The GIWAXS data provide further evidence of microscale

order and preferential orientation in the three films. The strong reflections along $Q_\perp$ at 0.395 (1.589 nm) for the mDPP correspond to the lamellar spacing,[215] and the PDI peak at 0.328 A^{-1} (1.923 nm) is one of several peaks in the correct region of the spectrum that indicates lamellar assembly. The peaks at 1.482 (0.424 nm) (mDPP)[102] and 1.564 A^{-1} (0.401 nm) (PDI)[216] along $Q_\perp$ are consistent with other PDI GIWAXS data[102] and correspond to the $\pi\cdots\pi$ stacking (Appendix C Fig. C26 and Table C3), suggesting that these dyes are arranged with the π-channels propagating parallel to the surface (Appendix C Fig. C21). The GIWAXS of the 2:1 mDPP:PDI films differs markedly. By comparing the GIWAXS data, a few conclusions can be drawn about the mDPP:PDI supramolecular polymer films. First, the absence of peaks in the mixed films between 1.162 and 1.181 A^{-1} that are prominent in the individual components confirms that this film is indeed composed of a new superstructure rather than just domains of individual components. Second, the radial nature of the peaks indicates there is no preferential orientation of the crystallites relative to the surface normal, although the $\pi\cdots\pi$ stacking peak at 1.8 A^{-1} is stronger along $Q_\perp$, suggesting a modest preference for propagation of the π- channels along the surface normal (Fig. 4.2 f). A more thorough analysis of the GIWAXS data will be provided in forthcoming publications. This hierarchical structure, whereby the solid-state structure is composed of a small fibers coiled into larger ropes, is consistent with all thin film characterization data and is remarkably similar to that arrived at with a similar donor–acceptor system that uses PDI to bridge two oligo(*p*-phenylenevinylene) units.[52]

4.3 Transient Absorption Spectroscopy

To compare the photoinduced charge transfer processes of the mDPP-PDI films to those previously reported [34-35] for solution aggregates, a brief description of the femtosecond (fs) and nanosecond (ns) transient absorption (TA) on the individual compounds and on the 2:1

mDPP:PDI mixture in toluene is provided. Photoexcitation of solutions of mDPP and PDI in toluene (Appendix C Fig. C26 a,b) results in the appearance of ground state bleaching from 523–594 nm with corresponding positive excited states features between 700 and 800 nm and lifetimes around 2–5 ns. Ground state bands observed at 650 and 578 nm are from stimulated emission for both mDPP and PDI, respectively. Upon assembly of mDPP and PDI into a 2:1 mixture (83 µM/42 µM), a new, negative feature at 622 nm is observed, which is not present in the individual electronic absorption spectra. We have previously shown from UV–vis data[34-35] that the peak at 622 nm appears as a result of aggregation, and calculations indicate the energy of this peak corresponds to a charge transfer band using the Weller treatment. In toluene, the charge separation energy (ΔG_{CS}) is estimated to be 2.0 eV (620 nm), and this peak appears in both solution aggregates (622 nm) and the supramolecular polymer film presented here (626 nm). The ground state recovery of the charge transfer band at 622 nm follows the charge recombination of mDPP$^{\bullet+}$ and PDI$^{\bullet-}$ radical ions previously reported by a others,[102] with both ions absorbing broadly from 700–800 nm. Individual kinetics fit as a sum of exponentials of the ground state charge transfer band bleach at 622 nm and the radical ions at 722 nm are identical. The dynamics are biexponential with a fast component of 33.1 ± 0.5 ps (76%) from charge recombination, and a slow component of 3.74 ± 0.18 ns (24%) matching those lifetimes of the individual chromophore excited state lifetimes. Further experiments were performed to disrupt H-bonding in the aggregates using 5% DMSO (Appendix C Fig. C26 d). In this case, the TA within the 2:1 DPP:PDI mixture resembles a linear combination of the individual compounds with the 622 nm ground state bleach noticeably absent from the spectra and a significant decrease in intensity of the broad absorption from 700–800 nm.
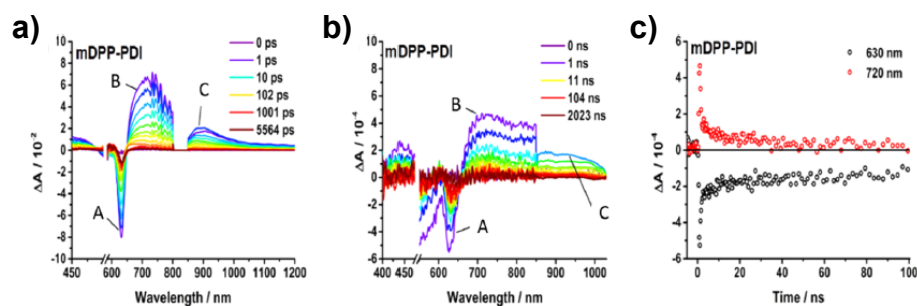
Fig. 4.4 (a) fs-TA spectra and (b) ns-TA spectra of films of 2:1 mDPP:PDI mixture upon 500 nm laser excitation. (c) Time–absorption profiles of the 2:1 mDPP:PDI mixture (4.5–5.5 ns delay) film at 630 and 720 nm illustrating the charge recombination.

fs-TA and ns-TA were used to investigate photoinduced charge transfer dynamics in air-free films of mDPP, PDI, and the 2:1 mDPP:PDI mixture. Ultrafast excited state kinetics and spectra were first examined for ^{1}*mDPP and ^{1}*PDI as a function of pump energy density and wavelength, and those kinetics were fit as a sum of exponentials (Appendix C Table C4 and Fig. C30). Laser irradiation of the PDI film at 500 nm produces peaks corresponding to ^{1}*PDI transitions from 620 to 1400 nm (Appendix C Fig. C32 a), with maxima at (a) 710 and 909 nm, consistent with the PDI excited state energies. The ^{1}*PDI deactivates multiexponentially, with lifetimes contributions of ~1 ps (72%), assigned to excited state annihilation, 41 ps (15%), and a long-lived component >6 ns that are similar to previously reported excited state absorption decays of other PDI-containing films.[35, 217] The mDPP films that were photoexcited at 500 nm produce ^{1}*mDPP features at 450 nm and (b) 606 nm along with a broad absorption from 640 to 1200 nm, with maxima at (d) 707 nm and (e) 885 nm (Appendix C Fig. C32 b) that are assigned to singlet excited state transitions (S_1–S_n). Negative features between 480 and 595 nm correspond to ground state bleach, and stimulated emission at (c) 630 nm −650 nm appears on the picosecond time scale. The kinetics at (c)–(e) follow identical multiexponential decays, with average lifetimes of ~3 ps (37%), 48 ps (35%), and 306 ps (26%) and a measurable long-lived component that persists on the nanosecond and microsecond time scales (Appendix C

Table C4). The multiexponential decay of the ~2 ps component can be rationalized by ^{1}*mDPP annihilation, whose contribution decreases with decreasing pump energies (Appendix C Fig. C30).

Upon photoexcitation of the 2:1 mDPP:PDI mixture film at 500 nm, positive features at ~450 nm along with a broad transient from 650 to 1200 nm (Fig. 4.4 a) with maxima at (b) 733 nm and (c) 902 nm form within the instrument response time (~70 fs). These transients are accompanied by a depletion of the charge transfer band (a) at 626 nm (Fig. 4.4 a). All positive signals at early times in the femtosecond transient absorption spectrum are nearly identical to spectroelectrochemical film data collected for the mDPP$^{\bullet+}$ and PDI$^{\bullet-}$ radical ions, confirming that charge separation occurs in the donor–acceptor films as it does in solution (Appendix C Fig. C25, Fig. C26 and Fig. C28). During the time window observable with the femtosecond transient absorption setup, these kinetics decay multiexponentially (Fig. 4.4 and Appendix C Table C4). Similar results were obtained upon photoexcitation at 625 nm (Appendix C Table C4 and Fig. C26 and C27). In the 2:1 mDPP:PDI films, the slowest charge recombination takes place within 32 ns, which was determined by monitoring the transient absorption features across the visible and NIR spectrum (Fig. 4.4 b). Interestingly, we observe an identical ~33 ps charge recombination component matching solution aggregate dynamics, with an amplitude reduced by half in the supramolecular polymer films, indicating that ion pairs are able to overcome coulomb energy to form free charge carriers in the condensed phase.[218] This slowest recombination is approximately 1000-fold greater than the 33 ps lifetime observed in the solution aggregates. However, the ground state bleach at the charge-transfer band at 626 nm is not fully recovered, and an appreciable amount (~5%) of this signal is left after 32 ns that was not observed in solution (Fig. 4.4 c) that suggests long-lived triplet states
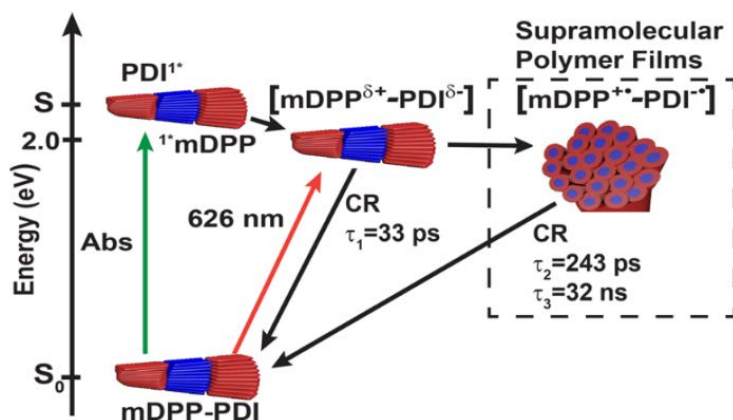
Fig. 4.5 Jablonski diagram comparing the photoinduced charge recombination (CR) pathways of mDPP:PDI in solution aggregates to those observed in supramolecular polymer films. Increased yields of free charges with extended lifetimes are observed in the films as charge delocalization increases.

may be formed from either individual mDPP or PDI or as a triplet excited state produced from photogenerated triplet radical pairs (Appendix C Fig. C28). Previous studies in related H-bonded[52, 206, 219] and covalent systems[102] have shown that the relative orientation of donor and acceptor components contributes to the emergent photophysics of similar systems, where charge separation occurs within 2–3 ps through the H-bond and charge separation through cofacial interactions occurs on the fs time scale. From the spectroscopic analysis, we were able to construct a Jablonski diagram (Fig. 4.5) describing the various photophysical processes occurring in these materials comparing solution aggregates with supramolecular polymer films following photoexcitation. These data suggest that in the mDPP-PDI supramolecular polymers studied herein, charge separation occurs through cofacial interactions, and this interpretation is further supported by ground-state charge transfer absorption band at 626 nm.[35] The increased recombination lifetimes observed in the mDPP:PDI films (τ_2= 243 ps and τ_3 = 32 ns) likely arise from charge delocalization through the π-channels in the fibers or hopping of charges between the fibers in the condensed phase,[220] and both experimental and theoretical efforts are being made to resolve

this source of this significant lifetime increase. The trends observed in the spectroscopic data of the 2:1 mDPP:PDI films are similar to the those observed for a covalently linked PDI–DPP–PDI system reported by Wasielewski et al.[102] following solvent annealing. Like them we observe a significant increase in charge carrier lifetimes in moving from solution to films, likely because of the ability of free charge carriers to move through the π-channels upon ordering.

4.4 Summary

In conclusion, TA was used to study charge dynamics in films composed of an electron rich mDPP donor and an electron poor PDI acceptor that coassemble into hierarchically ordered supramolecular polymers as a result of multiple noncovalent interactions operating in concert, and this proposed structure is consistent with all experimental data. TA results reveal that charge carrier lifetimes increase 1000-fold for the slowest charge recombination component in moving from solution to the solid state. These studies demonstrate that (1) supramolecular polymer structure can be translated from solution to the solid state, resulting in hierarchical films, and (2) photophysical properties can be enhanced as a result of long-range ordering. The approach to designing new photoactive films demonstrated herein, where hierarchical structure and photophysics are considered synergistically, could provide new strategies for sensing, energy harvesting, and molecular computing.

CHAPTER 5

DIKETOPYRROLOPYRROLE (DPP) ASSEMBLY INTO *J*- AGGREGATES

5.1 Background

The diketopyrrolopyrrole (DPP) heterocyclic scaffold with appended thiophenes [174, 221-225] is an organic semiconductor with tunable frontier molecular orbital levels that is an increasingly popular component of polymers,[34-35, 226-227] molecular electronics,[38, 227-229] supramolecular systems,[30-31, 45, 145, 226] and organic photovoltaics.[40, 52, 101-102, 105, 174, 192, 200, 226, 230] DPP forms highly ordered films,[227] a factor that contributes substantially to the remarkable optical and electronic properties of this dye. Our group has exploited these DPP–DPP noncovalent interactions in solution to template the cooperative assembly of donor–acceptor superstructures that form[34-35, 226-227] as a consequence of H-bonding between a diamidopyridine (DAP) group appended to a DPP (**1**) and the diimide groups of a perylene bisimide acceptor. In addition, $\pi\bullet\bullet\bullet\pi$ stacking orthogonal to the H-bonding axis produces chiral helices driven by (*S*)-2-methylbutyl side chains on **1**. These donor–acceptor systems are notable in that they undergo [35] photo-induced charge separation only upon formation of hierarchical donor–acceptor superstructures and they therefore demonstrate the principle of "emergence-upon-assembly", where unique properties that are absent in individual components arise following supramolecular assembly.[226] A systematic study of the aggregation of the individual components of this DPP-PDI system revealed that **1** assembles into *J*-aggregates, and the spectroscopic changes in variable temperature (VT) ultraviolet–visible (UV–Vis) titrations could be fit to an isodesmic binding model[34, 133] – where the binding strength between monomers is independent of the supramolecular polymer's degree of polymerization and that all binding steps are therefore energetically equivalent. Using this model, the Gibb's free energy (ΔG^o) of adding each new monomer

of **1** to the growing cluster was determined to be $-6.4\,\text{kcal}\,\text{mol}^{-1}$.[34] This previous work demonstrates the utility and promise of DPP as a versatile component in complex supramolecular systems and describes experimental methods for quantifying the thermodynamic assembly parameters that direct its supramolecular chemistry. Herein, we examine the assembly into *J*-aggregates of a series of molecules containing the DPP core to develop relationships between molecular structure, noncovalent interactions, and equilibrium thermodynamics. The resulting data could inform the design of stimuli-responsive systems that possess DPP as an active optical and electronic component.

Even the simplest supramolecular system organizes as the result of the simultaneous contributions of solvent, temperature, concentration, and multiple noncovalent interactions operating in concert. Because of this inherent complexity of supramolecular assembly,[231-238] anticipating how a system responds to changes in the molecular structure of the components is a difficult task. A popular approach to addressing this challenge is to systematically alter molecular structure and quantify[133] the effects on the thermodynamic assembly parameters (ΔH, ΔS, ΔG^{o}, and K), and these values can in turn be used to design systems with a predictable response to changes in temperature, concentration, or the addition of new analytes. This quantitative approach in supramolecular chemistry was pioneered by Cram *et al.*,[239-242] who, by varying the structures of crown ethers and determining the effects of these variations on the binding with a series of guests, were able to develop the principles of preorganization and complementarity that continue to govern host–guest chemistry.[243-245] More recently, sophisticated models[45, 77, 92, 94, 96, 118, 120-125, 127-131, 133-134, 194, 246] have been developed to describe the assembly of considerably more complex supramolecular systems, such as clusters and supramolecular polymers,[21-27] which consider binding events in a series to
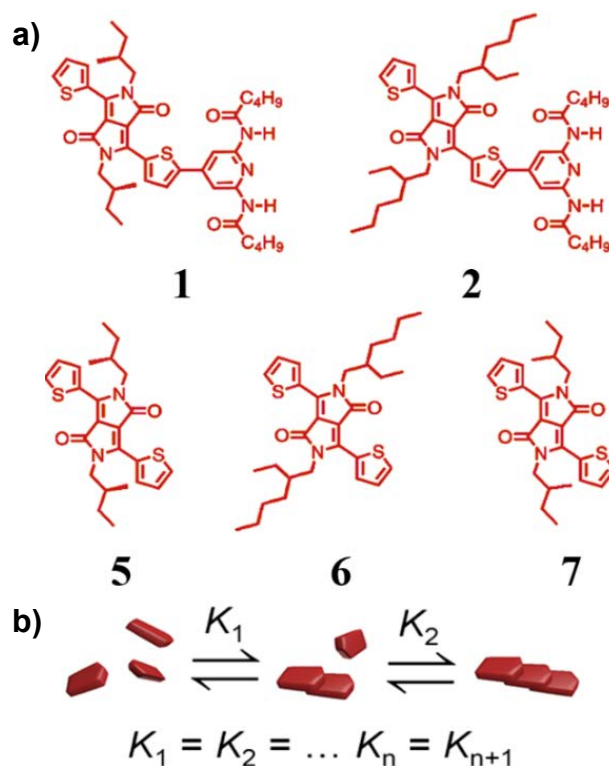
Fig. 5.1 (a) Diketopyrrolopyrrole derivatives whose aggregation was studied. (b) The isodesmic assembly process involves monomers assembling into J-aggregates such that association constant, K, is independent of stack size, *n*

create larger architectures. Understanding and anticipating the behavior of supramolecular systems through quantitative structure-activity relationships are now a commonplace and have led to breakthrough advances in the fields of molecular electronics,[247-249] drug delivery,[30-31, 250] and energy harvesting,[40, 52, 101-102, 175, 251] to name just a few, and these studies confirm that systematic structure-activity relationships continue to be an invaluable tool for understanding even the most cutting-edge chemical systems.

To this end, we describe herein a study that examines how the molecular structure of a series of DPP derivatives (**1**, **2**, **5, 6, 7**) affects their assembly into homoaggregates – organized assemblies consisting of a single molecular component. Single-crystal x-ray analysis and molecular modeling in conjunction with UV–Vis titrations were used to understand the thermodynamic underpinnings of aggregation and how the optical

properties of DPP arise from cluster size and structure. The DPP components, **1, 2, 5, 6, 7** (Fig. 5.1), whose binding was studied, vary in the length of their conjugated core, the presence or absence of H-bonding groups, and the length, branching, and chirality of the solubilizing side chains. By fitting the UV–Vis spectroscopic changes in response to variations in temperature and concentration to an isodesmic binding model, thermodynamic parameters for the equilibrium between disaggregated monomers and aggregated clusters for this series of DPP dyes were quantified. Using comparisons between the values of ΔH, ΔS, ΔG^o, and K for the different molecules in the library, we discuss how different noncovalent interactions – H-bonding, van der Waals forces, and π•••π stacking – contribute to the equilibrium between aggregated and disaggregated states. Finally, a new mathematical model is derived that shows how these thermodynamic data can be used to predict the mean stack size, $\acute{n}$, at a given set of solution conditions. We find that subtle changes in molecular structure have a dramatic impact on the isodesmic assembly of DPP and that these data could be used to design DPP scaffolds where the equilibrium between aggregated and disaggregated states could be tailored. In addition to providing valuable thermodynamic and structural data on this molecular scaffold of rapidly increasing scientific and technological interest, this study demonstrates the remarkably rich supramolecular chemistry that can be found in even the simplest assembly processes.

5.2 Fitting Ultraviolet–Visible Spectroscopic Data to an Isodesmic Binding Model

To determine ΔH, ΔS, ΔG^o, and K of homoaggregation of the DPP units, spectroscopic data were imported into Microsoft Excel 2010 and globally fit to the isodesmic binding model[34, 133, 200] described by equation 36:

$$A = \varepsilon_\infty \left([DPP]_t - \frac{2K[DPP]_t + 1 - \sqrt{2K[DPP]_t + 1}}{2K^2[DPP]_t} \right)$$
$$+ \varepsilon_m \left(\frac{2K[DPP]_t + 1 - \sqrt{2K[DPP]_t + 1}}{2K^2[DPP]_t} \right)$$

(36)

where $[DPP]_t$ is the total concentration of DPP in solution, $[DPP]$ is the concentration of DPP in solution remaining in monomeric form, ε_m is the theoretical monomer extinction coefficient, ε_∞ is the theoretical polymer extinction coefficient, T is the temperature in Kelvin, R is the universal gas constant, and K is the binding constant described by eq (37):

$$K = e^{\frac{-\Delta H}{RT} + \frac{\Delta S}{R}}$$

(37)

The generalized reduced gradient solving algorithm that is included with the Excel^{TM} software package minimized the weighted sum of square residuals (wSSR) between the experimental and the best fit data by allowing the solver to vary four fitting parameters: ΔH, ΔS, ε_m, and ε_∞. To ensure that the solutions are global rather than local minima, initial parameter values were varied systematically, and the wSSR were compared.

5.3 X-Ray Crystallography of Compound 5

Red single crystals of **5** suitable for x-ray diffraction analyses were obtained by evaporation of a methylene chloride solution crystallized in the monoclinic system. The systematic absences in the intensity data were consistent with either of the space groups $P2_1$ or $P2_1/m$. The structure could only be solved in the former space group, and attempts to solve the structure in the centrosymmetrical space group $P2_1/m$ were unsuccessful. Furthermore, the ADDSYM/PLATON[170, 252-253] (ADDSYM-EXT) test did not indicate any additional missed symmetry. However, ADDSYM and ADDSYM-EQL suggested the centrosymmetrical space group $P2_1/c$. The structural solution in $P2_1/c$ yielded high R values ($R1$ ~9% and wR2 ~30%) suggesting some form of twinning and/or pseudo center of inversion. In comparison, the structural solution in the

chiral space group $P2_1$ gave low R values ($R1 = 4.82\%$), and a Flack $x(u)$ parameter −0.08(10) indicating that the correct enantiomorph has been selected. The asymmetric carbon atoms C22 and C32 have S configurations, CCDC no. 1428552.

5.4 Results

"J-aggregate" refers to organized assemblies of dyes that adopt a slip-stacked orientation, whose geometry affects the excitonic coupling between adjacent dyes. The optical signatures of J-aggregation are a narrow absorption band, whose maximum is shifted bathochromically with respect to the monomer,[34, 170] and with a higher extinction coefficient, ε, and fluorescence quantum yield than the monomer. Previously, we established that **1** assembles[34] into J-aggregates and these clusters were used to template the formation of donor–acceptor superstructures that undergo photo-induced charge separation in solution[35] and in films.[227] To develop a fuller understanding of how structure affects assembly, a series of DPP containing molecules **1, 2, 5, 6, 7** were prepared that vary in their solubilizing side chains, the presence of chiral centers, and whether they possess H-bonding DAP groups (Fig. 5.1). The homoaggregation of each component of this series into J-aggregates was studied by VT UV–Vis spectroscopy to quantify the thermodynamic assembly parameters (ΔH, ΔS, ΔG^o, and K). These data can be used to predict how the equilibrium between aggregated clusters and disaggregated monomers shifts in response to changes in temperature and concentration. We have shown previously[34-35] that the UV–Vis spectrum of **1** changes in response to alterations to concentration and temperature and these manifest themselves through the presence of isosbestic points, vibronic sharpening, and change in ε that are consistent with J-aggregates in other dyes.[170, 254-256] VT UV–Vis spectroscopy is an attractive approach towards studying assembly into aggregates because of the wide availability of the requisite instrumentation,

but the drawback of this technique is that the information it provides about the organization of dyes within a cluster is limited, so we use UV–Vis data in combination with single-crystal x-ray analysis and molecular modeling to extrapolate the structural changes in solution that occur in response to changes in temperature and concentration. Herein, we describe in detail how VT UV–Vis data for **1** are fit to binding models to obtain values for ΔH, ΔS, ΔG^o, and K, and the extinction coefficient for the monomer, ε_m, and the supramolecular aggregates, ε_∞. Subsequently, we present the binding data for the other components in the series to provide insight into how molecular structure affects aggregation. Finally, a model is presented for predicting mean aggregate size at a given temperature and concentration.

5.4.1 Aggregation State of DPP Molecules

The equilibrium between aggregated and disaggregated states of DPPs is dependent upon both temperature and concentration, where increasing concentration drives aggregation, and the effect of temperature on clustering is governed by the interplay between ΔH and ΔS. The thermodynamic assembly parameters were quantified by taking spectroscopic data at a sufficient number of points along the range of conditions where the system behaves under equilibrium control and fitting these data to an isodesmic binding model. To obtain these VT UV–Vis spectra, the DPP derivatives (**1, 2, 5, 6, 7**) were dissolved in freshly distilled, spectroscopic grade toluene at concentrations ranging from 1–100 µM. Spectra of each solution were taken from 300–800 nm at temperatures ranging from 10–85 °C in 5 °C increments, with a 2-min delay after reaching the target temperature to ensure that the solution had reached thermodynamic equilibrium. For the DPP derivatives that contained the DAP unit (**1** and **2**), spectra were also taken in the presence of 1% dimethyl sulfoxide (DMSO) to disrupt H-bonding, and this was performed in an effort to isolate the energetic
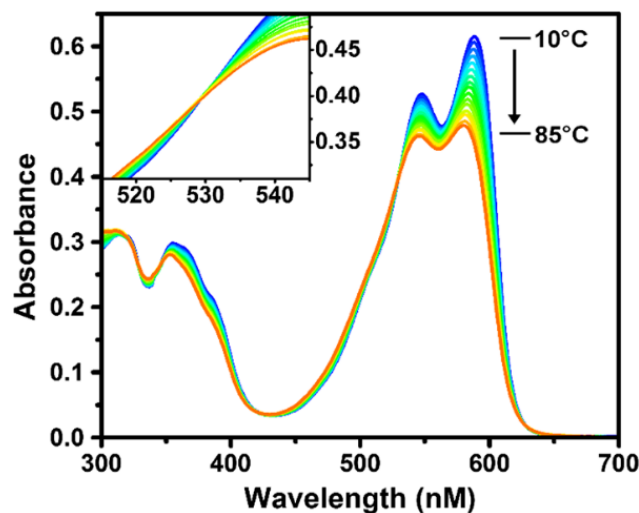
Fig. 5.2 Variable temperature ultraviolet–visible absorbance spectra of in toluene (20 μM) at temperatures ranging from 85 (red) to 10 °C (blue) in intervals of 5 °C. An isosbestic point is apparent at 529 nm, and pseudo-isosbestic points occur at 330, 349, 421, and between 548 and 586 nm.

contributions of H-bonding to overall supramolecular assembly. The VT UV–Vis spectrum of **1** is shown in Fig. 5.2 and displays the following spectral features that are common to all of the DPP derivatives studied in this work (Appendix D Fig. D6).

The ground state DPP spectra are characterized by three maxima, which for **1** occurs at 355, 548, and 586 nm. The relative peak intensities are dependent upon concentration and temperature, and this produces an isosbestic point at 529 nm – the hallmark of a thermodynamic equilibrium between two states – and pseudo-isosbestic points at 330, 349, 421, and between 548 and 586 nm. These changes in spectral shape are the result of excitonic coupling between dyes as they aggregate.[257] In addition to the isosbestic points, several other aspects of this spectrum are indicative of assembly into *J*-aggregates, including the vibronic sharpening and bathochromic shifting of the absorption maxima. It should be noted that blanket terms like *H*-aggregate and *J*-aggregate have only limited value in describing the geometry and spectroscopic properties of clusters and crystal structures provide substantially better guidance.

5.4.2. Single Crystal X-Ray Structures

The structure and properties of supramolecular assemblies are intimately linked, and subtle changes in the relative orientations of dyes within clusters can have a dramatic impact on their optical and electronic properties.[118, 257-258] So understanding the relationship between molecular and supramolecular structures is a critical step in designing new DPP-based materials and devices. UV–Vis solution data have limited value for determining the relative orientations of the DPP dyes within an aggregate. The structures and noncovalent interactions within solution supramolecular assemblies can be extrapolated from a single-crystal x-ray analysis.[259-263] To this end, we have attempted to grow single crystals of the DPP derivatives shown in Fig. 5.1, and a single-crystal x-ray structure was obtained for **5** (Fig. 5.3 (d–f)), while the crystal structure for **2** (Fig. 5.3 (a–c)) had been determined previously.[34] Having these two structures is particularly useful for analyzing the contributions of different noncovalent interactions on assembly because **2** contains the DAP group but **5** does not, and comparing these two crystal structures can provide insight on how the H-bonds enabled by this group affect packing in the solid-state, and, by extension, in solution. Compound **5** was crystallized as monoclinic ($P2_1$), and the x-ray structure confirmed that the side chains emanating from the nitrogen of the DPP core were homochiral (S)-2-methylbutyl groups. Compound **2** was also crystallized as monoclinic but was instead $P2_1/c$ with racemic side-chains. The interplanar spacing is smaller in **2** (3.427 Å) than **5** (3.659 Å), the latter of which crystallizes in a herringbone motif. In both cases, the slip-stacked geometry between adjacent dyes that is the hallmarks of J-aggregation occurs.[170] While the structure in solution is not necessarily identical to the crystal structure, observations such as the bathochromic shift and increased absorption intensity in response to aggregation suggest that the π-stacked structure in crystals is similar
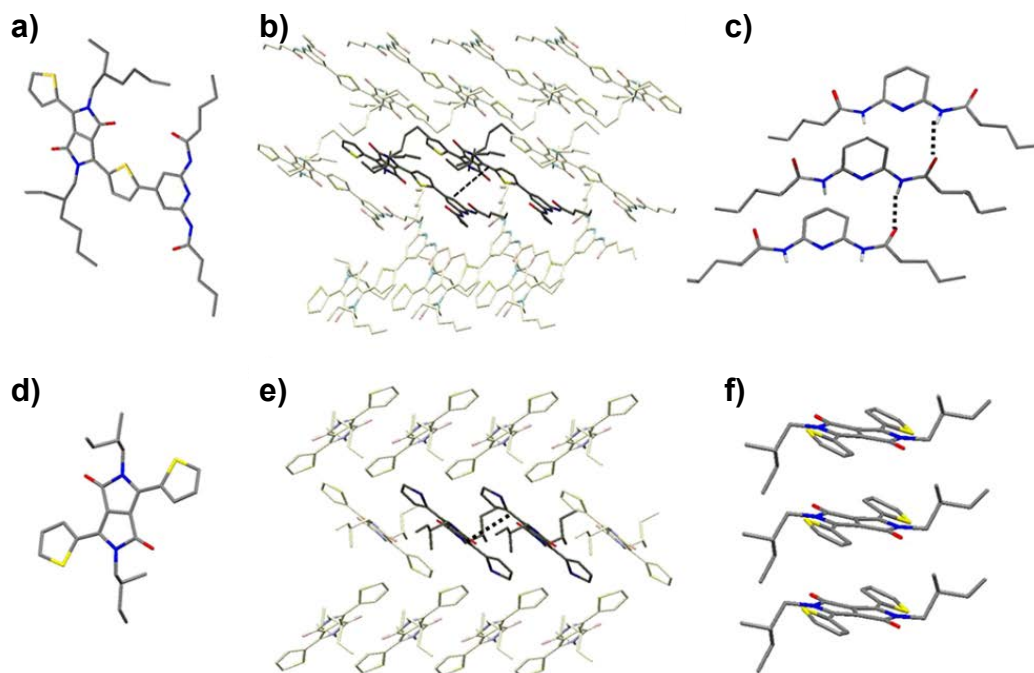
Fig. 5.3 (a–c) Single-crystal x-ray structures of **2** and (d–f) of **5**. Carbon atoms are shown in gray, oxygens are red, nitrogens are blue, sulfurs are yellow, and hydrogens, when displayed, are white. The dashed lines (a and d) represent the 3.427 and 3.659 Å π•••π stacking distances in **2** and **5**, respectively. The dotted line in (c) indicates H-bonding that occurs between diamidopyridine groups of adjacent molecules of **1**.

in solution and is typical of *J*-aggregates.[170] In addition, these structures are consistent with previous quantum chemical calculations for **1** in toluene,[34] and additional structural calculations for **3**, **4**, and **5**, which study packing in a toluene model (Appendix D Fig. D19) has remarkably similar π•••π interactions to those observed in the crystal structures.

5.4.3 Thermodynamic and Isodesmic Models

To determine the thermodynamic parameters for the formation of clusters from monomers for each of the DPP derivatives **1**, **2**, **5, 6, 7**, the VT UV–Vis data were imported into Microsoft Excel[TM] and fit to an isodesmic binding model using an algorithm that solves simultaneously for ΔH, ΔS, ε_m, and ε_∞ by minimizing the wSSR between the experimental data and the numerical fit. This method minimizes numerical fits to the absorbance for every temperature, concentration, and averaged extinction coefficients simultaneously and thereby increases the fit accuracy by capturing a wide dynamic range of the equilibrium.

The isodesmic binding model [34, 97, 133, 254] used is based on the assumptions (1) that the DPP forms aggregates that can grow to infinite size, (2) that the entropy and enthalpy of adding an additional monomer to the growing aggregate is independent of stack size, and (3) that the observed spectra can be modeled as a linear combination of two states, monomeric and aggregated, with independent extinction coefficients ε_m and ε_∞, respectively. There are several models that could represent DPP assembly,[97, 170] and some of these account for the possibility of multiple inequivalent assembly steps. For the current study, the isodesmic model was used because it provides reasonable fits to the spectroscopic data and because there is previous validation of this model with other self-assembling dye-systems.[97, 133, 170] While the lack of a substantial Cotton effect in the CD spectrum of the films of **1** or **5** does not necessarily support the isodesmic model, the presence of a significant Cotton effect would be a strong argument against using the isodesmic model, where all binding steps are assumed to proceed with equal binding energies and therefore would not provide structures with long-range emergent chirality.[246, 264-265] As will be discussed, this modeling approach provides thermodynamic data in agreement with experimental trends, and these data can be used to explain the role of DPP molecular structure on assembly.

In addition to structural and thermodynamic data on **1**, **2**, **5**, **6**, **7**, detailed instructions are provided for quantifying thermodynamic assembly parameters from spectroscopic data. The equations and step-by-step instructions for modeling and data fitting are provided in the experimental section and Supporting Information. Briefly, the VT UV–Vis data for a solution of a given concentration is a 3D surface composed of a mesh of points that contain the values for temperature, wavelength, and absorbance (Figs 5.4 a and Appendix D Table D8), and adding concentration data produces a hypersurface (Figs 5.4 b and Appendix D Table D9).
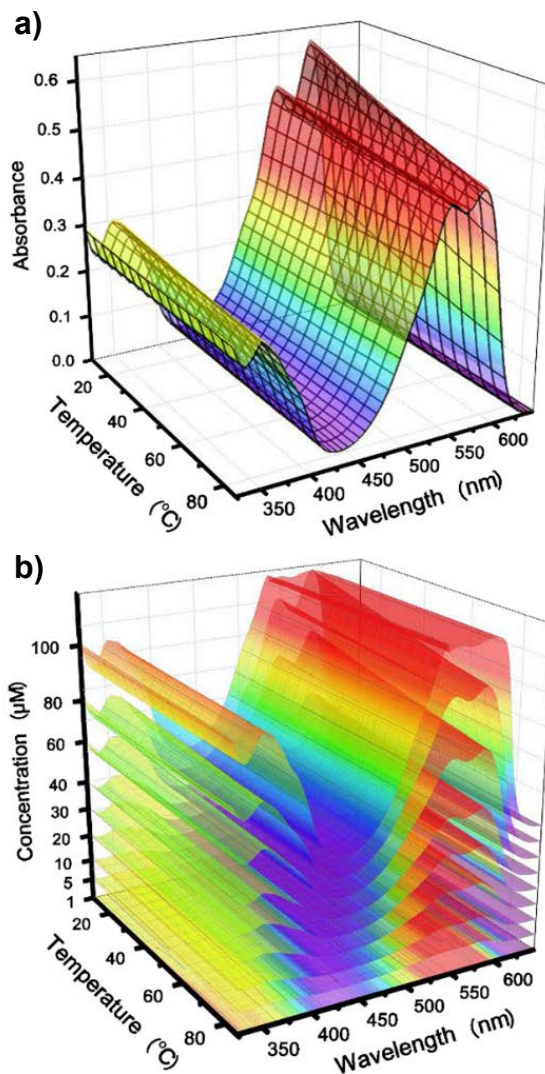
Fig. 5.4 (a) The isodesmic numerical fitting to the variable temperature spectra of **1** in toluene at 20 µM is displayed as a multicolored surface, and the black contour mesh is the experimental absorbance data. (b) A hypersurface displays numerical fits to collected absorbance spectra of **1** in toluene at varied concentration and temperature. Absorbance for each surface is shifted along the absorption axis to clearly represent surfaces taken at different concentrations.
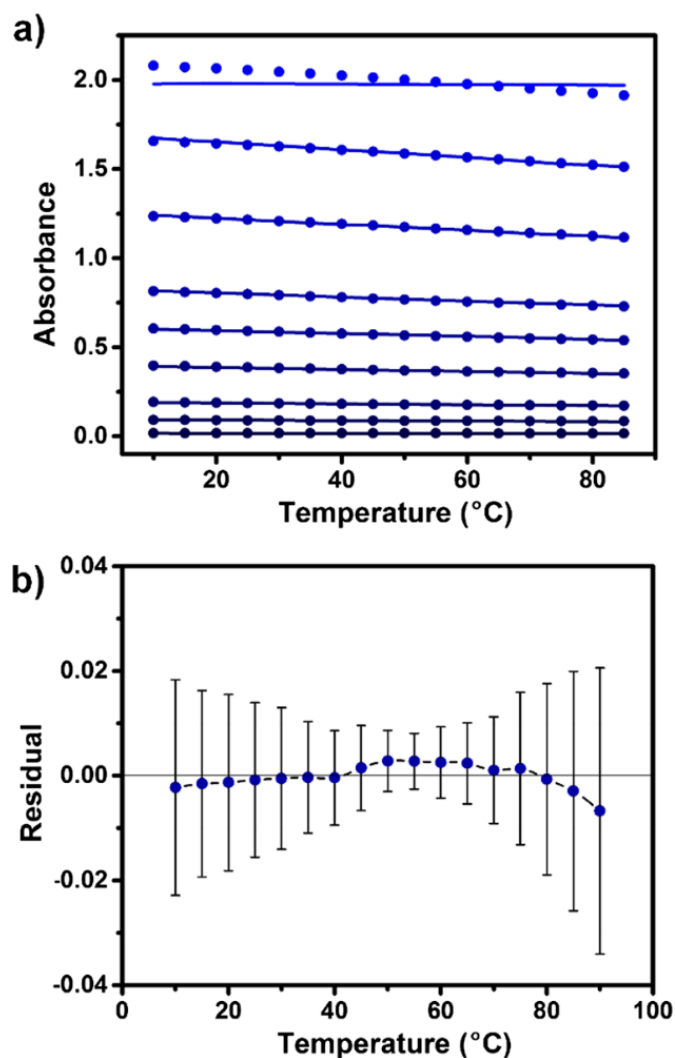
Fig. 5.5 (a) Scatterplot that includes collected averaged extinction coefficients of **1** at selected concentrations and varied temperatures as points. Model fittings are also shown as lines and are color matched to data points. Averaged extinction coefficients are calculated as mean absorbance from 325 to 375 and 500 to 600 nm. (b) A residual plot shows the average weighted sum of square residuals (wSSR) between model fitting and averaged extinction coefficients for 1 at all collected concentrations. Error is displayed as one standard deviation of the wSSR.

The isodesmic equations are entered into Excel, and the solver function varies the values of ΔH, ΔS, ε_m, and ε_∞ until the wSSR is minimized, thereby providing the thermodynamic assembly parameters. Points on the hypersurface where precipitation or clouding were observed are excluded from the fitting to minimize error. To ensure that the
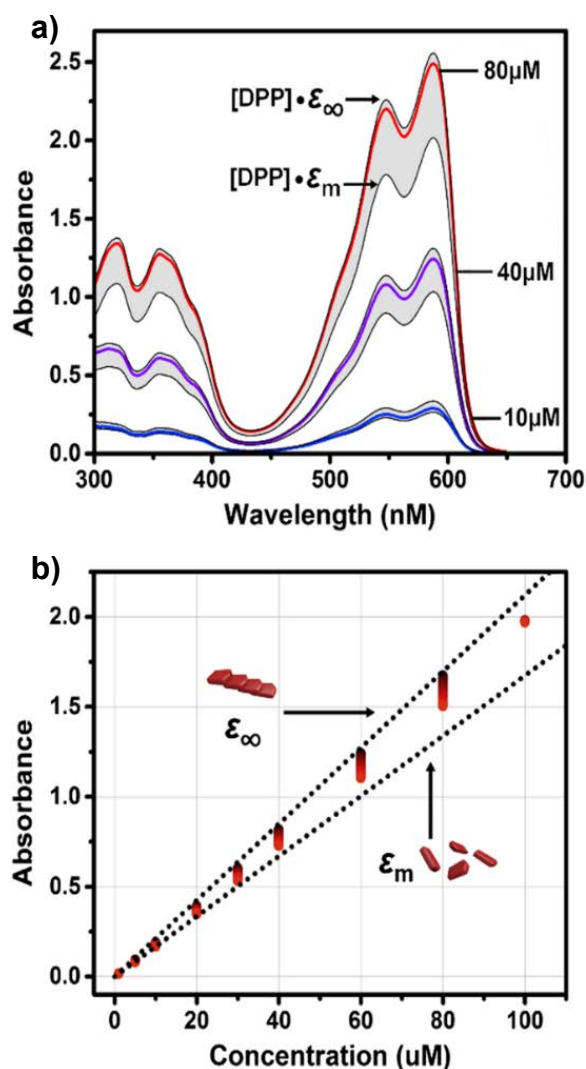
Fig. 5.6 (a) Absorbance spectra of **1** at 20 °C in toluene. Solution spectra at 5, 40, and 80 μM are displayed as colored lines. Gray ranges display the model-generated spectra from a purely monomeric species (lower absorption) to a purely aggregated species (higher absorption). The effective absorption coefficient corresponds to the amount of mDPP used to make the solution and not to the concentration of monomers or polymers. (b) Modified Beer–Lambert plot showing all collected absorbance values of **1** at selected concentrations and varied temperatures as points. Points in red are at 90 °C and darken to black at 10 °C. The lower dotted line represents the monomer absorption coefficient, ε_m, and the upper line represents the aggregate absorption coefficient, $\varepsilon\infty$. Absorbance is plotted as mean absorbance from 325 to 375 and 500 to 600 nm. DPP, diketopyrrolopyrrole.

data reflect global rather than local minima, the fits were validated using the Multistart tool in the solver to vary systematically the starting points for the numerical fits. Parameter solutions were dismissed if the resulting absorbance model did not match the slope and concavity of experimental data. The errors in the fits with respect to absorbance were

analyzed and displayed in Figs 5.5 and S14. The values obtained of ΔH, ΔS, ε_m, and ε_∞ for **1** were consistent with our previously determined results,[34] demonstrating the reproducibility of this analytical procedure. Previously, [34] by fitting absorbance changes at all wavelengths, ΔG^o was determined to be $-6.5 \pm 1.1\,\text{kcal}\,\text{mol}^{-1}$. In the current study, ΔG^o was calculated by fitting the mean absorbance values of absorption band wavelengths, and a nearly identical value of $-6.4 \pm 0.11\,\text{kcal}\,\text{mol}^{-1}$ was obtained.

A characteristic of the supramolecular assembly of chromophores is a deviation from Beer's law with assembly because the extinction coefficient of the aggregates is distinct from the monomer[254, 266] and this phenomenon is observed for DPP derivatives **1, 2, 5, 6, 7**. This occurs because the extinction coefficients for the monomer, ε_m, and the cluster, ε_∞ are different as a result of excitonic coupling[257] and therefore, the observed extinction coefficients in solution are a dynamic representation of the equilibrium position. It should be noted that the solution is never fully aggregated nor disaggregated, and the values of ε_m and ε_∞ can be determined only through numerical fittings, which provide values for ε_m and ε_∞ for selected wavelengths (330–380 and 470–570 nm) of 1.7×10^4 and $2.1 \times 10^4\,\text{cm}^{-1}\,\text{M}^{-1}$, respectively. The extinction coefficients are averaged from a range of wavelengths to minimize the effects of spectrum noise, as well as to accommodate the bathochromic shifting caused by aggregation. As expected for *J*-aggregates, extinction coefficients increase with assembly compared with the monomers. The absorbance intensities are never the total DPP in solution in all forms, $[\text{DPP}]_t$, multiplied by either ε_m and ε_∞; rather, these represent the upper and lower bounds of the absorption data (Figs 5.6 a and Appendix D Fig. D10), and as concentration increases or temperature decreases, the absorption data trend upwards towards the theoretical spectrum obtained by the multiplication of $[\text{DPP}]_t$ by ε_∞ (Figs 5.6 b and Appendix D Fig.D11).

Table 5. 1. Thermodynamic assembly parameters for diketopyrrolopyrrole derivatives **7** in toluene

	ΔH_a	ΔS_b	ΔG^o_c	$K \times 10^{-4}{}_d$	$\varepsilon_\infty \times 10^{-4}{}_e$	$\varepsilon_m \times 10^{-4}{}_f$
Compound	**kcal mol⁻¹**	**e.u.**	**kcal mol⁻¹**	**M⁻¹**	**cm⁻¹ M⁻¹**	**cm⁻¹ M⁻¹**
1	−7.4	−3.4	−6.4	5.1	2.2	1.7
2	−6.4	−0.31	−6.3	4.4	2.4	1.8
3	−1.9	12	−5.4	0.90	2.7	1.1
4	−3.1	8.2	−5.6	1.2	2.2	1.3
5	−1.8	13	−5.6	1.3	2.5	1.2

a) The error in ΔH for all compounds is ±0.96 kcal mol⁻¹.
b) The error in ΔS for all compounds is ±3.00 e.u.

c) The error of ΔG for all compounds is ±0.11 kcal mol⁻¹.

d) The error of K for all compounds is 11%.

e) The error of $\varepsilon\infty$ is 2.7% for all compounds. Polymer extinction coefficient, $\varepsilon\infty$, is derived from mean
absorbance from 330 to 380 and 500 to 600 nm for **1** and **2**; wavelengths are 330–380 and 470–570 nm for **5**, **6**, and **7** to match peak wavelengths.

f) The error of ε_m is 2.2% for all compounds. Monomer extinction coefficient, ε_m, is derived from mean absorbance from 330 to 380 and 500 to 600 nm for **1** and **2**; wavelengths are 330–380 and 470–570 nm for **5**, **6**, and **7** to match peak wavelengths

The thermodynamic assembly parameters for **7** are presented in Table 5. 1., and the relative values for ΔH, ΔS and ΔG^o are compared to understand relationships between molecular structure, noncovalent bonding, and aggregation. From the data in Table 5. 1., we find that the free energy of binding (ΔG^o) is greatest for **1** and **2** (−6.4 and −6.5 kcal mol⁻¹, respectively). In addition, ΔH and ΔS for these two molecules are within the error of the experimental approach. The ΔG^o for **1** and **2** are greater than for **5, 6, 7** (−5.4 to −5.6 kcal mol⁻¹), and this difference of ~1 kcal mol⁻¹ arises because of the additional H-bonding that occurs between the adjacent DAP units – as observed in the crystal structure of **2**. The aggregation of **1**and **2** was also studied by VT UV–Vis spectroscopy in a 99:1 toluene:DMSO solvent mixture because these solution conditions are known to disrupt the H-bonding.[34-35] We were unable to obtain a satisfactory fit to these spectroscopic data and thereby quantify the thermodynamic assembly parameters

precisely, but the spectral response to decreasing temperature or increasing concentration was diminished compared with the spectral changes that occurred in the absence of DMSO, indicating that aggregation was less favorable in the presence of DMSO. We interpret these differences as indicating that the driving force for aggregation is lower in the presence of DMSO because the DMSO disrupts H-bonding between DAP groups in adjacent DPP monomers. Compounds **5**, **6**, **7** differ in the length and chirality of the solubilizing alkyl chains appended to the nitrogens of the DPP heterocycle. Compound **5** has a (*S*)-2-methylbutyl side chains, **4** has racemic 2-ethylhexyl side chains, and **7** has racemic 2-methylbutyl side chains. The ΔG^o values for **5, 6, 7** are within the error of the experimental approach. Compound **6** has more favorable ΔH than **5** or **7** (−3.1 vs. −1.9 kcal mol^{-1}, respectively), but the homoaggregation of **6** is less entropically favorable than **5** or **7**. This may be a case of entropy–enthalpy compensation.[267-268] While longer side-chains may increase van der Waals contacts, assembling longer alkyl chains into aggregates requires restricting the rotations of more atoms, which proceeds with a concomitant entropic penalty. Thus, solubilizing chain length has a limited effect on the favorability of homoaggregation. By comparing **5** and **7**, we can analyze whether the presence of asymmetrically substituted carbons affects aggregation thermodynamics. Both enthalpy and entropy of aggregation for these two DPP derivatives are identical, and thus, we conclude that the presence of chiral centers does not affect assembly for this pair. This conclusion is consistent with an isodesmic assembly model, in which chirality is not expected to influence binding favorability. Previous research has shown that only sterically demanding chiral structures will contribute to chiral amplification.[37, 269-271] The chiral contributors in the DPP derivatives **1** and **5** used are all short branched alkanes with low steric demands and do not direct chiral assembly [270] in DPP homoaggregates.

The association constant, K, provides insight into how the equilibrium between monomeric and aggregated states shifts in response to external perturbations – particularly changes in temperature and concentration. The K values determined from fitting the UV–Vis data from **1**, **2**, **5**, **6**, **7** in toluene at 298 K are provided in Table 5. 1. The values range from $5.1 \times 10^4 \, \text{M}^{-1}$ for **1** to $0.90 \times 10^4 \, \text{M}^{-1}$ for **5**, and these numbers follow the same trends observed for the ΔG^o values. Equation 2 can be used to anticipate how K changes in response to increasing temperature (Fig. 5.7 a), and in heating from 10 to 85 °C, Ks for **1** and **2** decrease approximately eightfold, whereas Ks for **5**, **6**, **7** change only nominally over the same range of temperature. These data demonstrate that the DPPs that possess DAP groups have a more dramatic shifts in response to changes in temperature compared with those that do not organize with the assistance of H-bonds. The response to changes in concentration is similarly more pronounced for **1** and **2** than for **5**, **6**, **7**. Because DPP forms clusters, changes in temperature and concentration represent movement along a reaction coordinate involving aggregates of different sizes. The mean stack size, $\acute{n}$ – the average number of DPP monomers in a given stack – can be determined from K using Eq 38:

$$\acute{n} = \frac{2K^2[\text{DPP}]_t^2}{2K^2[\text{DPP}]_t + 1 - \sqrt{4K[\text{DPP}]_t + 1}} - K[\text{DPP}]_t$$

(38)

The $\acute{n}$ for **1**, **2**, **5**, **6**, **7** at a concentration of 20 μM with variations in temperature is plotted in Fig. 5.7 b, and the relationship between $\acute{n}$ and concentration at 298 K is shown in Fig. 5.7 c. Taken together, the changes in $\acute{n}$ with shifts concentration and temperature can be presented as a surface (Figs 5.7 d and Appendix D Fig. D16) that encompasses how $\acute{n}$ reacts to external perturbations. The trends observed for $\acute{n}$ follow those observed for K, where $\acute{n}$ decreases with increasing temperature or decreasing concentration and that

the change in $\dot{n}$ is more pronounced for compounds **1** and **2** than **5, 6, 7**. In this temperature and concentration range, $\dot{n}$ of **1** only barely exceeds 3 at 100 μM and 10 °C.

The equilibrium between aggregated and disaggregated state can also be understood in terms of the normalized mass fraction, X_n, of stacks of size n in solution. For example, X_3 is the percent of DPPs in solution that are in trimers under a given set of equilibrium conditions. The X_n can be determined according to Eq 39:

$$X_n = nK^{n-1}\left(\frac{2K[DPP]_t + 1 - \sqrt{2K[DPP]_t + 1}}{2K^2[DPP]_t}\right)^n / [DPP]_t$$

(39)

The X_n as a function of temperature and concentration for **1** are shown in Fig. 5.8a and 5.8b, respectively, and for all compounds in Appendix D Fig. D17 and D18. These plots demonstrate that $\dot{n}$ increases with both decreasing temperature and increasing concentration, although at 20 μM, **1** remains primarily in the monomeric form. The plot in Fig. 5.8b shows that at 50 μM and 25 °C, the maximum of the plot occurs at $n = 2$ and at 90 μM and 25 °C, the X_n of $n = 3$ are nearly equal. These curves are also a representation of the polydispersity of the aggregates in solution and show that although the $\dot{n}$ for a DPP at a given equilibrium point may be low, a significant amount of oligomers larger than $n = 2$ ($X_n > 50\%$) is present in solution. Extrapolating equations 38 and 39 to a higher concentration predicts microscale polymers of $\dot{n} = 20.9$ at 10 mM and 25 °C (Fig. 5.9 a), and a significant proportion of oligomers larger than $n = 33$ ($X_n > 50\%$) at 10 mM and 25 °C (Fig. 5.9 b). We should note that the isodesmic model used herein does not accommodate for chain combination processes that occur in step-growth polymerizations and may therefore underestimate molecular weight, and there is still a need to develop experimental methods that can independently verify cluster size.
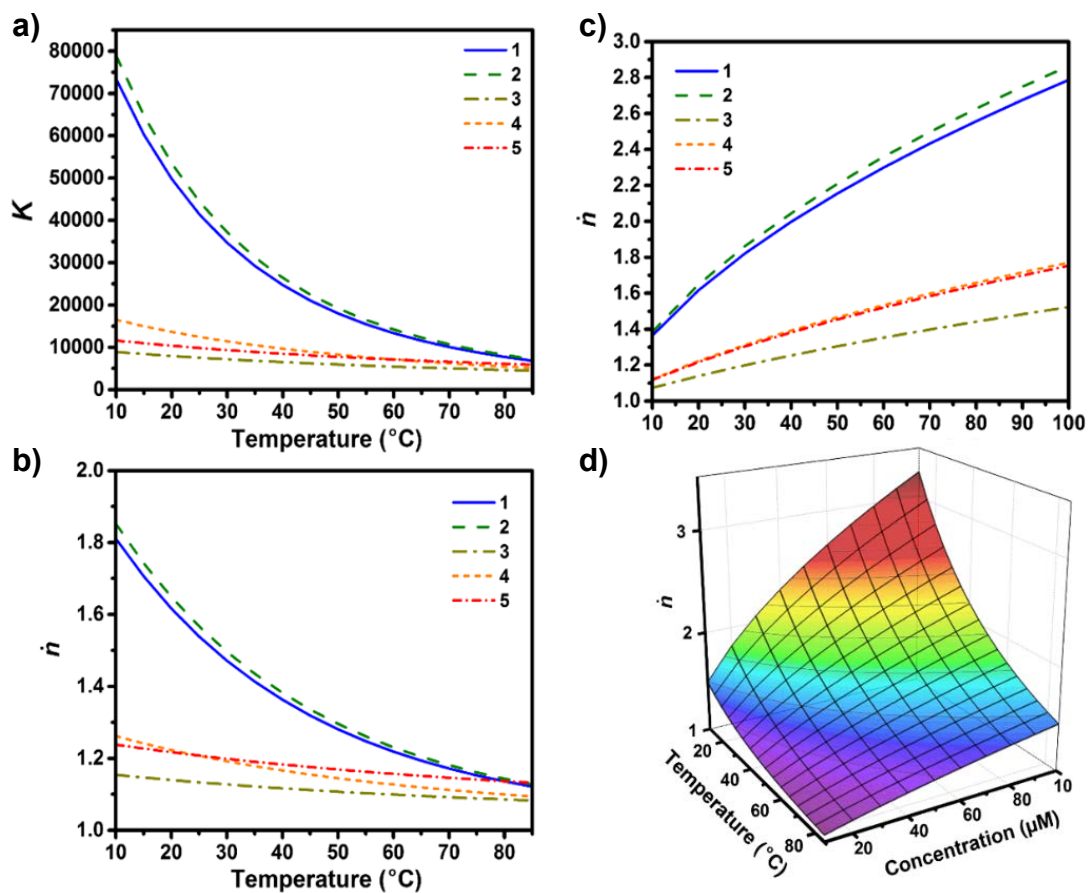
Fig. 5.7 (a) The aggregation constant at varied temperatures from eq 37. (b) Mean stack size, $\dot{n}$, for all compounds at varied temperatures and (c) at varied concentrations from eq 38 (d) $\dot{n}$ of 1 is displayed at various temperatures and concentrations from eq 39.
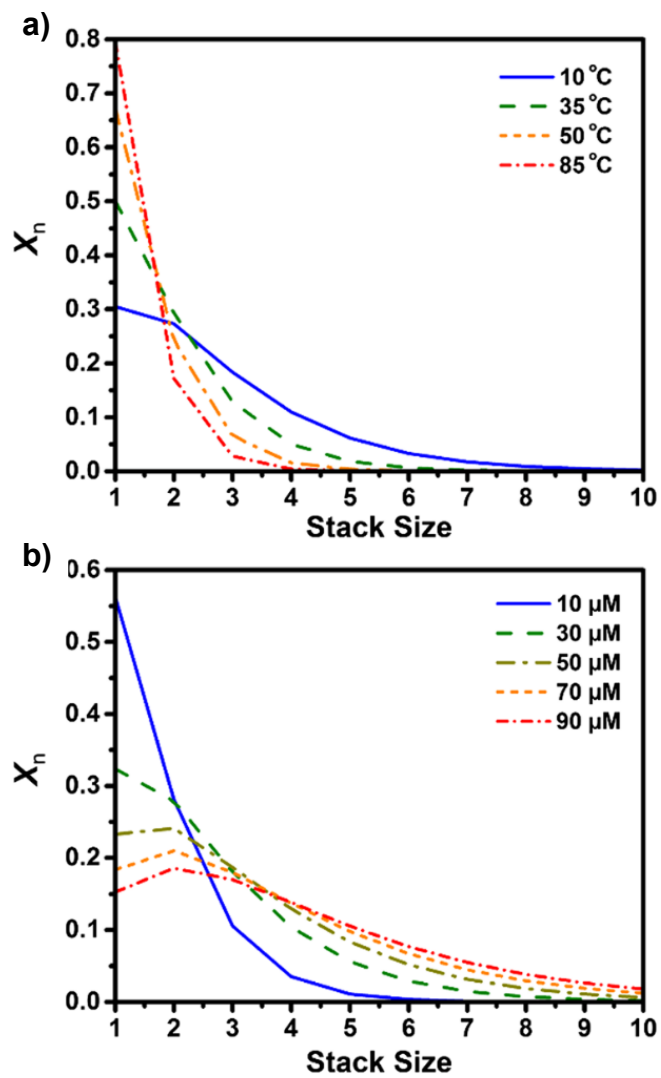
Fig. 5.8 (a) Mass fraction, X_n, as a discrete function of stack size at varied temperatures and 20 μM and (b) X_n at varied concentrations and 25 °C from eq 37.
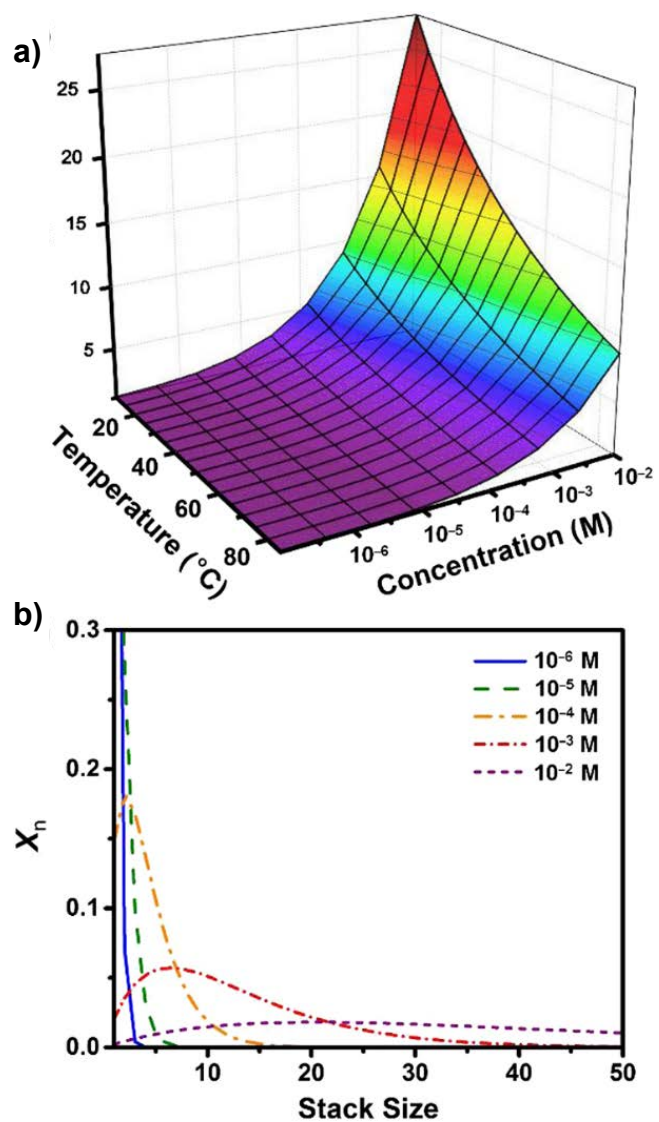
Fig. 5.9 (a) Mean stack size of, $\dot{n}$, is displayed at various temperatures and extrapolated concentrations from eq 38. (b) Mass fraction, X_n of is displayed at extrapolated concentrations and 25 °C from eq 37.

5.5 Summary

The assembly of a series of molecules containing the DPP heterocyclic scaffold with appended thiophenes into aggregates was studied using VT UV–Vis titrations, and the spectroscopic changes in response to shifts in temperature and concentration were fit to an isodesmic model to determine ΔH, ΔS, ΔG^o, and K for each molecule. These data show that the presence of DAP groups – with their ability to form H-bonds – in **1** and **2** enhances significantly the driving force for assembly into clusters. The structure of the aggregates that form is extrapolated from that of the solid-state and computational modeling. Crystal structures for **2** and **5** were obtained, and it was confirmed that these molecules assemble into slip-stacked geometries, which are often described as *J*-aggregates. Because the equilibrium involved is an assembly into aggregates, a significant amount of information is encompassed within the derived parameters. Herein, we have derived two new equations that relate K to mean stack size, $\dot{n}$, and the average mole fraction, X_n, of each stack size, n. Under the temperature and concentration conditions explored, we find that in this series of molecules, the presence of H-bonding DAP groups results in the formation of larger aggregates than those without the DAP groups.

This supramolecular system also reveals the richness beneath even the simplest noncovalent assembly. Through these studies, we have shown that the homoaggregation of chromophores is directed by the amalgamated contributions of $\pi\bullet\bullet\bullet\pi$ stacking, H-bonding, van der Waals contacts, solvent, concentration, and temperature. It is the subtle combination of all these variables operating in concert that determine size, structure, stability, and spectroscopic attributes of the resulting superstructures. The implications of this finding are that an abundance of complex structures and, in turn, emergent properties are accessible from simple molecules under the correct solution conditions. It should come

as no surprise then that the intricacy of nature – replete with hierarchical materials, refined optical and electronic systems, and stimuli-responsive dynamics – arises from coordinated behavior within multicomponent supramolecular schemes. Continued studies involving noncovalent assembly in non-natural systems could lead to new materials with sophisticated emergent optoelectronic behavior, environmentally benign manufacturing approaches, and a more complete understanding of life – a system that could be considered the self-perpetuating combination noncovalent contacts.[272] To this end, there is a need to continue studying supramolecular assembly until materials with the architectural complexity and emergent stimuli-responses of biology can be recreated in synthetic materials.

CHAPTER 6

SYNTHESIS OF DIKETOPYRROLOPYRROLE AND PERYLENE DERIVED BISDIIMIDE COMPOUND

1) **N,N'-(4-(5-(2,5-bis((S)-2-methylbutyl)-3,6-dioxo-4-(thiophen-2-yl)-2,3,5,6-tetrahydropyrrolo[3,4-c]pyrrol-1-yl)thiophen-2-yl)pyridine-2,6-diyl)dipentanamide**
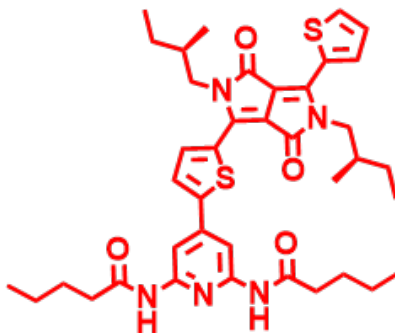
2,5-Dimethybutyl-3,6-bis(5-bromothiophen-2-yl)pyrrolo[3,4-c]-pyrrole-1,4-dione (2.1 mmol) 2,6-Divalerylamido-4-tributylstannylpyridine (1.1 mmol) and dichloropalladium(bistriphenylphosphine) (0.05 mmol) were dissolved in toluene and stirred under reflux overnight. After cooling to rt, the reaction mixture was concentrated in vacuo and the residue was purified by column chromatography (SiO$_2$, 5:1 CH$_2$Cl$_2$:EtOAc) to provide purple crystals (20% yield). ^{1}H NMR (400 MHz, CDCl$_3$, 25 °C): δ 9.01 (d, J = 4.0 Hz, 1H), 8.93 (d, J = 4.0 Hz, 1H), 8.22 (s, 2H), 7.70 (bs, 2H), 7.67 (d, J = 4.0 Hz, 1H), 7.64 (dd, J = 1.2, 4.0 Hz, 1H), 7.27 (d, J = 4.0 Hz, 1H), 4.07-3.93 (m, 4H), 2.42 (t, J = 8 Hz, 4H), 1.92 (m, 2H), 1.73 (qui, J = 8 Hz, 4H), 1.53-1.47 (m, 2H), 1.42 (sex, J = 8 Hz, 4H), 1.27-1.19 (m, 2H), 0.98-0.89 (m, 18H) ppm. ^{13}C NMR (500 MHz, CDCl$_3$, 25 °C): δ 171.88, 161.71, 161.62, 150.16, 146.13, 144.91, 140.87, 139.49, 136.45, 135.94, 130.99, 129.82, 128.58, 127.19, 108.82, 107.99, 105.72, 47.67, 37.60, 35.58, 35.42, 27.37, 27.02, 26.98, 22.35, 16.74, 16.61, 13.83, 11.29 ppm. HRMS m/z calcd for C$_{39}$H$_{50}$N$_5$O$_4$S$_2$ [(M+H)$^+$] :716.3304, found 716.

2) **N,N'-(4-(5-(2,5-bis(2-ethylhexyl)-3,6-dioxo-4-(thiophen-2-yl)-2,3,5,6-tetrahydropyrrolo[3,4-c]pyrrol-1-yl)thiophen-2-yl)pyridine-2,6-diyl)dipentanamide**
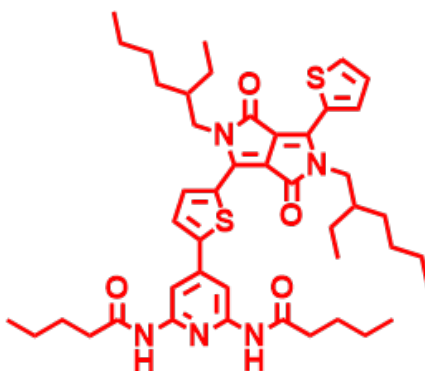
Di-bromo-di-alkyl-DPP (0.28 mmol), 2,6-Divalerylamido-4-tributylstannylpyridine (0.61 mmol) and dichloropalladium(bistriphenylphosphine) (0.028 mmol) were dissolved in toluene and stirred under reflux overnight. The reaction mixture was concentrated under reduced pressure, and the residue was purified by column chromatography (SiO$_2$ 5:1 CH$_2$Cl$_2$:EtOAc) to provide as purple crystals (45% yield). ^{1}H NMR (400 MHz, CDCl$_3$, 25 °C): δ 8.92 (dd, J = 1.2, 4.0 Hz, 1H), 8.90 (d, J = 4.0 Hz, 1H), 8.25 (s, 2H), 7.66 (d, J = 4.0 Hz, 1H), 7.64 (dd, J = 1.2, 4.0 Hz, 1H), 7.63 (s, 2H), 7.27 (d, J = 4.0 Hz, 1H), 4.08-4.02 (m, 4H), 2.40 (t, J = 8 Hz, 4H), 1.87 (b, 2H), 1.72 (qui, J = 8 Hz, 4H), 1.47-1.23 (m, 21H), 0.96 (t, J = 8 Hz, 6H), 0.92-0.82 (m, 12H) ppm. ^{13}C NMR (400 MHz, CDCl$_3$, 25 °C): δ 171.62, 161.72, 161.66, 150.23, 146.17, 144.80, 140.85, 139.65, 136.34, 135.59, 130.80, 130.78, 129.76, 128.47, 127.01, 108.83, 108.11, 105.75, 77.32, 77.01, 76.69, 45.93, 39.30, 39.07, 37.54, 30.32, 30.22, 28.43, 28.35, 27.32, 23.65, 23.55, 23.06, 22.31, 14.01, 13.97, 13.79, 10.56, 10.51 ppm. HRMS m/z calcd for C$_{45}$H$_{61}$N$_5$O$_4$S$_2$ [(M+H)+] 800.4243, found 800.4223.

3) 1,7-Di(4-ethyloctyl) perylene-3, 4:9, 10-tetracarboxylic acid diimide
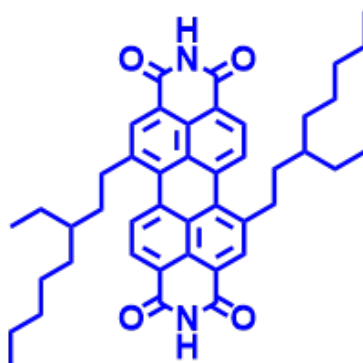
N,N'-dicyclohexyl-1,7-Di (4-ethyloctyl) perylene-3,4:9,10-tetracarboxylic acid diimide (0.67 mmol) and KOH (0.1 mol) were dissolved in a mixture of t-BuOH and H_2O. The solution was stirred for 25 h under reflux. Subsequently, HCl solution (2 N) was added dropwise to the cooled reaction, and the suspension was stirred for another 6 h. The precipitate was collected by filtration, washed with H_2O and air-dried. Without further purification and characterization, it was combined with NH_4OAc and dissolved in AcOH. The reaction mixture was stirred at 120 °C for 15 h. After cooling to rt, the resulting suspension was diluted with H_2O. After standing for 1 h, the dark precipitate was collected by filtration, washed with H_2O, and air-dried by aspiration. Further recrystallization in THF afforded 3 as a purple black solid (73% yield). ^{1}H NMR (400 MHz, $CDCl_3$, 25° C) δ: 8.72 (s, 2H), 8.65(d, 2H), 8.46(br, 2H), 8.27(d, 2H), 3.31(m, 4H), 1.97(m, 4H), 0.83-1.42 (m, 22H), 0.85(m, 12H). HRMS: m/z calcd for $C_{44}H_{50}N_2O_4$ [(M+H) +]:671.3843, Found: 671.3846.

4) N,N'-dicyclohexyl-1,7-Di (4-ethyloctyl) perylene-3,4:9,10-tetracarboxylic acid Diimide
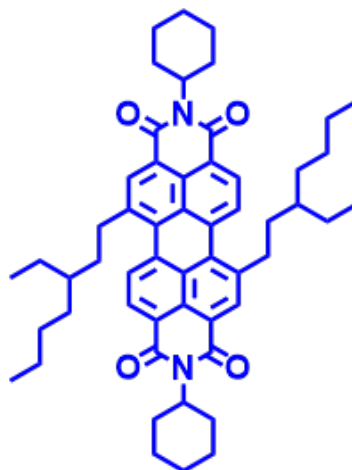
N,N'-dicyclohexyl-1, 7-Di (4-ethyloctynyl) perylene-3,4:9,10-tetracarboxylic acid diimide (0.97 mmol) and 5% Pd/C catalyst were added to degassed anhydrous THF. The reaction mixture was stirred and exposed to a H_2 atmosphere for 48 h at rt. The crude solution was filtered and concentrated. The residue was purified by column chromatography (SiO$_2$ 1:3 CH$_2$Cl$_2$:hexanes) to provide orange crystals (45% yield). ^{1}H NMR (400 MHz, CDCl$_3$, 25 °C): δ 8.67 (s, 2H), 8.60 (d, J = 8.0 Hz, 2H), 8.21 (d, J = 8.0 Hz, 2H), 5.10- 5.02 (m, 2H), 3.28 (t, J = 8.0 Hz, 4H), 2.64-2.54 (m, 4H), 1.94-1.91 (m, 8H), 1.79-1.73 (m, 6H), 1.50-1.25 (m, 28H), 0.89-0.84 (m, 12H). ^{13}C NMR (400 MHz, CDCl3, 25 °C): δ 164.17, 164.13, 141.18, 134.28, 134.18, 133.14, 129.05, 128.50, 127.98, 126.64, 122.45, 122.36, 53.92, 38.69, 36.27, 33.18, 32.82, 29.17, 28.97, 28.32, 26.56, 25.84, S9 25.47, 23.09, 14.15, 10.87. HRMS m/z calcd for C56H70N2O4 [(M+H)+] 835.5414, found 835.5416.

5) 2,5-Dimethybutyl-3,6-dithiophen-2-ylpyrrolo[3,4-c]pyrrole-1,4-dione
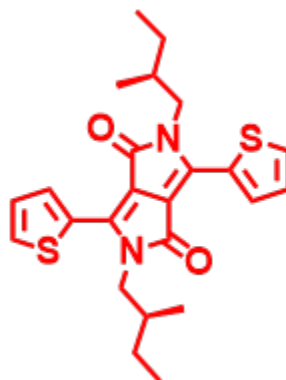
3,6-Dithiophen-2-yl-2,5-dihydropyrrolo[3,4-c]pyrrole-1,4-dione (16.7 mmol) and anhydrous K_2CO_3 (66.9 mmol) were dissolved into DMF and heated to 120 °C under N_2. (S)-(+)-1-Iodo-2-methylbutane (74.7 mmol) was added and the mixture was stirred for 15 h at 125 °C. The solution was cooled to rt, poured into ice water, filtered, and the filter cake was washed thoroughly with H_2O and MeOH. After drying in vacuo, the crude product was purified by column chromatography (SiO_2, CH_2Cl_2) to provide dark red powder (30% yield) ^1H NMR (400 MHz, $CDCl_3$, 25 °C): 8.97 (dd, J = 1.2, 4.0 Hz, 2H), 7.63 (dd, J = 1.2, 4.0 Hz, 2H), 7.27 (dd, J = 4.0, 5.2 Hz, 2H), 4.04-3.93 (m, 4H), 1.88-1.96 (m, 2H), 1.53-1.45 (m, 2H), 1.28-1.21 (m, 2H), 0.93-0.89 (m, 12H) ppm. 13C NMR (400 MHz, $CDCl_3$, 25 °C): 161.73, 140.35, 135.53, 130.62, 129.90, 128.49, 107.80, 47.61, 35.43, 26.98,16.60, 11.27. HRMS m/z calcd for $C_{24}H_{29}N_2O_2S_2$ [(M+H)]+: 440.1592, found 440.1576.

6) 2,5-Diethylhexyl-3,6-dithiophen-2-ylpyrrolo[3,4-c]pyrrole-1,4- dione
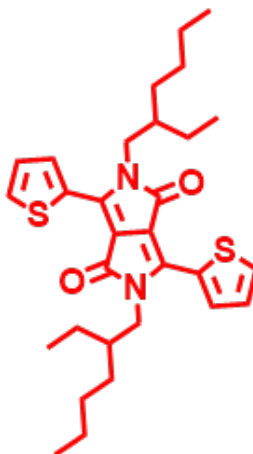
3,6-Dithiophen-2-yl-2,5-dihydropyrrolo[3,4-c]pyrrole-1,4-dione (43.3 mmol) and anhydrous potassium carbonate (173 mmol) were dissolved into N,N-dimethylformamide in a two-neck round flask and heated to 145°C under argon protection. 2-Ethylhexyl bromide (200 mmol) was injected one portion by syringe. When the reaction was stirred for 15 h at 145°C, the solution was cooled to room temperature, poured into of ice water, and then filtered. The filter cake was washed by water and methanol several times. After drying in vacuum, the crude product was purified by silica gel chromatography using dichloromethane as eluent to obtain a purple-black solid powder (76% yield). ^{1}H NMR (CDCl$_3$, 400 MHz): 8.95 (d, 2H), 7.62 (d, 2H), 7.27 (d, 2H), 4.03 (m, 4H), 1.85 (m, 2H), 1.36-1.22 (m, 16H), 0.85 (m, 12H).

7) Synthesis of 2,5-Dimethybutyl-3,6-dithiophen-2-ylpyrrolo[3,4-c]pyrrole-1,4-dione
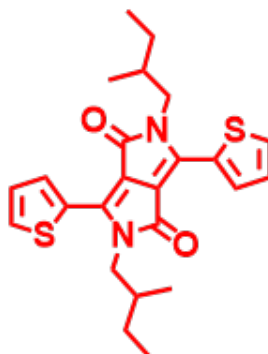
3,6- (bis-thiophen-2-yl) 2,5-Diketopyrrolo[3,4-c]pyrrole (1.66 mmol) and anhydrous K2CO3 (6.65 mmol) were dissolved into DMF and heated to 100 °C under Ar for 1 h. 1-bromo-2-methylbutane (6.62 mmol) was added slowly via syringe pump, and the mixture was stirred for 15 h at 115 °C. The solution was cooled to rt, poured into 20 mL of ice water, and organic layer was extracted with DCM. After drying in vacuo, the crude product was purified by column chromatography (SiO$_2$, CH$_2$Cl$_2$) to provide a dark red powder (11% yield) ^{1}H NMR (500 MHz, CDCl$_3$, 25 °C): 8.97 (dd, J = 1.2, 4.0 Hz, 2H), 7.63 (dd, J = 1.2, 4.0 Hz, 2H), 7.27 (dd, J = 4.0, 5.2 Hz, 2H), 4.04-3.93 (m, 4H), 1.88-1.96 (m, 2H), 1.53-1.45 (m, 2H), 1.28-1.21 (m, 2H), 0.93-0.89 (m, 12H) ppm. ^{13}C NMR (500 MHz, CDCl$_3$, 25 °C): 161.70, 140.32, 135.57, 130.65, 129.88, 128.49, 107.75, 47.58, 35.42, 26.95, 16.59, 11.27. HRMS m/z calculated for C$_{24}$H$_{29}$N$_2$O$_2$S$_2$ [(M+H)]+ : 441.1665, found 441.1651.

APPENDIX A
CHAPTER 2

General Methods

All solvents were dried using a Pure Solv MD-6 solvent purification system. All reagents and starting materials were purchased from commercial sources and used without further purification unless otherwise noted. Aqueous solutions were prepared from nanopure water purified from a Milli-Q plus system (Millipore Co.), with a resistivity over 18 MΩ cm-1. Chromatography purifications were performed using Sorbent Technologies Silica Gel (60 Å, 65 x 250 mesh). Thin-layer chromatography (TLC) was carried out using aluminum sheets precoated with silica gel 60 (EMD 40−60 mm, 230−400 mesh with 254 nm dye). TLC plates were visualized by UV-light and stained using a *p*-anisaldehyde or phosphomolybdic acid solution if required. All reactions were carried out under an inert atmosphere of N2 using standard Schlenk techniques unless otherwise noted. NMR spectra were obtained on either a Bruker AVANCE 400 and 500 MHz spectrometers. All chemical shifts are reported in δ units using the solvent residual signal as an internal standard and the coupling constant values (*J*) are reported in Hertz (Hz). The following abbreviations are used for signal multiplicities: s, singlet; d, doublet; t, triplet; q, quartet; quintet (qui); sextet (sex); m, multiplet; and br, broad. Electrospray Ionization Mass Spectroscopy (ESI-MS) spectra were acquired on an Agilent LC/MSD Trap XCT system. High-resolution mass spectral analyses were carried out on an Agilent 6200 LC/MSD TOF System. For all UV-Vis and CD measurements, the temperatures were corrected using an external digital thermometer with a microprobe accessory.

VARIABLE TEMPERATURE UV- VIS SPECTRA
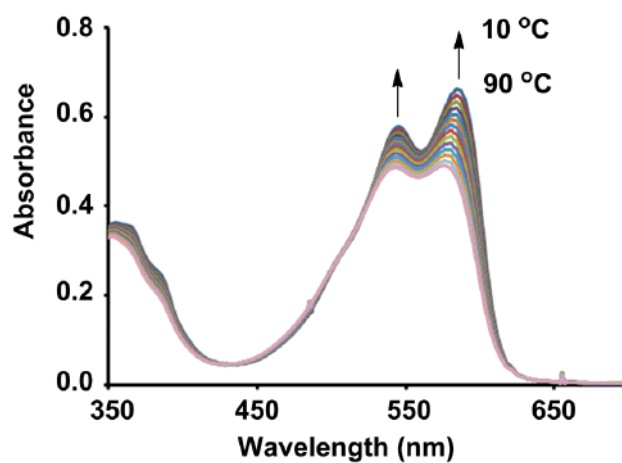
Fig. A1 Variable temperature UV-Vis of an 18.0 µM solution of 2 in toluene
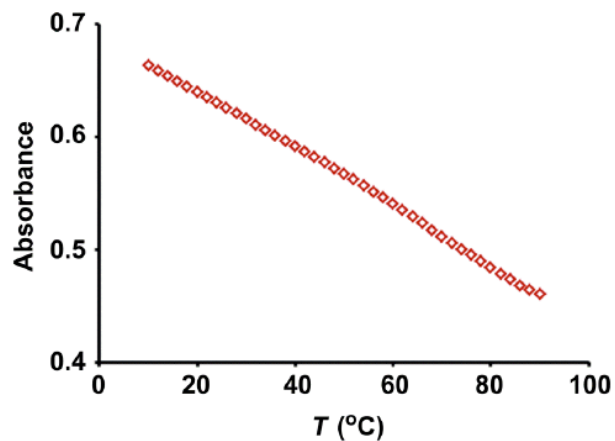
Fig. A2 The absorbance at 584 nm of a 18.0 uM of solution 2 in toluene versus sample temperature. Note a fully aggregated or disaggregated state is never reached.
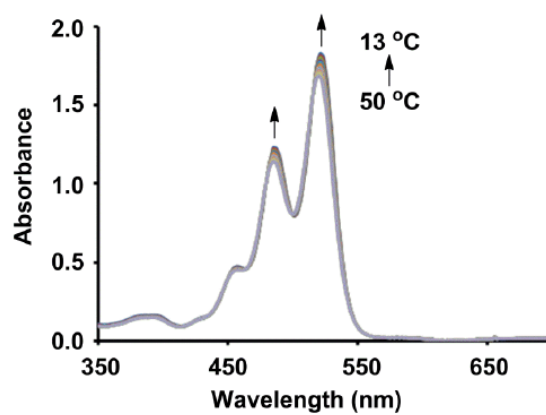
Fig. A3 Variable temperature UV-Vis of a 70 µM solution of **13** in toluene.
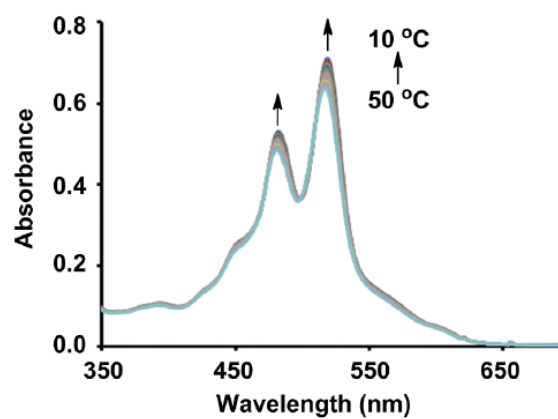
Fig. A4 Variable temperature UV-Vis of a 35 µM solution of **3** in 97:3 toluene:DMSO.
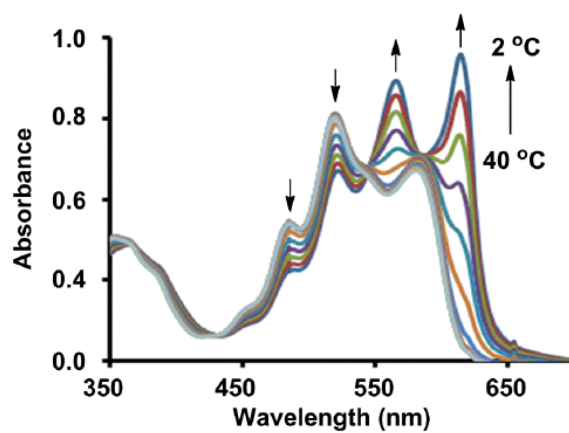
Fig. A5 Variable temperature UV-Vis of **2** (70µM) and **3** (35 µM) in toluene.
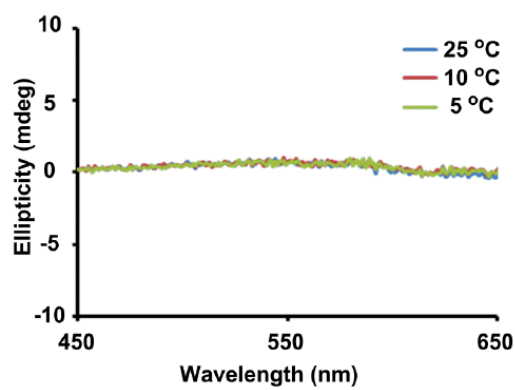
Fig. A6 Variable temperature circular dichroism spectra of a 70µM solution in toluene.
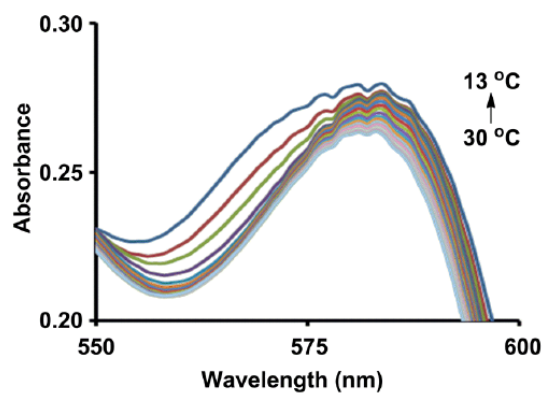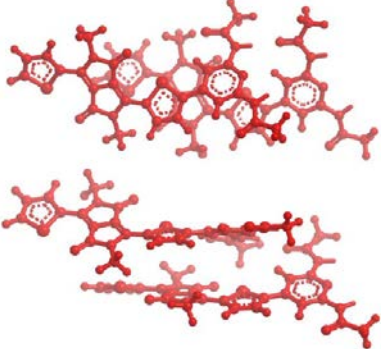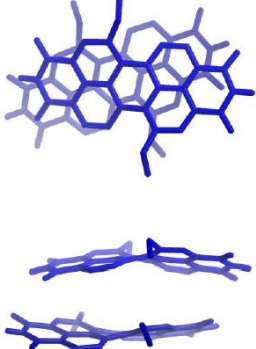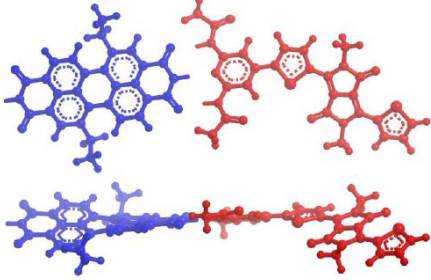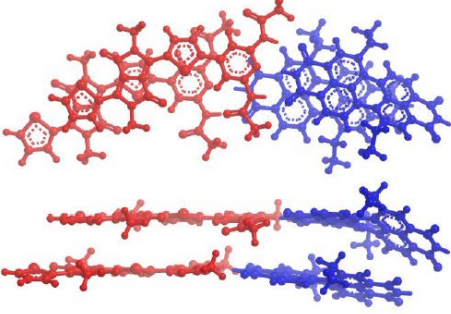
Fig. A7 Variable temperature UV-Vis of a mixture of **1** (70µM) and 3 (35µM) in toluene.

COMPUTING MODELING

The supporting information includes a separate compressed file that contains the

following .mol files which include the Cartesian Coordinates and Z-matrix for each

calculated structure:

- DPP dimer: mDPP_dimer.mol (A $\pi \bullet\bullet\bullet \pi$ stacked dimer consisting of two molecules of **1**).
- DPP dimer: mDPP_dimer.mol (A $\pi \bullet\bullet\bullet \pi$ stacked dimer consisting of two molecules of **1**)
- PDI dimer: PDI_dimer.mol (A $\pi \bullet\bullet\bullet \pi$ stacked dimer consisting of two molecules of **3**)
- **1** and **3** Mixture 1: DACS3h_monomer.mol (A H-bonded monomer consisting of one molecule of **3** and one molecule of **1**)
- DPP and PDI Mixture 2: DACS3h_pi_stacked.mol (A $\pi \bullet\bullet\bullet \pi$ stacked dimer consisting of two H-bonded **1:3** pairs π-stacked.)

Table A1. Computed structures of the different supramolecular aggregates formed in the titration experiments, with the corresponding calculated enthalpies of binding.

Molecule	Structure	Thermodynamic and Structural Properties
1 dimer		Δ E= − 10.55 kcal/mol
3 dimer		Δ E= − 2.68 kcal/mol
H- bonded **1** and **3**		Δ E= − 17.77 kcal/mol
1 and **3** heteroaggregate		$\Delta E_\pi = -6.34$ kcal/mol $\Delta E_H = -35.53$ kcal/mol $\Delta E_{tot} = -41.87$ kcal/mol

APPENDIX B
CHAPTER 3

General Methods

All chemicals were purchased from VWR or Aldrich Chemicals and used as received unless otherwise noted. DPP and PDI (as well as the cyclohexyl protected PDI) were synthesized following the previously reported literature procedures.[34] The UV-Vis measurements were performed on a Shimadzu UV-2600 spectrometer. The fluorescence measurements were done on a Varian Cary Eclipse fluorescence spectrometer equipped with a temperature controlling sample holder. Quartz cuvettes (Starna Inc.) with 1 cm path lengths were used throughout, and all solutions were prepared using volumetric glassware and spectroscopic grade solvents. Samples were degassed by purging 2 min with Ar prior to the measurement, and before each variable temperature series, the samples were heated to the highest measured temperature (70 °C) to ensure complete disaggregation. The temperature was then gradually lowered and given ten minutes to equilibrate. Temperatures were calibrated with a digital thermometer (Traceable VWR Digital Thermometer) to ensure accurate temperature measurement.

CYCLIC VOLTAMMETRY

Cyclic voltammograms (CV) were taken with a CH instruments potentiostat (CHI 660), using a polished glassy carbon working electrode, a Pt wire counter electrode, and a Ag/AgCl reference electrode. Tetrahydrofuran (THF) was used as the solvent with 0.1 M tetrabutylammonium hexafluorophosphate (Bu4NPF6, recrystallized 3x from EtOH), as the supporting electrolyte, and Ferrocene (Fc) as internal standard, to which oxidation and reduction potentials are given relative to. Before each measurement, the samples were purged with THF-saturated Ar.
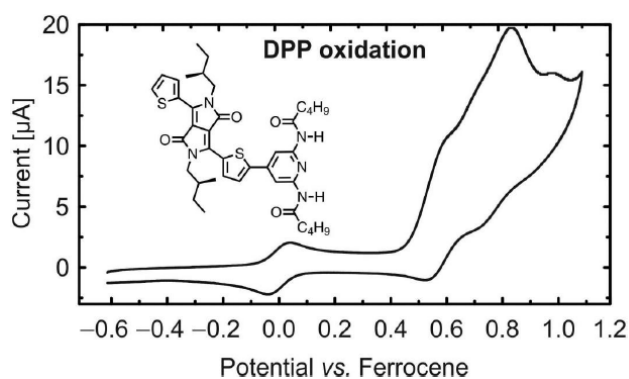
Fig. B1 CV of DPP (1mM) oxidation in THF with 0.1 M Bu4NPF6 as the supporting electrolyte. The half-wave potential of the first DPP oxidation was measured to 0.552 V relative to the oxidation of Fc.
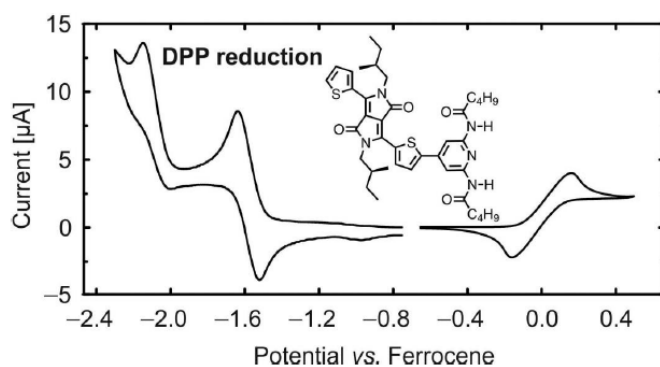
Fig. B2 CV of DPP (1mM) oxidation in THF with 0.1 M Bu$_4$NPF$_6$ as the supporting electrolyte. The half-wave potential of the first DPP oxidation was measured to -1.561 V relative to the oxidation of Fc.
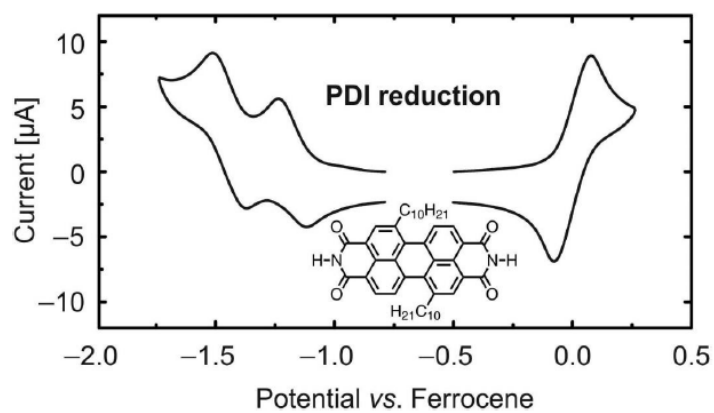
Fig. B3 CV of PDI (1mM) reduction (saturated solution at 60ºC) in THF with 0.1 M Bu$_4$NPF$_6$ as the supporting electrolyte. The half-wave potential of the first DPP oxidation was measured to -1.176 V relative to the oxidation potential of Fc.

UV-VIS MEASUREMENTS

Spectra of the Individual Compounds:

All UV-Vis measurements were taken in toluene (Alfa Aesar, spectrophotometric grade, 99.7+ %), using volumetric glassware to prepare the solutions and quartz cells for the measurement. Variable temperature UV-Vis measurements were performed on an Agilent 8453 spectrophotometer equipped with a temperature control accessory.
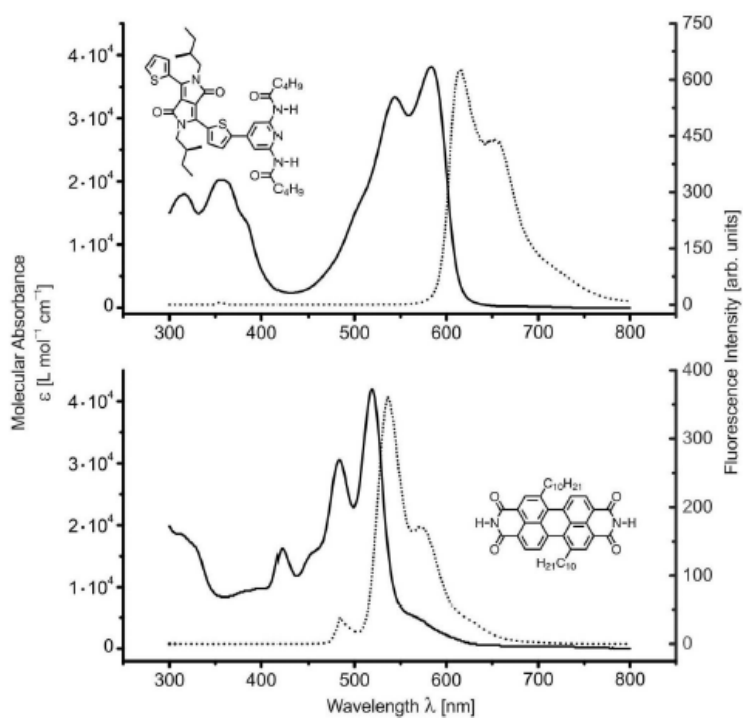
Fig. B4 Top: UV-Vis (solid line) and fluorescence (dotted line) spectrum of a 10 μM solution of DPP in toluene at room temperature. Bottom: UV-Vis (solid line) and fluorescence (dotted line) spectrum of a 25 μM solution of PDI in toluene and DMSO (9:1) at room temperature.

Variable Temperature Spectra of the 2:1 Aggregate:
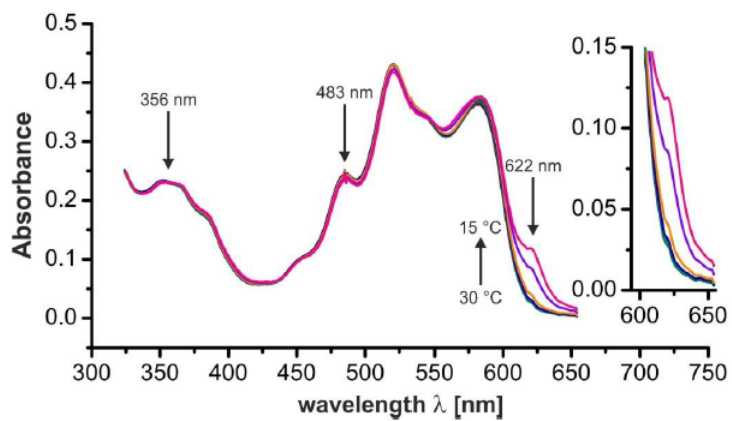
Fig. B5 Variable temperature UV-Vis spectra of a 70 µM solution of DPP in toluene with 0.5 eq. of PDI. The inset shows the growing charge-transfer band of the supramolecular aggregate at 622 nm.

SPECTRA OF THE RADICAL IONS:

To obtain spectral information on the DPP•+ radical cation, a spectroelectrochemical experiment was performed. In a quartz cuvette with 2 mm path length, a solution of DPP (0.1 mM) in THF with 0.1 M Bu4NPF6 was electrolyzed using a 5x5 mm gold mesh (size 100) that was placed into the spectrometer beam. Because of the small size of the cell, a reference electrode could not be accomodated and a Pt wire was used as a pseudo-reference electrode. The potential was gradually increased until changes in the UV-Vis spectrum were observed, and preliminary CV experiments indicated that 3.5 V applied vs. the pseudo-reference electrode were necessary to induce the first DPP oxidation. After holding the potential for 1.5 min, no further changes in the spectrum could be seen over time, and this steady state indicated that the maximum concentration of oxidized DPP was reached at the mesh electrode, with the oxidized species being reduced at the cathode. Subtracting the initial spectrum from that with applied potential after equilibration reveals the contribution of the oxidized species, that is the DPP•+ radical cation (Fig. B6)
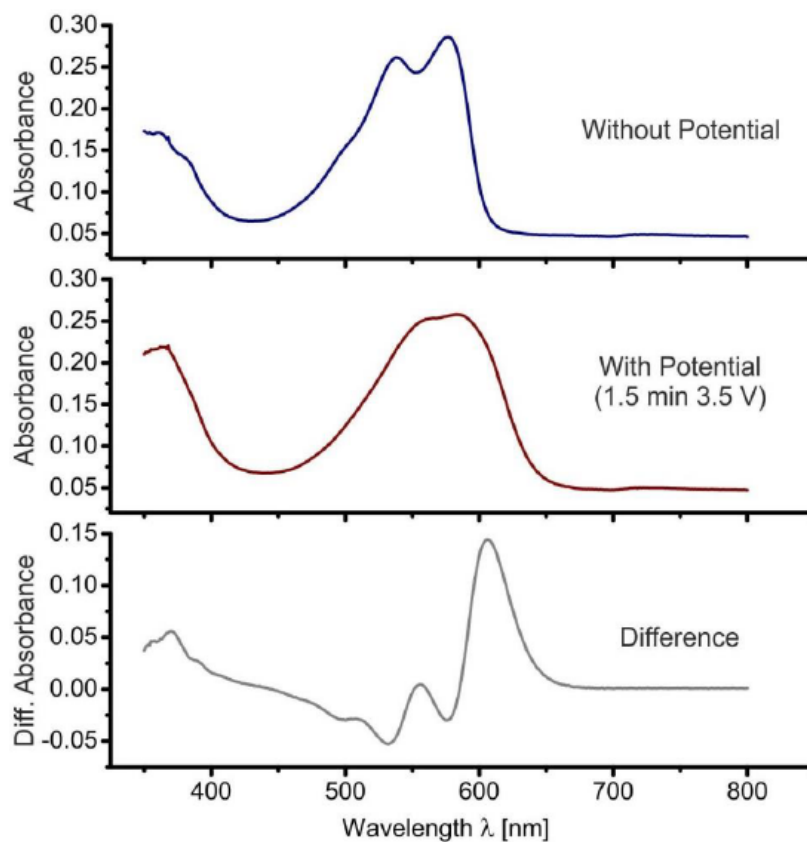
Fig. B6: Spectroelectrochemical experiment monitoring the DPP oxidation on an Au-mesh electrode. Spectrum without potential applied (top), as well as with 3.5 V (middle) applied *vs.* a Pt pseudo-reference electrode, and the difference spectrum (bottom), revealing the shape of the DPP•+ signal.

The PDI·⁻ was accessible by the *in-situ* reduction with fluoride anions as reported by Saha *et al.* (Fig. B7). [181-182] The experiment was carried out in THF, because the reducing agent Bu₄NF is not soluble in toluene.
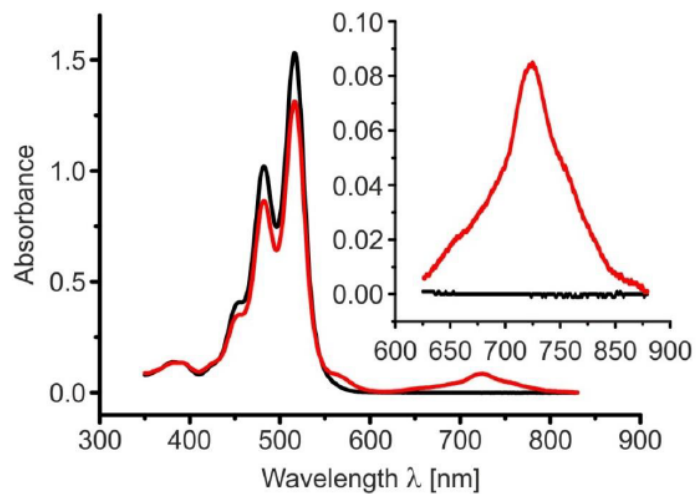
Fig. B7: UV-Vis spectrum of 25 µM *N,N'*-dicyclohexyl PDI in THF before (black), and after adding of 30 equivalents of Bu4NF. The inset shows the spectral signature of the PDI radical anion at λmax = 724 nm.

CALCULATION OF THE FRONTIER MOLECULAR ORBITAL ENERGIES

The energies of the frontier molecular orbitals were calculated using the approach described by Bauer, *et al*: [273] At first, the half-wave potentials for the reversible reduction processes of DPP and PDI were evaluated as an average between each cathodic (E_{pc}) and corresponding anodic potential (E_{pa}): $E_{1/2}(red/ox) = \frac{1}{2}(E_{pc} + E_{pa})$. Consequently, LUMO energy levels were estimated on the basis of the reference energy level of ferrocene, which is 4.8 eV below the vacuum level, [274] using the relation expressed in B-E1:

(B-E1)
$$E^{LUMO}: 4.8 + (E_{1/2}^{(red/ox)} - E_{1/2}^{Fc})\ eV$$

The value $E_{1/2}^{Fc}$ is zero if the oxidation and reduction potentials are referenced to the oxidation potential of ferrocene. While the HOMO and LUMO values do not represent any absolute solid-state or gas-phase ionization potentials, they are calculated relative to the same reference and can therefore be used to compare different compounds to one another. The results are summarized in Table B1.

Table B1: Summary of the electrochemical and UV-Vis spectroscopic data, as well as the resulting frontier orbital energies of DPP and PDI.

Compound	$E_{1/2}^{red/ox}$	E^{HOMO}	E^{LUMO}
DPP (ox)	+0.552	−5.35	--
DPP (red)	−1.561 V	--	−3.24 eV
PDI (red)	−1.176 V	−5.98	−3.63 eV

Optical band gaps of the individual compounds were evaluated by averaging the maxima of absorption and fluorescence (Table B2).

Table B2: Emission and absorption maxima of the individual compounds as well as the calculated bandgap energies.

Compound	$\lambda_{Abs\ max}$ [nm]	$\lambda_{Em\ max}$ [nm]	λ_{gap} [nm]	E_{gap} [eV]
DPP	584	613	599	2.07
PDI	519	536	528	2.35

FLUORESCENCE STUDIES

A titration was performed to evaluate the influence of concentration and temperature on aggregation induced fluorescence quenching: Starting with 2.5 mL of a 25 µM solution of PDI in toluene, we gradually added a solution of DPP in toluene (c = 4.805 10_{-4} mol L_{-1}), and the titration steps were chosen as 0, 0.08, 0.23, 0.50, 1.00, 2.00, 5.07, and 10.07 equivalents of DPP to PDI (see Table B3). After each addition, the sample was degassed by purging with Ar for approximately 2 minutes. The sample was then heated to 70 °C for 15 minutes to ensure complete disaggregation and subsequently, fluorescence spectra were recorded using λ_{Ex} = 356 nm (DPP excitation), and λ_{Ex} = 483 nm (PDI excitation). The sample was then cooled to 50 °C, 30 °C, 22 °C, and 15 °C, whereby at each temperature step the fluorescence spectra were recorded after giving the sample 10 minutes to equilibrate at the respective temperature. The samples were magnetically stirred during the measurements. Two sets of Reference Experiments (Fig. B8) were conducted to take dilution effects into account.
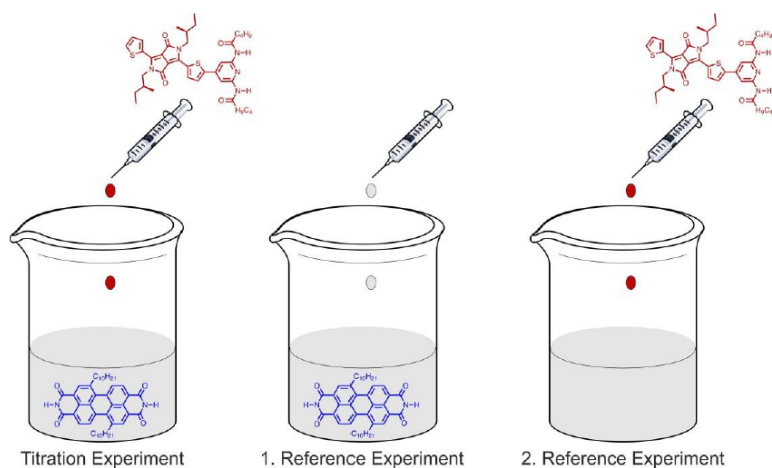
Fig. B8: Scheme of the fluorescence quenching titration: DPP was gradually added to a PDI solution, and the fluorescence of both compounds was taken at different temperatures. Following the same volumetric steps, two reference experiments were carried out. In the first (middle), toluene was added to the PDI to rule out respective dilution effects, while in the second, DPP was added to toluene to capture concentration effects on the DPP.

Table B3: Titration steps used for the variable temperature fluorescence quenching titration.

Vtot [mL]	VDPP [μL]	cPDI [μM]	cDPP [μM]	nDPP / nPDI
2.500	0	25.0	0.0	0.00
2.510	10	24.9	1.9	0.08
2.530	10	24.7	5.7	0.23
2.565	35	24.4	12.2	0.50
2.630	65	23.8	23.8	1.00
2.760	130	22.6	45.3	2.00
3.160	400	19.8	100.4	5.07
3.810	650	16.4	165.2	10.07

To decompose various effects that lead to the measured decrease in fluorescence intensity (see Fig. 3.1 d), a set of control experiments were performed (see Fig. B8). The first served to capture dilution effects on the PDI, so that instead of the titrating solution, toluene was added to the PDI solution (c_0 = 25 μM) in the same volume steps (see Table B3). The second reference experiment captured dilution effects of the DPP, and consequently, the DPP titrating solution (c = 481 μM) was added to plain toluene in the same volume steps.

If you assume that DPP and PDI do not interact (*i. e.*, that no aggregation-induced fluorescence quenching occurs), the overall intensity of a DPP fluorescence maximum in the mixture with the PDI, $I_{\lambda mix}$ (DPP), is composed of the pure DPP signal, $I_{\lambda pure}$ (DPP), and some contribution of the PDI at the same wavelength, $I_{\lambda pure}$ (PDI):

(B-E2) $$I_{\lambda mix}\,(DPP) = I_{\lambda pure}\,(DPP) + I_{\lambda pure}\,(PDI)$$

While the overall value $I_{\lambda mix}$ (DPP) is simply the measured fluorescence intensity from the mixture at a given wavelength, the latter two contributions are accessible by means of the two reference experiments. Having the individual contributions as well as the overall signal in hand, the relative fluorescence of the DPP can be calculated according to B-E3:

(B-E3)
$$I_{\lambda,\mathrm{rel}}(DPP) = \frac{[I_{\lambda,mix}(DPP) - I_{\lambda,pure}(DPP)]}{I_{\lambda,pure}(DPP)}$$

The value $I_{\lambda,\mathrm{rel}}(DPP)$ can be interpreted as a measure of how "ideal" the compound behaves within the mixture: a value of 1 indicates that DPP exhibits the same fluorescence as if there was no quencher in solution (second reference experiment). In conjunction with our observation that the absorption at the excitation wavelength does not change with temperature (see Fig. B10), values smaller than 1 indicate that the fluorescence is quenched, which in the DPP/PDI system begins at temperatures below 30 °C (Fig. 3.2 C), where aggregation commences.[34]

FLUORESCENCE OF THE DONOR-ACCEPTOR AGGREGATE BY EXCITATION INTO CHARGE TRANSFER BAND

To rule out whether the charge separated state decays via fluorescence, emission spectra at 622 nm excitation wavelength, where a charge transfer band arises upon aggregation, were taken from a sample of DPP (83 μM), and PDI (42 μM) in toluene before and after the addition of 5 % DMSO. The difference spectrum (Fig. B9) indicates that the detected fluorescence belongs to the individual compounds, so that direct photoexcitation into the charge separated state does not produce any additional signal, meaning that the charge separated undergoes radiationless decay. The difference spectrum shows a large negative peak at $\lambda = 622$ nm, which is a result of light scattering off of small PDI aggregates that vanish upon the addition of DMSO because of the much higher solubility.
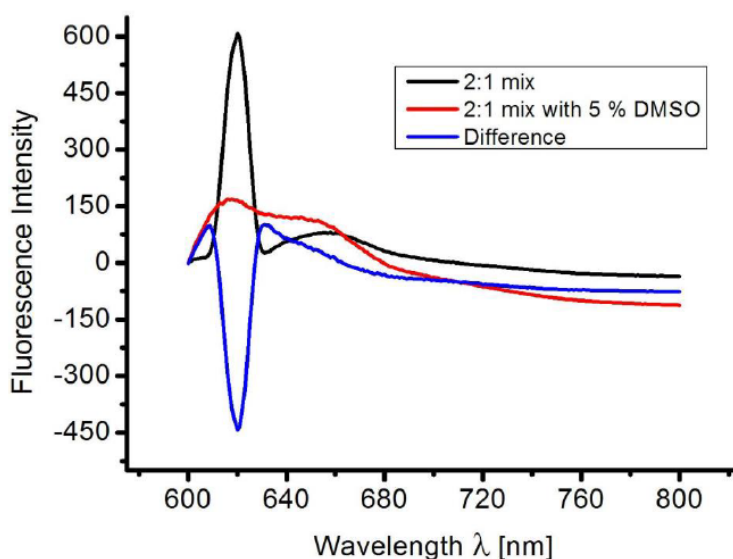
Fig. B9: Fluorescence spectra of a mixture of DPP (83 μM), and PDI (42 μM) in toluene before (black), and after (red) adding 5 % DMSO to induce chemical disaggregation. The difference spectrum (blue, obtained by subtracting fluorescence intensities before DMSO-induced disaggregation from the ones after) does not show negative features (apart from scattered excitation light at 622 nm), thereby indicating that the supramolecular aggregate does not fluoresce to any significant content.

Variable Temperature Fluorescence Spectroscopy of the 2:1 Aggregate
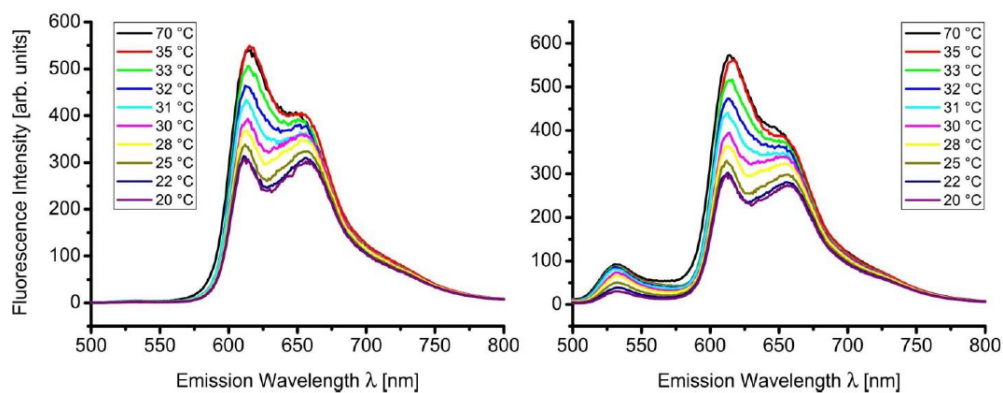
Fig. B10: Variable temperature fluorescence spectroscopy with the 2:1 mixture of DPP (45 µM) and PDI (23 µM) in toluene at 356 nm excitation (left), and 483 nm excitation (right).

To assess the temperature threshold for aggregation of a 2:1 mixture (45 µM DPP and 23 µM PDI in toluene; Table B3, line 6), the fluorescence spectra were measured between 70 °C and 20 °C by lowering the temperature in very small steps. The sample was excited at 356 nm (DPP excitation), and 483 nm (PDI excitation) and emission spectra recorded from 500 to 800 nm. As the temperature is lowered, quenching of the DPP fluorescence (Fig. B10 left), as well as of the PDI fluorescence (Fig. B10 right) is visible. The PDI fluorescence is largely diminished upon mixing, as those fluoresced photons can be absorbed by the DPP.

Variable Temperature Fluorescence Titration Spectra:

Starting point: Solution of PDI in toluene (c_0 = 25 μM, V_0 = 2.5 mL) in a septum-sealed, 1 cm quartz cuvette, to which DPP (solution in toluene, c = 4.805 10^{-4} mol L^{-1}) was gradually added.
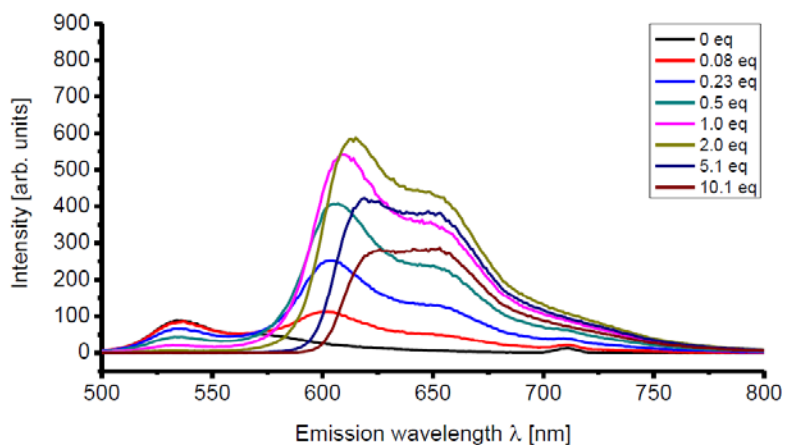
Fig. B11: Fluorescence quenching titration (addition of 481 μM DPP to 25 μM PDI in toluene), 70 °C, λ_{Ex} = 356 nm.
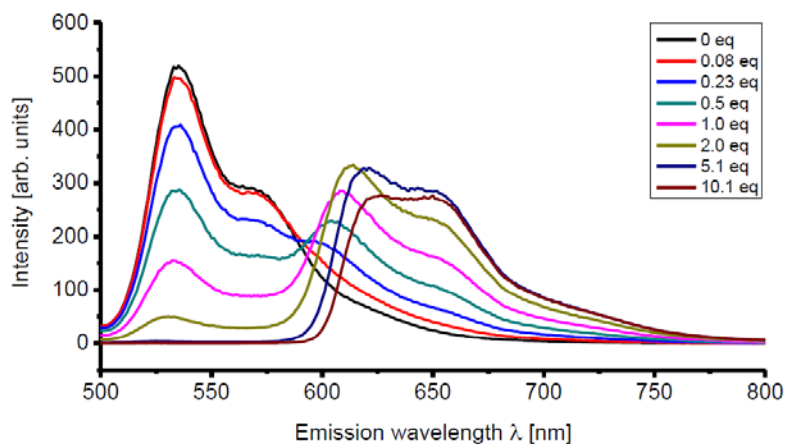
Fig. B12: Fluorescence quenching titration (addition of 481 μM DPP to 25 μM PDI in toluene), 70 °C, λ_{Ex} = 483 nm.
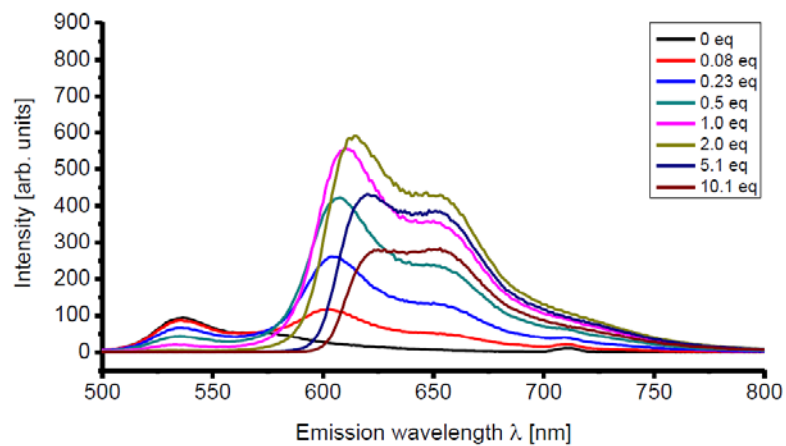
Fig. B13: Fluorescence quenching titration (addition of 481 μM DPP to 25 μM PDI in toluene), 50 °C, $\lambda_{Ex} = 356$ nm.
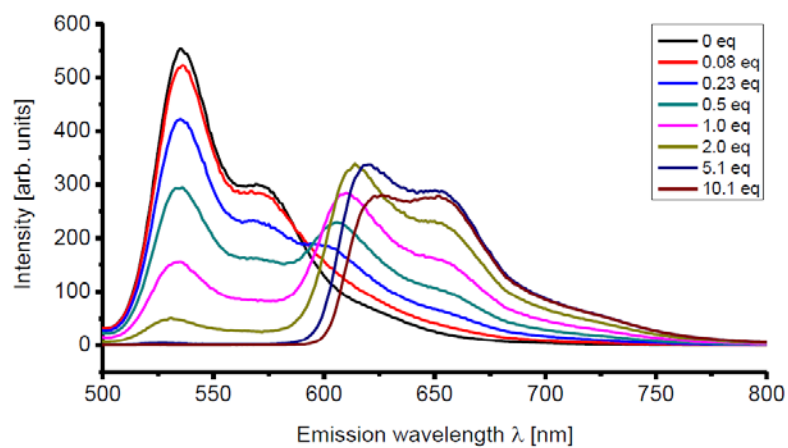
Fig. B14: Fluorescence quenching titration (addition of 481 μM DPP to 25 μM PDI in toluene), 50 °C, $\lambda_{Ex} = 483$ nm.
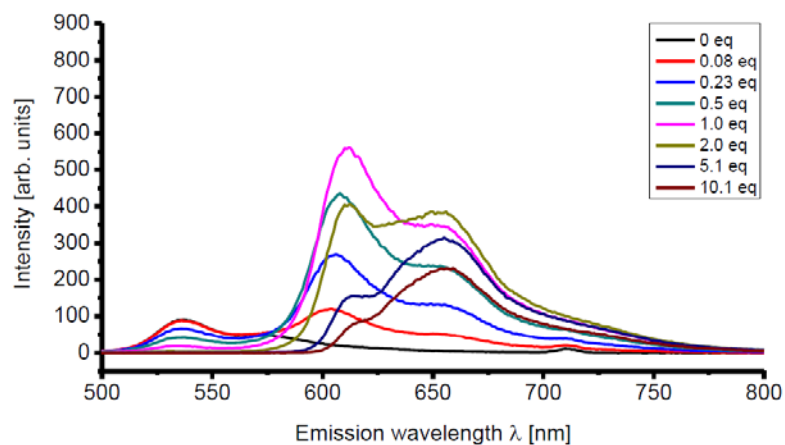
Fig. B15: Fluorescence quenching titration (addition of 481 μM DPP to 25 μM PDI in toluene), 30 °C, λEx = 356 nm.
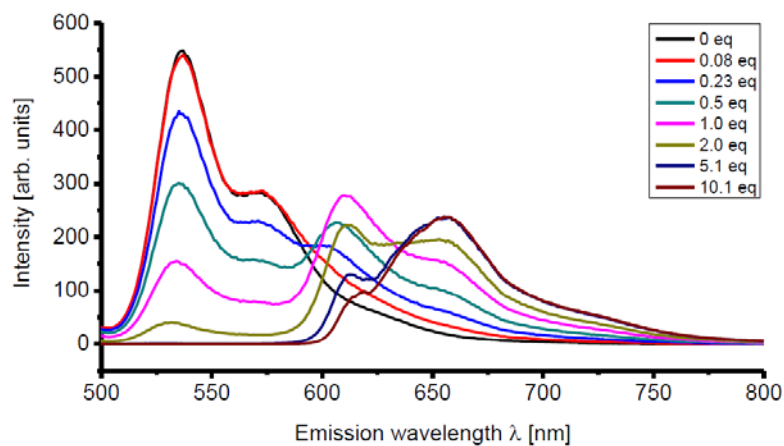
Fig. B16: Fluorescence quenching titration (addition of 481 μM DPP to 25 μM PDI in toluene), 30 °C, λ_{Ex} = 483 nm.
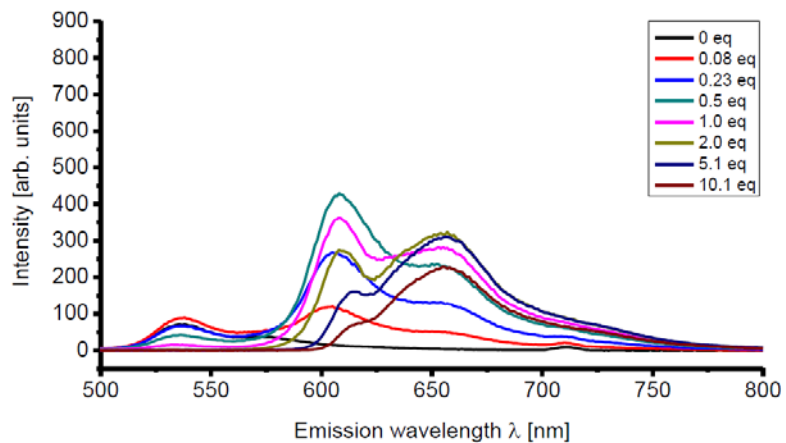
Fig. B17: Fluorescence quenching titration (addition of 481 µM DPP to 25 µM PDI in toluene), 22 °C, λ_{Ex} = 356 nm.
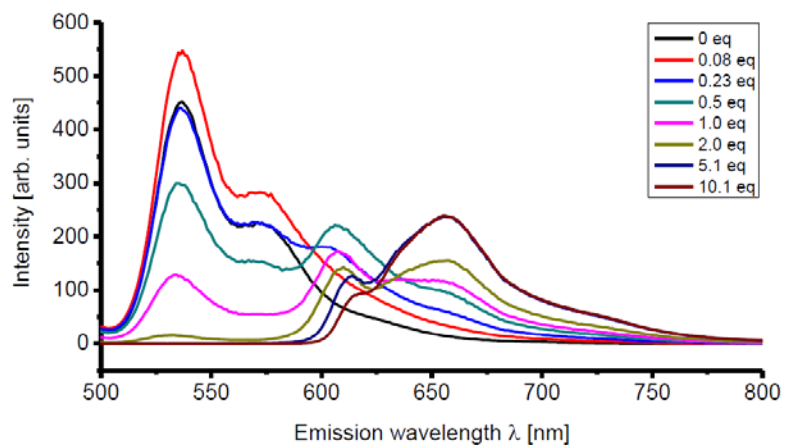
Fig. B18: Fluorescence quenching titration (addition of 481 µM DPP to 25 µM PDI in toluene), 22 °C, λ_{Ex} = 483 nm.
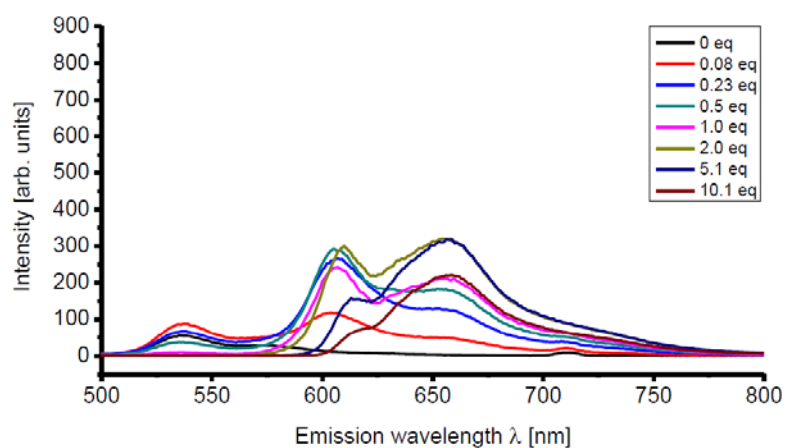
Fig. B19: Fluorescence quenching titration (addition of 481 μM DPP to 25 μM PDI in toluene), 15 °C, λ_{Ex} = 356 nm.
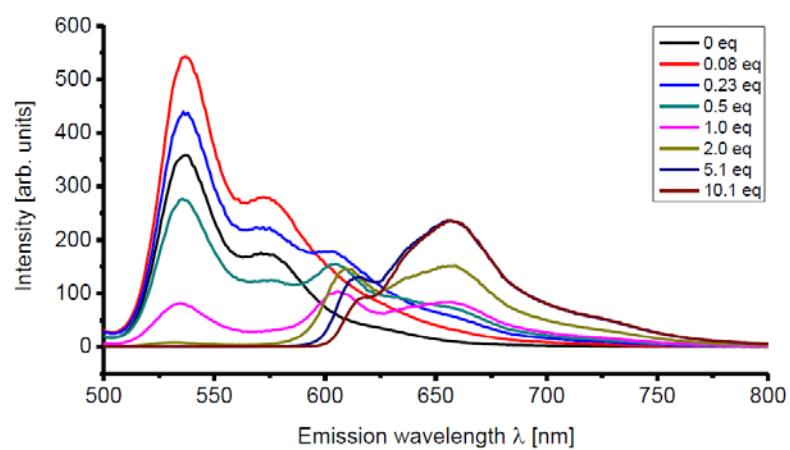
Fig. B20: Fluorescence quenching titration (addition of 481 μM DPP to 25 μM PDI in toluene), 15 °C, λ_{Ex} = 483 nm.

Reference Spectra for the Variable Temperature Titration (PDI dilution)

Starting point: Solution of PDI in toluene (c_0 = 25 µM, V_0 = 2.5 mL) in a septum-sealed, 1 cm quartz cuvette, to which toluene was gradually added using the same volumetric steps (see Table B3). This experiment takes into account dilution effects that the PDI experiences as the DPP solution is added during the titration.
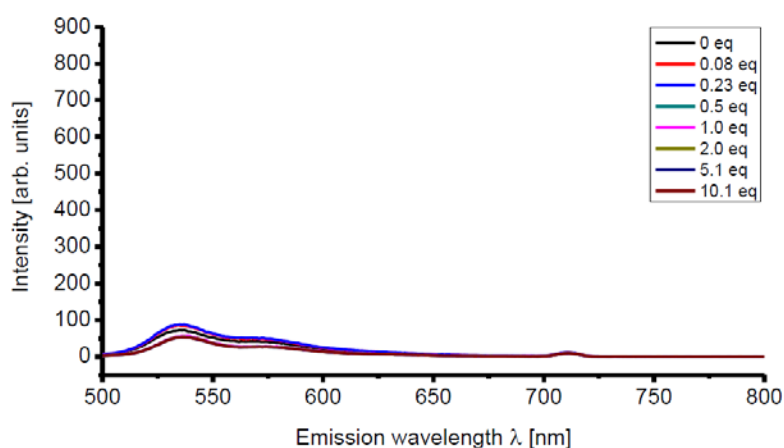
Fig. B21: Variable temperature PDI dilution 70 °C, λ_{Ex} = 356 nm.
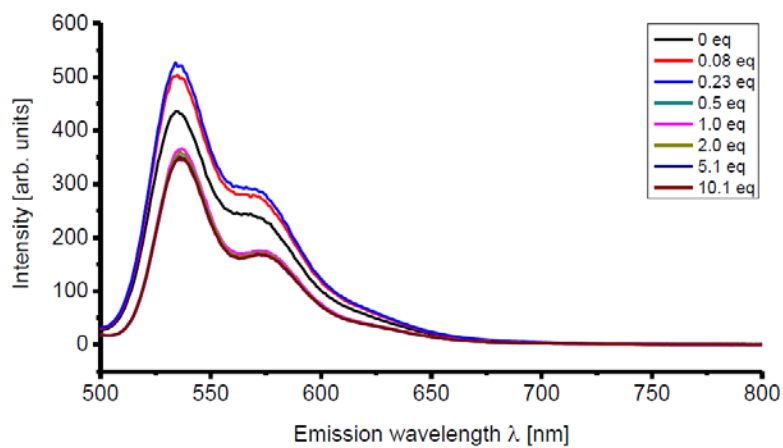
Fig. B22: Variable temperature PDI dilution 70 °C, λ_{Ex} = 483 nm.
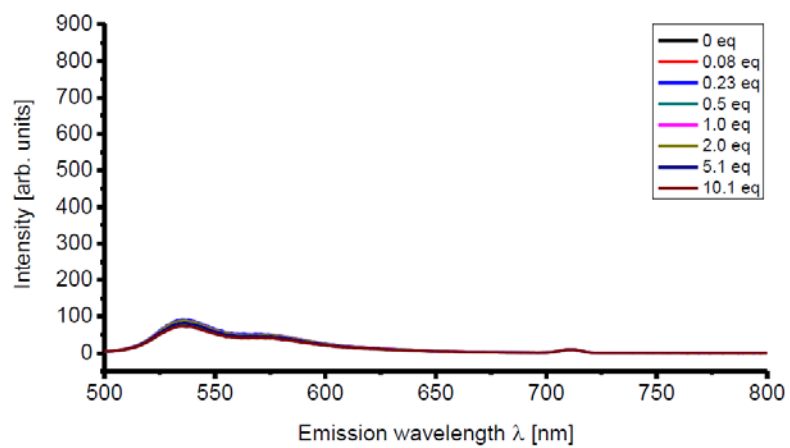
Fig. B23: Variable temperature PDI dilution 50 °C, λ_{Ex} = 356 nm.
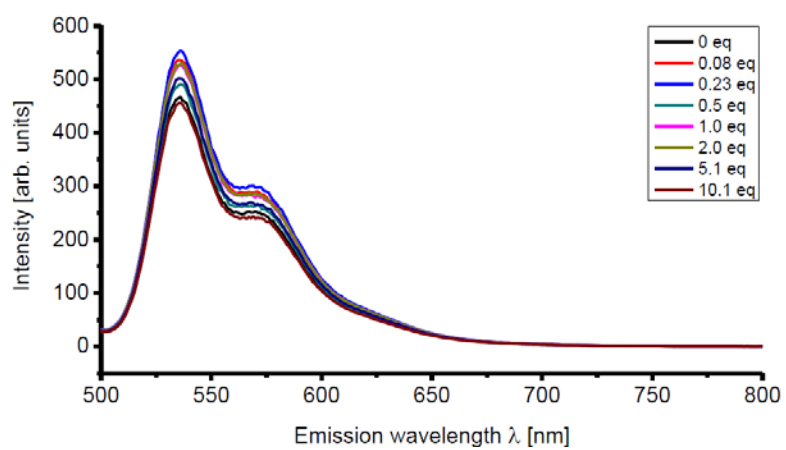
Fig. B24: Variable temperature PDI dilution 50 °C, λ_{Ex} = 483 nm.
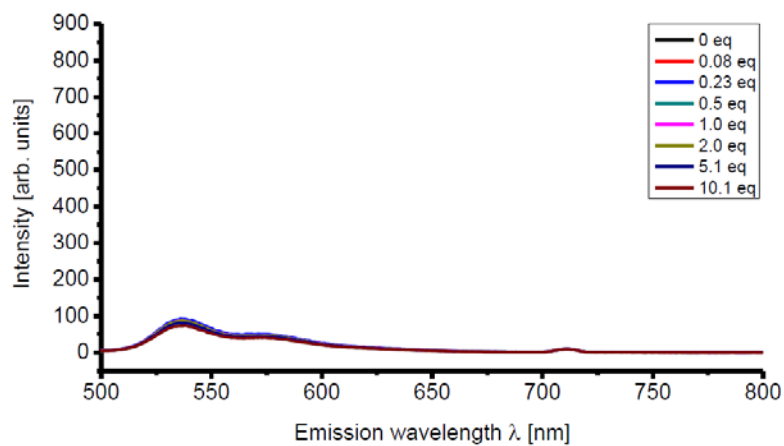
Fig. B25: Variable temperature PDI dilution 30 °C, λ_{Ex} = 356 nm.
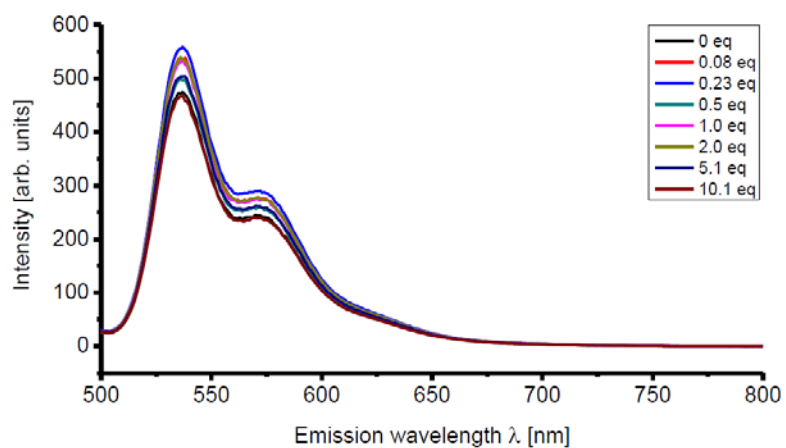
Fig. B26: Variable temperature PDI dilution 30 °C, λ_{Ex} = 483 nm.
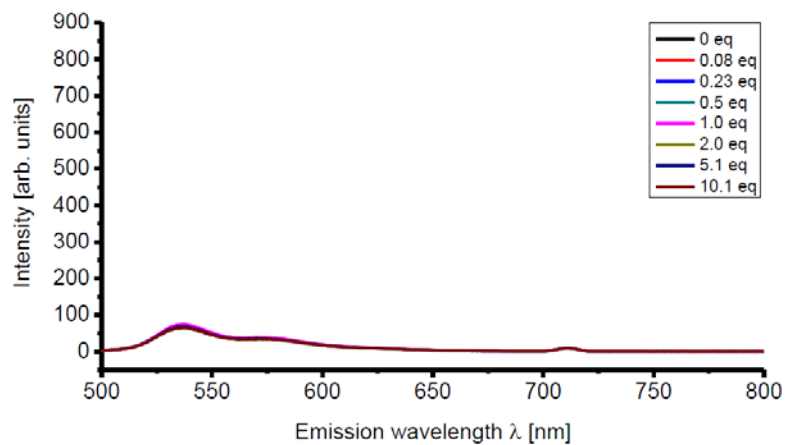
Fig. B27: Variable temperature PDI dilution 22 °C, λ_{Ex} = 356 nm.
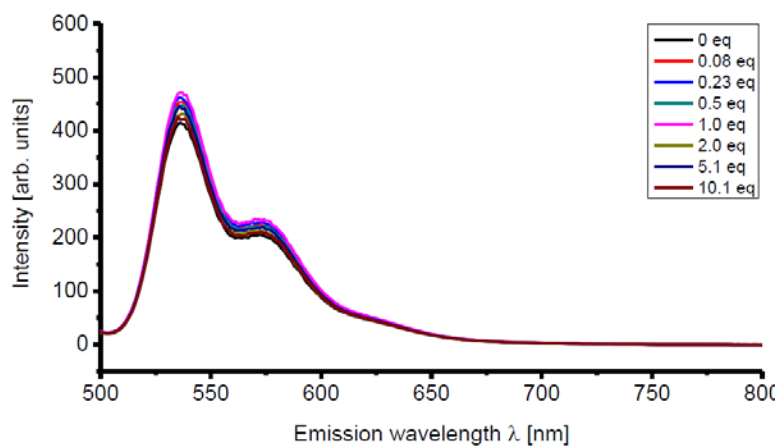
Fig. B28 Variable temperature PDI dilution 22 °C, λ_{Ex} = 483 nm.
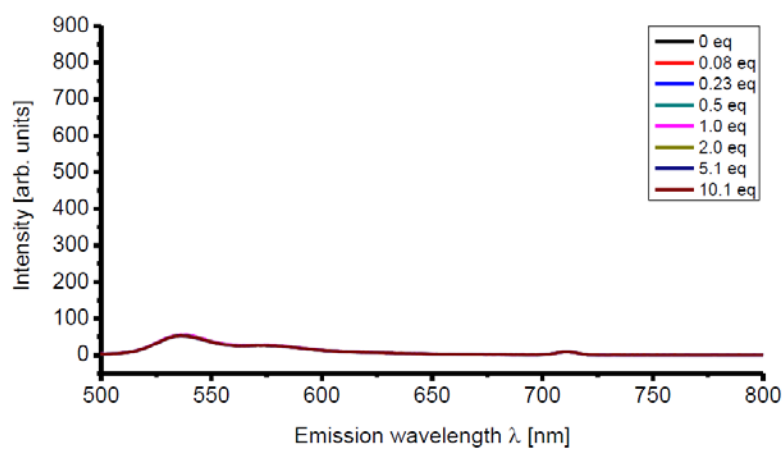
Fig. B29: Variable temperature PDI dilution 15 °C, $\lambda_{Ex} = 356$ nm.
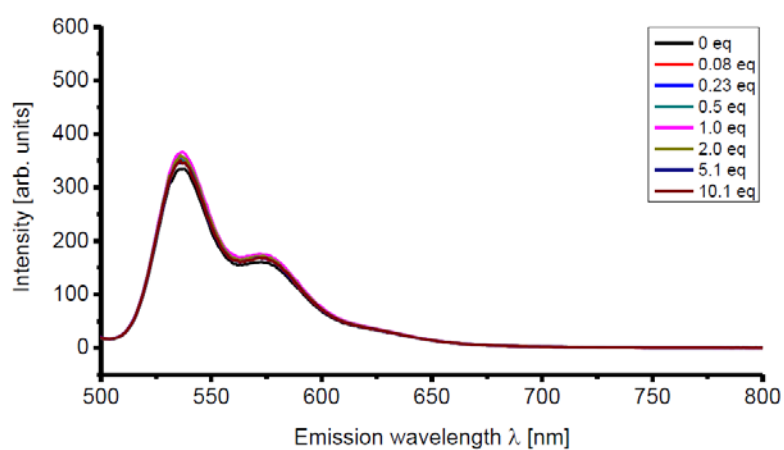
Fig. B30: Variable temperature PDI dilution 15 °C, $\lambda_{Ex} = 483$ nm.

Reference Spectra for the Variable Temperature Titration (DPP dilution)

Starting point: Toluene in a septum-sealed, 1 cm quartz cuvette (V_0 = 2.5 mL), to which DPP (solution in toluene, c = 4.805 10^{-4} mol L^{-1}) was gradually added using the same volumetric steps (see Table B3). This experiment takes into account dilution effects of the DPP, as its concentration changes during the titration experiment.
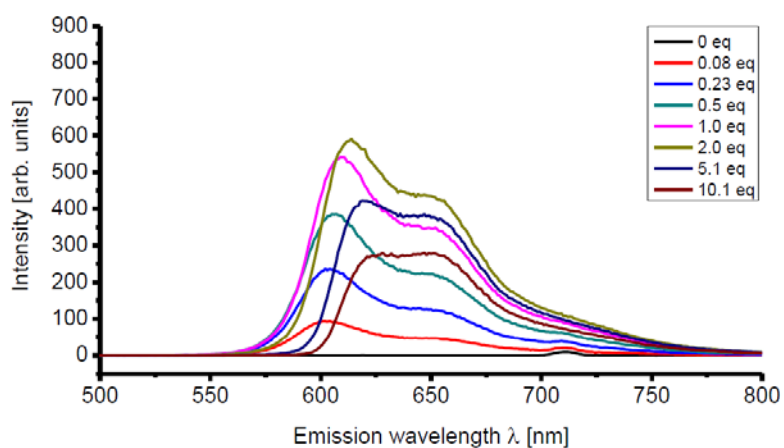
Fig. B31: Variable temperature increasing DPP concentration 70 °C, λ_{Ex} = 356 nm.
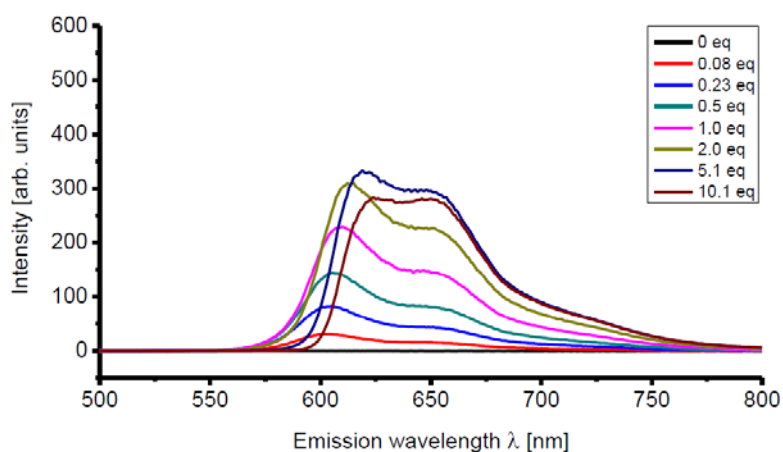
Fig. B32: Variable temperature increasing DPP concentration 70 °C, λ_{Ex} = 483 nm.
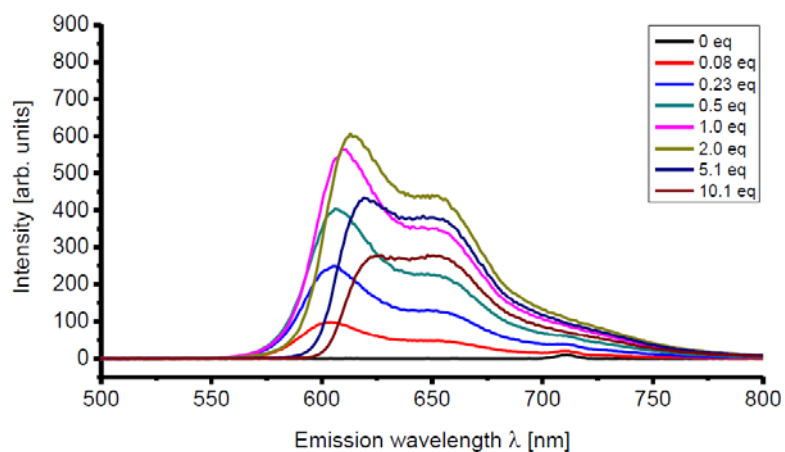
Fig. B33: Variable temperature increasing DPP concentration 50 °C, λ_{Ex} = 356 nm.
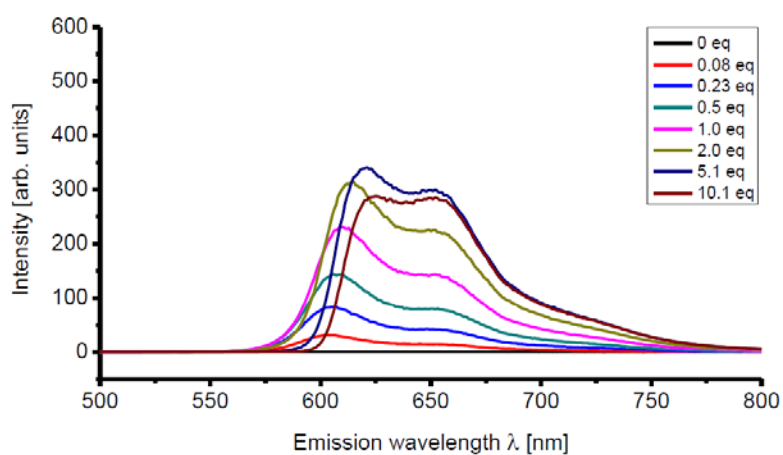
Fig. B34: Variable temperature increasing DPP concentration 50 °C, λ_{Ex} = 483 nm.
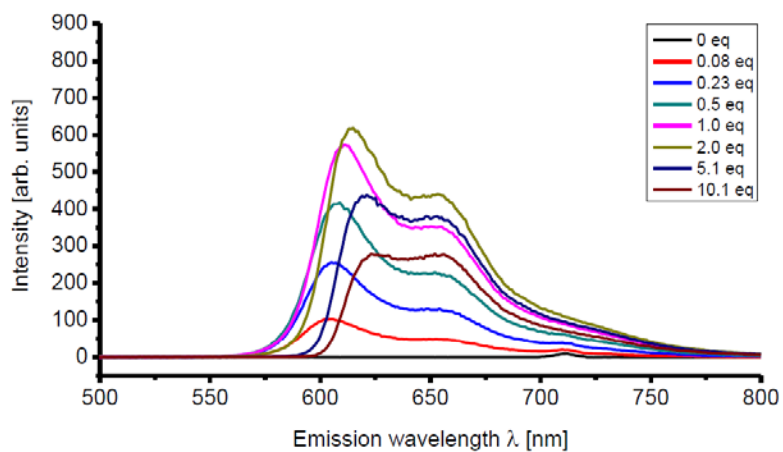
Fig. B35: Variable temperature increasing DPP concentration 30 °C, λ_{Ex} = 356 nm.
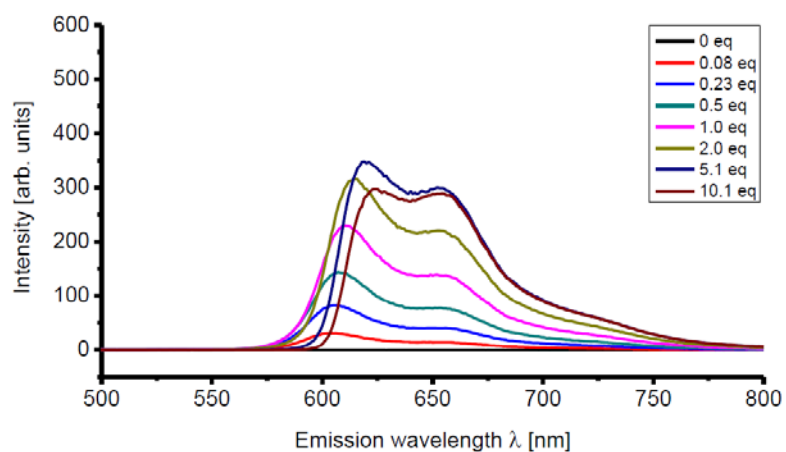
Fig. B36: Variable temperature increasing DPP concentration 30 °C, λ_{Ex} = 483 nm.
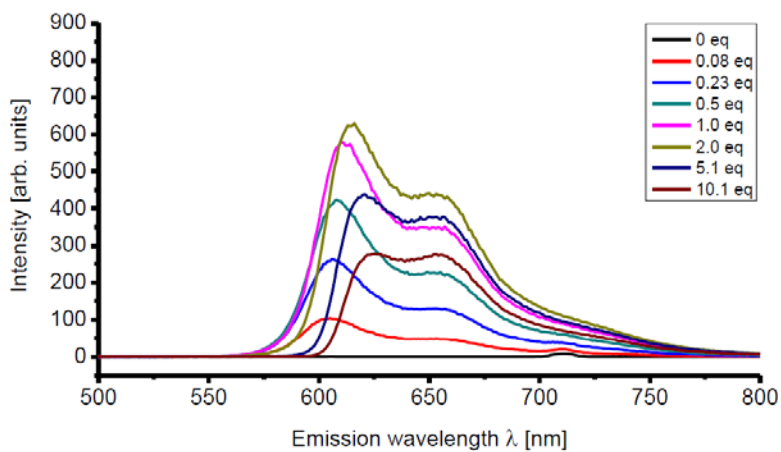
Fig. B37: Variable temperature increasing DPP concentration 22 °C, λ_{Ex} = 356 nm.
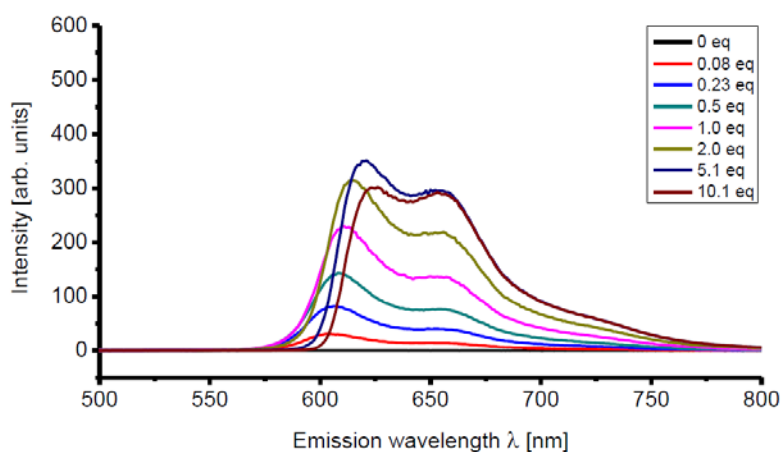
Fig. B38: Variable temperature increasing DPP concentration 22 °C, λ_{Ex} = 483 nm.
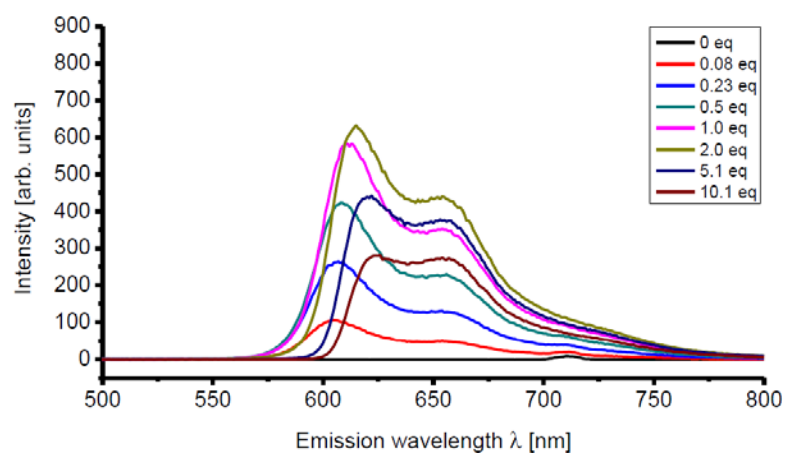
Fig. B39: Variable temperature increasing DPP concentration 15 °C, λ_{Ex} = 356 nm.
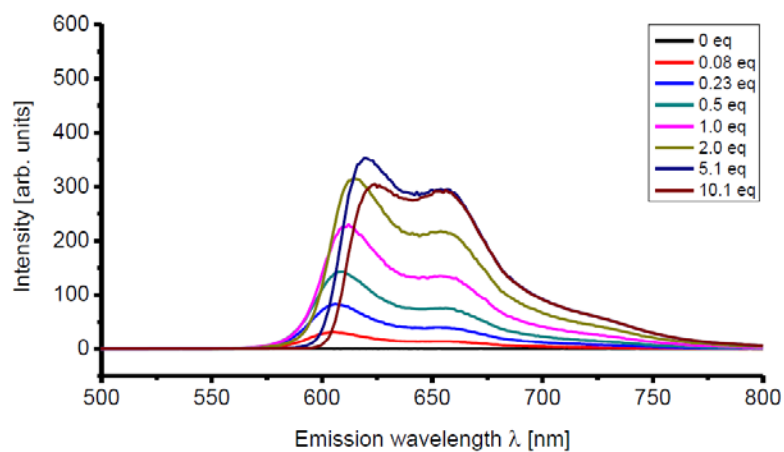
Fig. B40: Variable temperature increasing DPP concentration 15 °C, λ_{Ex} = 356 nm.

Control Experiment:

To verify our hypothesis that the DPP fluorescence is quenched because of photoinduced charge transfer to the PDI facilitated by H-bonding, we carried out a similar experiment with a PDI that was modified in the sense that its H-bonding sites were sterically blocked by means of N,N'-dicyclohexyl protection. While the initial, slight increase in DPP fluorescence as the sample is cooled still remains, the static fluorescence quenching does not emerge (Fig. B41 bottom). The terminal cyclohexyl groups effectively prevent DPP PDI heteroaggregation *via* H-bonding, so that photoinduced charge transfer is impossible in this system, and the relative DPP fluorescence remains close to unity over the entire temperature range examined (Fig. B41 top).
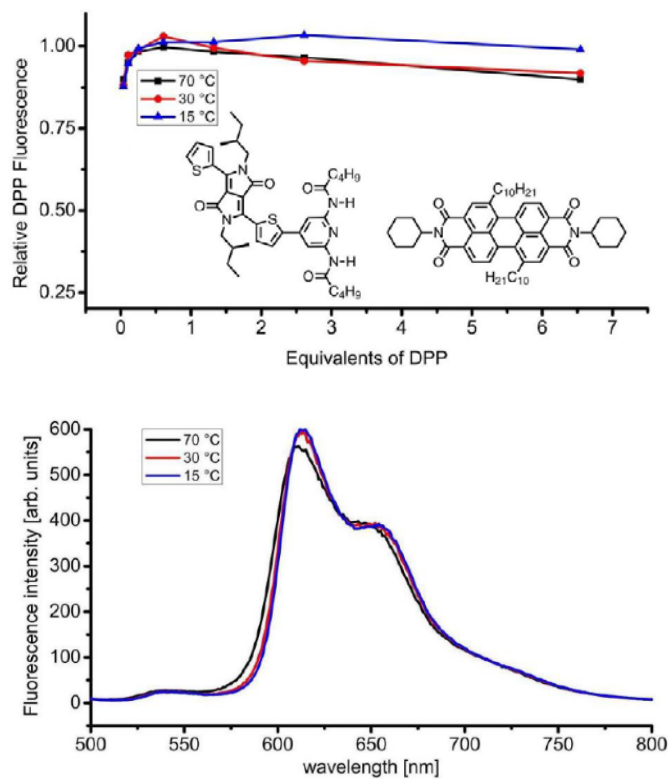
Fig. B41: Top: Relative DPP fluorescence intensity in the titration experiment with *N,N'*-dicyclohexyl protected PDI; no fluorescence quenching is visible, as the sterically blocked PDI does not provide H-binding sites (compare to Fig. 3.2 e). Bottom: Variable temperature fluorescence spectra of a mixture of DPP and the *N,N'*-dicyclohexyl protected PDI in toluene (c_{DPP} = 23 µM, c_{PDI} = 23 µM).

DYNAMIC LIGHT SCATTERING

DLS measurements were performed with a Malvern Zetasizer Nano ZS, using quartz cells with 1 cm path length, utilizing the 2:1 ratio of DPP to PDI in toluene with the concentrations according to the respective titration step ($V = 2.760$ mL, $c_{PDI} = 22.64$ μM, $c_{DPP} = 45.26$ μM), and two reference samples containing only one of the two species at the same concentration. Following the procedure from the variable temperature fluorescence measurements, the sample was heated to 70 °C for 15 minutes prior to each measurement series to ensure disaggregation. Whereas for the DPP reference sample ($c_{DPP} = 45.26$ μM), no aggregates could be measured over the entire temperature range from 70 °C down to 15 °C, the PDI sample ($c_{DPP} = 45.26$ μM) exhibited small particles (< 1000 nm) evenly over the entire measured temperature range, but unfortunately, the fixed-angle measuring technique did not allow any conclusion on the amount of particles. However, no particles were found in the mixture of both compounds at temperatures above 34 °C (Table B4). The average particle sizes were calculated by averaging over three independent series, each consisting of eleven measurements.

Table B4: DLS measurements on the 2:1 mixture of DPP (c = 45 μM) and PDI (c = 23 μM) in toluene. Aggregation and the related formation of large supramolecular clusters is observed at temperatures below 36 °C. The term n/a indicates no particles of detectable size are present.

Temperature [°C]	Average Size [nm]
70	n/a
50	n/a
48	n/a
46	n/a
44	n/a
42	n/a
40	n/a
38	n/a
36	n/a
34	1239
30	2961
25	1617
20	1685
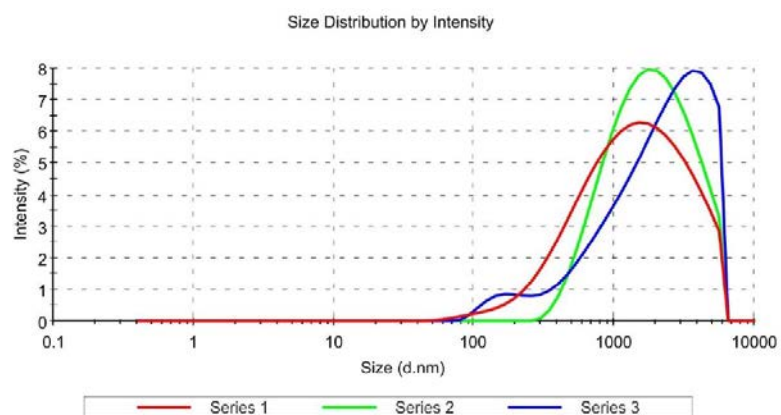
Fig. B42: DLS data of the 2:1 mixture of DPP (c = 45 μM) and PDI (c = 23 μM) in toluene at 34 °C.
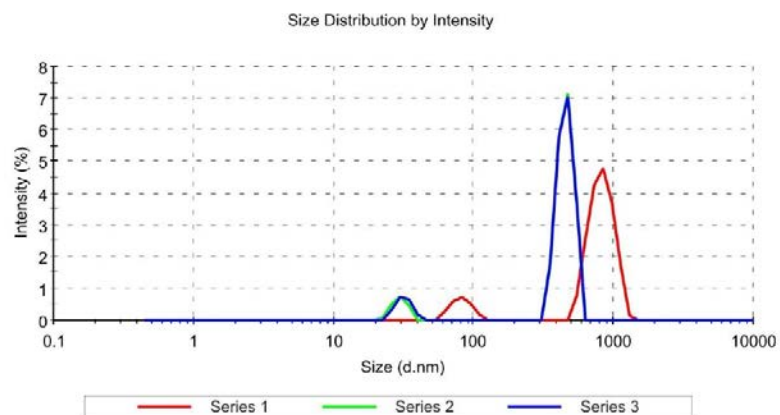
Fig. B43: DLS data of the 2:1 mixture of DPP (c = 45 μM) and PDI (c = 23 μM) in toluene at 30 °C.
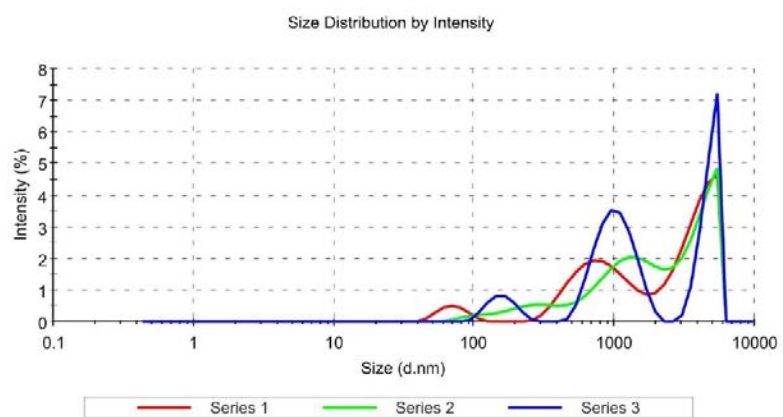
Fig. B44: DLS data of the 2:1 mixture of DPP (c = 45 μM) and PDI (c = 23 μM) in toluene at 25 °C.
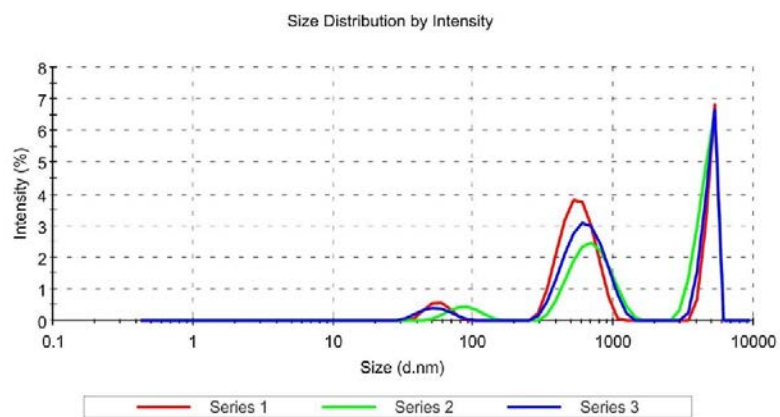
Fig. B45: DLS data of the 2:1 mixture of DPP (c = 45 µM) and PDI (c = 23 µM) in toluene at 20 °C.

TRANSIENT ABSORPTION SPECTROSCOPY

For measuring femtosecond transient absorption spectra at room temperature, samples were placed in quartz cells with a path length of 2 mm. The samples were excited using the frequency-doubled output of a Ti:Sapphire Laser (Coherent Libra, 1 Watt operating at 1 kHz) in conjunction with a Topas-C OPA, which generates 120 fs, 485 nm excitation pulses. A white light continuum for the probe pulse was generated by focusing the attenuated 800 nm fundamental into a 3 mm sapphire disk. Samples were irradiated with 1 µJ/pulse focused to a spot with a diameter of 200 µm. The total instrument response time for the pump-probe experiment was 200 fs. Transient absorption kinetics were fit to a sum of exponentials with a Gaussian instrument response function using the method of Levenberg-Marquard least-squares fitting. The letters in the graphs (Figures B46-49) label bands that are assigned in Table B5.
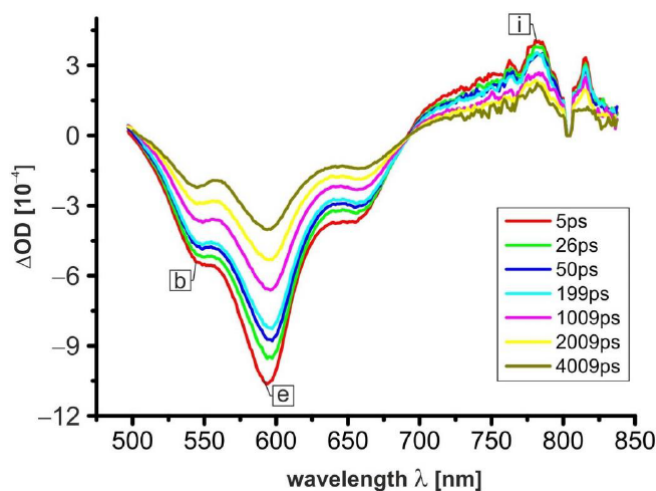
Fig. B46: Transient Absorption spectra of a solution of 0.1 mM DPP in toluene.
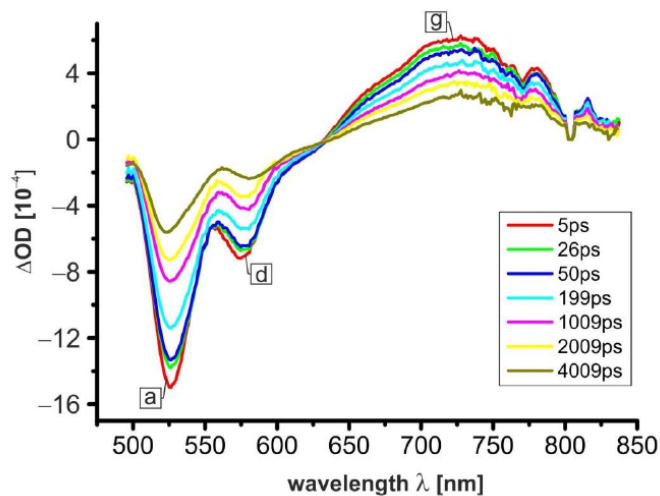
Fig. B47: Transient Absorption spectra of a solution of 0.05 mM PDI in toluene with 5 % DMSO.
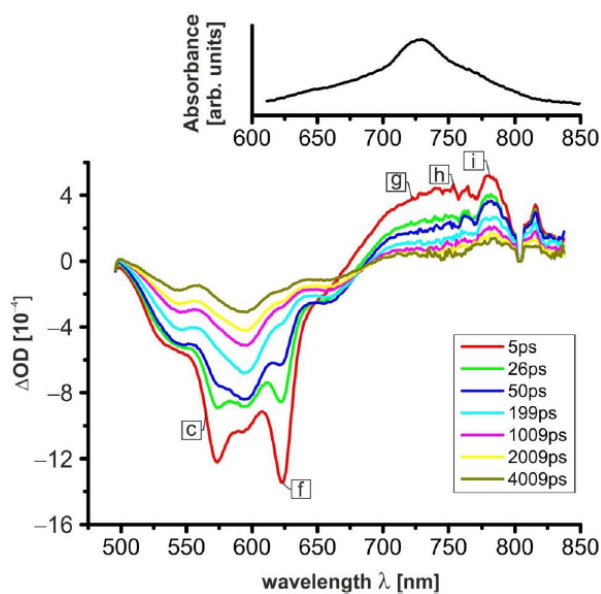
Fig. B48: Transient Absorption spectra of a solution of 0.1 mM DPP, and 0.05 mM PDI in toluene. The inset shows the spectral fingerprint of PDI$^{\bullet-}$ (from Fig. B7), indicating that the radical anion expresses a spectral feature that is expected to spread over the entire range of positive transient features.
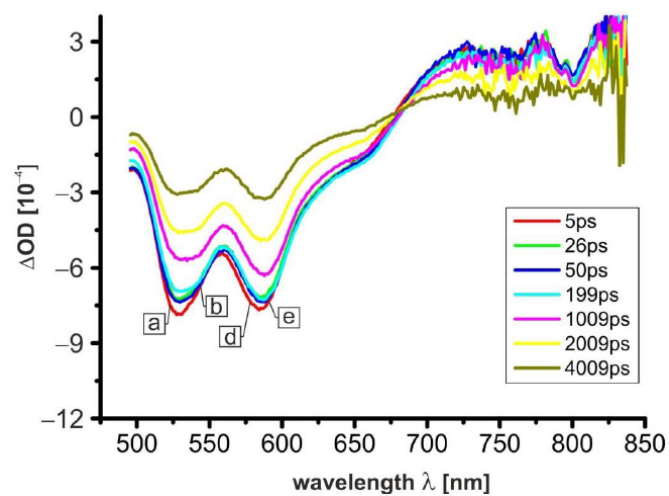
Fig. B49: Transient Absorption spectra of a solution of 0.1 mM DPP, and 0.05 mM PDI in toluene with 5 % DMSO.
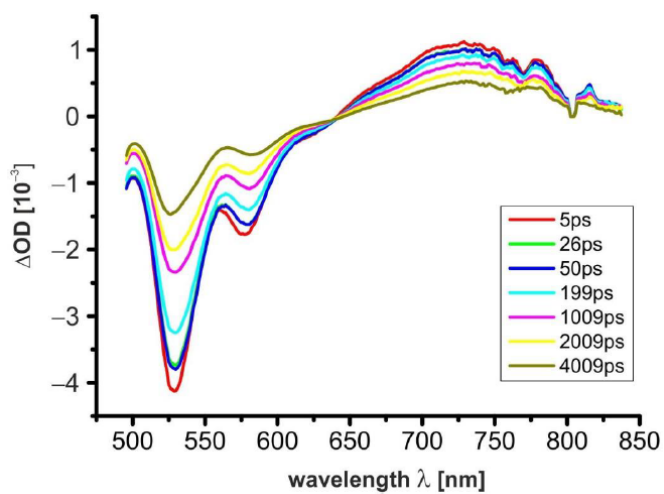
Fig. B50: Transient Absorption Spectra of a solution of 0.05 mM *N,N'*-dicyclohexyl PDI in toluene.
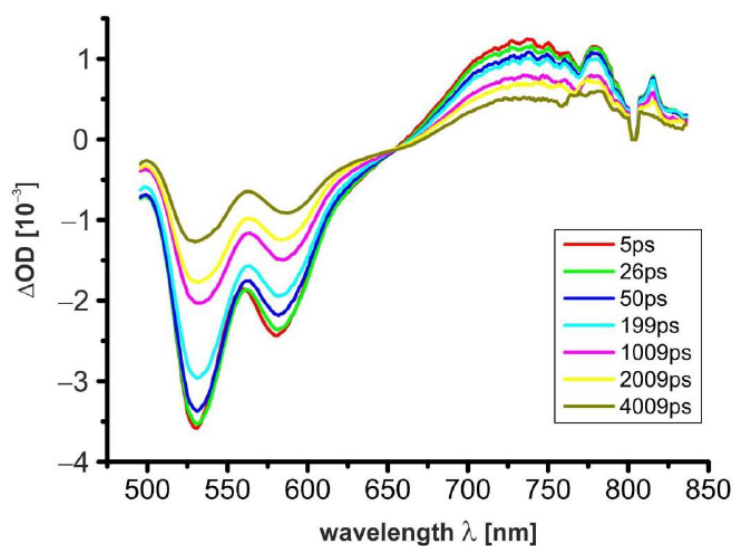
Fig. B51: Transient Absorption spectra of a solution of 0.1 mM DPP, and 0.05 mM *N,N'*-dicyclohexyl PDI in toluene.
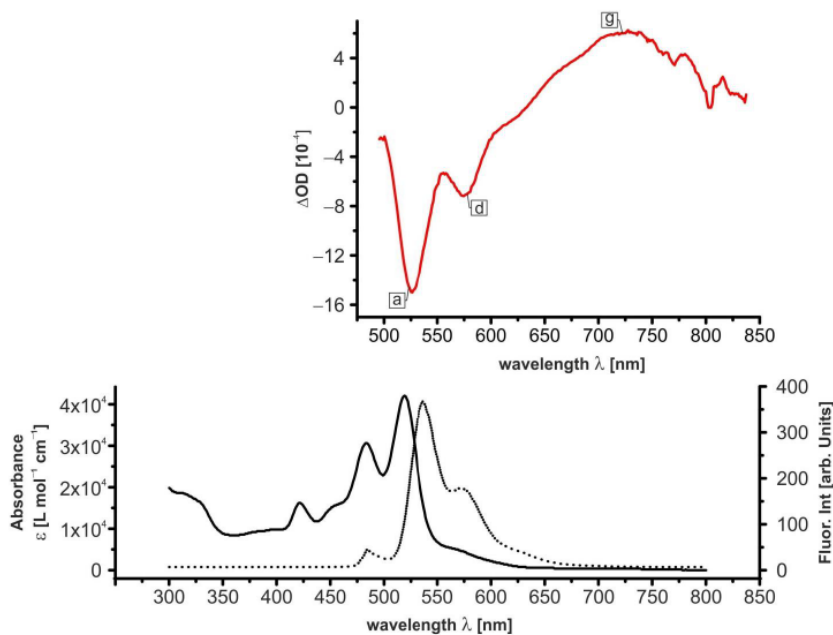
Fig. B52: Comparison of the fs-TA spectrum of PDI after 5 ps (top) with the UV-Vis spectrum (solid, bottom) and the fluorescence spectrum (dotted, bottom) of PDI in toluene (from Fig. B47, and Fig. B4, respectively). While the negative feature in the fs-TA spectrum at 523 nm represents a ground state bleach that is redshiftet because of convolution with stimulated emission, the negative feature at 578 nm (d) can solely be ascribed to stimulated emission.

Table B5: Overview showing the contributions of rise- (λ < 680 nm) and decay (λ > 680 nm) constants at several wavelengths for the individual compounds, the mixture, as well as for the chemically disaggregated mixture.

λ [nm]					Kinetics in the respective sample				
	DPP		PDI		2:1 Mixture		2:1 Mixture with 5 % DMSO		
	τ1 [ps] (%)	τ2 [ns] (%)	τ1 [ps] (%)	τ2 [ns] (%)	τ1 [ps] (%)	τ2 [ns] (%)	τ1 [ps] (%)	τ2 [ns] (%)	
523 (a)	104 ± 7 (9)	5.1 ± 0.2 (91)	245 ± 14 (35)	7.4 ± 0.4 (65)	54 ±2 (53)	4.2 ± 0.2 (47)	92 ± 10 (16)	4.9 ± 0.2 (84)	
544 (b)	150 ± 1 (22)	5.7 ± 0.2 (88)	535 ± 82 (27)	5.9 ± 0.5 (73)	102 ± 4 (35)	5.1 ± 0.2 (65)	--	4.3 ± 0.1 (100)	
565 (c)	64 ± 5 (25)	4.7 ± 0.2 (75)	156 ± 11 (34)	4.6 ± 0.2 (66)	38 ± 1 (59)	3.9 ± 0.2 (41)	3 ± 1 (18)	4.1 ± 0.1 (82)	
578 (d)	56 ± 3 (27)	5.5 ± 0.2 (73	206 ± 10 (27)	4.7 ± 0.1 (73)	39 ± 1 (56)	4.5 ± 0.2 (44)	5 ± 1 (12)	4.4 ± 0.1 (88)	
591 (e)	62 ± 3 (27)	5.4 ± 0.2 (73)	No valid fit	59 ± 2 (41)	4.8 ± 0.1 (59)	--	4.7 ± 0.1 (100)		
622 (f)	123 ± 9 (24)	5.2 ± 0.2 (76)	No valid fit	33 ± 1 (76)	3.7 ± 0.2 (24)	--	3.7 ± 0.1 (100)		
722 (g)	12 ± 1 (36)	7.5 ± 0.4 (64)	137 ± 8 (25)	8.6 ± 0.3 (75)	32 ± 1 (71)	6.3 ± 0.4 (29)	5 ± 1 (10)	4.2 ± 0.1 (90)	
755 (h)	14 ± 2 (28)	7.9 ± 0.4 (72)	99 ± 8 (23)	8.4 ± 0.4 (77)	36 ± 1 (66)	4.9 ± 0.3 (34)	No valid fit		
781 (i)	78 ± 7 (28)	7.9 ± 0.3 (72)	207 ± 19 (25)	9.5 ± 0.5 (75)	46 ± 1 (51)	6.4 ± 0.3 (49)	4 ± 2 (10)	5.2 ± 0.3 (90)	

CALCULATION OF CHARGE SEPARATION ENERGIES

Charge separation energies were calculated by using the Weller equation (B-E4):

$$\Delta G = E_{ox} - E_{red} - \frac{e^2}{r_{12}\varepsilon_s} + e^2 \left(\frac{1}{2r_1} + \frac{1}{2r_2} \right) \left(\frac{1}{\varepsilon_s} + \frac{1}{\varepsilon_{sp}} \right)$$

where ΔG is the free enthalpy for the charge transfer process, E_{ox} and E_{red} are the oxidation- and reduction potentials of the donor and acceptor, respectively. Computations at the B3LYP/6-31G(d,p)[141-142] level of theory were used to determine the charge separation distance (r_{12}), while the radii of DPP$^{\bullet+}$ (r_1) and PDI$^{\bullet-}$ (r_2) were estimated by taking the spatial extension of the respective HOMO and LUMO orbitals into account (Fig. B56). The value ε_s represents the overall polarity of the solvent of low polarity (in our case toluene), while ε_{sp} is the overall polarity of the solvent with higher polarity (in our case THF), in which the oxidation and reduction potentials were measured. The overall polarity is the product of the Coulombic 4π factor, the permittivity of the vacuum (ε_0), as well as the relative static permittivity of the respective solvent (ε_r).

The total reorganization energy of a system is given by the sum of the intrinsic reorganization energy (λ_i), and the static reorganization energy (λ_s):

$$\lambda = \lambda_i + \quad \text{(B-E5)}$$

The latter term was calculated using the Marcus relation:

$$\lambda_s = e^2 \left(\frac{1}{2r_1} + \frac{1}{2r_{12}} - \frac{1}{r_{12}} \right) \left(\frac{1}{\varepsilon_0} + \frac{1}{\varepsilon_s} \right) \quad \text{(B-E5)}$$

Wherein r_{12}, r_1 and r_2 are identical to those used in B-E4, ε_0 is the overall static permittivity of the solvent (low frequency), and ε_s is the high-frequency permittivity of the solvent, approximated by the square of the index of refraction.

To obtain the intrinsic reorganizational energy (λ_i) for the DPP and the PDI, density functional theory (DFT) computations at the B3LYP/6-31G(d,p) level of theory were employed (Table B5). For the charge separation and charge recombination processes, the overall reorganizational energies were calculated by adding the contributions of the individual compounds DPP and PDI.[185] For charge separation, the contribution of DPP was calculated by subtracting the energy of the optimized neutral structure from the single point energy of the neutral system at the atom configuration that corresponds to the radical cation (DPP$^{\bullet+}$). This value reflects the amount of energy needed to deform the optimized DPP structure towards that of the respective radical cation. Accordingly, the contribution of the PDI was calculated by subtracting the energy of the neutral structure from the single point energy of the neutral structure at the atom configuration that corresponds to the optimized radical anion (PDI$^{\bullet-}$). The reorganizational energies for charge recombination were calculated by taking into account the single point energies of the respective ions at the atom arrangements corresponding to the respective neutral structures. The overall results are summarized in Table B6.

Table B5: Computational results and intrinsic reorganization energies.

Species	E [Hartree] (Neutral)	E [Hartree] (Ion)	E [Hartree] (Neutral @ Ion)	E [Hartree] (Ion @ Neutral)	λ_i [eV] (CS)	λ_i [eV] (CR)
DPP / DPP•+	−1487.504656	−1487.584038	−1487.499897	−1487.579238	0.13	0.13
PDI / PDI•−	−2335.386035	−2335.168402	−2335.379905	−2335.161747	0.17	0.18
Sum					0.30	0.31

Table B6: Oxidation and reduction potentials as obtained by using cyclic voltammetry (referenced with the internal standard Ferrocene), distances obtained from computational results, as well as energies derived from the Weller equation (B-E4) and Marcus relation (B-E6). The energy for the charge separated state (ΔG) is given with respect to the ground state.

E_{ox} [V]	E_{red} [V]	r_1 [Å]	r_2 [Å]	r_{12} [Å]	ΔG [eV]	λ_s [eV]	λ_i [eV]	λ [eV]
0.553	−1.176	8	6	18	2.00	0.03	0.30	0.33

COMPUTATIONAL RESULTS

Density Functional Theory (DFT) computations were performed with the ORCA program package version 3.0.1.[188] Becke's three-parameter exchange functional was used in conjunction with the Lee-Young-Parr correlation functional (B3LYP) throughout, incorporating Pople's 6-31G(d,p) basis set, using 4 as the DFT integration grid size number. For geometry optimizations, the following convergence criteria were used (values in a. u.): Energy change: 0.00000500, RMS gradient: 0.00010000, MAX gradient: 0.00030000, RMS step: 0.00200000, MAX step: 0.00400000. The unrestricted Hartree Fock (UHF) reference wave function was used for open shell systems (DPP$^{\bullet+}$ and PDI$^{\bullet-}$), while closed shell systems (DPP, PDI, DPP–PDI) were treated with the restricted Hartree Fock (RHF) reference wave function. The carbon lengths of the alkyl chains were reduced to one and two in DPP and PDI, respectively, in order to minimize the computational expense. The Cartesian coordinates for each molecule are provided below.

Structure of *N*-Methyl-DPP		
Charge = 0, Multiplicity = 1		
optimized structure (Cart. coord. In Å):		
C 8.613335	0.168901	0.181897
C 8.359917	1.306825	0.905513
S 7.170903	-0.622587	-0.331226
C 6.974478	1.562834	1.044199
C 3.938769	-0.525571	-0.104462
C 6.166690	0.615629	0.425728
C 4.728367	0.527364	0.352139
N 3.854650	1.537010	0.762808
C 2.480686	1.151933	0.579674
C 4.152270	2.883557	1.214463
O 1.541763	1.892972	0.844993
C 2.565625	-0.185439	0.033210
C 1.776235	-1.265465	-0.352592
N 2.651566	-2.281390	-0.749852
C 4.023368	-1.872169	-0.627208
O 4.963441	-2.589859	-0.951800
C 0.339788	-1.384845	-0.352750
C 2.351706	-3.565602	-1.355884
C -0.459622	-2.513847	-0.504743
C -3.642783	1.082509	-0.359885
C -1.839865	-2.243976	-0.434185
C -2.129885	-0.906494	-0.235047
C -3.455931	-0.288903	-0.125011
S -0.669640	0.035433	-0.103601
C -4.562048	-1.084990	0.217114
C -5.808902	-0.462753	0.299940
C -4.940118	1.590769	-0.238829
N -6.995149	-1.138807	0.631513
N -6.005964	0.844585	0.081712
N -5.270757	2.939112	-0.444241
C -7.188681	-2.479329	0.895450
C -8.620206	-2.843450	1.260070
O -6.296449	-3.315015	0.868915
C -4.460141	3.986447	-0.839324
C -5.198358	5.304003	-1.024393
O -3.262677	3.875718	-1.051506
H 9.575145	-0.257117	-0.071735
H 9.133601	1.938403	1.327175
H 6.592468	2.407300	1.597946
H 4.832899	3.391786	0.525316
H 4.579548	2.890832	2.223323
H 3.197513	3.412264	1.240166
H 1.647699	-3.456945	-2.185818
H 1.950084	-4.278353	-0.627033
H 3.301045	-3.954152	-1.729340
H -0.070112	-3.510864	-0.647013
H -2.835615	1.743005	-0.644203
H -2.601877	-3.006345	-0.546735
H -4.476802	-2.138581	0.434850
H -7.794334	-0.520148	0.664221
H -6.255929	3.119179	-0.303543
H -8.851662	-3.815872	0.821324
H -9.358846	-2.108609	0.927065
H -8.696255	-2.943626	2.348317
H -4.505066	6.119636	-0.814185
H -5.520725	5.395050	-2.067896
H -6.079762	5.398354	-0.382851
E(B3LYP/6-31G(d,p) = –2335.386035 H		

Structure of N-Methyl-DPP•+		
Charge = +1, Multiplicity = 2		
optimized structure (Cart. coord. In Å):		
C 8.613335	0.168901 0	0.181897
C 8.359917	1.306825	0.905513
S 7.170903	-0.622587	-0.331226
C 6.974478	1.562834	1.044199
C 3.938769	-0.525571	-0.104462
C 6.166690	0.615629	0.425728
C 4.728367	0.527364	0.352139
N 3.854650	1.537010	0.762808
C 2.480686	1.151933	0.579674
C 4.152270	2.883557	1.214463
O 1.541763	1.892972	0.844993
C 2.565625	-0.185439	0.033210
C 1.776235	-1.265465	-0.352592
N 2.651566	-2.281390	-0.749852
C 4.023368	-1.872169	-0.627208
O 4.963441	-2.589859	-0.951800
C 0.339788	-1.384845	-0.352750
C 2.351706	-3.565602	-1.355884
C -0.459622	-2.513847	-0.504743
C -3.642783	1.082509	-0.359885
C -1.839865	-2.243976	-0.434185
C -2.129885	-0.906494	-0.235047
C -3.455931	-0.288903	-0.125011
S -0.669640	0.035433	-0.103601
C -4.562048	-1.084990	0.217114
C -5.808902	-0.462753	0.299940
C -4.940118	1.590769	-0.238829
N -6.995149	-1.138807	0.631513
N -6.005964	0.844585	0.081712
N -5.270757	2.939112	-0.444241
C -7.188681	-2.479329	0.895450
C -8.620206	-2.843450	1.260070
O -6.296449	-3.315015	0.868915
C -4.460141	3.986447	-0.839324
C -5.198358	5.304003	-1.024393
O -3.262677	3.875718	-1.051506
H 9.575145	-0.257117	-0.071735
H 9.133601	1.938403	1.327175
H 6.592468	2.407300	1.597946
H 4.832899	3.391786	0.525316
H 4.579548	2.890832	2.223323
H 3.197513	3.412264	1.240166
H 1.647699	-3.456945	-2.185818
H 1.950084	-4.278353	-0.627033
H 3.301045	-3.954152	-1.729340
H -0.070112	-3.510864	-0.647013
H -2.835615	1.743005	-0.644203
H -2.601877	-3.006345	-0.546735
H -4.476802	-2.138581	0.434850
H -7.794334	-0.520148	0.664221
H -6.255929	3.119179	-0.303543
H -8.851662	-3.815872	0.821324
H -9.358846	-2.108609	0.927065
H -8.696255	-2.943626	2.348317
H -4.505066	6.119636	-0.814185
H -5.520725	5.395050	-2.067896
H -6.079762	5.398354	-0.382851
E(UB3LYP/6-31G(d,p) = –2335.168402 H		

Structure of *N*-Methyl-DPP		
Charge = 0, Multiplicity = 1		
optimized structure (Cart. coord. In Å):		
C 8.613335	0.168901	0.181897
C 8.359917	1.306825	0.905513
S 7.170903	-0.622587	-0.331226
C 6.974478	1.562834	1.044199
C 3.938769	-0.525571	-0.104462
C 6.166690	0.615629	0.425728
C 4.728367	0.527364	0.352139
N 3.854650	1.537010	0.762808
C 2.480686	1.151933	0.579674
C 4.152270	2.883557	1.214463
O 1.541763	1.892972	0.844993
C 2.565625	-0.185439	0.033210
C 1.776235	-1.265465	-0.352592
N 2.651566	-2.281390	-0.749852
C 4.023368	-1.872169	-0.627208
O 4.963441	-2.589859	-0.951800
C 0.339788	-1.384845	-0.352750
C 2.351706	-3.565602	-1.355884
C -0.459622	-2.513847	-0.504743
C -3.642783	1.082509	-0.359885
C -1.839865	-2.243976	-0.434185
C -2.129885	-0.906494	-0.235047
C -3.455931	-0.288903	-0.125011
S -0.669640	0.035433	-0.103601
C -4.562048	-1.084990	0.217114
C -5.808902	-0.462753	0.299940
C -4.940118	1.590769	-0.238829
N -6.995149	-1.138807	0.631513
N -6.005964	0.844585	0.081712
N -5.270757	2.939112	-0.444241
C -7.188681	-2.479329	0.895450
C -8.620206	-2.843450	1.260070
O -6.296449	-3.315015	0.868915
C -4.460141	3.986447	-0.839324
C -5.198358	5.304003	-1.024393
O -3.262677	3.875718	-1.051506
H 9.575145	-0.257117	-0.071735
H 9.133601	1.938403	1.327175
H 6.592468	2.407300	1.597946
H 4.832899	3.391786	0.525316
H 4.579548	2.890832	2.223323
H 3.197513	3.412264	1.240166
H 1.647699	-3.456945	-2.185818
H 1.950084	-4.278353	-0.627033
H 3.301045	-3.954152	-1.729340
H -0.070112	-3.510864	-0.647013
H -2.835615	1.743005	-0.644203
H -2.601877	-3.006345	-0.546735
H -4.476802	-2.138581	0.434850
H -7.794334	-0.520148	0.664221
H -6.255929	3.119179	-0.303543
H -8.851662	-3.815872	0.821324
H -9.358846	-2.108609	0.927065
H -8.696255	-2.943626	2.348317
H -4.505066	6.119636	-0.814185
H -5.520725	5.395050	-2.067896
H -6.079762	5.398354	-0.382851
E(B3LYP/6-31G(d,p) = –2335.386035 H		

Structure of N-Methyl-DPP$^{\bullet+}$		
Charge = +1, Multiplicity = 2		
optimized structure (Cart. coord. In Å):		
C 8.613335	0.168901 0	0.181897
C 8.359917	1.306825	0.905513
S 7.170903	-0.622587	-0.331226
C 6.974478	1.562834	1.044199
C 3.938769	-0.525571	-0.104462
C 6.166690	0.615629	0.425728
C 4.728367	0.527364	0.352139
N 3.854650	1.537010	0.762808
C 2.480686	1.151933	0.579674
C 4.152270	2.883557	1.214463
O 1.541763	1.892972	0.844993
C 2.565625	-0.185439	0.033210
C 1.776235	-1.265465	-0.352592
N 2.651566	-2.281390	-0.749852
C 4.023368	-1.872169	-0.627208
O 4.963441	-2.589859	-0.951800
C 0.339788	-1.384845	-0.352750
C 2.351706	-3.565602	-1.355884
C -0.459622	-2.513847	-0.504743
C -3.642783	1.082509	-0.359885
C -1.839865	-2.243976	-0.434185
C -2.129885	-0.906494	-0.235047
C -3.455931	-0.288903	-0.125011
S -0.669640	0.035433	-0.103601
C -4.562048	-1.084990	0.217114
C -5.808902	-0.462753	0.299940
C -4.940118	1.590769	-0.238829
N -6.995149	-1.138807	0.631513
N -6.005964	0.844585	0.081712
N -5.270757	2.939112	-0.444241
C -7.188681	-2.479329	0.895450
C -8.620206	-2.843450	1.260070
O -6.296449	-3.315015	0.868915
C -4.460141	3.986447	-0.839324
C -5.198358	5.304003	-1.024393
O -3.262677	3.875718	-1.051506
H 9.575145	-0.257117	-0.071735
H 9.133601	1.938403	1.327175
H 6.592468	2.407300	1.597946
H 4.832899	3.391786	0.525316
H 4.579548	2.890832	2.223323
H 3.197513	3.412264	1.240166
H 1.647699	-3.456945	-2.185818
H 1.950084	-4.278353	-0.627033
H 3.301045	-3.954152	-1.729340
H -0.070112	-3.510864	-0.647013
H -2.835615	1.743005	-0.644203
H -2.601877	-3.006345	-0.546735
H -4.476802	-2.138581	0.434850
H -7.794334	-0.520148	0.664221
H -6.255929	3.119179	-0.303543
H -8.851662	-3.815872	0.821324
H -9.358846	-2.108609	0.927065
H -8.696255	-2.943626	2.348317
H -4.505066	6.119636	-0.814185
H -5.520725	5.395050	-2.067896
H -6.079762	5.398354	-0.382851
E(UB3LYP/6-31G(d,p) = –2335.168402 H		

Structure of Diethyl-PDI		
Charge = 0, Multiplicity = 1		
optimized structure (Cart. coord. In Å):		
C -1.255257	5.017115	-0.451667
N -0.044369	5.646874	-0.161280
C -1.228786	3.536680	-0.375193
O -2.246234	5.671031	-0.741074
C -2.383145	1.421695	-0.489021
C 4.887968	1.096000	-0.028437
C -2.380582	2.814728	-0.629729
C -0.026507	2.851582	-0.062386
C 0.000216	1.426052	-0.009564
C -1.254328	-0.740528	0.145892
C 1.164023	3.573771	0.206840
C 3.730650	0.907492	0.971421
C 1.172790	5.057229	0.177631
C 2.314567	2.891212	0.537663
O 2.154498	5.742556	0.423141
C 1.238632	-0.709864	-0.114615
C -0.000215	-1.426053	-0.009563
C -1.238630	0.709863	-0.114616
C 1.254329	0.740528	0.145892
C -4.887966	-1.095998	-0.028437
C 2.398122	1.481436	0.513579
C -2.398122	-1.481436	0.513580
C -3.730649	-0.907490	0.971421
C -1.172791	-5.057229	0.177631
N 0.044367	-5.646875	-0.161281
C -2.314567	-2.891212	0.537664
O -2.154500	-5.742556	0.423140
C -1.164023	-3.573771	0.206841
C 0.026506	-2.851582	-0.062385
C 1.228785	-3.536681	-0.375192
C 2.380582	-2.814730	-0.629728
C 2.383146	-1.421697	-0.489020
C 1.255255	-5.017117	-0.451668
O 2.246232	-5.671033	-0.741075
H -0.051923	6.660662	-0.197817
H -3.300563	0.890999	-0.696703
H 5.818227	0.692163	0.383616
H 4.698086	0.598158	-0.985301
H 5.049544	2.156583	-0.245719
H -3.280921	3.348871	-0.915229
H 3.998392	1.435358	1.895711
H 3.630401	-0.144668	1.244978
H 3.188671	3.476669	0.808752
H -5.818226	-0.692160	0.383615
H -4.698084	-0.598156	-0.985301
H -5.049543	-2.156581	-0.245718
H -3.998391	-1.435356	1.895712
H -3.630400	0.144669	1.244978
H 0.051920	-6.660662	-0.197819
H -3.188672	-3.476668	0.808752
H 3.280920	-3.348873	-0.915229
H 3.300564	-0.891001	-0.696702
E(B3LYP/6-31G(d,p) = −1487.504656 H		

Structure of Diethyl-PDI˙⁻		
Charge = -1, Multiplicity = 2		
optimized structure (Cart. coord. In Å):		
C -1.271886	4.998964	-0.437141
N -0.048646	5.625340	-0.179681
C -1.241028	3.538538	-0.356820
O -2.265568	5.679557	-0.704081
C -2.405260	1.423713	-0.462794
C 4.919223	1.076221	0.025561
C -2.405502	2.800790	-0.595137
C -0.028849	2.856004	-0.065386
C -0.002043	1.421193	-0.005336
C -1.252784	-0.733269	0.141167
C 1.170146	3.577648	0.172129
C 3.732411	0.907388	0.992674
C 1.181405	5.041102	0.133105
C 2.335430	2.883329	0.498801
O 2.164458	5.754822	0.348016
C 1.240693	-0.699712	- 0.099590
C 0.002043	-1.421193	- 0.005336
C -1.240693	0.699711	-0.099591
C 1.252784	0.733269	0.141167
C -4.919223	-1.076220	0.025561
C 2.415434	1.493249	0.494989
C -2.415434	-1.493249	0.494989
C -3.732411	-0.907388	0.992674
C -1.181406	-5.041102	0.133105
N 0.048646	-5.625340	- 0.179681
C -2.335431	-2.883329	0.498801
O -2.164458	-5.754823	0.348016
C -1.170146	-3.577648	0.172128
C 0.028849	-2.856004	-0.065386
C 1.241028	-3.538538	- 0.356820
C 2.405502	-2.800790	-0.595136
C 2.405260	-1.423713	-0.462793
C 1.271886	-4.998964	-0.437141
O 2.265568	-5.679558	-0.704081
H -0.056667	6.637519	-0.220834
H -3.314283	0.884075	-0.686221
H 5.839376	0.667140	0.459873
H 4.745835	0.572627	-0.931683
H 5.092279	2.134762	-0.195841
H -3.305092	3.337951	-0.879591
H 3.987341	1.431615	1.923823
H 3.614712	-0.144221	1.262508
H 3.205376	3.476045	0.770633
H -5.839376	-0.667139	0.459873
H -4.745835	-0.572627	-0.931682
H -5.092279	-2.134761	-0.195841
H -3.987341	-1.431615	1.923823
H -3.614711	0.144221	1.262508
H 0.056667	-6.637519	-0.220834
H -3.205376	-3.476045	0.770633
H 3.305092	-3.337951	-0.879591
H 3.314283	-0.884075	-0.686220
E(B3LYP/6-31G(d,p) = −2335.386035 H		

Structure of DPP–PDI Aggregate:

Charge = 0, Multiplicity = 1
optimized structure (Cart. coord. In Å):

C	5.060279	2.463432	1.588490	C -12.957886	1.185626	1.681736
N	5.690683	1.252487	1.875318	C -11.491884	1.168890	1.735006
N	5.690683	1.252487	1.875318	S -13.889358	-0.286482	1.674975
C	3.579295	2.440465	1.677614	C -10.804987	2.310055	2.170701
O	5.711142	3.453759	1.292426	C -9.408561	2.273692	2.203207
C	1.466903	3.599608	1.579267	C -9.363137	0.094027	1.432312
C	1.130513	-3.670435	2.057621	N -8.644984	3.372621	2.622101
C	2.858901	3.593701	1.426803	N -8.686979	1.188221	1.846646
C	2.894021	1.240711	1.998425	N -8.553143	-0.990811	1.080044
C	1.469239	1.217019	2.063308	C -9.097497	4.615663	3.028888
C	-0.692900	2.476496	2.230468	C -7.996125	5.569891	3.465416
C	3.616484	0.049491	2.263318	O -10.275487	4.947420	3.069836
C	0.953919	-2.510854	3.057235	C -8.941511	-2.212074	0.551074
C	5.100801	0.037781	2.220909	C -7.782240	-3.169229	0.318754
C	2.935870	-1.099410	2.601993	O -10.097061	-2.520468	0.297999
O	5.783602	-0.945972	2.462467	H 6.704251	1.257901	1.830200
C	-0.668334	-0.018377	1.978857	H 0.937157	4.517998	1.374006
C	-1.380603	1.222682	2.083993	H 0.730554	-4.598923	2.476979
C	0.755551	2.457261	1.960842	H 0.622269	-3.482736	1.105785
C	0.783535	-0.035704	2.227581	H 2.188335	-3.833596	1.828938
C	-1.040798	6.111416	2.053075	H 3.392649	4.492263	1.135333
C	1.525356	-1.180417	2.590791	H 1.491616	-2.776865	3.976183
C	-1.430541	3.622858	2.600911	H -0.094929	-2.408418	3.342205
C	-0.852032	4.955237	3.054265	H 3.522178	-1.974076	2.869049
C	-5.003006	2.383695	2.289268	H -0.632290	7.040578	2.462555
N	-5.611991	1.185430	1.958597	H -0.547572	5.918789	1.094468
C	-2.839391	3.541051	2.633343	H -2.101587	6.276721	1.839554
O	-5.683242	3.377248	2.547851	H -1.375450	5.225503	3.980212
C	-3.525468	2.388822	2.309009	H 0.200630	4.851999	3.324261
C	-2.805367	1.198419	2.040704	H -6.649860	1.183819	1.924200
C	-3.496744	-0.001465	1.738485	H -3.419225	4.417742	2.907128
C	-2.779452	-1.157816	1.483221	H -3.315280	-2.059037	1.204436
C	-1.386292	-1.163115	1.613490	H -0.859637	-2.082239	1.404011
C	-4.971833	-0.010047	1.671950	H -23.318110	-4.296589	1.548610
O	-5.624851	-1.012961	1.381643	H -21.916985	-6.345589	2.441334
C	-22.251119	-4.322993	1.726802	H -19.396740	-5.760727	2.666058
C	-21.502761	-5.375908	2.189378	H -17.399761	-5.694590	1.628635
S	-21.300627	-2.916167	1.431301	H -17.398114	-5.385638	3.390617
C	-20.128767	-5.054408	2.305189	H -15.922559	-5.112758	2.439496
C	-18.305950	-1.710136	1.653717	H -17.579945	2.187519	0.083337
C	-19.826369	-3.749909	1.930828	H -18.062172	2.559495	1.764255
C	-18.561305	-3.055539	1.911848	H -19.248555	1.877113	0.634470
N	-17.326706	-3.654834	2.172174	H -15.924768	2.726817	1.562794
C	-16.249700	-2.704090	2.087843	H -11.227501	-0.864837	0.988230
C	-17.012248	-5.048607	2.422426	H -13.410895	3.312231	1.637529
O	-15.076427	-3.013686	2.258472	H -11.310927	3.203974	2.498804
C	-16.910866	-1.459347	1.761567	H -7.633452	3.244357	2.609732
C	-16.661579	-0.104219	1.556010	H -7.550612	-0.865772	1.218751
N	-17.899790	0.496782	1.306037	H -8.238332	6.565239	3.086210
C	-18.968546	-0.461782	1.344790	H -6.999658	5.271782	3.137052
O	-20.138435	-0.163213	1.126549	H -8.002181	5.627398	4.559825
C	-15.406422	0.603009	1.591381	H -8.156868	-4.029381	-0.235999
C	-18.197032	1.865533	0.927357	H -6.965550	-2.691079	-0.229200
C	-15.153103	1.972253	1.589034	H -7.372403	-3.506776	1.276969
C	-10.760332	0.037466	1.355397			
C	-13.783752	2.294675	1.644338			

E(B3LYP/6-31G(d,p) = –3822.918991 H

RENDERING OF THE OPTIMIZED STRUCTURES
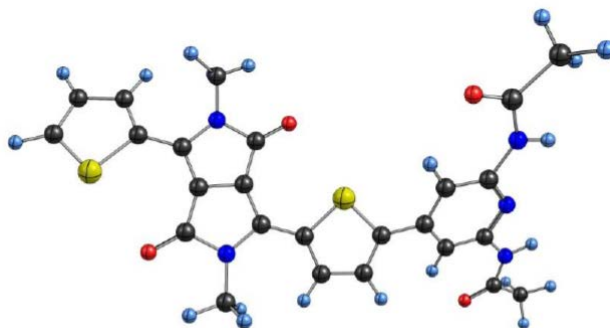
Fig. B53: Optimized structure of the DPP (alkyl chains shortened to one carbon).
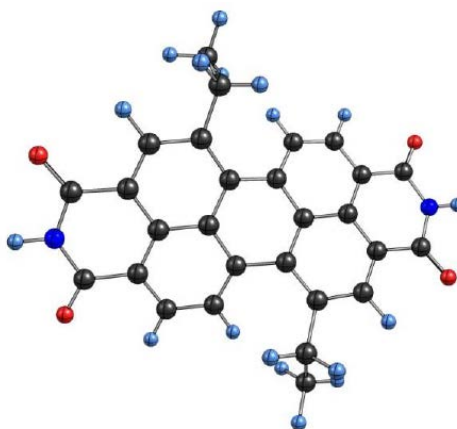
Fig. B54: Optimized structure of the PDI (alkyl chains shortened to two carbons).
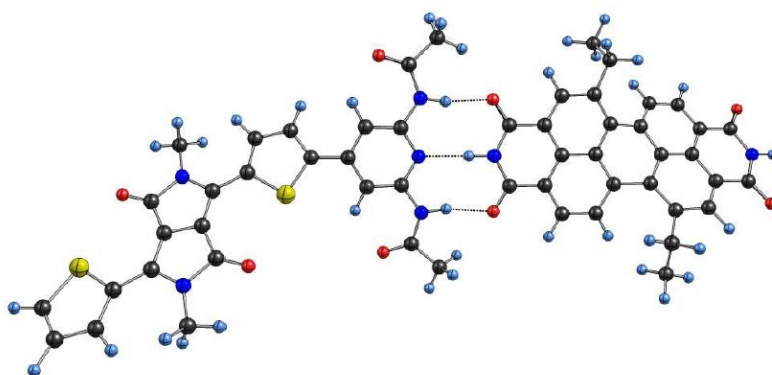
Fig. B55: Optimized structure of the DPP-PDI aggregate showing the triple H-bond.

MOLECULAR ORIBITAL PLOTS:
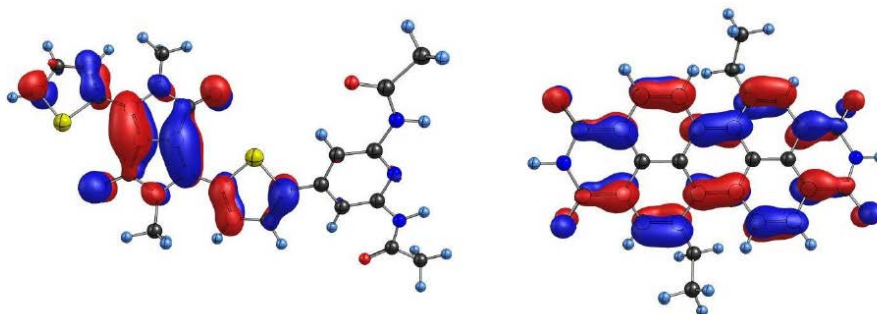
Fig. B56: Natural bond orbitals (HF/3-21G) showing the HOMO of the DPP (left), as well as the LUMO of the PDI (right). The orbitals were plotted using a contour value of 0.035.

GENERAL METHODS

All chemicals were purchased through VWR or Aldrich Chemicals and used as received unless otherwise noted. mDPP and PDI were synthesized following previously reported procedures.[34] The molecules were characterized by ^{1}H NMR, ^{13}C NMR, and high resolution mass spectrometry, and all spectral data were consistent with previously published reports.[34-35,] The UV-Vis measurements were performed on a Shimadzu UV-2600 spectrometer, ATR-IR measurements were taken using a Perkin FT-IR Frontier spectrometer with a universal diamond top-plate for ATIR-IR measurements, circular dichroism (CD) spectroscopy was performed on a Jasco-810 Spectropolarimeter, cross polarized microscopy images were taken with a Leica DM2700 P microscope with a 530 nm polarizer and a 20x objective, Spectroelectrochemistry was taken using CH Electronics Model 650E Workstation to apply potential and the Shimazdzu UV-1800 spectrophotometer to take spectra, AFM images were taken on a Park System XE 150 Scanning probe microscope using Nanosensors^{TM} PP NCHR probes under non-contact mode.

FILM PREPARATION

Thin films composed of mDPP, PDI, or a 2:1 mixture of mDPP:PDI were prepared on glass slides. First, glass slides were cleaned by washing with ethyl acetate and methanol, then the cleaned slides were exposed O_2 plasma from a Harrick Plasma Cleaner PDC-32 G. The films were prepared by drop casting a heated solution onto the freshly prepared glass. The solutions consisted of mDPP (50 μM), PDI (50 μM), or mDPP (45 μM) and PDI (23 μM) dissolved in spectroscopic grade toluene. The solutions were heated to 90 °C, and 60 μl of the appropriate solution were added to the slides and allowed to slowly evaporate at room temperature in the dark, a process which takes ~ 4 hours. This dropcasting was repeated 3 times to create films sufficiently thick for analysis. To create air free films, films were introduced into a glove box and a glass slide was laid on top of the film, and the film was sealed between the two glass plates with an epoxy glue.

UV-VIS SPECTROSCOPY

Heteroaggregate assembly is dependent on H-bonding and $\pi\cdots\pi$ stacking between mDPP and PDI. In previous reports [34] we showed mDPP and PDI form heteroaggregates with characteristic peaks in the UV-Vis spectrum that are indicative of assembly. Specifically a new charge transfer peak arose at 622 nm upon superstructure formation. Thus, we performed UV-Vis spectroscopy on the three films to determine whether these new bands that emerged upon assembly in solution occurred in the thin films as well, which would indicate the formation of similar $\pi\cdots\pi$ stacking. In the 2:1 mDPP:PDI films, (Fig. C1 a) a new peak emerges at 626 nm indicating the formation of a donor-acceptor superstructure in the film. There is a bathochromic 4 nm shift of the aggregate peak (Fig. C1 b) from solution (navy blue) [34] to solid state (purple), and we attribute the 4 nm shift to the difference in dielectric environment between solution and solid. UV-Vis is also important for understanding the ground-state spectroscopic properties of the donors, acceptors, and aggregates.
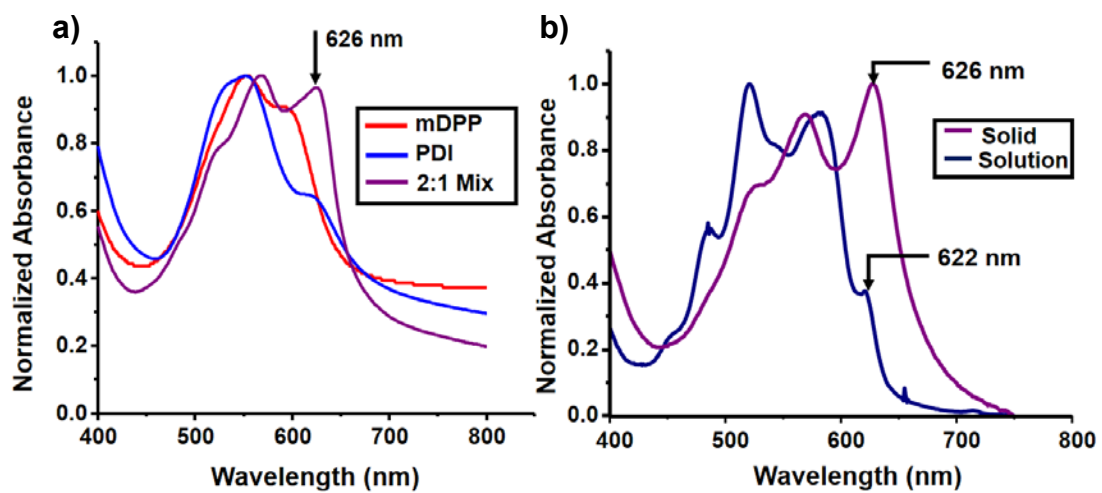
Fig. C1: (a) UV-Vis spectrum of mDPP film (red), PDI film (blue), and the 2:1 mDPP: PDI film (purple).(b) UV-Vis spectrum of 2:1 mDPP: PDI mixture in solution (navy blue) and the drop cast 2:1 mDPP: PDI film (purple). Graphs were normalized to the maximum absorption band.

INFRARED SPECTROSCOPY

Attenuated total reflectance (ATR) IR spectroscopy was carried out to analyze the H-bonding in the solid state. For ATR-IR measurements, the films were scratched into a powder, and the IR spectra were taken of the powder using a universal diamond top-plate, and after each measurement, the crystal was cleaned with ethyl acetate to ensure no traces from the previous compound remained. The ATR-IR spectra provided evidence that mDPP self-aggregates through H-bonding. However, when the donor self-aggregates, there is an amine hydrogen on the DAP group that does not participate in the H-bonding. The ATR-IR spectrum of mDPP (Fig. C2, red line) displays a sharp peak at 3392 cm^{-1}, which corresponds to the unbound amine N-H stretch and a broad peak at 3281 cm^{-1} indicative of an H-bound N-H bound stretch.[275] To create the heteroaggregate, both amine groups are H-bonded to the carbonyls of the acceptor, thus eliminating the amine stretch at 3392 cm^{-1}, and the N-H stretch peak corresponding to the H- bonded amines shifted to 3281 cm^{-1} indication that all DAP N-H groups participate in H-bonds with the PDI carbonyls.
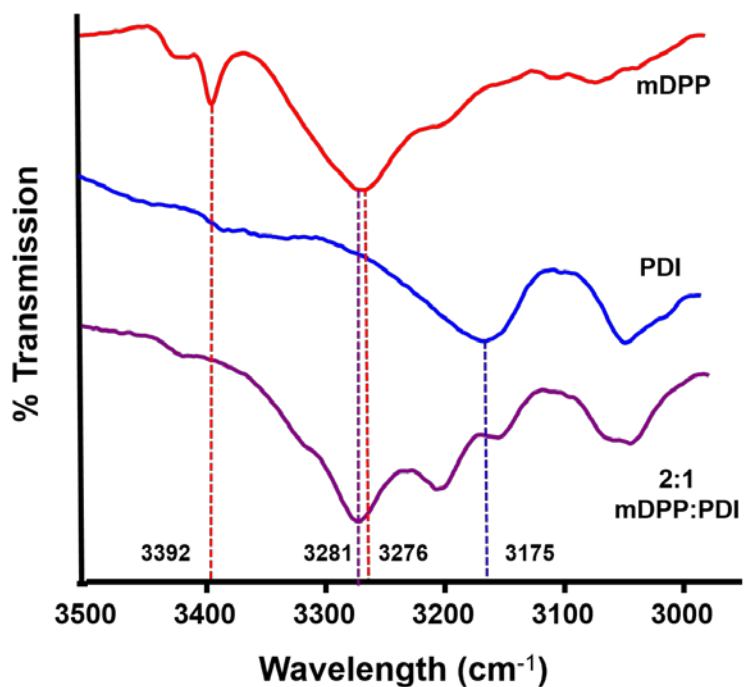
Fig. C2: ATR-IR of mDPP film (red), PDI film (blue) and 2:1 mDPP:PDI (purple). The dashed line at 3392 cm^{-1} labels the unbound the N-H stretch of the DAP group in the donor (red). The peak corresponding to the H-bound N-H shifts from 3276 cm^{-1} to 3281 cm^{-1} in the mDPP- PDI film. The 3175 cm^{-1} in the PDI corresponding to the C-H stretch, remains in 2:1 mixture. Data was normalized by matching intensities of the strongest peaks, and the graphs were offset for clarity.

SOLID STATE NMR

The monomers and the 2:1 mixture were first prepared in a toluene solution, then heated to 100 degrees to prevent any kind of pre-formed aggregation. Each solution was then slowly cooled to room temperature then the solvent was evaporated. The crystals remaining were then used for NMR studies. Solid-state NMR spectroscopy (ssNMR) was employed to further establish the H-bonding between the mDPP and PDI. All spectra were collected on a Varian VNMRS 400 MHz wide-bore spectrometer equipped with a 1.6 mm triple-resonance probe operating in ^{1}H/^{13}C/^{15}N mode. ^{1}H MAS NMR experiments, ^{1}H$\rightarrow$^{13}C cross-polarization magic-angle-spinning (CP-MAS) experiments, two-dimensional (2D) ^{1}H-^{13}C heteronuclear correlation (HETCOR) and ^{1}H-^{1}H back-to-back (BABA) dipolar DQ/SQ correlation NMR experiments were performed in this work. The ^{1}H MAS NMR experiments were collected using the DEPTH sequence, to remove background signal from outside the coil. The spectra were collected using a 1.5 μs ^{1}H π/2 pulse, a 50 kHz sweep width at a MAS speed of 40 kHz. The recycle delay times are 10 s, 20 s, and 20 s for mDPP, PDI and 2:1 mDPP:PDI, respectively. For the ^{1}H$\rightarrow$^{13}C CP-MAS experiments, a 1.5 μs ^{1}H π/2 pulse was used, followed by a 1.0 ms ramped (10 %) ^{1}H spin-lock pulse and a ^{13}C contact pulse with a radio frequency (rf) field strength of 100 kHz. The rf field strength of the ramped ^{1}H pulse during contact time was optimized to the (-1) spinning band of the Hartmann-Hahn matching profile (65 kHz.) The CP-MAS experiments were performed with a 25 kHz sweep width, a recycle delay of 3.0 s and a two-pulse phase-modulated (TPPM) ^{1}H decoupling level of 150 kHz at a MAS speed of 35 kHz for all samples. The 2D ^{1}H-^{13}C HETCOR NMR experiments were collected using the same CP conditions described above. The sweep widths of direct dimension and indirect dimension are 50 kHz

and 17.5 kHz respectively with 16 complex t_1 points. A recycle delay of 3.0 s and a TPPM

^{1}H decoupling with a rf field strength of 150 kHz was used during acquisition. ^{1}H-^{1}H

BABA dipolar DQ/SQ correlation NMR experiments were carried out at a MAS speed of

40 kHz with one rotor period BABA for excitation and reconversion, a 1.5 μs ^{1}H π/2 pulse,

relaxation delay of 5.0 s, and 32 complex t_1 points. The sweep widths of direct dimension

and indirect dimension are 50 kHz and 20 kHz respectively. In all experiments, the

chemical shifts of ^{1}H and ^{13}C were indirectly referenced to adamantane, ^{1}H (1.63 ppm) and

^{13}C (38.56 ppm).
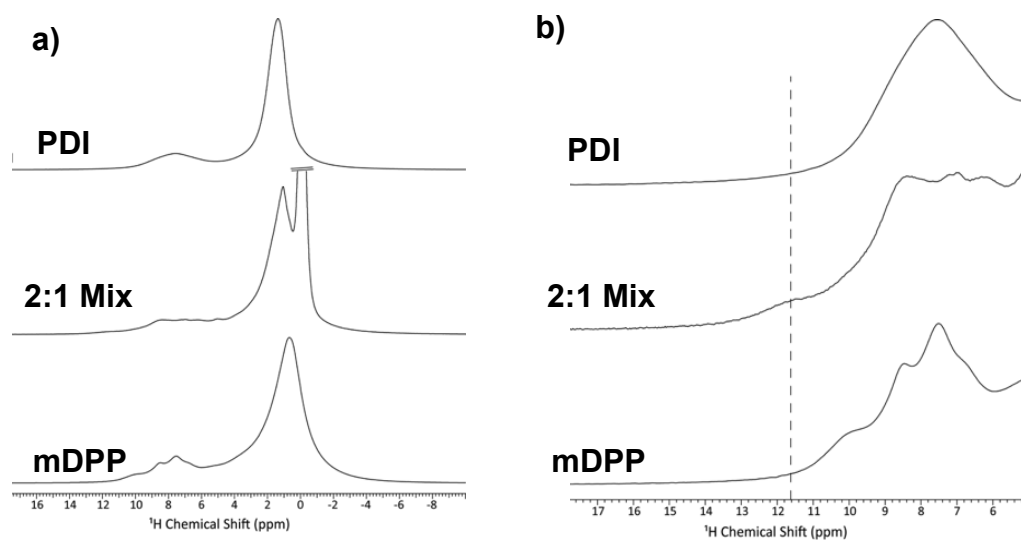
Fig. C3: 1D NMR data of each monomer (a) and the 2:1 mixture. Blow up of the spectra (b) shows a new resonance at 11.7 ppm for the 2:1 mixture. Large ^{1}H chemical shift indicative of strong H-bonding is observed for the 2:1 mixture.
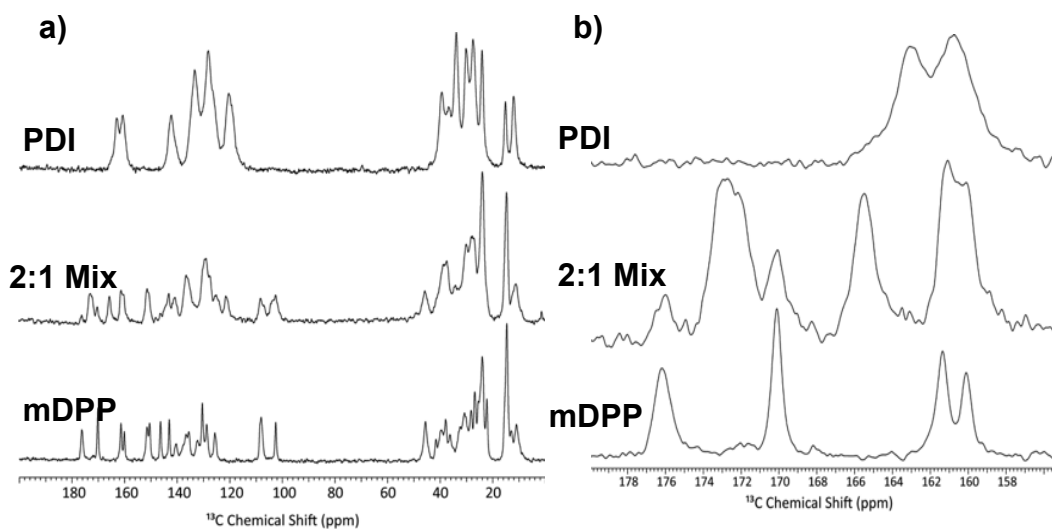
Fig. C4: Appearance of new ^{13}C carbonyl resonances in the 2:1 Mixture spectrum. This is likely due the carbonyls participation in H-bonding or the H-bonding of adjacent groups.
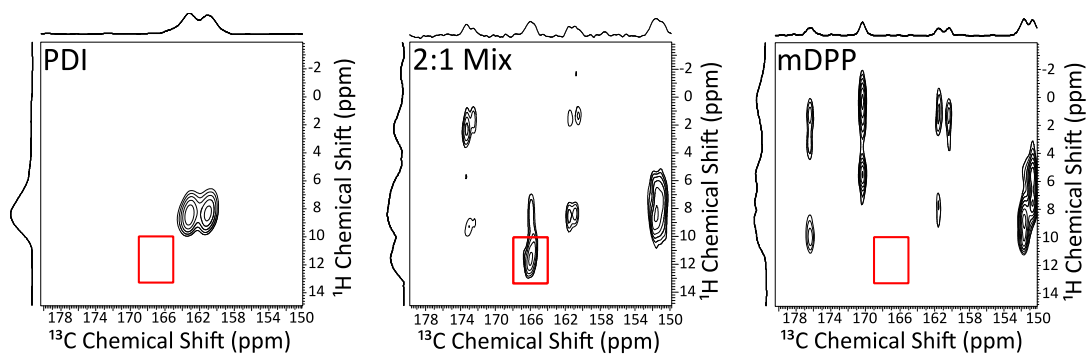
Fig. C5: The strong H-bonding ^{1}H resonance (11.7 ppm) correlates with the ^{13}C environment at 166 ppm. This is consistent with H-bonding of mDPP amide groups with PDI carbonyls.
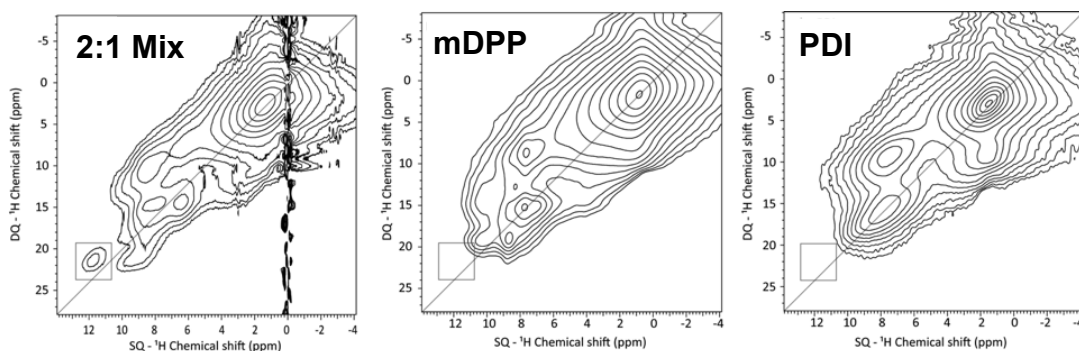
Fig. C6: The strong H-bonding resonance at 11.7 ppm is isolated from itself (no on diagonal correlation is observed) and correlates to the amide protons of mDPP. This is also all consistent with the H-bonding model presented for the 2:1 mixture.

CIRCULAR DICHROSIM (CD) SPECTROSCOPY

An important aspect of the mDPP:PDI system is the emergent chirality upon supramolecular polymer formation, evidenced by new peaks in the CD spectra. In this system, the chirality is driven by the (*s*)-2-methyl hexyl group on the mDPP side chain. We have shown previously [34] that although the source of chirality is on the mDPP, the solution spectra of the mDPP does not result in any measureable Cotton effect. However upon aggregation with the achiral PDI, a significant bisignated Cotton effect occurs, indicative of homochiral helical aggregates (Fig. C7). CD measurements were repeated on the film, and similar observations were made. While the CD of the PDI film had no Cotton effect, a small cotton effect was observed with the mDPP films indicating some ordering occurs in the film. Nevertheless, a strong bisignated Cotton effect is observed in the mDPP:PDI drop cast film, with significant peak shifts compared to the mDPP film. Importantly, the shape and peaks matched the solution CD spectrum of the donor-acceptor aggregates (Fig. C8).
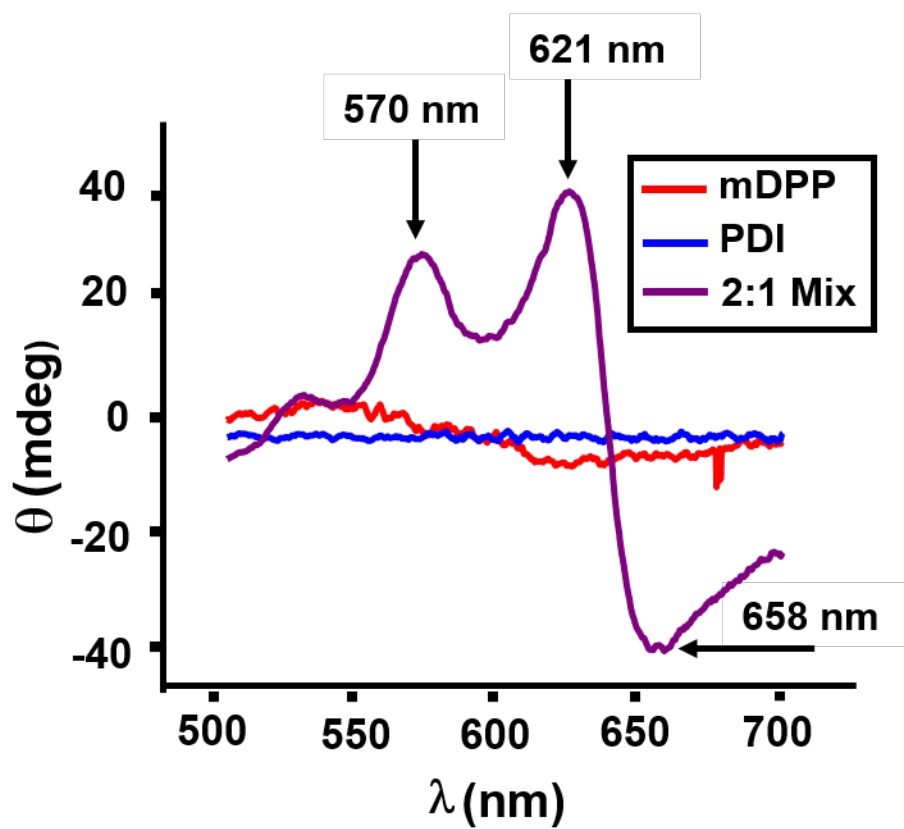
Fig. C7: Thin film CD spectra of mDPP (red), PDI (blue), and 2:1 mDPP: PDI mixture (purple). Arrows indicate the new peaks that emerged upon mixing the donor and acceptor in the films.
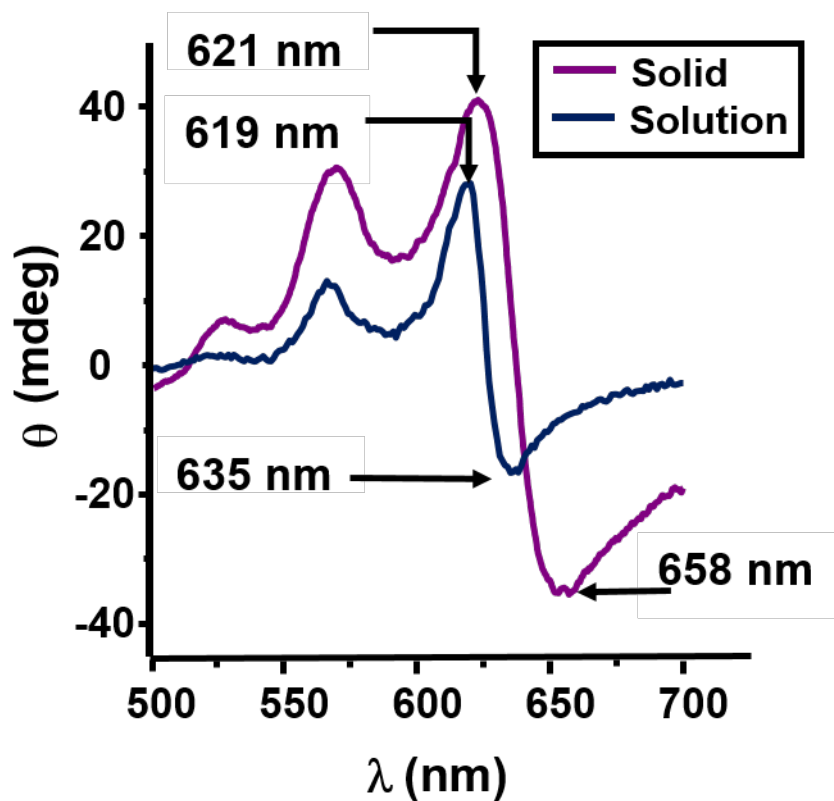
Fig. C8: Comparison of CD measurements of the 2:1 mDPP:PDI mixture in the thin film (purple) and in solution (navy blue). Concentrations of the solution in spectroscopic grade toluene for solution CD measurements was a 2:1 mixture of mDPP (45 μM) and PDI (23 μM).

CRYSTAL STRUCUTRE OF DIETHYL HEXYL mDPP

We have reported previously the crystal structure of ethyl hexyl mDPP[1]. This structure differs from mDPP solely in absence of homochirality in the side chain. We have reproduced the structure here to show the interactions of the amides is consistent with our interpretation of the film ATR-IR data. CCDC 933783
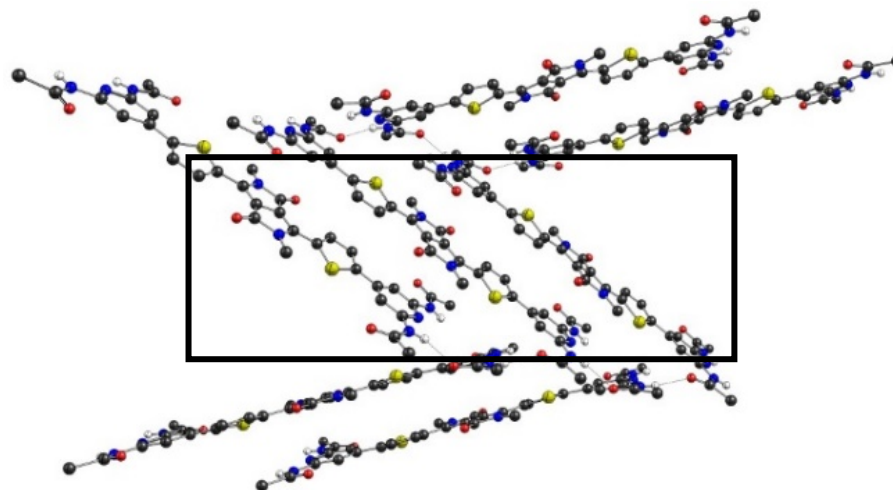
Fig. C9: Crystal structure of the homoaggregate mDPP (alkyl chains shortened to one carbon).
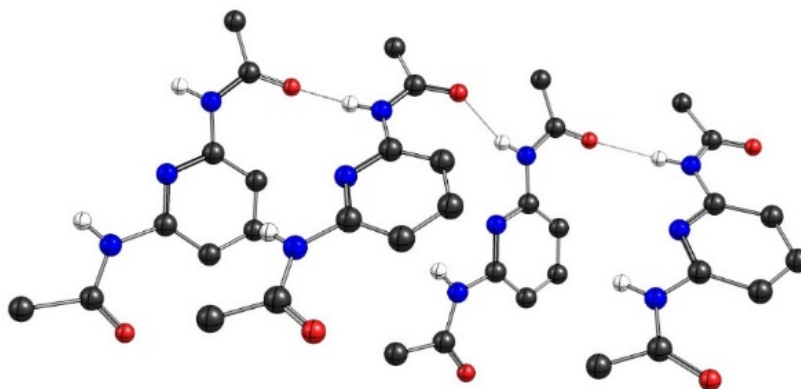
Fig. C10: Section of homoaggregate mDPP showing the DAP side chain H-bonding interaction (dotted line). The model demonstrates that in the homoaggregated stack of mDPP, only one amide N-H is bound in a H-bond with the amide carbonyl of an adjacent DAP.

ATOMIC FORCE MICROSCOPY

Atomic Force Microscopy (AFM) images were carried out to analyze the nanoscale and microscale morphologies of the various films. Previous experiments indicate the development of a new aggregate in the 2:1 mDPP:PDI film that is not present in the monomer films. AFM images were acquired in noncontact mode using Nanoprobe spm tips with a spring constant 10 N/m. Only small aggregates were formed in the mDPP films (Fig. C11 a). In the PDI films (Fig. C11 b), more uniform surface coverage was observed. In the 2:1 mDPP: PDI film (Fig. C11 c) a film with high surface coverage consisting of overlapping wires was observed.

Measuring Film Thickness
To measure the film thickness, portions of the films were removed from the glass slide by wiping the films with a cotton swab dipped in dichloromethane, then AFM was used to measure the film heights.
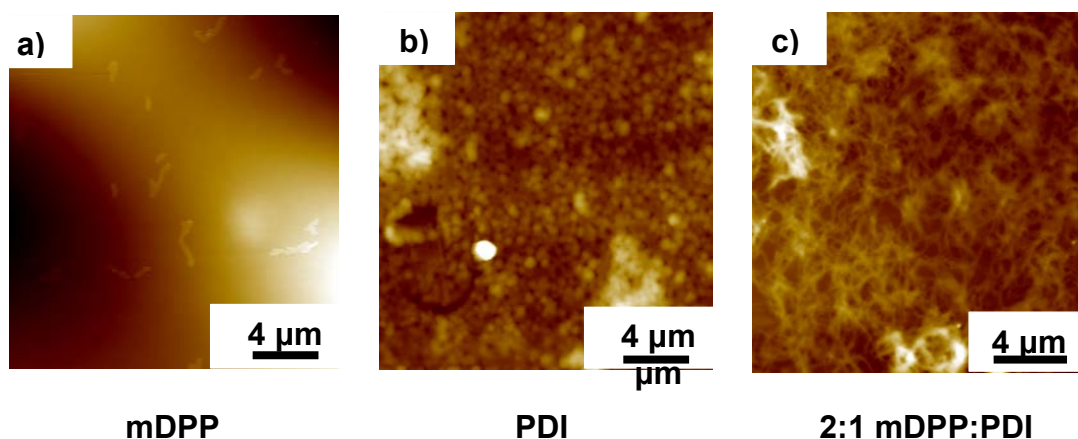
mDPP   PDI   2:1 mDPP:PDI

Fig. C11: AFM Topography images of the (a) mDPP, (b) PDI, and the (c) 2:1 mDPP:PDI mixtures on the glass slides.
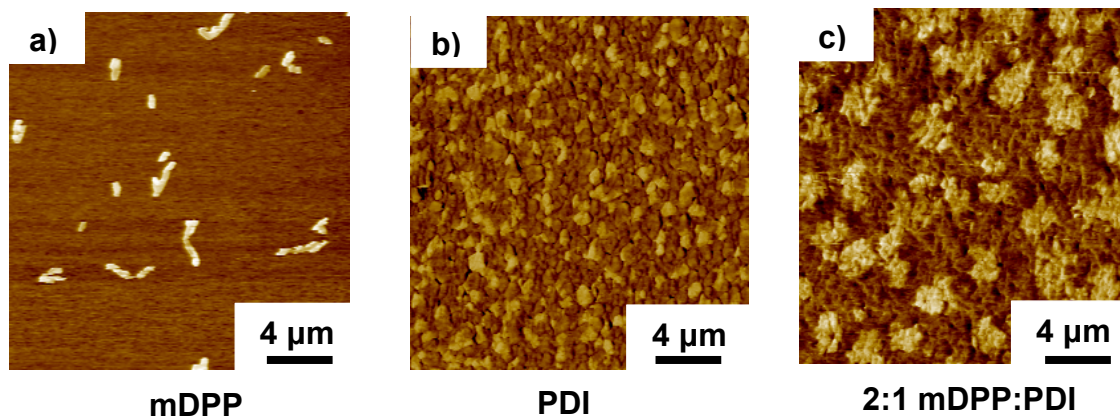
Fig. C12: Lateral force AFM images of the (a) mDPP, (b) PDI, and the (c) 2:1 mDPP:PDI mixture on film.
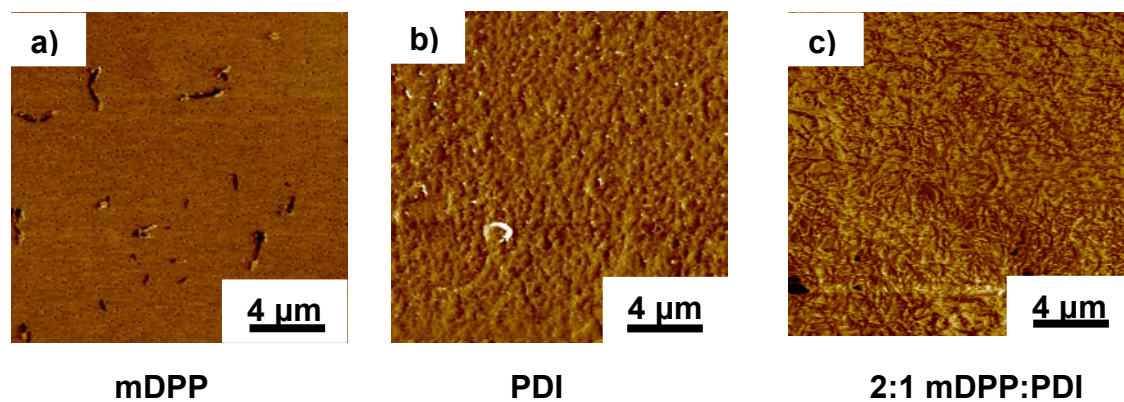
Fig. C13: AFM phase images of the (a) mDPP, (b) PDI, and the (c) 2:1 mDPP:PDI mixture on the glass slides.
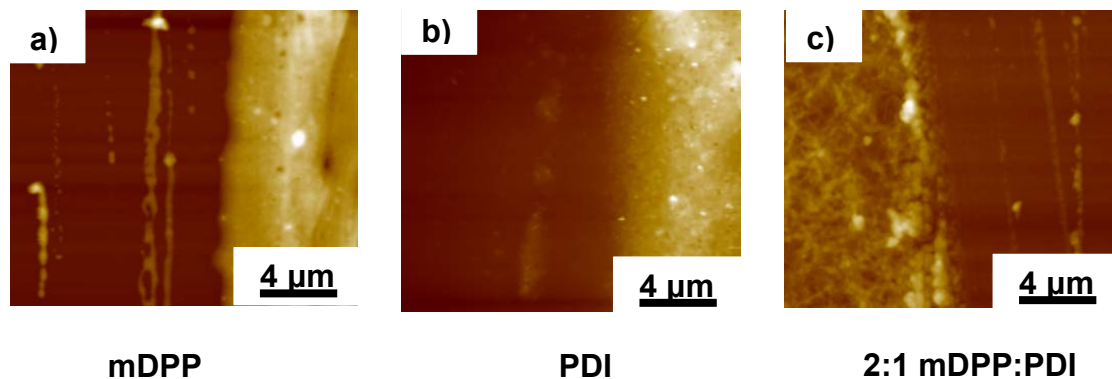
Fig. C14: AFM height profile images at the film edges of (a) mDPP, (b) PDI, and the (c) 2:1 mDPP:PDI mixture on the glass slides.
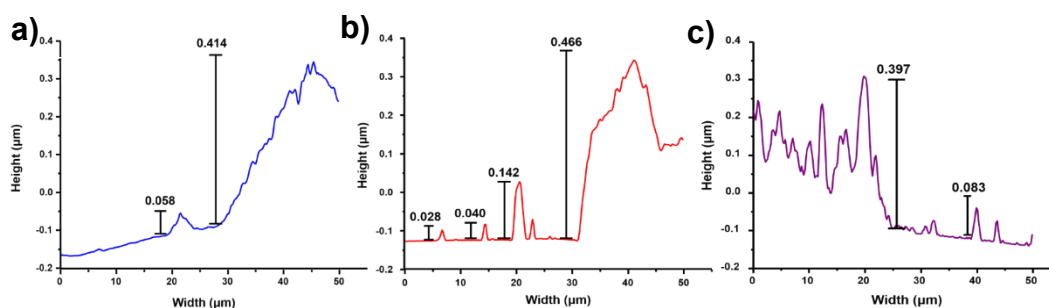
Fig. C15: Height profiles of (a) mDPP, (b) PDI, and (c) 2:1 mDPP: PDI mixture films. Arrows indicate points that were taken to measure film thickness. Numbers indicate the thickness in μm of that particular peak.

Table C1: Heights are calculated from the average of six profiles at different points across the films.

Compound	Height Average $\bar{x}$ (μm)	Standard Deviation σ (μm)
2:1 Mixture	0.318	0.054
mDPP	0.519	0.054
PDI	0.714	0.160

Table C2: Lengths and root mean square (RMS) roughness are calculated from average of six profiles at different points across the film.

Compound	Length Average $\bar{x}$ (μm)	Standard Deviation σ (μm)	RMS Roughness (μm)
2:1 Mixture	3.54	1.26	0.221
mDPP	2.02	0.936	0.137
PDI	1.19	0.108	0.260

GRAZING INCIDENT WIDE ANGLE X-RAY SCATTERING (GIWAXS) DATA

GIWAXS was performed at the G2 station at Cornell High Energy Synchrotron Source (CHESS) using a beam energy of 11.825 +/- 0.01 keV (λ = 1.0486 +/- 0.001 nm), selected using a single-crystal Be crystal monochromator. Motorized slits were used to define a 0.2 × 3 (V×H) mm^2 beam, with a typical flux of 2×10^{10} photons/s. The data were collected using a 640-element 1D diode-array, of which each element incorporates its own pulse counting electronics capable of count rates of ~10^5 photons/s. A set of 0.1° Soller slits were used on the detector arm to define the in-plane resolution. The scattering geometry is described in detail elsewhere.[4] Each data set was collected by scanning the detector with the sample stationary. The incidence angle α between the beam and sample surface was 0.175°. Axes labels Q_∞ and $Q_\|$ are defined using the GISAXS convention $Q_\infty = 4\pi/\lambda\sin(\delta/2)$ and $Q_\| = 4\pi/\lambda\sin(\nu/2)$, where δ and ν are the vertical and horizontal scattering angles, respectively.[5] At $\alpha=\delta=0$, $\hbar Q_\|$ and $\hbar Q_\infty$ (where $\hbar$ is Planck's constant) are the components of momentum transfer parallel and perpendicular to the sample surface, respectively.
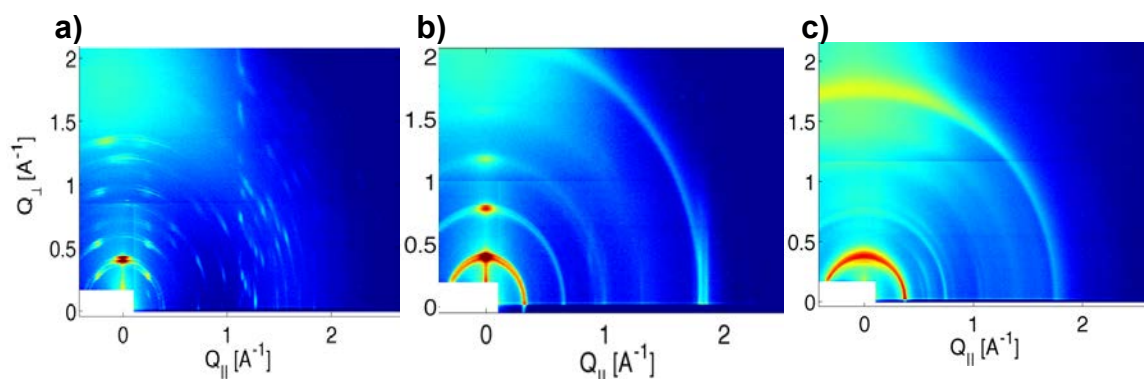
Fig. C16: GIWAXS data of (a) mDPP films, (b) PDI films, and (c) the 2:1 mDPP:PDI film.
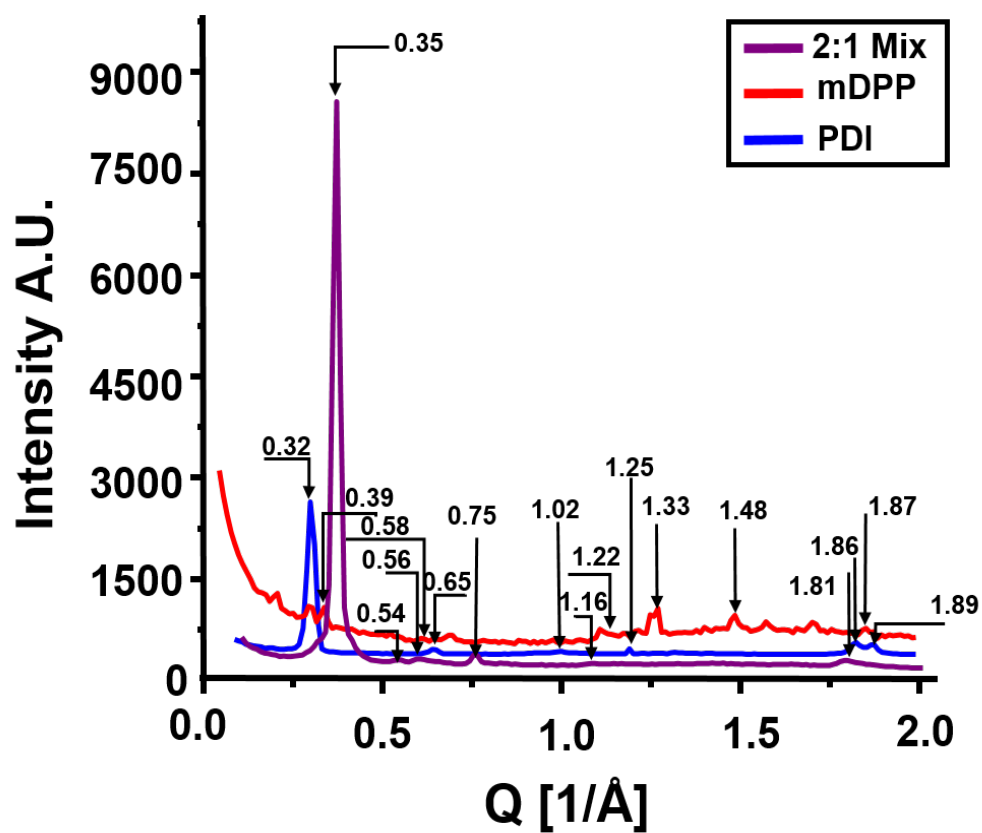
Fig. C17: GIWAXS intensities of mDPP film (red), PDI film (blue) and 2:1 mDPP:PDI (purple) along Q⊥. Arrows indicate highest intensities for each compound. The values of the intensity peaks of mDPP (red) were multiplied by 10.
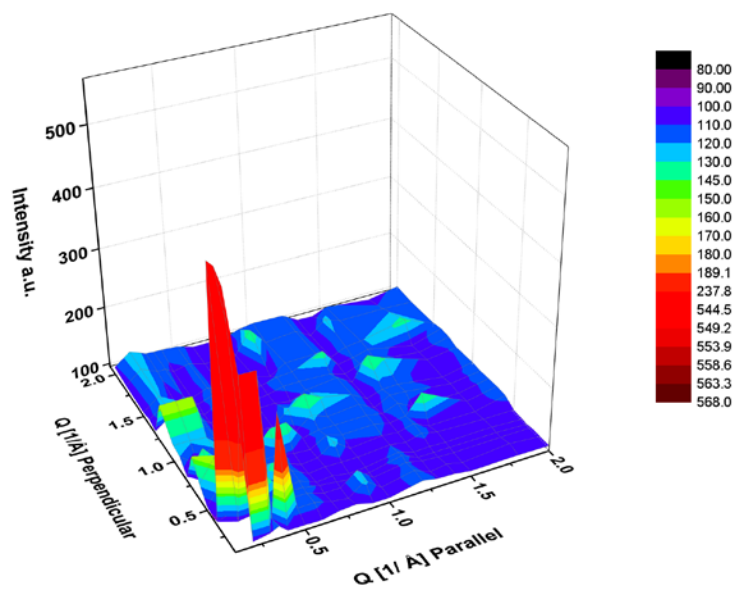
Fig. C18: 3D surface area plot of mDPP GIWAXS data.
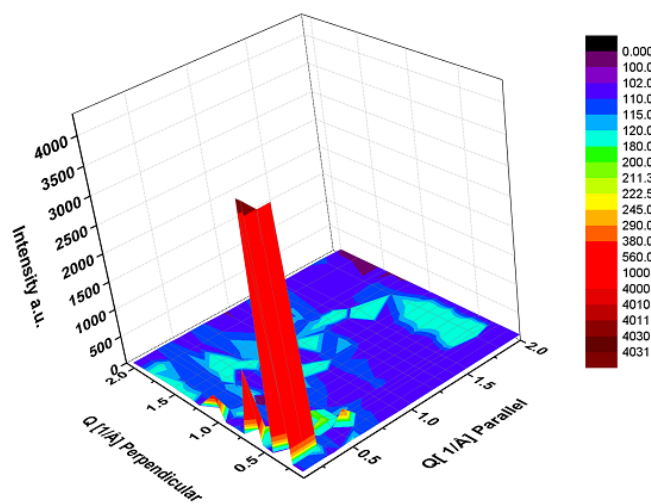
Fig. C19: 3D surface area plot of PDI GIWAXS data.
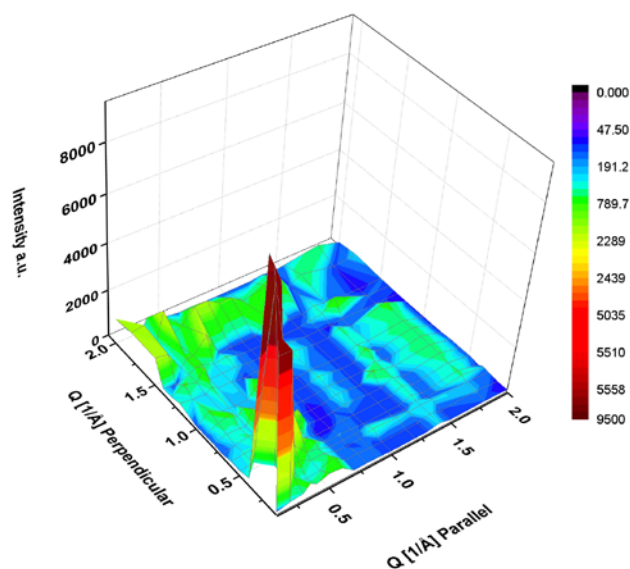
Fig. C20: 3D surface area plot of 2:1 mDPP:PDI GIWAXS data

Table C3: From the GIWAXS data peak positions (A^{-1}), corresponding diameters (nm) and the ratio of intensities between $Q\perp/ Q_\parallel$ are shown. Data was converted to nm using Bragg's equation ($2* \pi / Q$). Ratios were calculated by comparing the intensity of the $Q\perp/ Q_\parallel$ and compare the peak intensities.

mDPP			PDI			2:1 Mixture		
A^{-1}	D nm	Ratio Intensity $Q\perp/ Q_\parallel$	A^{-1}	D nm	Ratio Intensity $Q\perp/ Q_\parallel$	A^{-1}	D nm	Ratio Intensity $Q\perp/ Q_\parallel$
0.395	1.589	2.85	0.328	1.923	2.91	0.352	1.787	2.31
0.584	1.074	0.96	0.659	0.953	1.97	0.542	1.158	2.19
1.227	0.512	1.12	1.022	0.615	1.84	0.561	1.120	1.98
1.335	0.470	1.01	1.251	0.502	1.02	0.753	0.834	0.94
1.482	0.424	1.98	1.564	0.401	1.97	1.162	0.542	1.56
1.872	0.335	2.13	1.863	0.337	0.98	1.810	0.347	2.41
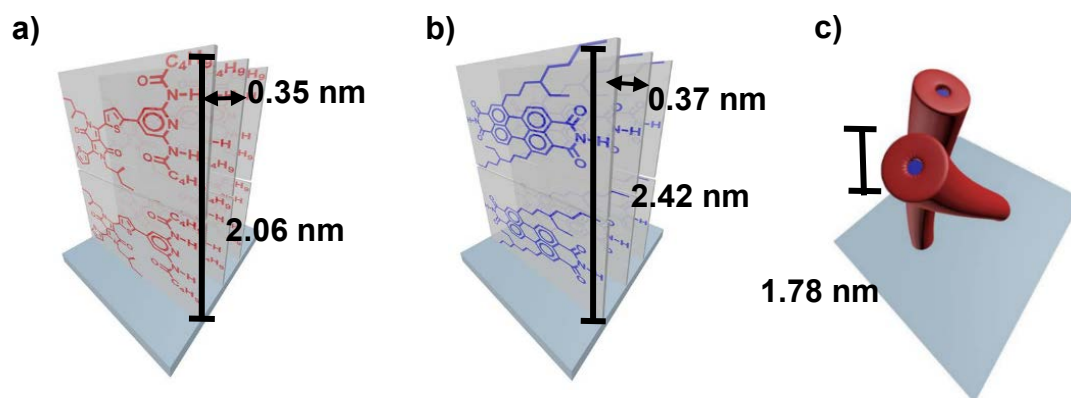
Fig. C21: The orientation distribution of (a) mDPP and (b) PDI and (c) the 2:1 mixture as a unit cell with edge-on arrangement with distances between monomers.

SCANNING ELECTRON MICROSCOPE SEM MEASUREMENTS

Scanning electron microscope (SEM) was performed to analyze morphologies of the 2:1

mixture films. The films were coated with a 20 nm thick palladium coat using a Cressington

108 Auto Sputter Coater and SEM measurements were performed in a FEI XL-SEM

microscope. Large structure are bundled individual wires snaking every which way (C22

a). Higher magnifications show the individual wires intertwining with each other (C22 b-

d).
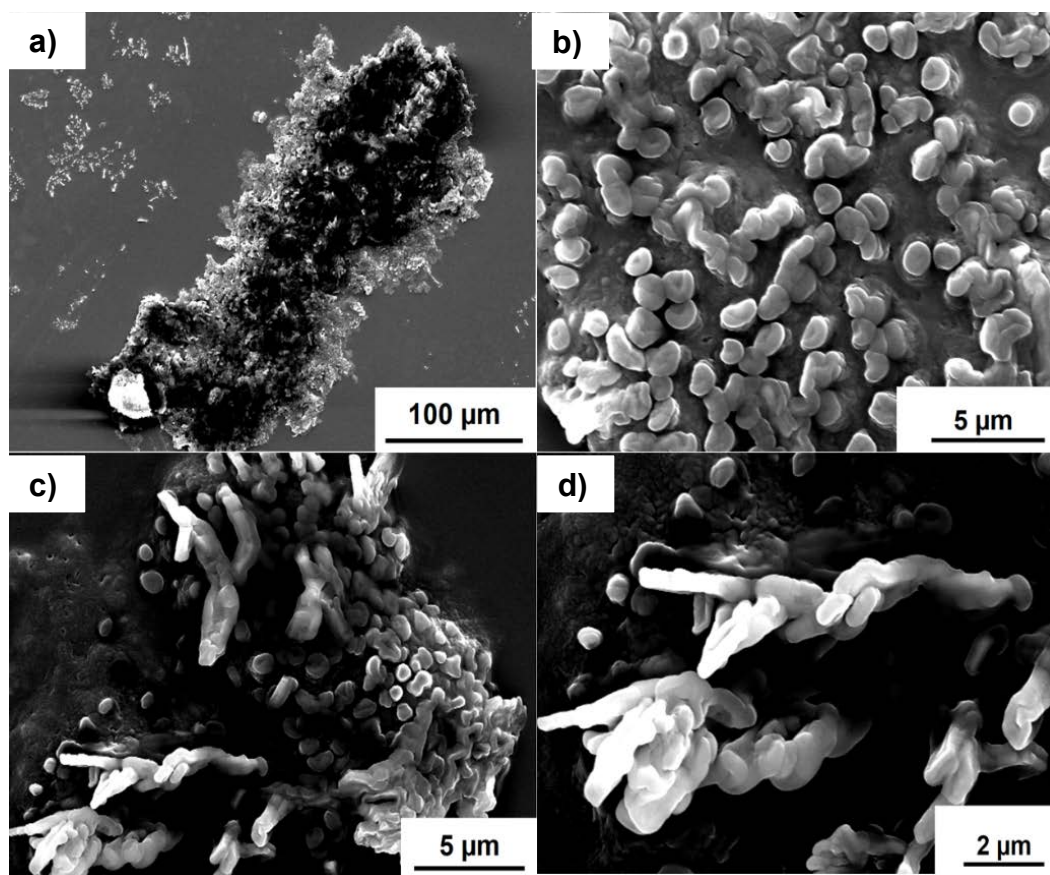
Fig. C22: (a) SEM image of flake of 2:1 mDPP:PDI hierarchal films near edges of film. (b-d) SEM images at different magnifications of a bundle of wires

POLARIZED OPTICAL MICROSCOPY

Polarized optical microscopy (POM) was performed to analyze film morphologies. All POM measurements were done on a Lecia DM750 P polarizing microscope. The mDPP films were comprised of small crystals (Fig. C23 a). PDI films are composed powders (Fig. 23 b) and the 2:1 mDPP:PDI mixture forms continuous film across the surface (Fig. C24).
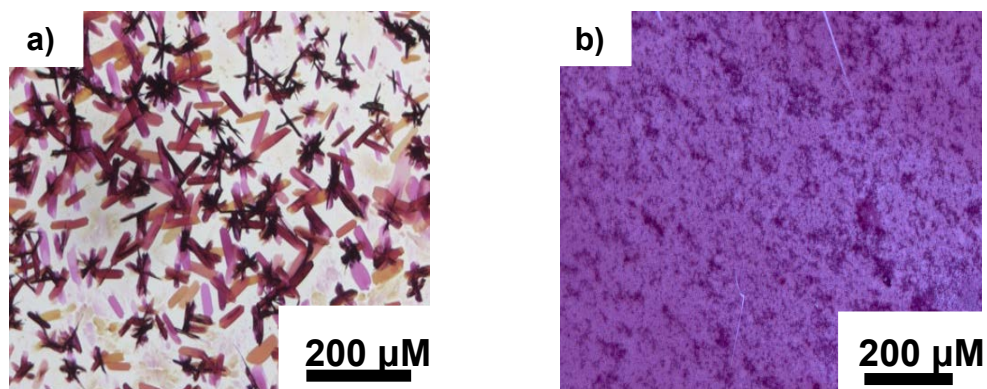
Fig. C23: Polarized optical microscope image of (a) mDPP film and (b) PDI under 200 x magnification.
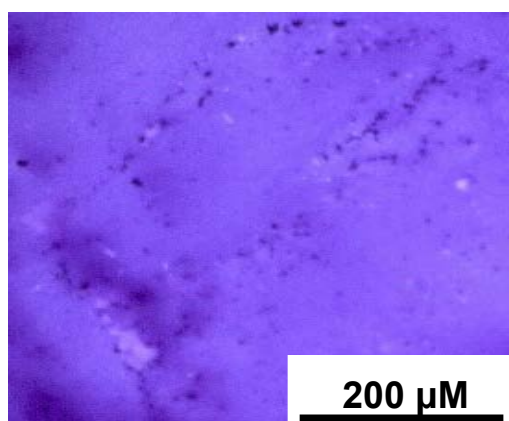
Fig. C24: Polarized optical microscope image of mixture film under 200 x magnification.

SPECTROELECTROCHEMISTRY

Spectroelectrochemistry was performed to determine the spectral signatures of the cations and anions of the mDPP and PDI, respectively. Spectroelectrochemistry was performed on the individual monomers. Each compound was drop cast onto an ITO working electrode. Conductive copper tape was applied directly on to the ITO. The ITO slide was then submerged in a 100 mM aqueous solution of KNO_4 supporting electrolyte with a Pt counter electrode and a Ag wire quasi reference electrode. The PDI molecule was reduced at a potential of −0.8 V vs. Ag wire. The mDPP molecule was oxidized at 0.6 V vs. Ag wire.
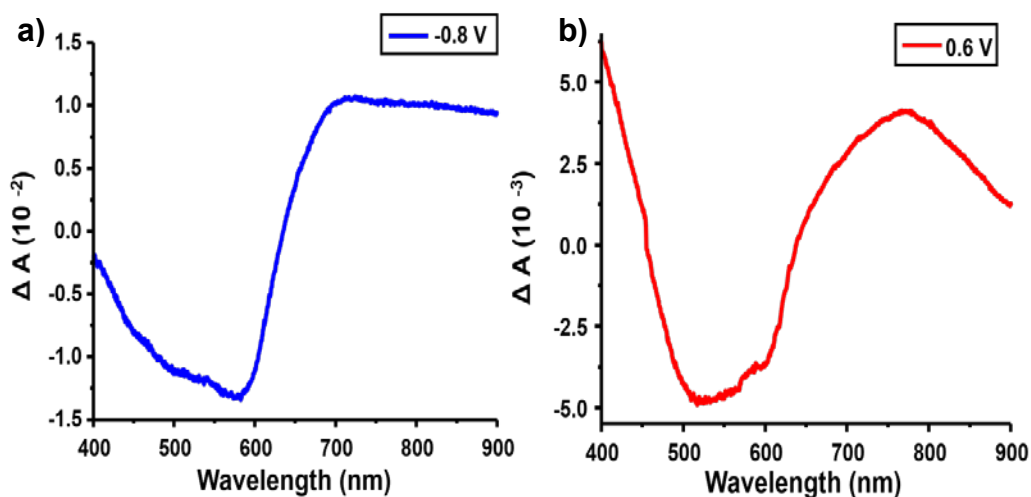
Fig. C25: Differential absorption spectra upon electrochemical reduction of PDI (a) and oxidation of mDPP (b) films.

TRANSIENT ABSORPTION SPECTROSCOPY

Optical transient absorption (TA) measurements were performed with an apparatus based on a commercial amplified Ti:sapphire laser system (Spectra-Physics Mai Tai Oscillator (80MHz) and 5W Spitfire Ace Amplifier pumped by a 527 nm Nd:YLF Empower laser) operating at 1 kHz and pumps an optical parametric amplifier (OPA, Spectra Physics, Topas) to produce excitation pulses at 500 and 625 nm. The power was varied from 160 nJ/pulse to 640 nJ/pulse at a pump diameter of 0.6 mm resulting in energy densities of 1.4×10^{-5} to 5.8×10^{-5} J/cm^2 on neat films. The data was collected through a Helios/EOS spectrometer (Ultrafast Systems), where the probe is delayed relative to the pump on a mechanical delay line. The pump beam is chopped at half the repetition rate of the laser, so that the absorption change (ΔA) can be measured as a function of delay time, where ΔA = -log($I_{\text{pump + probe}}/I_{\text{probe}}$). The data was chirp-corrected using the Ultrafast Systems Surface Xplorer Software over the spectral range in the visible (450 to 800 nm) and near-infrared (800-1200 nm). For the femtosecond transient absorption (fsTA) measurements the widths of the pump and probe pulses were estimated at about 70 fs, for nanosecond transient absorption (nsTA) at 2 ns. The transient absorption changes for a particular probe wavelength as a function of time were analyzed by fitting the kinetics with a multiexponential model convoluted with a Gaussian instrument response function (IRF), using ~70 fs / 2 ns FWHM, where $\Delta A(t) = IRF + (\sum_i^3 A_i e^{-k_i \tau})$.
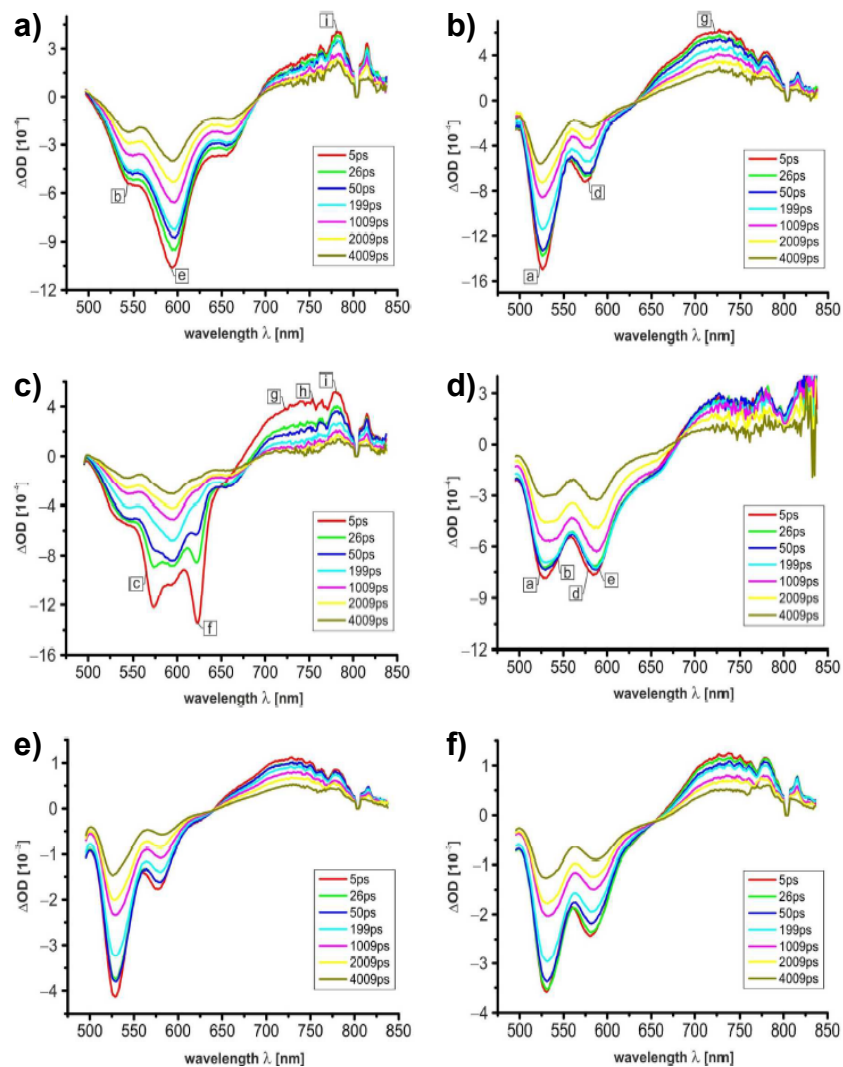
Fig. C26: Transient Absorption spectra of a solution aggregates photoexcited at 485nm: (a) of 0.1 mM DPP in toluene, (b) A solution of 0.05 mM PDI in toluene with 5 % DMSO, (c) A solution of 0.1 mM DPP, and 0.05 mM PDI in toluene, (d) A solution of 0.1 mM DPP, and 0.05 mM PDI in toluene with 5 % DMSO, (e) A solution of 0.05 mM *N,N'*-dicyclohexyl PDI in toluene, and (f) A solution of 0.1 mM DPP, and 0.05 mM *N,N'*-dicyclohexyl PDI in toluene.
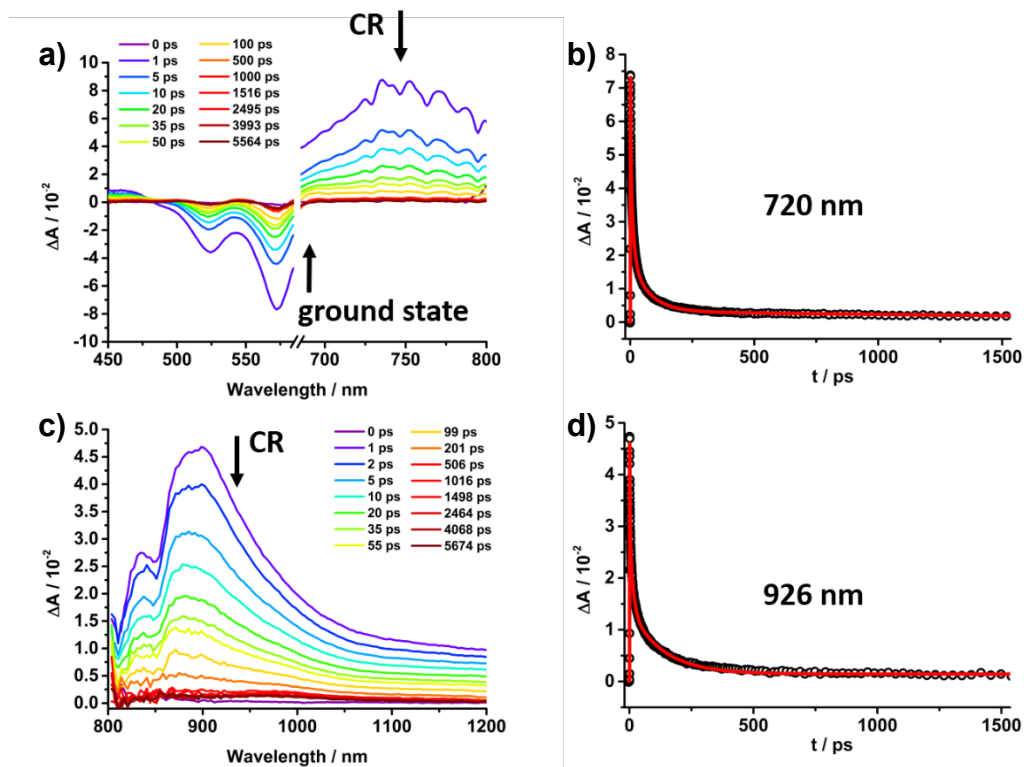
Fig. C27: fsTA spectra in the (a) visible and (c) near-infrared of the 2:1 mDPP:PDI mixture film upon 625 nm photoexcitation (640 nJ/pulse, 5.8×10^{-5} J/cm^2) and corresponding kinetics at (b) 720 and (d) 926 nm, monitoring the charge recombination (CR).
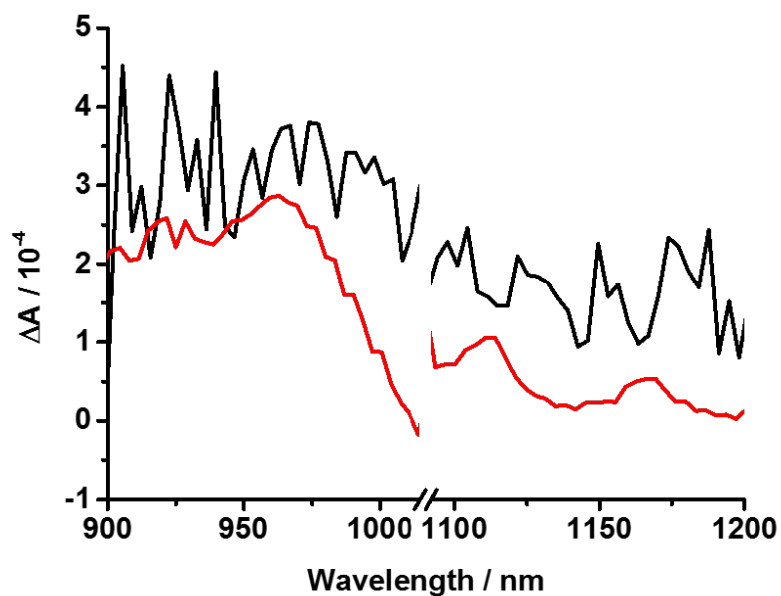
Fig. C28: Black: fsTA spectrum in the near-infrared mDPP film upon 625 nm photoexcitation (640 nJ/pulse, 5.8x10-5 J/cm2) after 4.5 ns. **Red**: nsTA spectrum of the 2:1 mDPP-PDI mixture film upon 500 nm photoexcitation (320 nJ/pulse, 2.9x10-5 J/cm2) that may be long-lived triplet states.

Table C4: Kinetic data obtained from multiwavelength analysis (average over 8-10 wavelengths from 450-1200 nm) of fsTA and nsTA spectra of the three films (mDPP, PDI, mDPP-PDI), where t_{1-3} are the lifetimes and A_{1-3} the corresponding amplitudes. In all cases ground state bleach and excited / CS state deactivation correlate to each other. Note that a fourth lifetime component is observed in all fsTA experiments exceeding the limits of our setup (5.5 ns).

mDPP fsTA						
λ_{ex} = 500 nm	A_1 / %	t_1 / ps	A_2 / %	t_2 / ps	A_3 / %	t_3 / ps
640 nJ / pulse	58	2.1 ± 0.6	25	35 ± 9	17	234 ± 69
160 nJ / pulse	38	3.2 ± 1.1	36	48 ± 19	26	306 ± 138
λ_{ex} = 625 nm	A_1 / %	t_1 / ps	A_2 / %	t_2 / ps	A_3 / %	t_3 / ps
640 nJ / pulse	46	1.2 ± 0.2	33	17 ± 8	21	159 ± 53
160 nJ / pulse	31	3.8 ± 0.8	35	53 ± 24	34	380 ± 104
PDI fsTA						
λ_{ex} = 500 nm	A_1 / %	t_1 / ps	A_2 / %	t_2 / ps	A_3 / %	t_3 / ps
640 nJ / pulse	77	0.8 ± 0.1	17	18 ± 6	6	256 ± 102
160 nJ / pulse	64	1.4 ± 0.5	32	41 ± 19	11	224 ± 107
λ_{ex} = 625 nm	A_1 / %	t_1 / ps	A_2 / %	t_2 / ps	A_3 / %	t_3 / ps
640 nJ / pulse	47	0.7 ± 0.3	33	5 ± 0.5	20	103 ± 57
160 nJ / pulse	41	1 ± 0.8	42	18 ± 14	17	144 ± 64
mDPP-PDI fsTA						
λ_{ex} = 500 nm	A_1 / %	t_1 / ps	A_2 / %	t_2 / ps	A_3 / %	t_3 / ps
640 nJ / pulse	43	2.1 ± 0.3	42	24 ± 6	15	215 ± 56
160 nJ / pulse	34	3.1 ± 0.9	41	33 ± 6	25	243 ± 76
λ_{ex} = 625 nm	A_1 / %	t_1 / ps	A_2 / %	t_2 / ps	A_3 / %	t_3 / ps
640 nJ / pulse	41	1 ± 0	36	13 ± 3	23	116 ± 33
160 nJ / pulse	25	3.4 ± 2.5	56	26 ± 5	19	294 ± 108
mDPP-PDI nsTA						
λ_{ex} = 500 nm	A_1 / %	t_1 / ns	A_2 / %	t_2 / ns	A_3 / %	t_3 / ns
120 nJ/pulse (vis) 320 nJ/pulse (nir)	84	< 1	12	32 ± 16	4	1014 ± 242
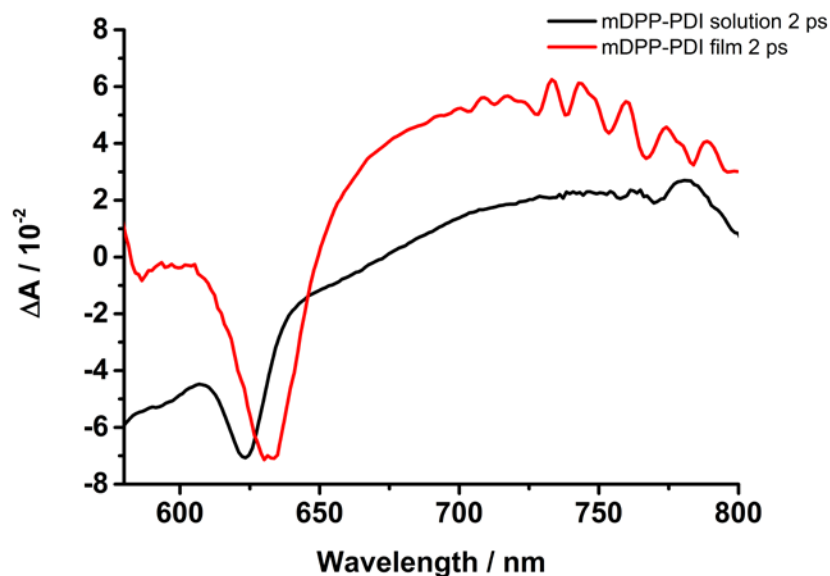
Fig. C28: Black: fsTA spectrum in the visible of the 2:1 mDPP-PDI mixture in toluene solution 2 ps after 485 nm photoexcitation. [34] **Red:** fsTA spectrum in the visble of the 2:1 mDPP-PDI mixture film upon 500 nm photoexcitation (640 nJ/pulse, 5.8×10^{-5} J/cm^2).
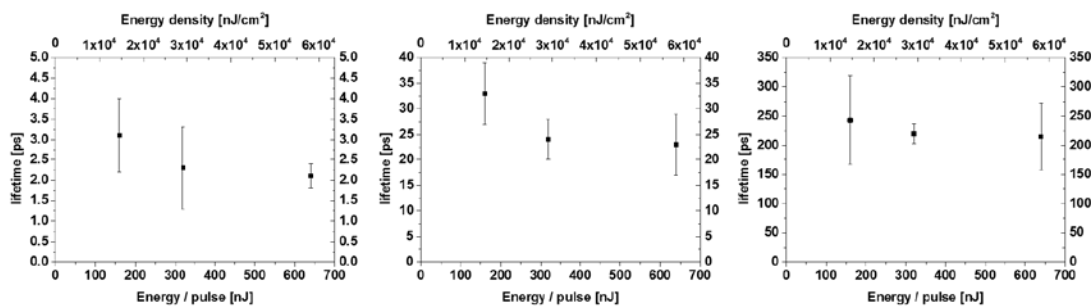
Fig. C29: Pump energy - lifetime dependence for the three observed lifetimes in fsTA experiments upon 500 nm photoexcitation of the 2:1 mDPP-PDI film at three different pump energies (160, 320 and 640 nJ/pulse or 1.4×10^{-5}, 2.9×10^{-5} and 5.8×10^{-5} J/cm^2). Note that similar behavior was observed for all photoexcited samples at both excitation wavelengths (500 and 625 nm)
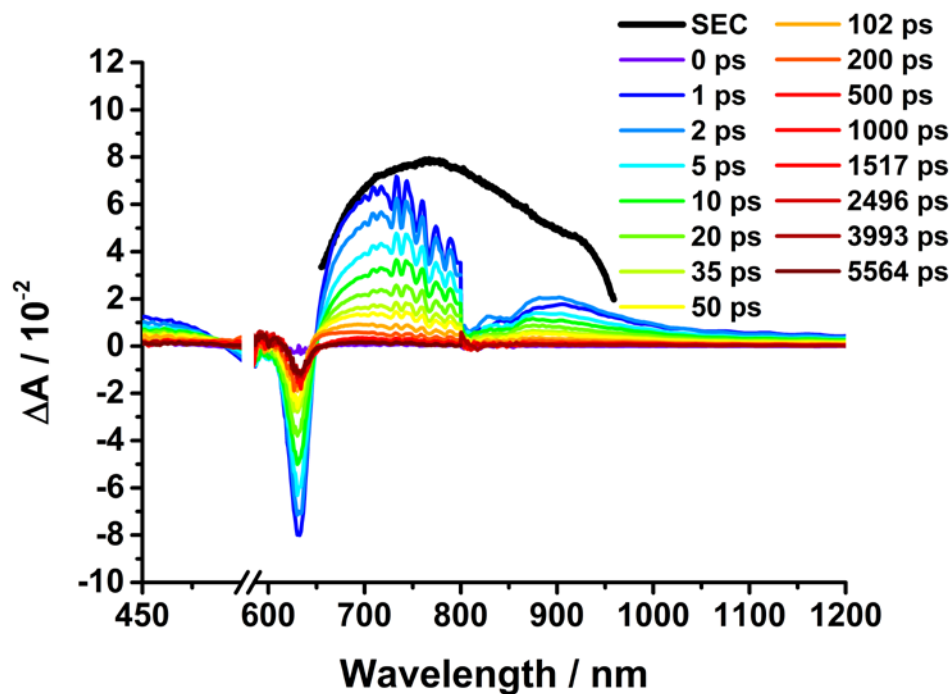
Fig. C30: fsTA spectra of the 2:1 mDPP:PDI film upon 500 nm photoexcitation (640 nJ/pulse, 5.8×10^{-5} J/cm^2) and the sum of the spectroelectrochemical spectra upon oxidation of mDPP and reduction of PDI (black).
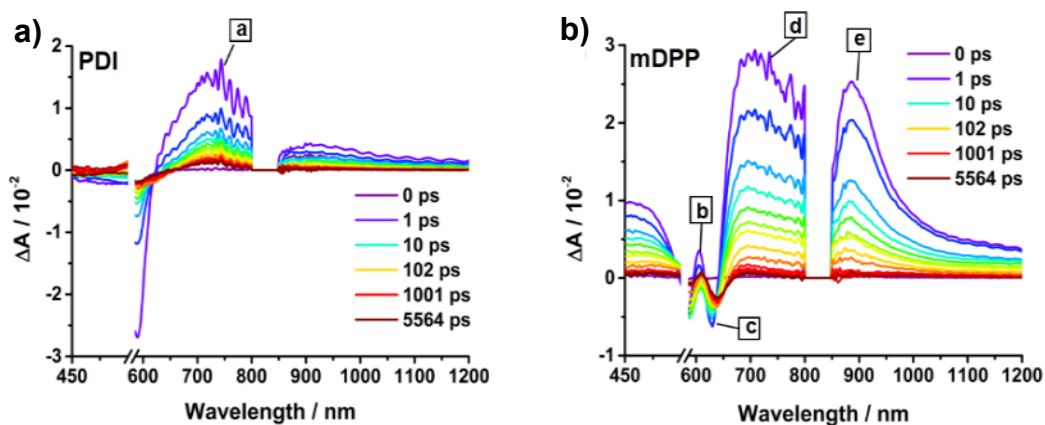
Fig. C31: fsTA spectra of a) air-free PDI film and b) air-free mDPP film following ~70 fs excitation at 500 nm.
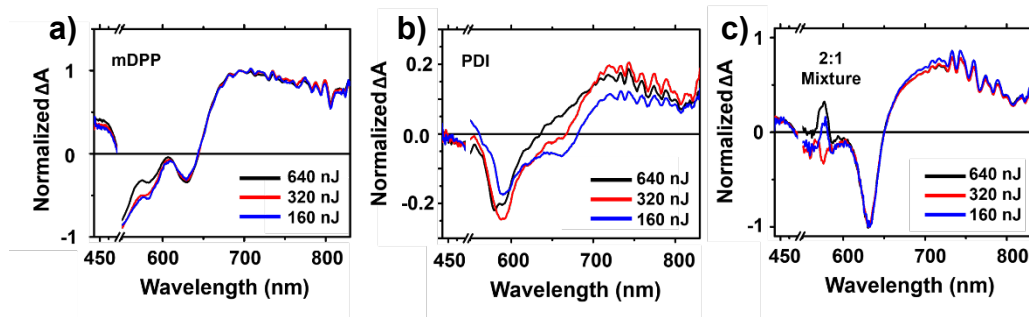
Fig. C32: Pump power dependent fsTA spectra for a) mDPP film, normalized at 695 nm b) PDI film, normalized 525 nm and c) 2:1 mDPP:PDI mixture film, normalized at 630 nm. All the spectra are at 5 ps after 500 nm photoexcitation.

Table C5: Table representing the number of photons per area (cm^2) for 500 nm excitation pulse

power (nJ/pulse)	Fluence (Joules/cm^2)	Fluence (photons/cm^2)
160	14×10^{-6}	3.52×10^{13}
320	29×10^{-6}	7.30×10^{13}
640	58×10^{-6}	1.46×10^{14}

APPENDIX D
CHAPTER 5

GENERAL METHODS

Chromatography purifications were performed using Sorbent Technologies Silica Gel (60 Å, 65 x 250 mesh). Thin-layer chromatography (TLC) was carried out using aluminum sheets precoated with silica gel 60 (EMD 40−60 mm, 230−400 mesh with 254 nm dye). TLC plates were visualized by UV-light. All reactions were carried out under an inert atmosphere of Ar using standard Schlenk techniques unless otherwise noted. NMR spectra were obtained on a Bruker Ultrashield 500 MHz spectrometer. All chemical shifts are reported in δ units using the solvent residual signal as an internal standard and the coupling constant values (J) are reported in Hertz (Hz). The following abbreviations are used for signal multiplicities: s, singlet; d, doublet; t, triplet; q, quartet; quintet (qui); sextet (sex); m, multiplet; and br, broad. Mass spectroscopy were done on a Bruker micrOTOF-Q II.

X-RAY CRYSTALLOGRAPHY

Red single crystals of **5** suitable for x-ray diffraction analyses were obtained by evaporation from a methylene chloride solution. The crystals of **5** were glued onto the end of a thin glass fiber. X-ray intensity data were measured with a Bruker SMART APEX2 CCD-based diffractometer using Mo Kα radiation (λ = 0.71073 Å).[276] The raw data frames were integrated with the SAINT+ program by using a narrow-frame integration algorithm.[276] Corrections for Lorentz and polarization effects were also applied with SAINT+. An empirical absorption correction based on the multiple measurement of equivalent reflections was applied using the program SADABS. The structure was solved by a

combination of direct methods and difference Fourier syntheses, and refined by full-matrix least-squares on F^2, by using the SHELXTL software package[277-278]. All non-hydrogen atoms were refined with anisotropic displacement parameters unless otherwise stated. Hydrogen atoms were placed in geometrically idealized positions and included as standard riding atoms during the least-squares refinements. Crystal data, data collection parameters, and results of the analyses are listed in Table D1.
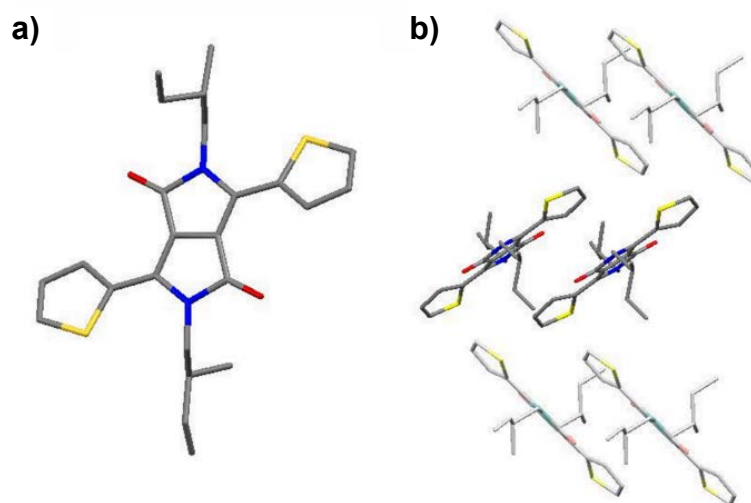
Fig. D1: a) Structure of **5**, and b) crystal packing arrangement of 3.

Table D1. Crystallographic data for **5**

	5
Empirical formula	$C_{24}H_{28}N_2O_2S_2$
Formula weight	440.64
Crystal system	Monoclinic
Lattice parameters	
a (Å)	13.1491(8)
b (Å)	5.6799(3)
c (Å)	16.1842(9)
α (°)	90
β (°)	106.064(1)
γ (°)	90
V (Å^3)	1161.53(11)
Space group	$P2_1$ (# 4)
Z value	2
ρ_{calc} (g / cm^3)	1.260
μ (Mo Kα) (mm^{-1})	0.252
Temperature (K)	296
$2\Theta_{max}$ (°)	56.0
No. Obs. ($I > 2\sigma(I)$)	4035
No. Parameters	274
Goodness of fit	1.020
Max. shift in cycle	0.001
Residuals*:R1; wR2	0.0482; 0.1338
Absorption Correction, Max/min	Multi-scan 0.9704/0.9104
Absolute structure Flack parameter	-0.08(10)
Largest peak in Final Diff. Map (e$^-$ / Å^3)	0.289

$*R = \Sigma_{hkl}(||F_{obs}|-|F_{calc}||)/\Sigma_{hkl}|F_{obs}|$; $R_w = [\Sigma_{hkl}w(|F_{obs}|-|F_{calc}|)^2/\Sigma_{hkl}wF_{obs}^2]^{1/2}$, $w = 1/\sigma^2(F_{obs})$; GOF $= [\Sigma_{hkl}w(|F_{obs}|-|F_{calc}|)^2/(n_{data}-n_{vari})]^{1/2}$.
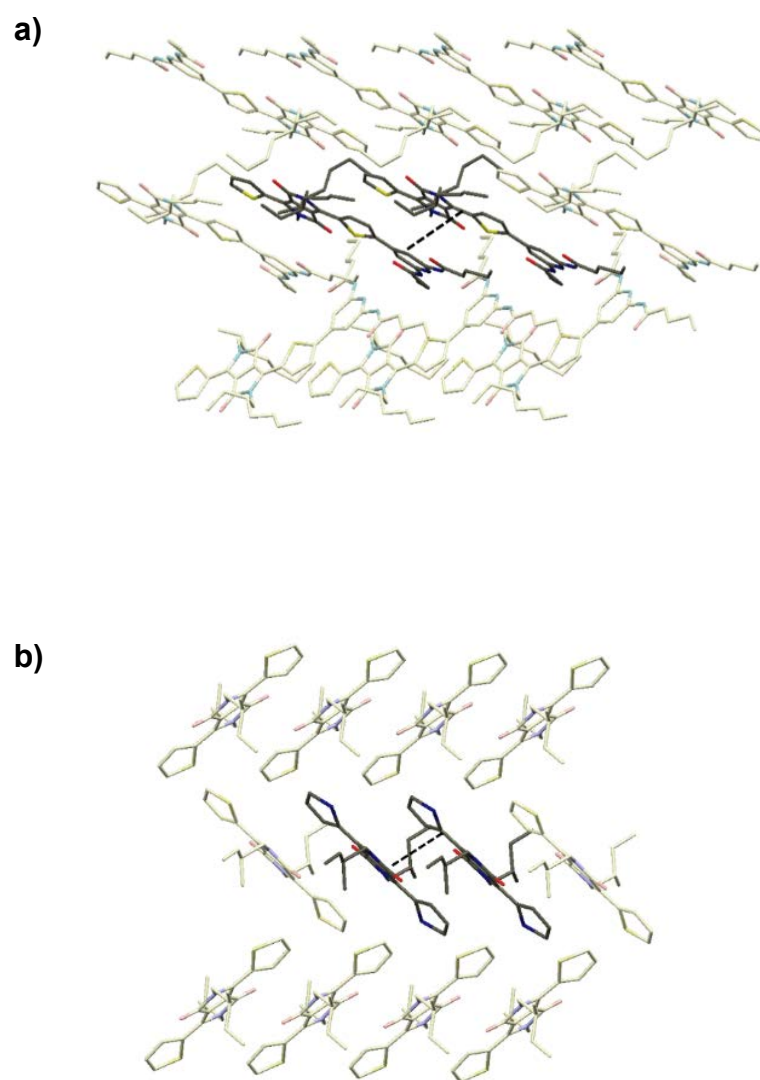
Fig. D2: a) Crystal structure of **2** with dashed line representing 3.427 Å, and b) crystal structure of **2** with dashed line representing 3.659 Å.

VARIABLE TEMPERATURE UV-VIS AND CIRCULAR DICHROISM SPECTROSCOPY

DPP derivatives were weighed with a Mettler Toledo ML analytical balance and dissolved in spectrophotometric grade distilled toluene unless stated otherwise. Each solution was diluted from a 100 µM stock solution using a Rainin displacement micropipette. Solutions were placed in Starna 1 cm quartz cells, and spectra were taken in a Shimadzu UV-1800 spectrophotometer equipped with a Fischer Scientific R20 Heated Bath, and temperatures were calibrated for toluene solutions using an external thermocouple. Spectra for each DPP derivative and each concentration were measured at 5 $^{\circ}$C intervals between 10 $^{\circ}$C and 85 $^{\circ}$C, using a 3 min equilibration time after the target temperature had been reached. Circular dichroism (CD) spectroscopy was performed on a Jasco-810 Spectropolarimeter, and VT studies were conducted with a Jasco PTC-423S Peltier Cell Holder. Spectra were normalized by subtracting the raw baseline values from non-absorbing wavelengths (750 – 800nm) from the entire spectrum. Absorbance values used for fitting were calculated as mean absorbance from 330 – 380 nm and 500 – 600 nm for **1** and **2**; wavelengths are 330 – 380 nm and 470 – 570 nm for **5**, **6**, and **7**. The model surfaces in **Fig. D5** were generated with the collected spectra as templates, which were then multiplicatively increased or decreased to match the template mean absorbance to the mean absorbance predicted by the numerical fit.
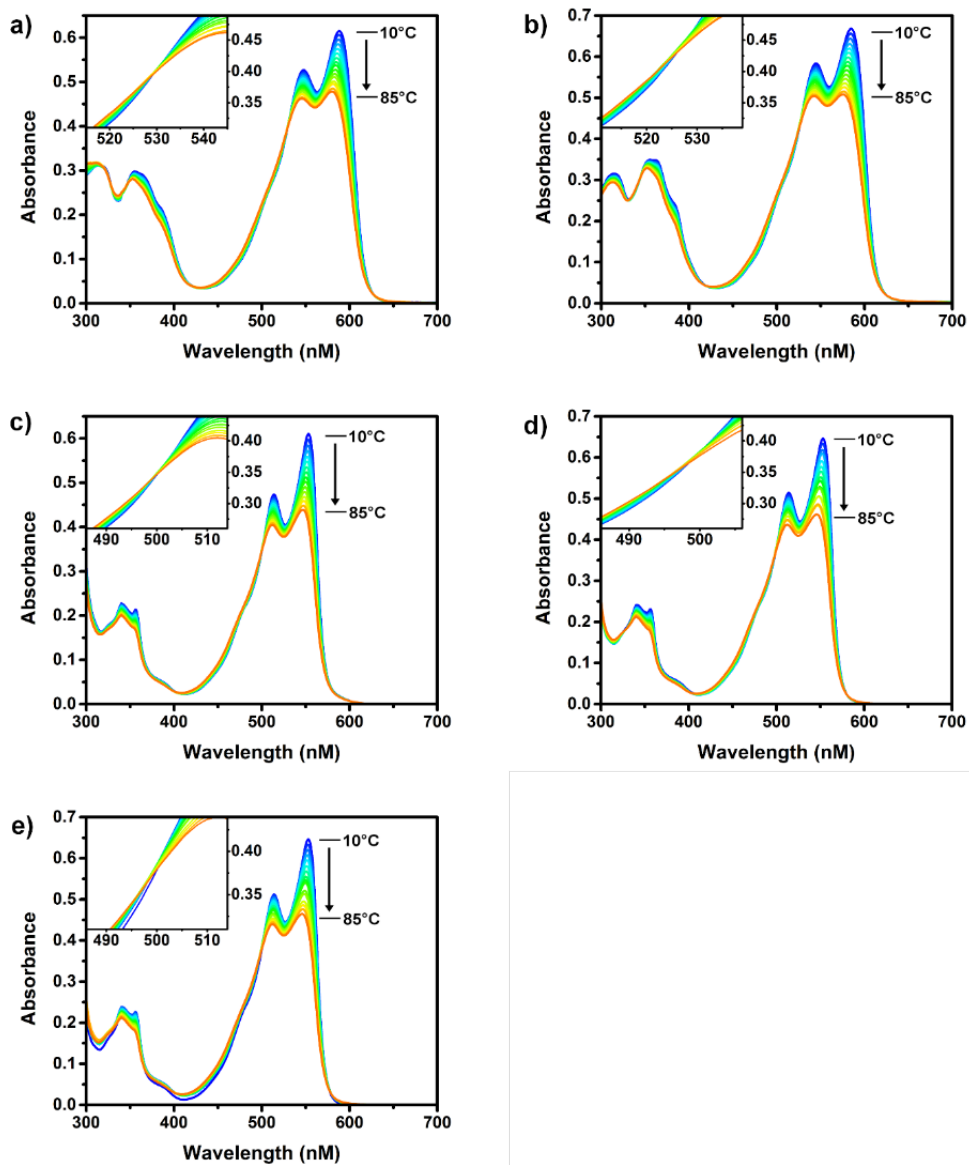
Fig. D3: a) UV-Vis spectra at 20 μM in toluene for compounds **1**, b) **2**, c) **5**, d) **6**, and e) **7**. Isosbestic points are displayed in insets.
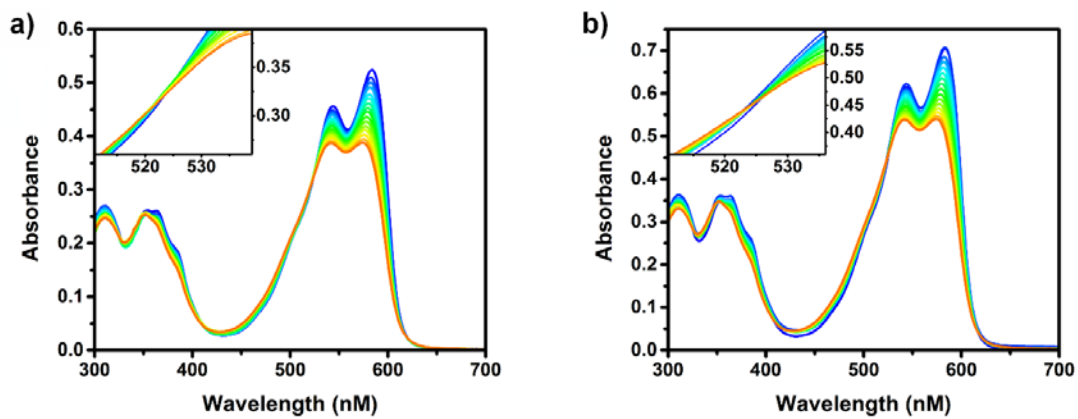
Fig D4: a) UV-Vis spectra of **1** and b) **2** in toluene and 1% DMSO at 20 μM. Isosbestic points are displayed in insets.
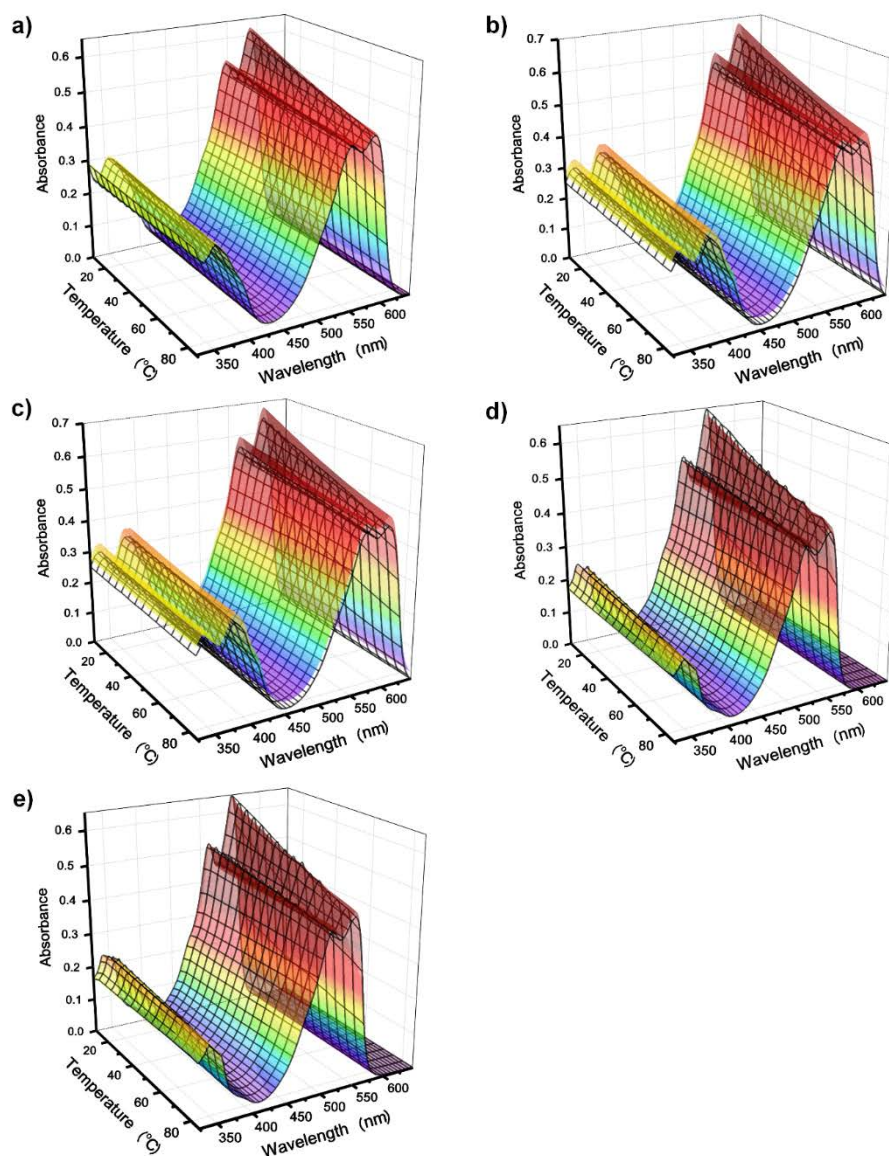
Fig D5: a) UV-Vis data at 20 μM in toluene for compounds **1**, b) **2**, c) **5**, d) **6**, and e) **7**. The raw data is presented as a mesh and the model fit to those spectra is presented as a colored surface.
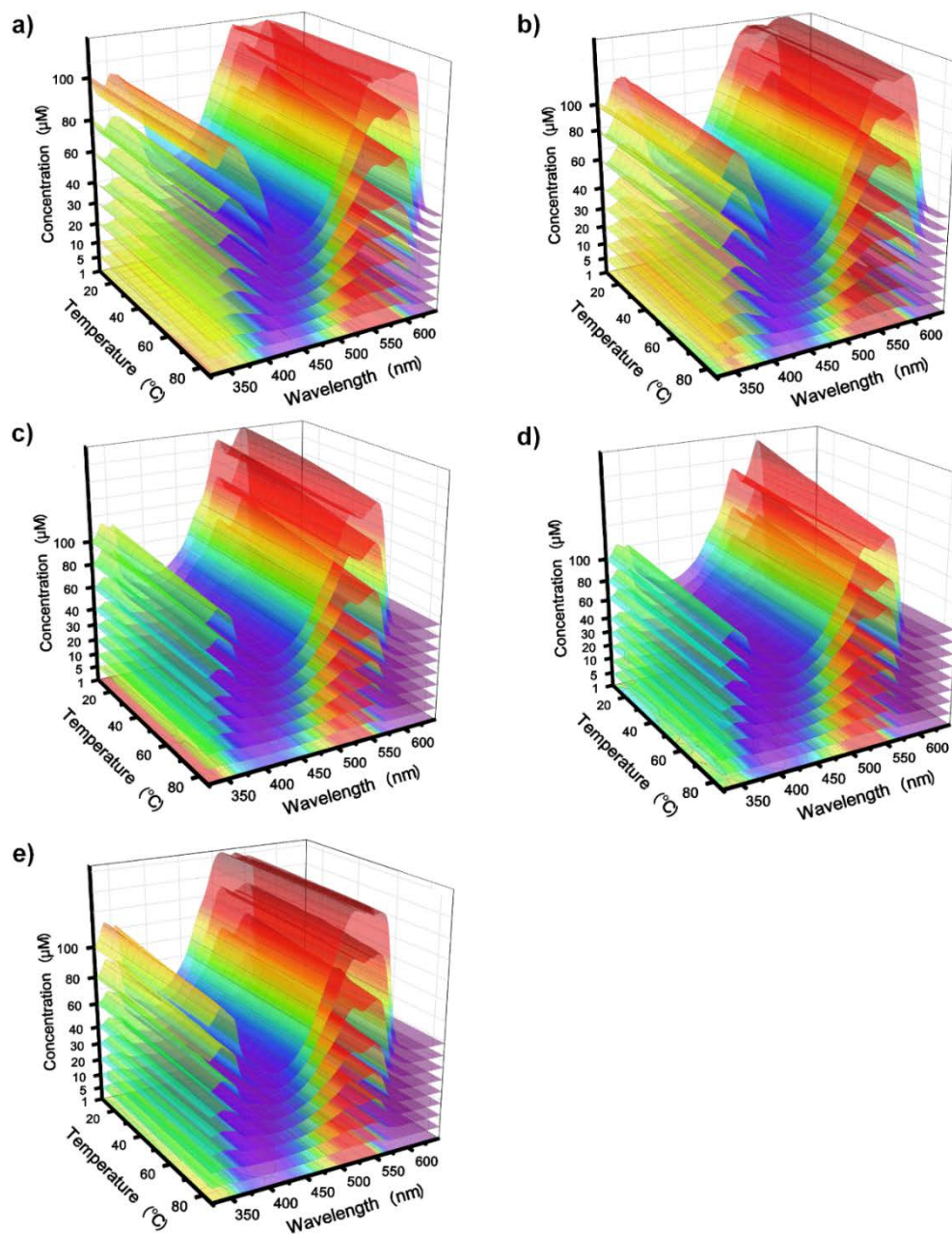
Fig D6: a) VT and variable concentration UV-Vis data as hypersurfaces for compounds **1**, b) **2**, c) **5**, d) **6**, and e) **7** in toluene. Spectra surfaces are offset on the concentration axis to separate layers.
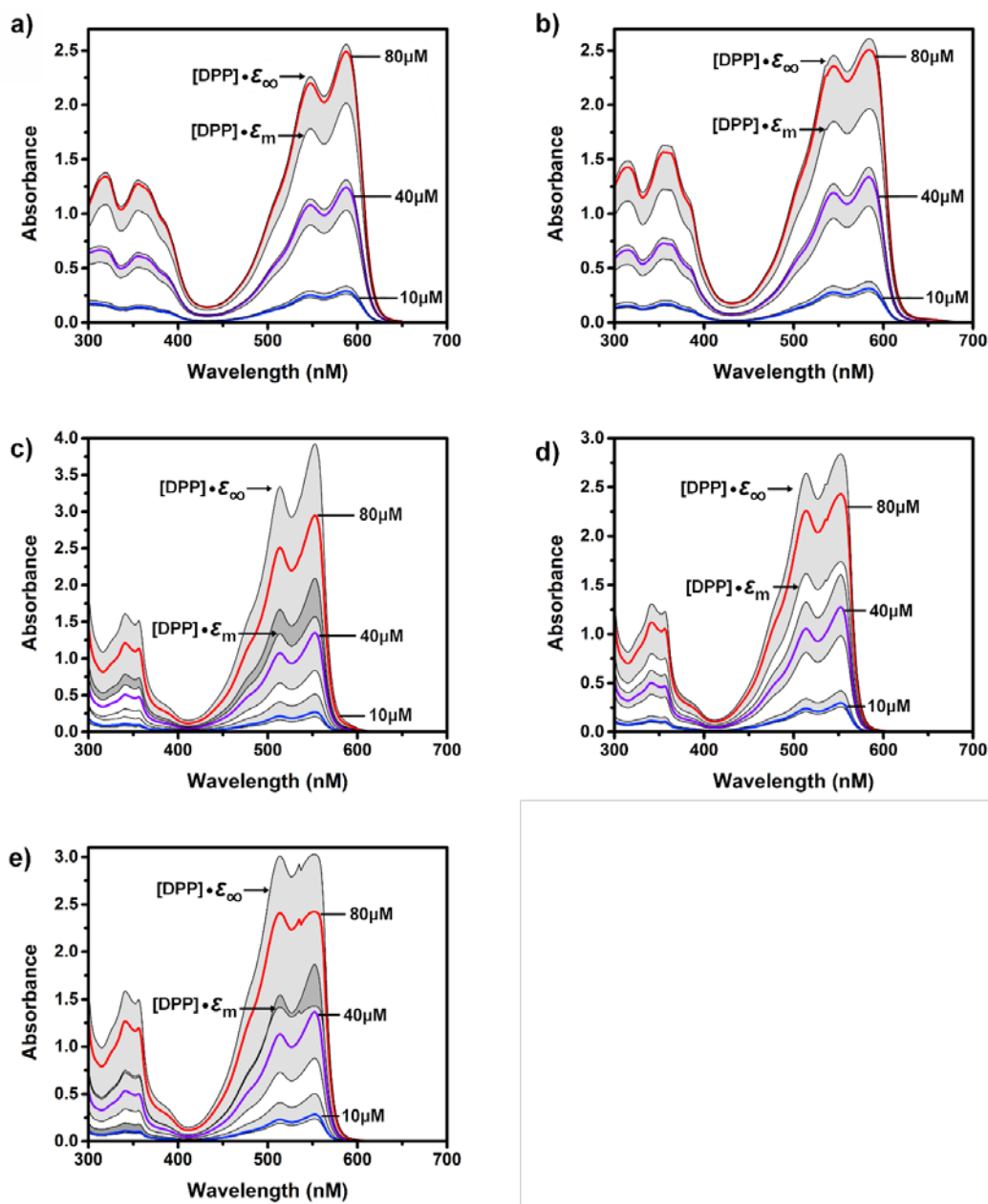
Fig D7: a) UV-Vis spectra for compounds **1**, b) **2**, c) **5**, d) **6**, and e) **7**. Absorbance spectra at DPP derivatives at 20 °C in toluene displayed between the calculated spectrum of a fully polymerized ([DPP] $\cdot$ ε_∞) and a fully monomerized ([DPP] $\cdot$ ε_m) solution. [DPP] is the total concentration of DPP and ε is the extinction coefficient.
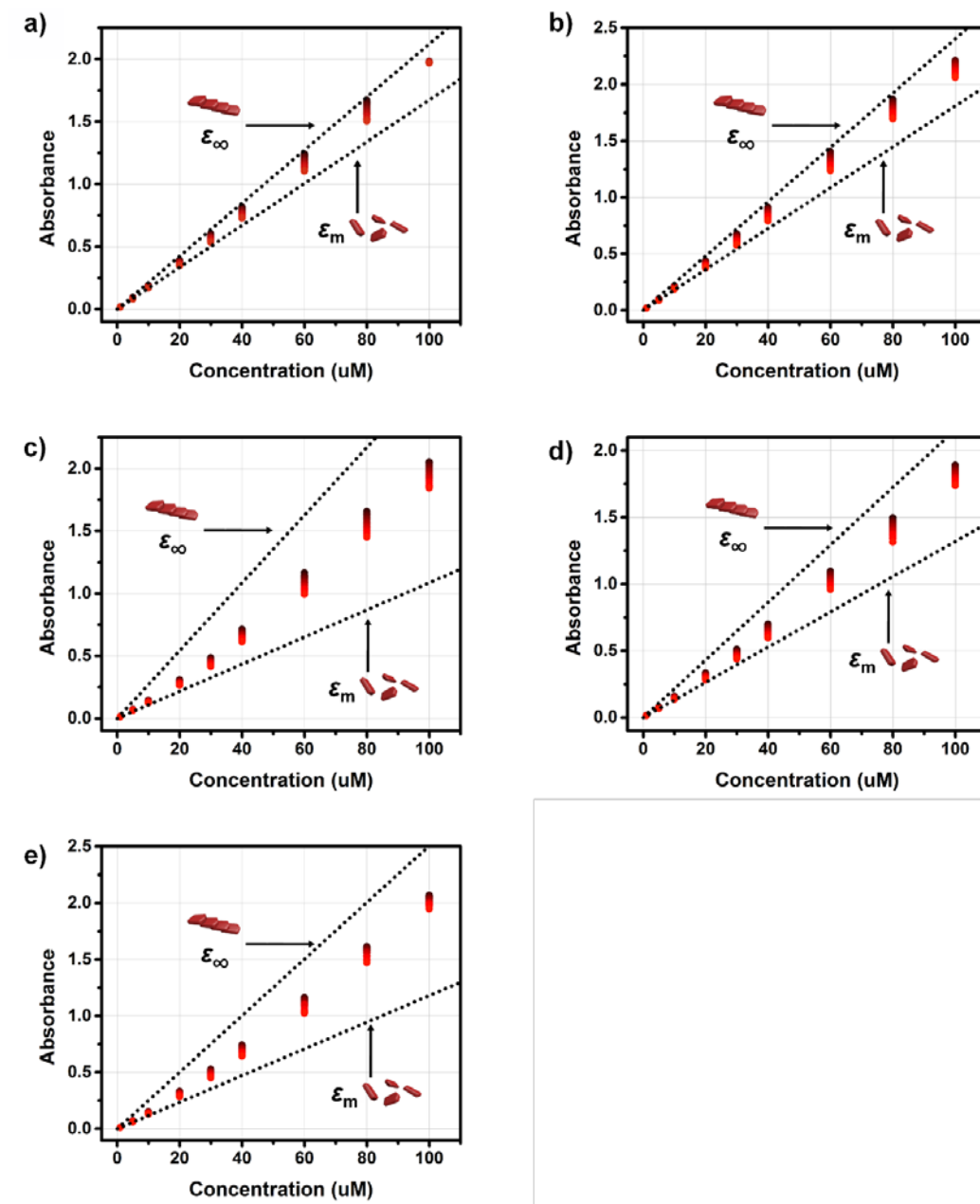
Fig. D8: a) Modified Beer's Law plots for compounds **1**, b) **2**, c) **5**, d) **6**, and e) **7**. Plots display collected absorbance values as points and the extinction coefficient of polymer (ε_∞) and monomer (ε_m) of DPP derivatives in toluene.
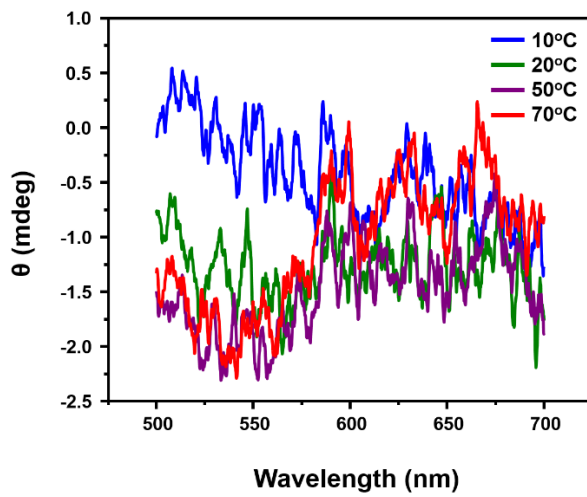
Fig. D9: The VT CD spectra of **5** (100 μM).
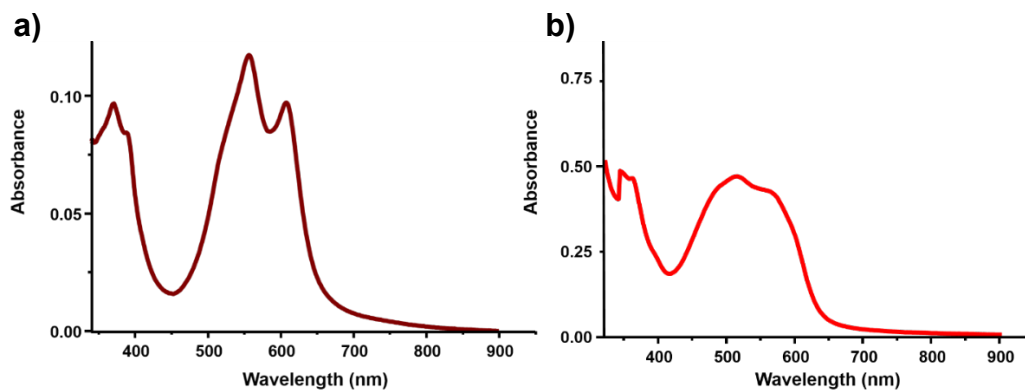
Fig. D10: a) The solid state UV-VIS of **2** and b) **5** with peak ratios (A_{548}/A_{586}) of 1.21 and 1.06 respectively.

SPECTROSCOPIC DETERMINATION OF THERMODYNAMICS PARAMETERS

To determine thermodynamic binding parameters (ΔG°, ΔH, ΔS, K) for the aggregation of DPP into clusters, a modified isodesmic model[279] was applied to the spectroscopic data using Microsoft Excel[TM] 2010. Variable concentration and VT spectral data were imported, and the General Reduced Gradient (GRG) solver algorithm was used to minimize the weighted Square Sum Residual (wSSR) between the model and the data to provide the thermodynamic binding parameters. The isodesmic model used to quantify thermodynamic binding parameters is described in detail below:

Isodesmic Model

Eq. S1
$$K = \frac{[(\text{DPP})_{n+1}]}{[(\text{DPP})_n][\text{DPP}]}$$

Assumes that aggregation energies are equivalent regardless of stack size.

$$A = \varepsilon_\infty \left(\text{(image)} \right) + \varepsilon_m \left(\text{(image)} \right)$$

Assumes that extinction coefficients of polymers are equivalent regardless of stack size.

Eq. S2
$$[\text{DPP}]_t = [\text{DPP}] \sum_{n=1}^{\infty} n(K[\text{DPP}])^{n-1}$$

Total concentration of mDPP is quantified as a infinite series of its stacks, accounting for each stack size and the probability of each stack size existing.

Eq. S3
$$[\text{DPP}]_t = \frac{[\text{DPP}]}{(1 - K[\text{DPP}])^2}$$

The series rewritten as a function of the concentration of mDPP monomer.

Eq. S4
$$[\text{DPP}] = \frac{\left(2K[\text{DPP}]_t + 1 - \sqrt{4K[\text{DPP}]_t + 1}\right)}{2K^2[\text{DPP}]_t}$$

The series solution can be solved for the concentration of mDPP monomer.

Eq. S5
$$A = \varepsilon_\infty \left([\text{DPP}]_t - \frac{\left(2K[\text{DPP}]_t + 1 - \sqrt{4K[\text{DPP}]_t + 1}\right)}{2K^2[\text{DPP}]_t}\right) + \varepsilon_m \left(\frac{2K[\text{DPP}]_t + 1 - \sqrt{4K[\text{DPP}]_t + 1}}{2K^2[\text{DPP}]_t}\right)$$

Substituting for the concentration of stacked and monomer mDPP models the expected absorbance resulting from both species.

Model Equation

Eq. S6
$$A = \varepsilon_\infty \left([\text{DPP}]_t - \frac{\left(2K[\text{DPP}]_t + 1 - \sqrt{4K[\text{DPP}]_t + 1}\right)}{2K^2[\text{DPP}]_t}\right) + \varepsilon_m \left(\frac{2K[\text{DPP}]_t + 1 - \sqrt{4K[\text{DPP}]_t + 1}}{2K^2[\text{DPP}]_t}\right)$$

Eq. S7
$$K = e^{-\frac{dH}{R(T)} + \frac{dS}{R}}$$

Fitting parameters:
$$\left\{ \begin{array}{l} \varepsilon_\infty = \text{aggregated extinction coefficient} \\ \varepsilon_m = \text{monomer extinction coefficient} \\ dH = \text{enthalpy of aggregation} \\ dS = \text{entropy of aggregation} \end{array} \right\}$$

Eq. S6 derived below is used to provide a framework for Excel fitting. Based on given temperature and concentration conditions as well as the fitting parameters, the model can calculate the predicted absorbance of a solution.

Eq. S8 ## Weighted SSR
$$\text{wSSR} = \sum_i \frac{(A_i^{\text{exp}} - A_i^{\text{calc}})^2}{A_i^{\text{exp}}}$$

Fits were performed by systematically varying ΔH, ΔS, ε_∞, and ε_m using the GRG algorithm and minimizing the wSSR between the UV-Vis experimental data and the model.
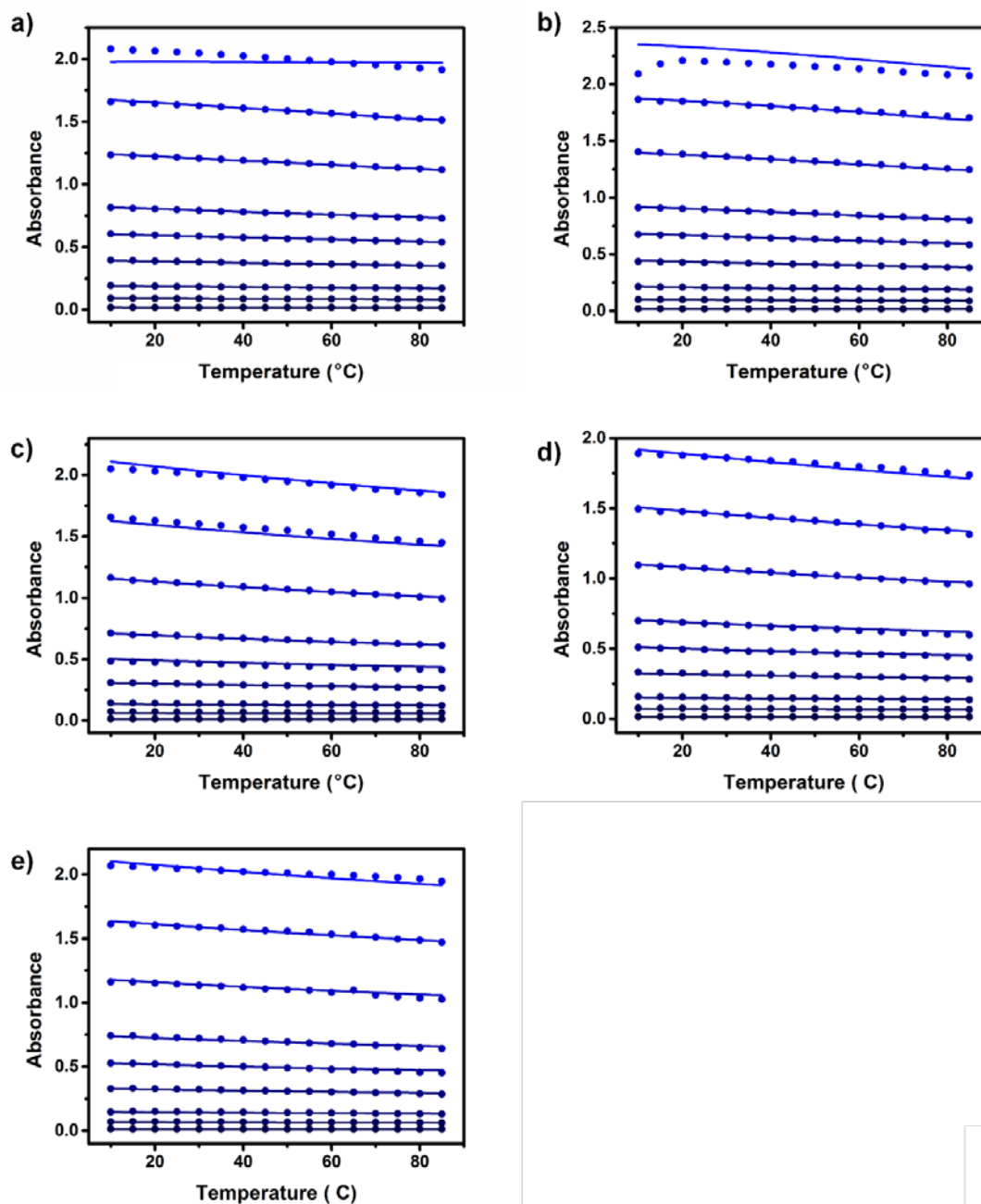
Fig. D11: a) Scatterplot showing all collected mean absorbance of compounds **1**, b) **2**, c) **5**, d) **6**, and e) **7**, at selected concentrations in toluene (1 μM to 100 μM) and varied temperatures as points. Model fittings are also shown as lines and are color matched to data points. Absorbance is calculated as mean absorbance from 330 – 380 nm and 500 – 600 nm for **1** and **2**; wavelengths are 330 – 380 nm and 470 – 570 nm for **5**, **6**, and **7** in order to match peak wavelengths.
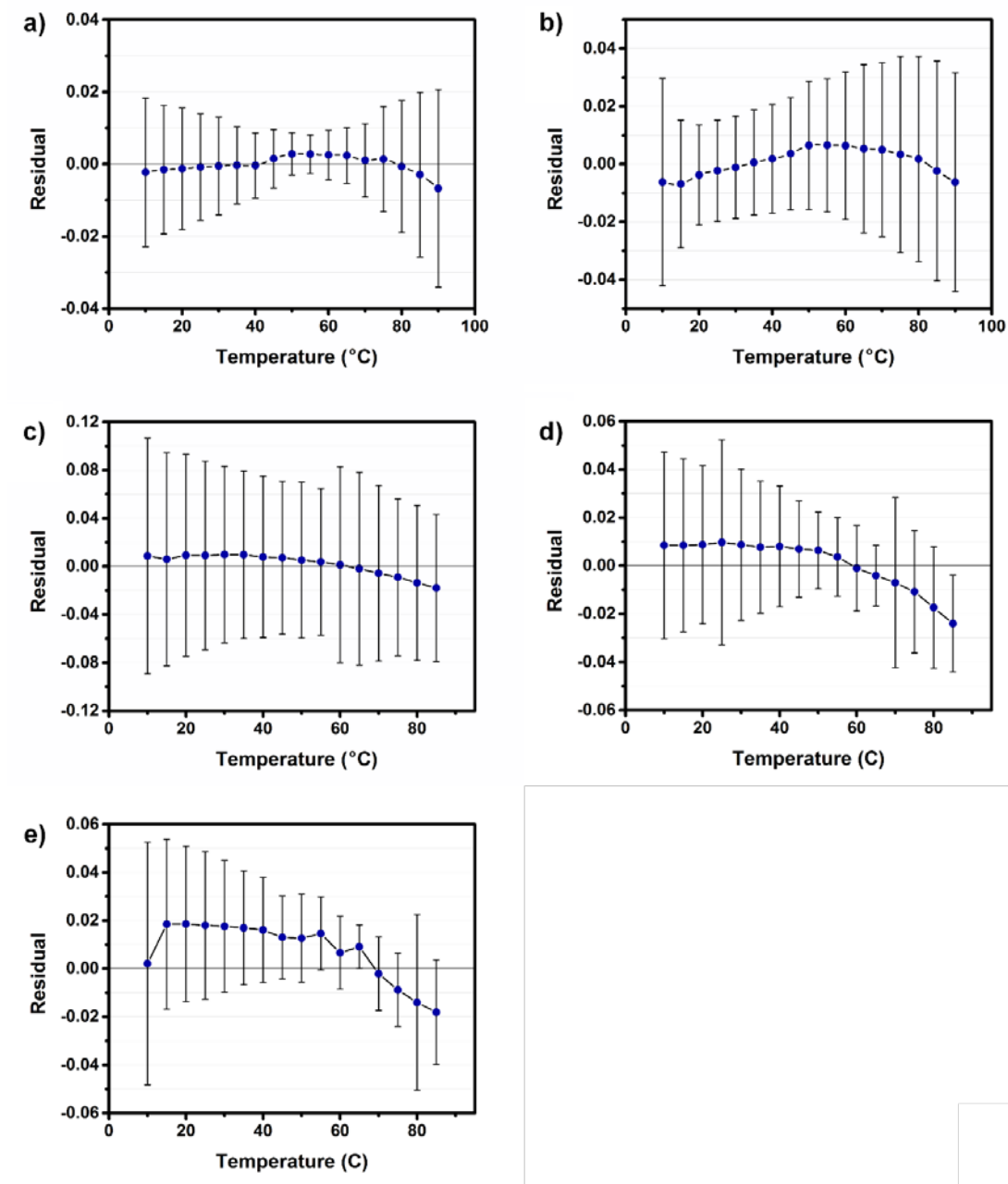
Fig. D12: a) Residual plots for compounds **1**, b) **2**, c) **5**, d) **6**, and e) **7**. Plots show the mean wSSR between model fitting and absorbance data for species at all collected concentrations. Error is displayed as one standard deviation from the mean of the weighted residuals
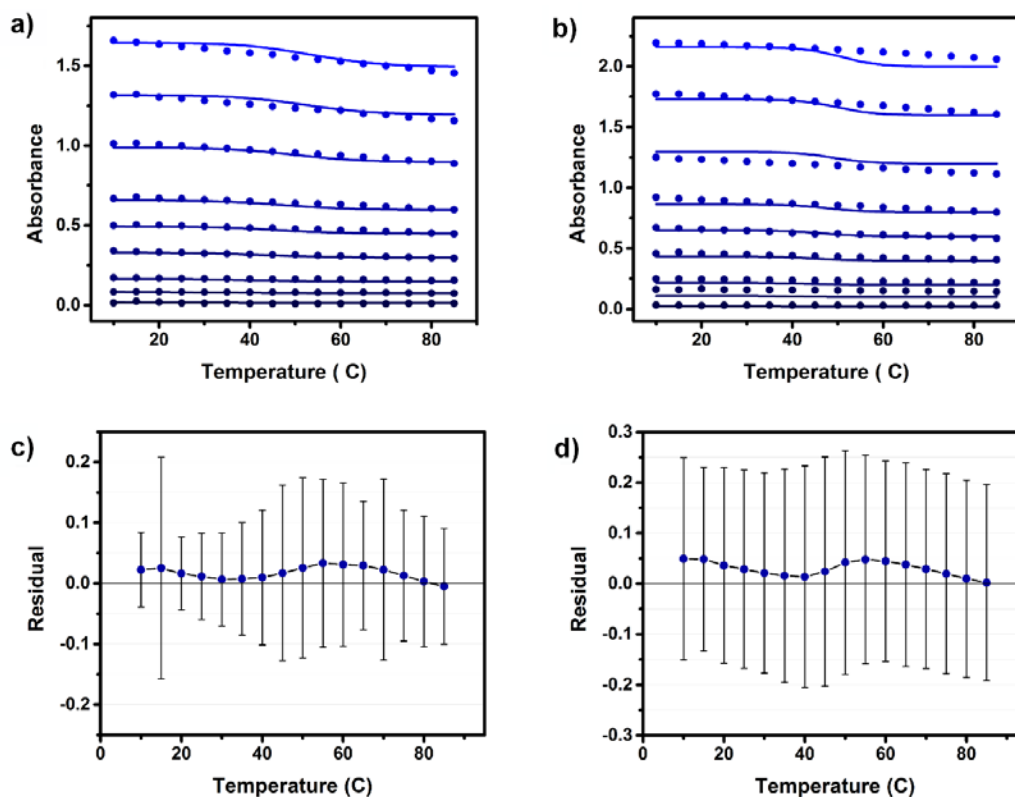
Fig. D13: a) Scatterplot showing all collected mean absorbance of compounds **1** and b) **2** at selected concentrations in toluene and 1% DMSO (1 μM to 100 μM) and varied temperatures as points. Model fittings are also shown as lines and are color matched to data points. Absorbance is calculated as mean absorbance from 330 – 380 nm and 500 – 600 nm. c) Residual plots for compounds **1** and d) **2**, showing the mean wSSR between model fitting and absorbance data for species at all collected concentrations. Error is displayed as one standard deviation from the mean of the weighted residuals. The wSSRs plotted in c) and d) are significantly larger than those of the same compounds in absence of DMSO.

MEAN AGGREGATE SIZE AND MOLE FRACTION

From the determined thermodynamic parameters, the stack size distribution of each compound can be found. The derivation for equations describing mean stack size, $\dot{n}$, and mole fraction, X_n, are described below:

Based on the total concentration of DPP, $[DPP]_t$, relative to the concentration of monomer, $[DPP]$[279],

$$[DPP]_t = [DPP] \sum_{n=1}^{\infty} n(K[DPP])^{n-1} \qquad \textbf{Eq. S9}$$

The concentration of monomers included in a stack size, n, is shown as Eq. S10

$$([DPP])_n = nK^{n-1}[DPP]^n \qquad \textbf{Eq. S10}$$

Dividing by total concentration of DPP gives the mole fraction of a polymer with size n,

$$X_n = nK^{n-1}[DPP]^n/[DPP]_t \qquad \textbf{Eq. S11}$$

And substituting for the concentration of monomer[279] provides Eq. S12

$$X_n = nK^{n-1} \left(\frac{2K[DPP]_t + 1 - \sqrt{2K[DPP]_t + 1}}{2K^2[DPP]_t} \right)^n / [DPP]_t \qquad \textbf{Eq. S12}$$

The concentration of all stacks of size n ($n > 0$), $[DPP]_n$, can be quantified in the following series.

$$[DPP]_n = \sum_{n=1}^{\infty} K^{n-1}[DPP]^n \qquad \textbf{Eq. S13}$$

This series is simplified to a geometric series,

$$[DPP]_n = [DPP] \sum_{n=0}^{\infty} (K[DPP])^n \qquad \textbf{Eq. S14}$$

Which has the following solution for the concentration of polymers of size n.

$$[DPP]_n = [DPP]/1 - K[DPP] \qquad \textbf{Eq. S15}$$

The measurement of average stack size $\dot{n}$ is as shown below.

$$\dot{n} = [DPP]_t/[DPP]_n \qquad \textbf{Eq. S16}$$

Substituting for $[DPP]_t$, $[DPP]_n$, and subsequently substituting for $[DPP]$ gives Eq. S17.

$$\dot{n} = \frac{2K^2[DPP]_t^2}{2K^2[DPP]_t + 1 - \sqrt{4K[DPP]_t + 1}} - K[DPP]_t \qquad \textbf{Eq. S17}$$
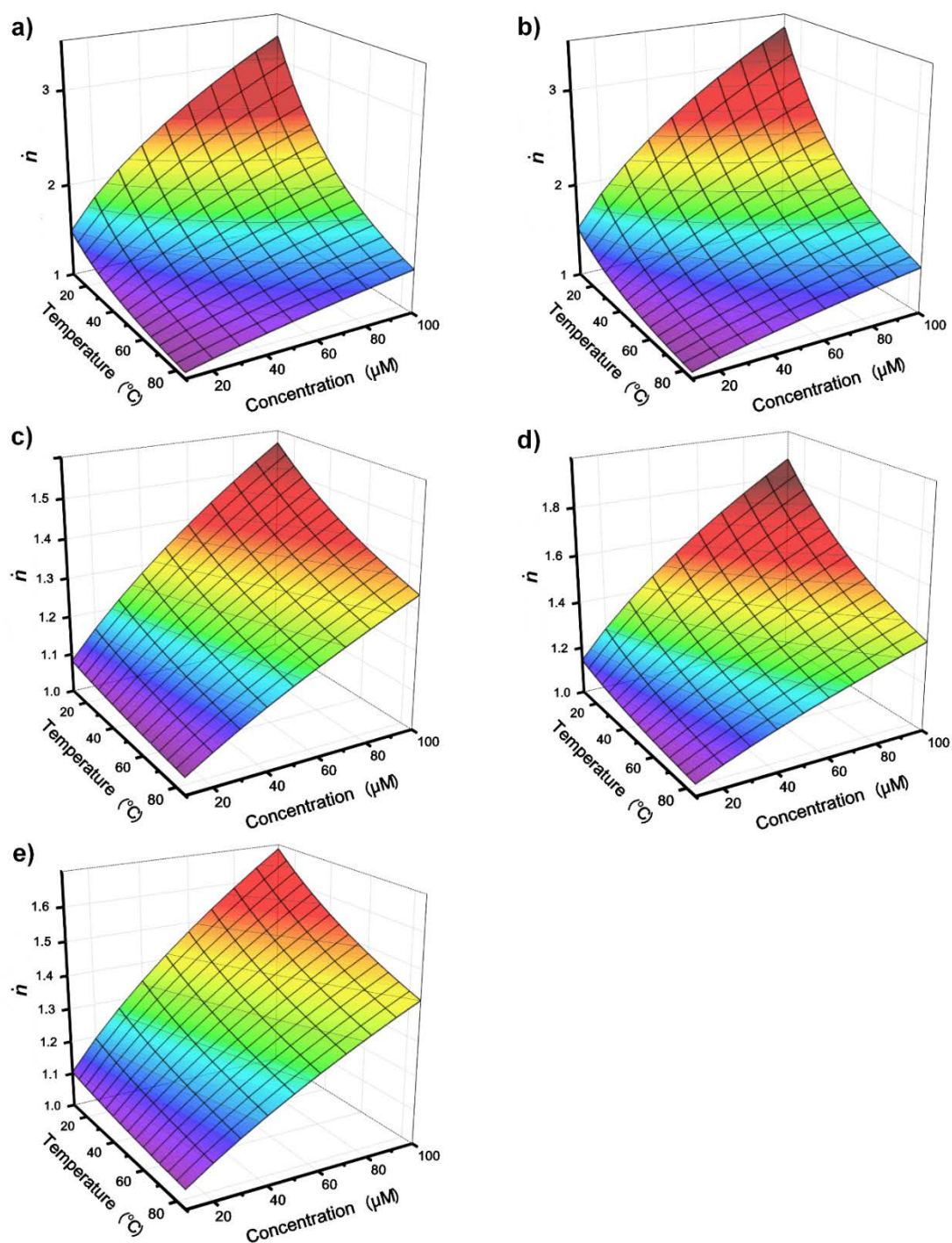
Fig. D14: a) Mean stack size, $\dot{n}$, for compounds **1**, b) **2**, c) **5**, d) **6**, and e) **7**. Surfaces displayed represent $\dot{n}$ at varied temperatures and concentrations in toluene, based on data from fittings and **Eq. S17**.
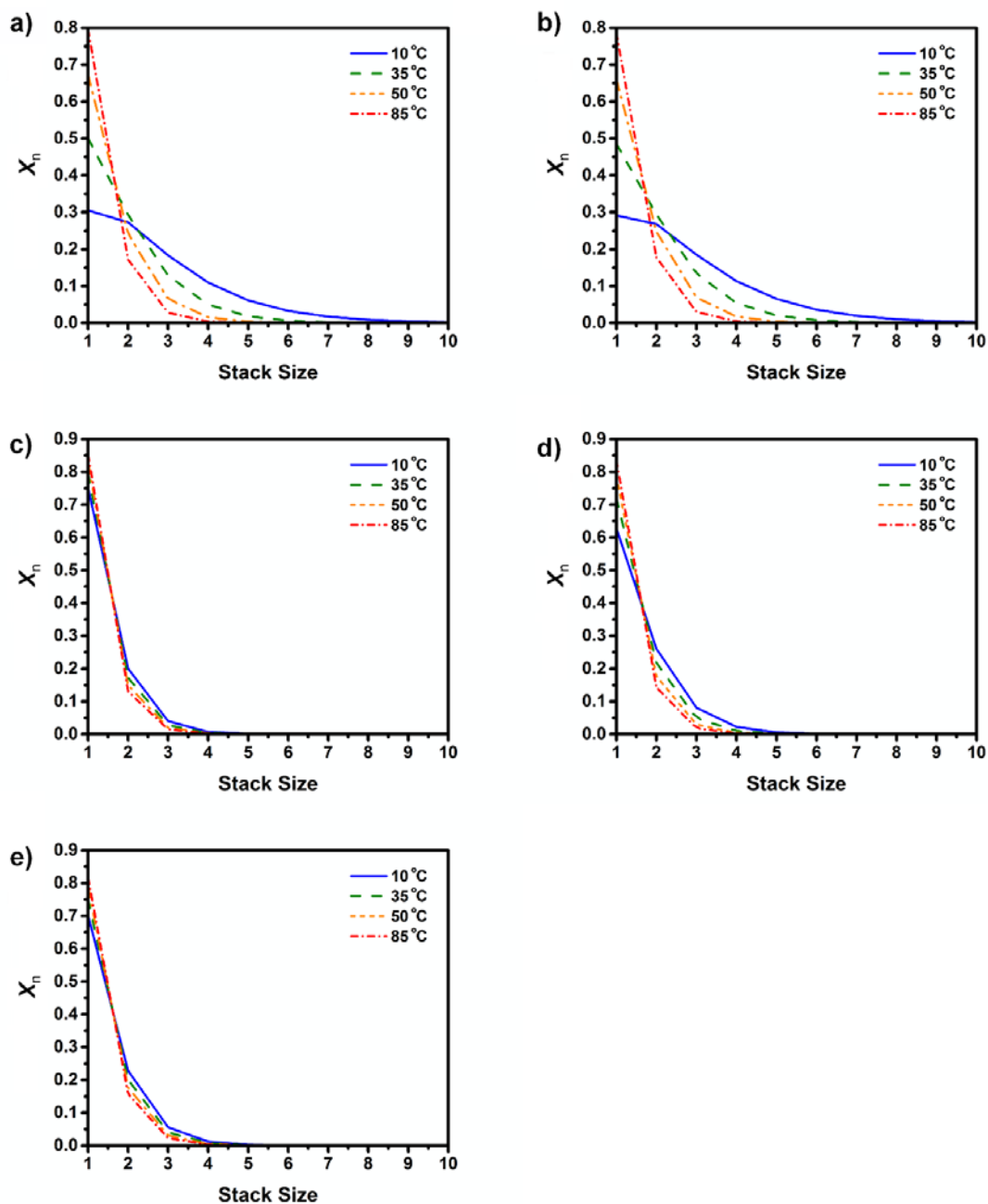
Fig. D15: a) Mass fraction, X_n, for compounds **1**, b) **2**, c) **5**, d) **6**, and e) **7** at varied temperatures and at 20 μM in toluene. The mass fractions of polymer lengths of size n, X_n, are calculated from **Eq. S12** and data from fittings.
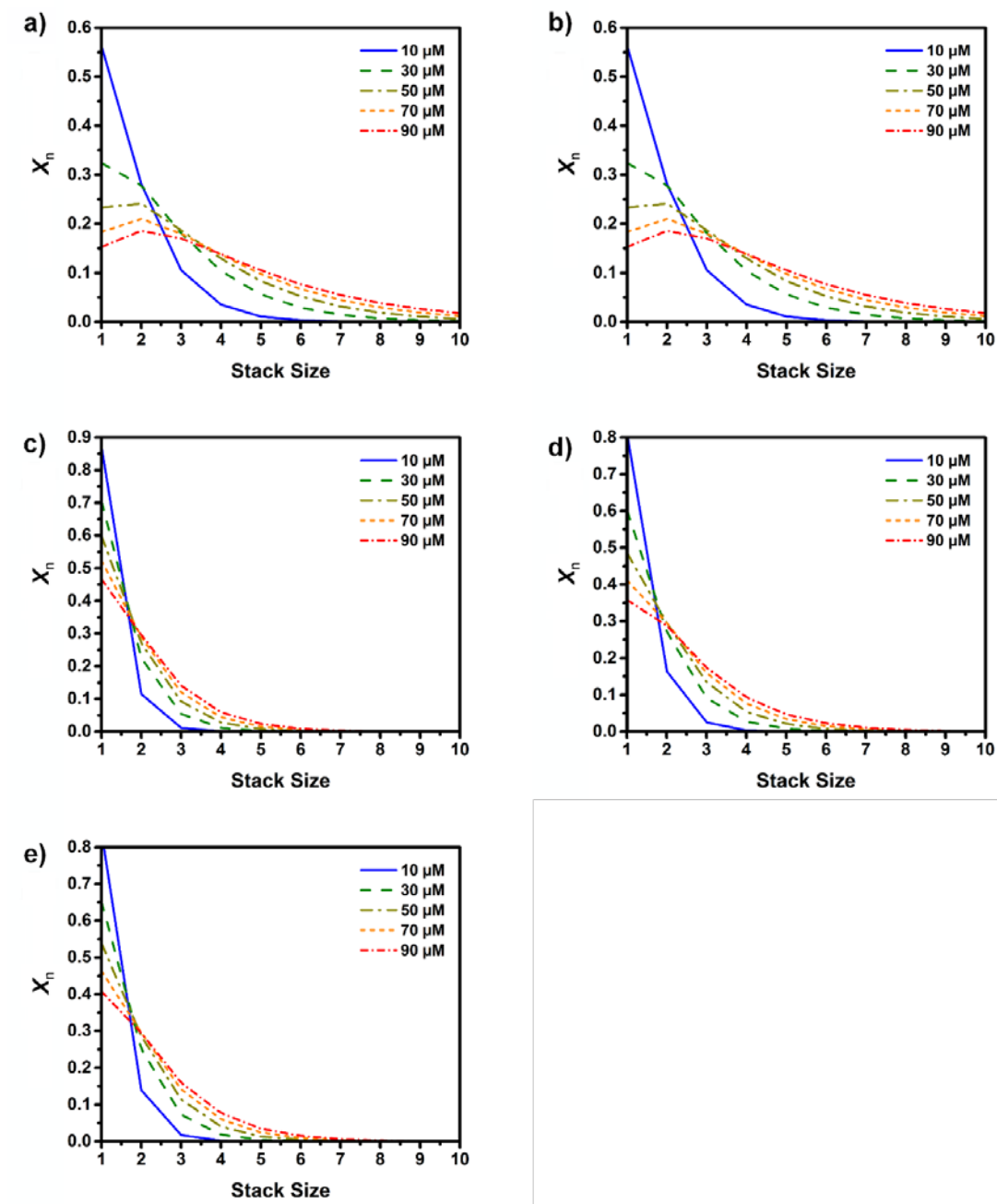
Fig. D16: a) Mass fraction, X_n, for compounds **1**, b) **2**, c) **5**, d) **6**, and e) **7** at varied concentrations and at 25 °C in toluene. The mass fractions of polymer lengths of size n, X_n, are calculated from **Eq. S12** and data from fittings.

QUANTUM CHEMICAL CALULATIONS

Geometric optimizations were found using ORCA1 computational software[188]. Optimization was performed using the BP86 functional, a double-zeta basis, the RI-J approximation and DFT-D3 dispersion correction, and COSMO interpretations for toluene solvent. Compounds were constructed and manipulated using JMOL2[280], Mercury3[281], and Avogadro4 computational software[282].
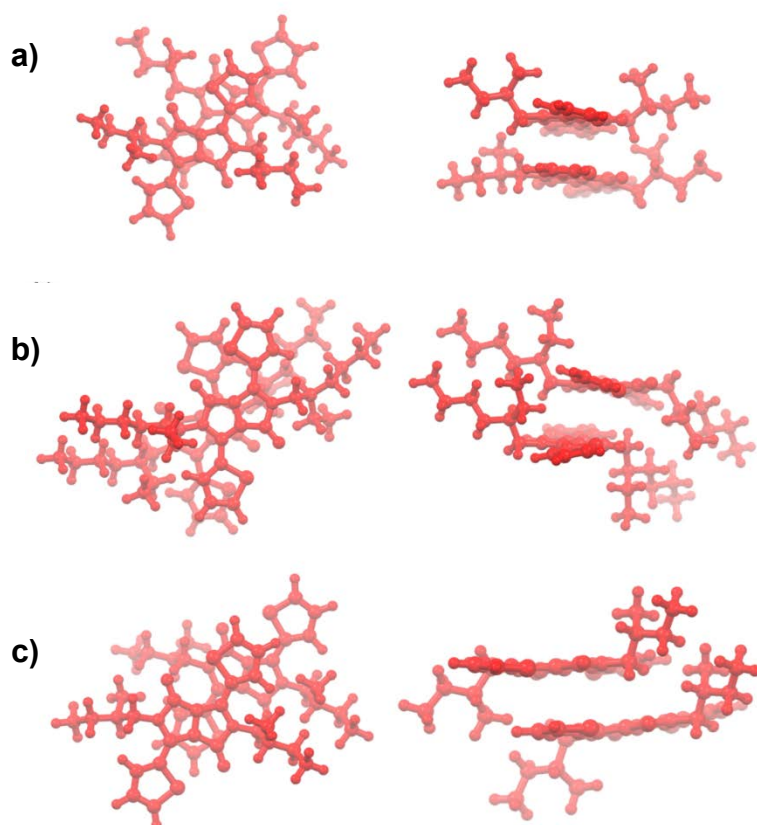
Fig. D17: a) Geometric optimization of **5**, b) **6**, and c) **7** dimers in toluene.

REFERENCES

1. Tsien, R. Y., The Green Fluorescent Protein. *Annu. Rev. Biochem.* **1998,** *67*, 509-544.

2. Birge, R. R., Photophysics and Molecular Electronic Applications of the Rhodopsins. *Annu. Rev. Phys. Chem.* **1990,** *41*, 683-733.

3. Feher, G.; Allen, J. P.; Okamura, M. Y.; Rees, D. C., Structure and Function of Bacterial Photosynthetic Reaction Centres. *Nature* **1989,** *339*, 111-116.

4. Zouni, A.; Witt, H.-T.; Kern, J.; Fromme, P.; Krauss, N.; Saenger, W.; Orth, P., Crystal Structure of Photosystem II from Synechococcus Elongatus at 3.8 [angst] Resolution. *Nature* **2001,** *409*, 739-743.

5. Cogdell, R. J.; Gall, A.; Köhler, J., The Architecture and Function of the Light-Harvesting Apparatus of Purple Bacteria: from Single Molecules to in vivo Membranes. *Quar. Rev. Biophys.* **2006,** *39*, 227-324.

6. Mitzi, D. B.; Chondroudis, K.; Kagan, C. R., Organic-Inorganic Electronics. *IBM J. Res Dev.* **2001,** *45*, 29-45.

7. Ordinario, D. D.; Phan, L.; Walkup Iv, W. G.; Jocson, J.-M.; Karshalev, E.; Hüsken, N.; Gorodetsky, A. A., Bulk Protonic Conductivity in a Cephalopod Structural Protein. *Nat Chem* **2014,** *6* , 596-602.

8. Sun, Y.; Rogers, J. A., Inorganic Semiconductors for Flexible Electronics. *Adv. Mater.s* **2007,** *19*, 1897-1916.

9. Roco, M. C.; Hersam, M. C.; Mirkin, C. A., *Nanotechnology Research Directions for Societal Needs in 2020*. 1 ed.; Springer Netherlands: 2011; Vol. 1, p 690.

10. Lehn, J.-M., From Supermolecules to Supramolecular Assemblies. In *Supramolecular Chemistry*, Wiley-VCH Verlag GmbH and Co. KGaA: 2006; pp 81-87.

11. Whitesides, G. M.; Simanek, E. E.; Mathias, J. P.; Seto, C. T.; Chin, D.; Mammen, M.; Gordon, D. M., Noncovalent Synthesis: Using Physical-Organic Chemistry To Make Aggregates. *Acc. Chem. Res.* **1995,** *28*, 37-44.

12. Fyfe, M. C. T.; Stoddart, J. F., Synthetic Supramolecular Chemistry. *Acc. Chem. Res.* **1997,** *30* , 393-401.

13. Jones, M. R.; Osberg, K. D.; Macfarlane, R. J.; Langille, M. R.; Mirkin, C. A., Templated Techniques for the Synthesis and Assembly of Plasmonic Nanostructures. *Chem. Rev.* **2011,** *111*, 3736-3827.

14.   Wojtecki, R. J.; Meador, M. A.; Rowan, S. J., Using the Dynamic Bond to Access Macroscopically Responsive Structurally Dynamic Polymers. *Nat Mater* **2011,** *10*, 14-27.

15.   Herbst, F.; Döhler, D.; Michael, P.; Binder, W. H., Self-Healing Polymers via Supramolecular Forces. *Macromolecules* **2013,** *34*, 203-220.

16.   Schenning, A. P. H. J.; Meijer, E. W., Supramolecular Electronics; Nanowires from Self-Assembled [small pi]-conjugated Systems. *Chem. Comm.* **2005**, 3245-3258

17.   Seeman, N. C., At the Crossroads of Chemistry, Biology, and Materials: Structural DNA Nanotechnology. *Chem. and Bio.* **2003,** *10* , 1151-1159.

18.   Storhoff, J. J.; Mirkin, C. A., Programmed Materials Synthesis with DNA. *Chem. Rev.* **1999,** *99*, 1849-1862.

19.   Chen, C.-L.; Zhang, P.; Rosi, N. L., A New Peptide-Based Method for the Design and Synthesis of Nanoparticle Superstructures: Construction of Highly Ordered Gold Nanoparticle Double Helices. *J. Am. Chem. Soc.* **2008,** *130*, 13555-13557.

20.   Han, X.; Zheng, Y.; Munro, C. J.; Ji, Y.; Braunschweig, A. B., Carbohydrate Nanotechnology: Hierarchical Assembly using Nature's other Information Carrying Biopolymers. *Curr. Op. Biotechn.* **2015,** *34*, 41-47.

21.   Brunsveld, L.; Folmer, B. J. B.; Meijer, E. W.; Sijbesma, R. P., Supramolecular Polymers. *Chem. Rev.* **2001,** *101*, 4071-4098.

22.   Cornelissen, J. J. L. M.; Rowan, A. E.; Nolte, R. J. M.; Sommerdijk, N. A. J. M., Chiral Architectures from Macromolecular Building Blocks. *Chem. Rev.* **2001,** *101*, 4039-4070.

23.   Aida, T.; Meijer, E. W.; Stupp, S. I., Functional Supramolecular Polymers. *Science* **2012,** *335*, 813-817.

24.   Fox, J. D.; Rowan, S. J., Supramolecular Polymerizations and Main-Chain Supramolecular Polymers. *Macromolecules* **2009,** *42*, 6823-6835.

25.   Appel, E. A.; del Barrio, J.; Loh, X. J.; Scherman, O. A., Supramolecular Polymeric Hydrogels. *Chem. Soc. Rev.* **2012,** *41*, 6195-6214.

26.   Liu, Y.; Wang, Z.; Zhang, X., Characterization of Supramolecular Polymers. *Chem. Soc. Rev.* **2012,** *41* (18), 5922-5932.

27.   Yang, L.; Tan, X.; Wang, Z.; Zhang, X., Supramolecular Polymers: Historical Development, Preparation, Characterization, and Functions. *Chem. Rev.* **2015,** *115*, 7196-7239.

28.   South, C. R.; Leung, K. C. F.; Lanari, D.; Stoddart, J. F.; Weck, M., Noncovalent Side-Chain Functionalization of Terpolymers. *Macromolecules* **2006,** *39*, 3738-3744.

29.   South, C. R.; Higley, M. N.; Leung, K. C. F.; Lanari, D.; Nelson, A.; Grubbs, R. H.; Stoddart, J. F.; Weck, M., Self-Assembly with Block Copolymers through Metal Coordination of SCS–PdII Pincer Complexes and Pseudorotaxane Formation. *Chem. Eur. J.* **2006,** *12*, 3789-3797.

30.   Ku, T.-H.; Chien, M.-P.; Thompson, M. P.; Sinkovits, R. S.; Olson, N. H.; Baker, T. S.; Gianneschi, N. C., Controlling and Switching the Morphology of Micellar Nanoparticles with Enzymes. *J. Am. Chem. Soc.* **2011,** *133* (22), 8392-8395.

31.   Zhuang, J.; Gordon, M. R.; Ventura, J.; Li, L.; Thayumanavan, S., Multi-stimuli Responsive Macromolecules and their Assemblies. *Chem. Soc. Rev.* **2013,** *42*, 7421-7435.

32.   Petkau-Milroy, K.; Sonntag, M. H.; Brunsveld, L., Modular Columnar Supramolecular Polymers as Scaffolds for Biomedical Applications. *Chem. Eur. J.* **2013,** *19*, 10786-10793.

33.   Wasielewski, M. R., Photoinduced Electron Transfer in Supramolecular Systems for Artificial Photosynthesis. *Chem. Rev.* **1992,** *92*, 435-461.

34.   Rieth, S.; Li, Z.; Hinkle, C. E.; Guzman, C. X.; Lee, J. J.; Nehme, S. I.; Braunschweig, A. B., Superstructures of Diketopyrrolopyrrole Donors and Perylenediimide Acceptors Formed by Hydrogen-Bonding and $\pi\cdots\pi$ Stacking. *J. Phys. Chem. C* **2013,** *117*, 11347-11356.

35.   Ley, D.; Guzman, C. X.; Adolfsson, K. H.; Scott, A. M.; Braunschweig, A. B., Cooperatively Assembling Donor–Acceptor Superstructures Direct Energy Into an Emergent Charge Separated State. *J. Am. Chem. Soc.* **2014,** *136*, 7809-7812.

36.   Bielawski, C. W.; Benitez, D.; Grubbs, R. H., An "Endless" Route to Cyclic Polymers. *Science* **2002,** *297*, 2041-2044.

37.   Percec, V.; Dulcey, A. E.; Balagurusamy, V. S. K.; Miura, Y.; Smidrkal, J.; Peterca, M.; Nummelin, S.; Edlund, U.; Hudson, S. D.; Heiney, P. A.; Duan, H.; Magonov, S. N.; Vinogradov, S. A., Self-Assembly of Amphiphilic Dendritic Dipeptides into Helical Pores. *Nature* **2004,** *430*, 764-768.

38. Percec, V.; Glodde, M.; Bera, T. K.; Miura, Y.; Shiyanovskaya, I.; Singer, K. D.; Balagurusamy, V. S. K.; Heiney, P. A.; Schnell, I.; Rapp, A.; Spiess, H. W.; Hudson, S. D.; Duan, H., Self-Organization of Supramolecular Helical Dendrimers into Complex Electronic Materials. *Nature* **2002,** *417*, 384-387.

39. Tomalia, D. A.; Baker, H.; Dewald, J.; Hall, M.; Kallos, G.; Martin, S.; Roeck, J.; Ryder, J.; Smith, P., A New Class of Polymers: Starburst-Dendritic Macromolecules. *Polym J* **1985,** *17*, 117-132.

40. Gorodetsky, A. A.; Chiu, C.-Y.; Schiros, T.; Palma, M.; Cox, M.; Jia, Z.; Sattler, W.; Kymissis, I.; Steigerwald, M.; Nuckolls, C., Reticulated Heterojunctions for Photovoltaic Devices. *Angew. Chem. Int. Ed.* **2010,** *49*, 7909-7912.

41. Johnson, J. A.; Lu, Y. Y.; Burts, A. O.; Lim, Y.-H.; Finn, M. G.; Koberstein, J. T.; Turro, N. J.; Tirrell, D. A.; Grubbs, R. H., Core-Clickable PEG-Branch-Azide Bivalent-Bottle-Brush Polymers by ROMP: Grafting-Through and Clicking-To. *J. Am. Chem. Soc.* **2011,** *133*, 559-566.

42. Nese, A.; Li, Y.; Averick, S.; Kwak, Y.; Konkolewicz, D.; Sheiko, S. S.; Matyjaszewski, K., Synthesis of Amphiphilic Poly(N-vinylpyrrolidone)-b-poly(vinyl acetate) Molecular Bottlebrushes. *ACS Macro Letters* **2012,** *1*, 227-231.

43. Yan, J.; Li, W.; Zhang, A., Dendronized Supramolecular Polymers. *Chem. Comm.* **2014,** *50*, 12221-12233.

44. Pochan, D. J.; Chen, Z.; Cui, H.; Hales, K.; Qi, K.; Wooley, K. L., Toroidal Triblock Copolymer Assemblies. *Science* **2004,** *306*, 94-97.

45. Jonkheijm, P.; Hoeben, F. J. M.; Kleppinger, R.; van Herrikhuyzen, J.; Schenning, A. P. H. J.; Meijer, E. W., Transfer of π-Conjugated Columnar Stacks from Solution to Surfaces. *J. Am. Chem. Soc.* **2003,** *125*, 15941-15949.

46. Ashton, P. R.; Baxter, I.; Cantrill, S. J.; Fyfe, M. C. T.; Glink, P. T.; Stoddart, J. F.; White, A. J. P.; Williams, D. J., Supramolecular Daisy Chains. *Angew. Chem. Int. Ed.* **1998,** *37*, 1294-1297.

47. Yang, S. K.; Ambade, A. V.; Weck, M., Main-Chain Supramolecular Block Copolymers. *Chem. Soc. Rev.* **2011,** *40*, 129-137.

48. Oh, M.; Mirkin, C. A., Chemically Tailorable Colloidal Particles from Infinite Coordination Polymers. *Nature* **2005,** *438*, 651-654.

49. Percec, V.; Imam, M. R.; Peterca, M.; Leowanawat, P., Self-Organizable Vesicular Columns Assembled from Polymers Dendronized with Semifluorinated Janus Dendrimers Act As Reverse Thermal Actuators. *J. Am. Chem. Soc.* **2012,** *134*, 4408-4420.

50.   Leung, K. C. F.; Mendes, P. M.; Magonov, S. N.; Northrop, B. H.; Kim, S.; Patel, K.; Flood, A. H.; Tseng, H.-R.; Stoddart, J. F., Supramolecular Self-Assembly of Dendronized Polymers: Reversible Control of the Polymer Architectures through Acid−Base Reactions. *J. Am. Chem. Soc.* **2006,** *128* , 10707-10715.

51.   Hartgerink, J. D.; Beniash, E.; Stupp, S. I., Self-Assembly and Mineralization of Peptide-Amphiphile Nanofibers. *Science* **2001,** *294*, 1684-1688.

52.   Würthner, F.; Chen, Z.; Hoeben, F. J. M.; Osswald, P.; You, C.-C.; Jonkheijm, P.; Herrikhuyzen, J. v.; Schenning, A. P. H. J.; van der Schoot, P. P. A. M.; Meijer, E. W.; Beckers, E. H. A.; Meskers, S. C. J.; Janssen, R. A. J., Supramolecular p−n-Heterojunctions by Co-Self-Organization of Oligo(p-phenylene Vinylene) and Perylene Bisimide Dyes. *J. Am. Chem. Soc.* **2004,** *126*, 10611-10618.

53.   Dehm, V.; Chen, Z.; Baumeister, U.; Prins, P.; Siebbeles, L. D. A.; Würthner, F., Helical Growth of Semiconducting Columnar Dye Assemblies Based on Chiral Perylene Bisimides. Org. Lett. **2007,** *9*, 1085-1088.

54.   Appel, E. A.; Biedermann, F.; Rauwald, U.; Jones, S. T.; Zayed, J. M.; Scherman, O. A., Supramolecular Cross-Linked Networks via Host−Guest Complexation with Cucurbit[8]uril. *J. Am. Chem. Soc.* **2010,** *132* , 14251-14260.

55.   Ryu, J.-H.; Roy, R.; Ventura, J.; Thayumanavan, S., Redox-Sensitive Disassembly of Amphiphilic Copolymer Based Micelles. *Langmuir* **2010,** *26* , 7086-7092.

56.   Niu, Z.; Gibson, H. W., Polycatenanes. *Chem. Rev.* **2009,** *109*, 6024-6046.

57.   Xia, J.; Zhang, X.; Matyjaszewski, K., Synthesis of Star-Shaped Polystyrene by Atom Transfer Radical Polymerization Using an "Arm First" Approach. *Macromolecules* **1999,** *32* , 4482-4484.

58.   Wang, L.; Weber, W. P., Synthesis and Properties of Novel Comb Polymers: Unsaturated Carbosilane Polymers with Pendent Oligo(oxyethylene) Groups. *Macromolecules* **1993,** *26*, 969-974.

59.   Wang, J.; Lu, H.; Kamat, R.; Pingali, S. V.; Urban, V. S.; Cheng, J.; Lin, Y., Supramolecular Polymerization from Polypeptide-Grafted Comb Polymers. *J. Am. Chem. Soc.* **2011,** *133*, 12906-12909.

60.   Zhang, A.; Okrasa, L.; Pakula, T.; Schlüter, A. D., Homologous Series of Dendronized Polymethacrylates with a Methyleneoxycarbonyl Spacer between the Backbone and Dendritic Side Chain: Synthesis, Characterization, and Some Bulk Properties. *J. Am. Chem. Soc.* **2004,** *126*, 6658-6666.

61.   Zhang, M.; Müller, A. H. E., Cylindrical Polymer Brushes. *J. Poly. Sci. Part A: Poly. Chem.***2005,** *43*, 3461-3481.

62. Sheiko, S. S.; Sumerlin, B. S.; Matyjaszewski, K., Cylindrical molecular brushes: Synthesis, characterization, and properties. *Prog. Poly. Sci.* **2008,** *33* , 759-785.

63. Esser-Kahn, A. P.; Sottos, N. R.; White, S. R.; Moore, J. S., Programmable Microcapsules from Self-Immolative Polymers. *J. Am. Chem. Soc.* **2010,** *132*, 10266-10268.

64. Sagi, A.; Weinstain, R.; Karton, N.; Shabat, D., Self-Immolative Polymers. *J. Am. Chem. Soc.* **2008,** *130*, 5434-5435.

65. Peterson, G. I.; Larsen, M. B.; Boydston, A. J., Controlled Depolymerization: Stimuli-Responsive Self-Immolative Polymers. *Macromolecules* **2012,** *45*, 7317-7328.

66. Caruso, M. M.; Davis, D. A.; Shen, Q.; Odom, S. A.; Sottos, N. R.; White, S. R.; Moore, J. S., Mechanically-Induced Chemical Changes in Polymeric Materials. *Chem. Rev.* **2009,** *109*, 5755-5798.

67. Black, A. L.; Lenhardt, J. M.; Craig, S. L., From Molecular Mechanochemistry to Stress-Responsive Materials. *J. Mater. Chem.* **2011,** *21*, 1655-1663.

68. Sijbesma, R. P.; Beijer, F. H.; Brunsveld, L.; Folmer, B. J. B.; Hirschberg, J. H. K. K.; Lange, R. F. M.; Lowe, J. K. L.; Meijer, E. W., Reversible Polymers Formed from Self-Complementary Monomers Using Quadruple Hydrogen Bonding. *Science* **1997,** *278*, 1601-1604.

69. Hoeben, F. J. M.; Jonkheijm, P.; Meijer, E. W.; Schenning, A. P. H. J., About Supramolecular Assemblies of π-Conjugated Systems. *Chem. Rev.* **2005,** *105*, 1491-1546.

70. Zhang, S.; Yu, Z.; Govender, T.; Luo, H.; Li, B., A Novel Supramolecular Shape Memory Material Based on Partial α-CD–PEG Inclusion Complex. *Polymer* **2008,** *49*, 3205-3210.

71. Li, J.; Li, X.; Ni, X.; Wang, X.; Li, H.; Leong, K. W., Self-Assembled Supramolecular Hydrogels formed by Biodegradable PEO–PHB–PEO Triblock Copolymers and α-cyclodextrin for Controlled Drug Delivery. *Biomaterials* **2006,** *27*, 4132-4140.

72. Yoon, H.-J.; Jang, W.-D., Polymeric Supramolecular Systems for Drug Delivery. *J. Mater. Chem.* **2010,** *20*, 211-222.

73. Wasielewski, M. R., Self-Assembly Strategies for Integrating Light Harvesting and Charge Separation in Artificial Photosynthetic Systems. *Acc. Chem. Res.* **2009,** *42*, 1910-1921.

74.   Tysseling-Mattiace, V. M.; Sahni, V.; Niece, K. L.; Birch, D.; Czeisler, C.; Fehlings, M. G.; Stupp, S. I.; Kessler, J. A., Self-Assembling Nanofibers Inhibit Glial Scar Formation and Promote Axon Elongation after Spinal Cord Injury. *J. Neurosci.* **2008,** *28*, 3814-3823.

75.   Li, S.-L.; Xiao, T.; Lin, C.; Wang, L., Advanced Supramolecular Polymers Constructed by Orthogonal Self-Assembly. *Chem. Soc. Rev.* **2012,** *41* , 5950-5968.

76.   Watson, J. D.; Crick, F. H. C., Molecular Structure of Nucleic Acids: A Structure for Deoxyribose Nucleic Acid. *Nature* **1953,** *171*, 737-738.

77.   Schenning, A. P. H. J.; Jonkheijm, P.; Peeters, E.; Meijer, E. W., Hierarchical Order in Supramolecular Assemblies of Hydrogen-Bonded Oligo(p-phenylene vinylene)s. *J. Am. Chem. Soc.* **2001,** *123* (3), 409-416.

78.   Yang, S. K.; Zimmerman, S. C., Hydrogen Bonding Modules for Use in Supramolecular Polymers. *Isr. J. Chem.* **2013,** *53*, 511-520.

79.   Chen, X. M.; Liu, G. F., Double-Stranded Helices and Molecular Zippers Assembled from Single-Stranded Coordination Polymers Directed by Supramolecular Interactions. *Chemistry* **2002,** *8*, 4811-4817.

80.   Yan, X.; Jiang, B.; Cook, T. R.; Zhang, Y.; Li, J.; Yu, Y.; Huang, F.; Yang, H.-B.; Stang, P. J., Dendronized Organoplatinum(II) Metallacyclic Polymers Constructed by Hierarchical Coordination-Driven Self-Assembly and Hydrogen-Bonding Interfaces. *J. Am. Chem. Soc.* **2013,** *135*, 16813-16816.

81.   Burattini, S.; Colquhoun, H. M.; Fox, J. D.; Friedmann, D.; Greenland, B. W.; Harris, P. J. F.; Hayes, W.; Mackay, M. E.; Rowan, S. J., A Self-Repairing, Supramolecular Polymer System: Healability as a Consequence of Donor-Acceptor [small pi]-[small pi] Stacking Interactions. *Chem. Comm.* **2009,** 6717-6719.

82.   Star, A.; Liu, Y.; Grant, K.; Ridvan, L.; Stoddart, J. F.; Steuerman, D. W.; Diehl, M. R.; Boukai, A.; Heath, J. R., Noncovalent Side-Wall Functionalization of Single-Walled Carbon Nanotubes. *Macromolecules* **2003,** *36*, 553-560.

83.   Haino, T.; Watanabe, A.; Hirao, T.; Ikeda, T., Supramolecular Polymerization Triggered by Molecular Recognition between Bisporphyrin and Trinitrofluorenone. *Angew. Chem. Int. Ed.* **2012,** *51*, 1473-1476.

84.   Miyauchi, M.; Takashima, Y.; Yamaguchi, H.; Harada, A., Chiral Supramolecular Polymers Formed by Host−Guest Interactions. *J. Am. Chem. Soc.* **2005,** *127*, 2984-2989.

85.   Dong, S.; Gao, L.; Chen, J.; Yu, G.; Zheng, B.; Huang, F., A Supramolecular Polymer Formed by the Combination of Crown Ether-Based and Charge-Transfer Molecular Recognition. *Poly. Chem.***2013,** *4*, 882-886.

86.   Yan, X.; Wang, F.; Zheng, B.; Huang, F., Stimuli-Responsive Supramolecular Polymeric Materials. *Chem. Soc. Rev.* **2012,** *41*, 6042-6065.

87.   Weizmann, Y.; Braunschweig, A. B.; Wilner, O. I.; Cheglakov, Z.; Willner, I., A Polycatenated DNA Scaffold for the One-step Assembly of Hierarchical Nanostructures. *Proc. Natl. Acad. Sci. USA* **2008,** *105*, 5289-5294.

88.   Bria, M.; Bigot, J.; Cooke, G.; Lyskawa, J.; Rabani, G.; Rotello, V. M.; Woisel, P., Synthesis of a Polypseudorotaxane, Polyrotaxane, and Polycatenane using 'Click' Chemistry. *Tetrahedron* **2009,** *65*, 400-407.

89.   Harada, A.; Takashima, Y.; Yamaguchi, H., Cyclodextrin-based Supramolecular Polymers. *Chem. Soc. Rev.* **2009,** *38*, 875-882.

90.   Zheng, B.; Wang, F.; Dong, S.; Huang, F., Supramolecular Polymers Constructed by Crown Ether-Based Molecular Recognition. *Chem. Soc. Rev.* **2012,** *41*, 1621-1636.

91.   Flory, P. J., *Principles of Polymer Chemistry*. 1 ed.; Cornell University Press: Ithica 1953; p 688.

92.   Zhao, D.; Moore, J. S., Nucleation-Elongation: a Mechanism for Cooperative Supramolecular Polymerization. *Org. Biomol. Chem.* **2003,** *1* , 3471-91.

93.   De Greef, T. F. A.; Smulders, M. M. J.; Wolffs, M.; Schenning, A. P. H. J.; Sijbesma, R. P.; Meijer, E. W., Supramolecular Polymerization. *Chem. Rev.* **2009,** *109*, 5687-5754.

94.   Martin, R. B., Comparisons of Indefinite Self-Association Models. *Chem. Rev.* **1996,** *96* , 3043-3064.

95.   Rowan, S. J.; Cantrill, S. J.; Cousins, G. R.; Sanders, J. K.; Stoddart, J. F., Dynamic Covalent Chemistry. *Angew Chem Int Ed Engl* **2002,** *41*, 898-952.

96.   Hirschberg, J. H. K. K.; Brunsveld, L.; Ramzi, A.; Vekemans, J. A. J. M.; Sijbesma, R. P.; Meijer, E. W., Helical Self-Assembled Polymers from Cooperative Stacking of Hydrogen-Bonded Pairs. *Nature* **2000,** *407*, 167-170.

97.   Smulders, M. M. J.; Nieuwenhuizen, M. M. L.; de Greef, T. F. A.; van der Schoot, P.; Schenning, A. P. H. J.; Meijer, E. W., How to Distinguish Isodesmic from Cooperative Supramolecular Polymerisation. *Chem. Eur. J.***2010,** *16*, 362-367.

98.   Green, M. M.; Reidy, M. P.; Johnson, R. D.; Darling, G.; O'Leary, D. J.; Willson, G., Macromolecular Stereochemistry: the Out-of-Proportion Influence of Optically Active Comonomers on the Conformational Characteristics of Polyisocyanates. The Sergeants and Soldiers Experiment. *J. Am. Chem. Soc.* **1989,** *111*, 6452-6454.

99.   Anderson, T. W.; Sanders, J. K.; Pantos, G. D., The Sergeants-and-Soldiers Effect: Chiral Amplification in Naphthalenediimide Nanotubes. *Org. Biomol. Chem.* **2010,** *8*, 4274-80.

100.   Lewis, N. S.; Nocera, D. G., Powering the Planet: Chemical Challenges in Solar Energy Utilization. *Proc. Natl. Acad. Sci. USA* **2006,** *103* , 15729-15735.

101.   Chiu, C.-Y.; Kim, B.; Gorodetsky, A. A.; Sattler, W.; Wei, S.; Sattler, A.; Steigerwald, M.; Nuckolls, C., Shape-shifting in Contorted Dibenzotetrathienocoronenes. *Chem. Sci.* **2011,** *2*, 1480-1486.

102.   Hartnett, P. E.; Dyar, S. M.; Margulies, E. A.; Shoer, L. E.; Cook, A. W.; Eaton, S. W.; Marks, T. J.; Wasielewski, M. R., Long-lived Charge Carrier Generation in Ordered Films of a Covalent Perylenediimide-Diketopyrrolopyrrole-Perylenediimide Molecule. *Chem. Sci.* **2015,** *6*, 402-411.

103.   Calderon, R. M. K.; Valero, J.; Grimm, B.; de Mendoza, J.; Guldi, D. M., Enhancing Molecular Recognition in Electron Donor–Acceptor Hybrids via Cooperativity. *J. Am. Chem. Soc.* **2014,** *136*, 11436-11443.

104.   Sun, D.; Tham, F. S.; Reed, C. A.; Chaker, L.; Boyd, P. D. W., Supramolecular Fullerene-Porphyrin Chemistry. Fullerene Complexation by Metalated "Jaws Porphyrin" Hosts. *J. Am. Chem. Soc.* **2002,** *124* (23), 6604-6612.

105.   Walker, B.; Tamayo, A. B.; Dang, X.-D.; Zalar, P.; Seo, J. H.; Garcia, A.; Tantiwiwat, M.; Nguyen, T.-Q., Nanoscale Phase Separation and High Photovoltaic Efficiency in Solution-Processed, Small-Molecule Bulk Heterojunction Solar Cells.Adv. Funct. Mater. **2009,** *19* , 3063-3069.

106.   Kuhlbrandt, W.; Wang, D. N.; Fujiyoshi, Y., Atomic Model of Plant Light-Harvesting Complex by Electron Crystallography. *Nature* **1994,** *367*, 614-621.

107.   Lehn, J.-M., Toward Complex Matter: Supramolecular Chemistry and Self-Organization. *Proc. Natl. Acad. Sci. USA* **2002,** *99* , 4763-4768.

108.   Bushey, M. L.; Nguyen, T.-Q.; Zhang, W.; Horoszewski, D.; Nuckolls, C., Using Hydrogen Bonds to Direct the Assembly of Crowded Aromatics. *Angew. Chem. Int. Ed.* **2004,** *43*, 5446-5453.

109. Nguyen, T.-Q.; Martel, R.; Bushey, M.; Avouris, P.; Carlsen, A.; Nuckolls, C.; Brus, L., Self-assembly of 1-D Organic Semiconductor Nanostructures. *Phys. Chem. Chem. Phys.* **2007,** *9*, 1515-1532.

110. Palmer, L. C.; Stupp, S. I., Molecular Self-Assembly into One-Dimensional Nanostructures. *Acc. Chem. Res.* **2008,** *41*, 1674-1684.

111. Palermo, V.; Schwartz, E.; Finlayson, C. E.; Liscio, A.; Otten, M. B. J.; Trapani, S.; Müllen, K.; Beljonne, D.; Friend, R. H.; Nolte, R. J. M.; Rowan, A. E.; Samorì, P., Macromolecular Scaffolding: The Relationship Between Nanoscale Architecture and Function in Multichromophoric Arrays for Organic Electronics. *Adv. Mater.* **2010,** *22*, E81-E88.

112. Kim, P.; Zarzar, L. D.; He, X.; Grinthal, A.; Aizenberg, J., Hydrogel-actuated Integrated Responsive Systems (HAIRS): Moving Towards Adaptive Materials. *Cur. Opin. Solid State Mater. Sci.* **2011,** *15*, 236-245.

113. Coskun, A.; Spruell, J. M.; Barin, G.; Dichtel, W. R.; Flood, A. H.; Botros, Y. Y.; Stoddart, J. F., High Hopes: Can Molecular Electronics Realise its Potential? *Chem. Soc. Rev.* **2012,** *41* , 4827-4859.

114. Buerkle, L. E.; Rowan, S. J., Supramolecular Gels Formed from Multi-Component Low Molecular Weight Species. *Chem. Soc. Rev.* **2012,** *41* , 6089-102.

115. Giaimo, J. M.; Lockard, J. V.; Sinks, L. E.; Scott, A. M.; Wilson, T. M.; Wasielewski, M. R., Excited Singlet States of Covalently Bound, Cofacial Dimers and Trimers of Perylene-3,4:9,10-bis(dicarboximide)s. *J. Phys. Chem. A* **2008,** *112* , 2322-2330.

116. Grimm, B.; Schornbaum, J.; Jasch, H.; Trukhina, O.; Wessendorf, F.; Hirsch, A.; Torres, T.; Guldi, D. M., Step-by-step Self-Assembled Hybrids that Feature Control over Energy and Charge Transfer. *Proc. Natl. Acad. Sci. USA* **2012,** *109*, 15565-15571.

117. Sun, Y.; Welch, G. C.; Leong, W. L.; Takacs, C. J.; Bazan, G. C.; Heeger, A. J., Solution-Processed Small-Molecule Solar Cells with 6.7% Efficiency. *Nat Mater* **2012,** *11*, 44-48.

118. Würthner, F.; Thalacker, C.; Sautter, A., Hierarchical Organization of Functional Perylene Chromophores to Mesoscopic Superstructures by Hydrogen Bonding and π–π Interactions. *Adv. Mater.* **1999,** *11*, 754– 758.

119. Würthner, F.; Thalacker, C.; Sautter, A.; Schärtl, W.; Ibach, W.; Hollricher, O., Hierarchical Self-Organization of Perylene Bisimide–Melamine Assemblies to Fluorescent Mesoscopic Superstructures. *Chem. Eur. J.* **2000,** *6*, 3871–3886.

120. Würthner, F.; Thalacker, C.; Diele, S.; Tschierske, C., Fluorescent J-type Aggregates and Thermotropic Columnar Mesophases of Perylene Bisimide Dyes. *Chem. Eur. J.* **2001,** *7*, 2245–2253.

121. Thalacker, C.; Würthner, F., Chiral Perylene Bisimide–Melamine Assemblies: Hydrogen Bond-Directed Growth of Helically Stacked Dyes with Chiroptical Properties. *Adv. Funct. Mater.* **2002,** *12*, 209-218.

122. van der Boom, T.; Hayes, R. T.; Zhao, Y.; Bushard, P. J.; Weiss, E. A.; Wasielewski, M. R., Charge Transport in Photofunctional Nanoparticles Self-Assembled from Zinc 5,10,15,20-Tetrakis(perylenediimide)porphyrin Building Blocks. *J. Am. Chem. Soc.* **2002,** *124* , 9582-9590.

123. Sinks, L. E.; Rybtchinski, B.; Iimura, M.; Jones, B. A.; Goshe, A. J.; Zuo, X.; Tiede, D. M.; Li, X.; Wasielewski, M. R., Self-Assembly of Photofunctional Cylindrical Nanostructures Based on Perylene-3,4:9,10-bis(dicarboximide). *Chem. Mater.* **2005,** *17*, 6295-6303.

124. George, S. J.; Ajayaghosh, A., Self-Assembled Nanotapes of Oligo(p-phenylene vinylene)s: Sol–Gel-Controlled Optical Properties in Fluorescent π-Electronic Gels. *Chem. Eur. J.* **2005,** *11* , 3217-3227.

125. Jonkheijm, P.; van der Schoot, P.; Schenning, A. P. H. J.; Meijer, E. W., Probing the Solvent-Assisted Nucleation Pathway in Chemical Self-Assembly. *Science* **2006,** *313*, 80-83.

126. Barberá, J.; Puig, L.; Romero, P.; Serrano, J. L.; Sierra, T., Propeller-like Hydrogen-Bonded Banana−Melamine Complexes Inducing Helical Supramolecular Organizations. *J. Am. Chem. Soc.* **2006,** *128*, 4487-4492.

127. Yagai, S.; Monma, Y.; Kawauchi, N.; Karatsu, T.; Kitamura, A., Supramolecular Nanoribbons and Nanoropes Generated from Hydrogen-Bonded Supramolecular Polymers Containing Perylene Bisimide Chromophores. *Org. Lett.* **2007,** 1137-1140.

128. Seki, T.; Yagai, S.; Karatsu, T.; Kitamura, A., Formation of Supramolecular Polymers and Discrete Dimers of Perylene Bisimide Dyes Based on Melamine−Cyanurates Hydrogen-Bonding Interactions. *J. Org. Chem.* **2008,** *73*, 3328-3335.

129. Seitz, W.; Jimenez, A. J.; Carbonell, E.; Grimm, B.; Rodriguez-Morgade, M. S.; Guldi, D. M.; Torres, T., Synthesis and Photophysical Properties of a Hydrogen-Bonded Phthalocyanine-Perylenediimide Assembly. *Chem. Comm.* **2010,** *46*, 127-129.

130. Korevaar, P. A.; George, S. J.; Markvoort, A. J.; Smulders, M. M. J.; Hilbers, P. A. J.; Schenning, A. P. H. J.; De Greef, T. F. A.; Meijer, E. W., Pathway Complexity in Supramolecular Polymerization. *Nature* **2012,** *481*, 492-496.

131. Yagai, S.; Ohta, K.; Gushiken, M.; Iwai, K.; Asano, A.; Seki, S.; Kikkawa, Y.; Morimoto, M.; Kitamura, A.; Karatsu, T., Photoreversible Supramolecular Polymerisation and Hierarchical Organization of Hydrogen-Bonded Supramolecular Co-polymers Composed of Diarylethenes and Oligothiophenes. *Chem. Eur. J.* **2012,** *18*, 2244-2253.

132. Zhao, D.; Moore, J. S., Nucleation-elongation: a Mechanism for Cooperative Supramolecular Polymerization. *Org.Biomol. Chem.* **2003,** *1*, 3471-3491.

133. Chen, Z.; Lohr, A.; Saha-Moller, C. R.; Wurthner, F., Self-Assembled [small pi]-Stacks of Functional Dyes in Solution: Structural and Thermodynamic Features. *Chem. Soc.Rev.* **2009,** *38* (2), 564-584.

134. van der Schoot, P. P. A. M., *Theory of Supramolecular Polymerization*. 2 ed.; CRC Press: Boca Raton, FL,, 2005.

135. Baxter, N. J.; Williamson, M. P.; Lilley, T. H.; Haslam, E., Stacking interactions between caffeine and methyl gallate. *J. Chem. Soc., Faraday Transactions* **1996,** *92* (2), 231-234.

136. Berl, V.; Schmutz, M.; Krische, M. J.; Khoury, R. G.; Lehn, J.-M., Supramolecular Polymers Generated from Heterocomplementary Monomers Linked through Multiple Hydrogen-Bonding Arrays—Formation, Characterization, and Properties. *Chem. Eur. J.* **2002,** *8*, 1227–1244.

137. Odille, F. G. J.; Jónsson, S.; Stjernqvist, S.; Rydén, T.; Wärnmark, K., On the Characterization of Dynamic Supramolecular Systems: A General Mathematical Association Model for Linear Supramolecular Copolymers and Application on a Complex Two-Component Hydrogen-Bonding System. *Chem. Eur. J.* **2007,** *13*, 9617-9636.

138. Evstigneev, V. P.; Mosunov, A. A.; Buchelnikov, A. S.; Hernandez Santiago, A. A.; Evstigneev, M. P., Complete Solution of the Problem of One-Dimensional Non-Covalent Non-Cooperative Self-Assembly in Two-Component Systems. *J Chem Phys* **2011,** *134* , 194902.

139. Brunsveld, L.; Meijer, E. W.; Rowan, A. E.; Nolte, R. J. M., *Chiral Discotic Molecules: Expression and Amplification of Chirality*. John Wiley and Sons, Inc: Hoboken, NJ, 2004; Vol. 24.

140. Frisch, M. J. T., G. W.; Schlegel, H. B.; Scuseria, G. E.; Robb, M. A.; Cheeseman, J. R.; Scalmani, G.; Barone, V.; Mennucci, B.; Petersson, G. A.; Nakatsuji, H.; Caricato, M.; Li, X.; Hratchian, H. P.; Izmaylov, A. F.; Bloino, J.; Zheng, G.; Sonnenberg, J. L.; Hada, M.; Ehara, M.; Toyota, K.; Fukuda, R.; Hasegawa, J.; Ishida, M.; Nakajima, T.; Honda, Y.; Kitao, O.; Nakai, H.; Vreven, T.; Montgomery, J. A., Jr.; Peralta, J. E.; Ogliaro, F.; Bearpark, M.; Heyd, J. J.; Brothers, E.; Kudin, K. N.; Staroverov, V. N.; Kobayashi, R.; Normand, J.; Raghavachari, K.; Rendell, A.; Burant, J. C.; Iyengar, S. S.; Tomasi, J.; Cossi, M.; Rega, N.; Millam, J. M.; Klene, M.; Knox, J. E.; Cross, J. B.; Bakken, V.; Adamo, C.; Jaramillo, J.; Gomperts, R.; Stratmann, R. E.; Yazyev, O.; Austin, A. J.; Cammi, R.; Pomelli, C.; Ochterski, J. W.; Martin, R. L.; Morokuma, K.; Zakrzewski, V. G.; Voth, G. A.; Salvador, P.; Dannenberg, J. J.; Dapprich, S.; Daniels, A. D.; Farkas, Ö.; Foresman, J. B.; Ortiz, J. V.; Cioslowski, J.; Fox, D. J. Gaussian 09, Revision B.01. 2010.

141. Becke, A. D., Density-Functional Thermochemistry. III. The Role of Exact Exchange. *J. Chem. Phys.* **1993,** *98*, 5648-5652.

142. Lee, C.; Yang, W.; Parr, R. G., Development of the Colle-Salvetti Correlation-Energy Formula into a Functional of the Electron Density. *Phys. Rev. B* **1988,** *37*, 785-789.

143. Hariharan, P. C.; Pople, J. A., The Influence of Polarization Functions on Molecular Orbital Hydrogenation Energies. *Theoretica chimica acta* **1973,** *28*, 213-222.

144. Kirkus, M.; Wang, L.; Mothy, S.; Beljonne, D.; Cornil, J.; Janssen, R. A. J.; Meskers, S. C. J., Optical Properties of Oligothiophene Substituted Diketopyrrolopyrrole Derivatives in the Solid Phase: Joint J- and H-Type Aggregation. *J. Phys. Chem. A* **2012,** *116*, 7927-7936.

145. Würthner, F., Bay-substituted Perylene Bisimides: Twisted Fluorophores for Supramolecular Chemistry. *Pure and Applied Chemistry* **2009,** *78* (12), 2341–2349.

146. Chen, Z.; Baumeister, U.; Tschierske, C.; Würthner, F., Effect of Core Twisting on Self-Assembly and Optical Properties of Perylene Bisimide Dyes in Solution and Columnar Liquid Crystalline Phases. *Chem. Eur. J.* **2007,** *13* (2), 450-465.

147. Lim, J. M.; Kim, P.; Yoon, M.-C.; Sung, J.; Dehm, V.; Chen, Z.; Wurthner, F.; Kim, D., Exciton Delocalization and Dynamics in Helical [small pi]-Stacks of Self-Assembled Perylene Bisimides. *Chem. Sci.* **2013,** *4* (1), 388-397.

148. Kaiser, T. E.; Wang, H.; Stepanenko, V.; Würthner, F., Supramolecular Construction of Fluorescent J-Aggregates Based on Hydrogen-Bonded Perylene Dyes. *Angew. Chem. Int. Ed.* **2007,** *46* (29), 5541-5544.

149. Wang, H.; Kaiser, T. E.; Uemura, S.; Wurthner, F., Perylene Bisimide J-aggregates with Absorption Maxima in the NIR. *Chem/ Comm.* **2008**, 1181-1183.

150. Kaiser, T. E.; Stepanenko, V.; Würthner, F., Fluorescent J-Aggregates of Core-Substituted Perylene Bisimides: Studies on Structure−Property Relationship, Nucleation−Elongation Mechanism, and Sergeants-and-Soldiers Principle. *J. Am. Chem. Soc.* **2009,** *131* , 6719-6732.

151. Chen, Z.; Stepanenko, V.; Dehm, V.; Prins, P.; Siebbeles, L. D. A.; Seibt, J.; Marquetand, P.; Engel, V.; Würthner, F., Photoluminescence and Conductivity of Self-Assembled π–π Stacks of Perylene Bisimide Dyes. *Chem. Eur. J.* **2007,** *13*, 436-449.

152. Schwartz, E.; Palermo, V.; Finlayson, C. E.; Huang, Y.-S.; Otten, M. B. J.; Liscio, A.; Trapani, S.; González-Valls, I.; Brocorens, P.; Cornelissen, J. J. L. M.; Peneva, K.; Müllen, K.; Spano, F. C.; Yartsev, A.; Westenhoff, S.; Friend, R. H.; Beljonne, D.; Nolte, R. J. M.; Samorì, P.; Rowan, A. E., "Helter-Skelter-Like" Perylene Polyisocyanopeptides. *Chem. Eur. J.* **2009,** *15*, 2536-2547.

153. Cornil, J.; Beljonne, D.; Calbert, J.-P.; Brédas, J.-L., Interchain Interactions in Organic π-Conjugated Materials: Impact on Electronic Structure, Optical Response, and Charge Transport. *Adv. Mater.* **2001,** *13*, 1053–1067.

154. Hunter, C. A.; Anderson, H. L., What is Cooperativity? *Angew. Chem. Int. Ed.* **2009,** *48*, 7488-7499.

155. Ercolani, G.; Schiaffino, L., Allosteric, Chelate, and Interannular Cooperativity: A Mise au Point. *Angew. Chem. Int. Ed.* **2011,** *50*, 1762-1768.

156. Stoddart, J. F., Editorial: From Supramolecular to Systems Chemistry: Complexity Emerging out of Simplicity. *Angew. Chem. Int. Ed.* **2012,** *51*, 12902-12903.

157. Remy, A.; Gerwert, K., Coupling of Light-Induced Electron Transfer to Proton Uptake in Photosynthesis. *Nat. Struct. Mol. Biol.* **2003,** *10*, 637-644.

158. Lawrence, D. S.; Jiang, T.; Levett, M., Self-Assembling Supramolecular Complexes. *Chem. Rev.* **1995,** *95*, 2229-2260.

159. Gust, D.; Moore, T. A.; Moore, A. L., Mimicking Photosynthetic Solar Energy Transduction. *Acc. Chem. Res.* **2001,** *34*, 40-48.

160. Fukuzumi, S., Development of Bioinspired Artificial Photosynthetic Systems. *Phys. Chem. Chem. Phys.* **2008,** *10*, 2283-2297.

161. Saha, S.; Stoddart, J. F., Photo-driven Molecular Devices. *Chem. Soc. Rev.* **2007,** *36* , 77-92.

162. Imahori, H.; Guldi, D. M.; Tamaki, K.; Yoshida, Y.; Luo, C.; Sakata, Y.; Fukuzumi, S., Charge Separation in a Novel Artificial Photosynthetic Reaction Center Lives 380 ms. *J. Am. Chem. Soc.* **2001,** *123*, 6617-6628.

163. de Miguel, G.; Wielopolski, M.; Schuster, D. I.; Fazio, M. A.; Lee, O. P.; Haley, C. K.; Ortiz, A. L.; Echegoyen, L.; Clark, T.; Guldi, D. M., Triazole Bridges as Versatile Linkers in Electron Donor–Acceptor Conjugates. *J. Am. Chem. Soc.* **2011,** *133*, 13036-13054.

164. Wessendorf, F.; Grimm, B.; Guldi, D. M.; Hirsch, A., Pairing Fullerenes and Porphyrins: Supramolecular Wires That Exhibit Charge Transfer Activity. *J. Am. Chem. Soc.* **2010,** *132* , 10786-10795.

165. Frischmann, P. D.; Mahata, K.; Wurthner, F., Powering the Future of Molecular Artificial Photosynthesis with Light-Harvesting Metallosupramolecular Dye Assemblies. *Chem. Soc. Rev.* **2013,** *42*, 1847-1870.

166. Wasielewski, M. R., Energy, Charge, and Spin Transport in Molecules and Self-Assembled Nanostructures Inspired by Photosynthesis. *J. Org. Chem.* **2006,** *71*, 5051-5066.

167. Jimenez, A. J.; Calderon, R. M. K.; Rodriguez-Morgade, M. S.; Guldi, D. M.; Torres, T., Synthesis, Characterization and Photophysical Properties of a Melamine-Mediated Hydrogen-Bound Phthalocyanine-Perylenediimide Assembly. *Chem. Sci.* **2013,** *4*, 1064-1074.

168. Wang, F.; Gillissen, M. A. J.; Stals, P. J. M.; Palmans, A. R. A.; Meijer, E. W., Hydrogen Bonding Directed Supramolecular Polymerisation of Oligo(Phenylene-Ethynylene)s: Cooperative Mechanism, Core Symmetry Effect and Chiral Amplification. *Chem. Eur. J.* **2012,** *18*, 11761-11770.

169. Gunderson, V. L.; Smeigh, A. L.; Kim, C. H.; Co, D. T.; Wasielewski, M. R., Electron Transfer within Self-Assembling Cyclic Tetramers Using Chlorophyll-Based Donor–Acceptor Building Blocks. *J. Am. Chem. Soc.* **2012,** *134*, 4363-4372.

170. Würthner, F.; Kaiser, T. E.; Saha-Möller, C. R., J-Aggregates: From Serendipitous Discovery to Supramolecular Engineering of Functional Dye Materials. *Angew. Chem. Int. Ed.* **2011,** *50*, 3376-3410.

171. Cañas-Ventura, M. E.; Aït-Mansour, K.; Ruffieux, P.; Rieger, R.; Müllen, K.; Brune, H.; Fasel, R., Complex Interplay and Hierarchy of Interactions in Two-Dimensional Supramolecular Assemblies. *ACS Nano* **2011,** *5*, 457-469.

172. Safont-Sempere, M. M.; Fernández, G.; Würthner, F., Self-Sorting Phenomena in Complex Supramolecular Systems. *Chem. Rev.* **2011,** *111*, 5784-5814.

173. Shahar, C.; Baram, J.; Tidhar, Y.; Weissman, H.; Cohen, S. R.; Pinkas, I.; Rybtchinski, B., Self-Assembly of Light-Harvesting Crystalline Nanosheets in Aqueous Media. *ACS Nano* **2013,** *7*, 3547-3556.

174. Tamayo, A. B.; Tantiwiwat, M.; Walker, B.; Nguyen, T.-Q., Design, Synthesis, and Self-assembly of Oligothiophene Derivatives with a Diketopyrrolopyrrole Core. *J. Phys. Chem. C* **2008,** *112*, 15543-15552.

175. Wurthner, F., Perylene Bisimide Dyes as Versatile Building Blocks for Functional Supramolecular Architectures. *Chem. Comm.* **2004,** 1564-1579.

176. Karsten, B. P.; Bouwer, R. K. M.; Hummelen, J. C.; Williams, R. M.; Janssen, R. A. J., Charge Separation and (Triplet) Recombination in Diketopyrrolopyrrole-Fullerene Triads. *Photochem. Photobio. Sci.* **2010,** *9*, 1055-1065.

177. Karsten, B. P.; Smith, P. P.; Tamayo, A. B.; Janssen, R. A. J., Excitation Energy Shuttling in Oligothiophene–Diketopyrrolopyrrole–Fullerene Triads. *J. Phys. Chem. A* **2012,** *116*, 1146-1150.

178. Gosztola, D.; Niemczyk, M. P.; Svec, W.; Lukas, A. S.; Wasielewski, M. R., Excited Doublet States of Electrochemically Generated Aromatic Imide and Diimide Radical Anions. *J. Phys. Chem. A* **2000,** *104*, 6545-6551.

179. Jiménez, A. J.; Grimm, B.; Gunderson, V. L.; Vagnini, M. T.; Krick Calderon, S.; Rodríguez-Morgade, M. S.; Wasielewski, M. R.; Guldi, D. M.; Torres, T., Synthesis, Characterization, and Photoinduced Energy and Electron Transfer in a Supramolecular Tetrakis (Ruthenium(II) Phthalocyanine) Perylenediimide Pentad. *Chem. Eur. J.* **2011,** *17* , 5024-5032.

180. Rodríguez-Morgade, M. S.; Torres, T.; Atienza-Castellanos, C.; Guldi, D. M., Supramolecular Bis(rutheniumphthalocyanine)−Perylenediimide Ensembles: Simple Complexation as a Powerful Tool toward Long-Lived Radical Ion Pair States. *J. Am. Chem. Soc.* **2006,** *128*, 15145-15154.

181. Guha, S.; Goodson, F. S.; Corson, L. J.; Saha, S., Boundaries of Anion/Naphthalenediimide Interactions: From Anion−π Interactions to Anion-Induced Charge-Transfer and Electron-Transfer Phenomena. *J. Am. Chem. Soc.* **2012,** *134*, 13679-13691.

182. Goodson, F. S.; Panda, D. K.; Ray, S.; Mitra, A.; Guha, S.; Saha, S., Tunable Electronic Interactions Between Anions and Perylenediimide. *Org. Biomol. Chem.* **2013,** *11*, 4797-4803.

183. Weller, A., Photoinduced Electron Transfer in Solution: Exciplex and Radical Ion Pair Formation Free Enthalpies and their Solvent Dependence. In *Zeitschrift für Physikalische Chemie*, 1982; Vol. 133, p 93.

184. Marcus, R. A., On the Theory of Oxidation-Reduction Reactions Involving Electron Transfer. I. *J.Chem. Phys,* **1956,** *24*, 966-978.

185. Greenfield, S. R.; Svec, W. A.; Gosztola, D.; Wasielewski, M. R., Multistep Photochemical Charge Separation in Rod-like Molecules Based on Aromatic Imides and Diimides. *J. Am. Chem. Soc.* **1996,** *118*, 6767-6777.

186. Scott, A. M.; Miura, T.; Ricks, A. B.; Dance, Z. E. X.; Giacobbe, E. M.; Colvin, M. T.; Wasielewski, M. R., Spin-Selective Charge Transport Pathways through p-Oligophenylene-Linked Donor−Bridge−Acceptor Molecules. *J. Am. Chem. Soc.* **2009,** *131* , 17655-17666.

187. Barbara, P. F.; Meyer, T. J.; Ratner, M. A., Contemporary Issues in Electron Transfer Research. *J. Phys. Chem.* **1996,** *100* , 13148-13168.

188. Neese, F., The ORCA program system. *Wiley Interdisciplinary Reviews: Comp. Mole. Sci.* **2012,** *2*, 73-78.

189. Closs, G. L.; Miller, J. R., Intramolecular Long-Distance Electron Transfer in Organic Molecules. *Science* **1988,** *240* (4851), 440-447.

190. Paulson, B. P.; Miller, J. R.; Gan, W.-X.; Closs, G., Superexchange and Sequential Mechanisms in Charge Transfer with a Mediating State between the Donor and Acceptor. *J. Am.Chem.Soc.***2005,** *127*, 4860-4868.

191. Jakob, M.; Berg, A.; Stavitski, E.; Chernick, E. T.; Weiss, E. A.; Wasielewski, M. R.; Levanon, H., Photoinduced Electron Transfer through Hydrogen Bonds in a Rod-like Donor–Acceptor Molecule: A Time-Resolved EPR study. *Chemical Physics* **2006,** *324* (1), 63-71.

192. van der Poll, T. S.; Love, J. A.; Nguyen, T.-Q.; Bazan, G. C., Non-Basic High-Performance Molecules for Solution-Processed Organic Solar Cells. *Adv. Mater.* **2012,** *24* (27), 3646-3649.

193. Kyaw, A. K. K.; Wang, D. H.; Wynands, D.; Zhang, J.; Nguyen, T.-Q.; Bazan, G. C.; Heeger, A. J., Improved Light Harvesting and Improved Efficiency by Insertion of an Optical Spacer (ZnO) in Solution-Processed Small-Molecule Solar Cells. *Nano Letters* **2013,** *13*, 3796-3801.

194. Zhong, Y.; Kumar, B.; Oh, S.; Trinh, M. T.; Wu, Y.; Elbert, K.; Li, P.; Zhu, X.; Xiao, S.; Ng, F.; Steigerwald, M. L.; Nuckolls, C., Helical Ribbons for Molecular Electronics. *J. Am. Chem. Soc.* **2014,** *136*, 8122-8130.

195. Kobori, Y.; Yamauchi, S.; Akiyama, K.; Tero-Kubota, S.; Imahori, H.; Fukuzumi, S.; Norris, J. R., Primary Charge-Recombination in an Artificial Photosynthetic Reaction Center. *Proc. Natl. Acad. Sci. U S A* **2005,** *102*, 10017-10022.

196. Rao, A.; Chow, P. C. Y.; Gelinas, S.; Schlenker, C. W.; Li, C.-Z.; Yip, H.-L.; Jen, A. K. Y.; Ginger, D. S.; Friend, R. H., The Role of Spin in the Kinetic Control of Recombination in Organic Photovoltaics. *Nature* **2013,** *500* , 435-439.

197. Schuster, D. I.; Cheng, P.; Jarowski, P. D.; Guldi, D. M.; Luo, C.; Echegoyen, L.; Pyo, S.; Holzwarth, A. R.; Braslavsky, S. E.; Williams, R. M.; Klihm, G., Design, Synthesis, and Photophysical Studies of a Porphyrin-Fullerene Dyad with Parachute Topology; Charge Recombination in the Marcus Inverted Region. *J. Am. Chem. Soc.* **2004,** *126*, 7257-7270.

198. Hammarström, L.; Hammes-Schiffer, S., Artificial Photosynthesis and Solar Fuels. *Acc. Chem. Res.* **2009,** *42*, 1859-1860.

199. Ramanan, C.; Smeigh, A. L.; Anthony, J. E.; Marks, T. J.; Wasielewski, M. R., Competition between Singlet Fission and Charge Separation in Solution-Processed Blend Films of 6,13-Bis(triisopropylsilylethynyl)pentacene with Sterically-Encumbered Perylene-3,4:9,10-bis(dicarboximide)s. *J. Am. Chem. Soc.* **2012,** *134*, 386-397.

200. Credgington, D.; Jamieson, F. C.; Walker, B.; Nguyen, T.-Q.; Durrant, J. R., Quantification of Geminate and Non-Geminate Recombination Losses within a Solution-Processed Small-Molecule Bulk Heterojunction Solar Cell. *Adv. Mater.* **2012,** *24*, 2135-2141.

201. Burattini, S.; Greenland, B. W.; Merino, D. H.; Weng, W.; Seppala, J.; Colquhoun, H. M.; Hayes, W.; Mackay, M. E.; Hamley, I. W.; Rowan, S. J., A Healable Supramolecular Polymer Blend Based on Aromatic $\pi-\pi$ Stacking and Hydrogen-Bonding Interactions. *J. Am. Chem. Soc.* **2010,** *132*, 12051-12058.

202. Romulus, J.; Henssler, J. T.; Weck, M., Postpolymerization Modification of Block Copolymers. *Macromol.* **2014,** *47*, 5437-5449.

203. Zhang, X.; Whitten, D. G., Preface to the Supramolecular Chemistry at Interfaces Special Issue. *Langmuir* **2011,** *27*, 1245-1245.

204. Greenfield, S. R.; Wasielewski, M. R., Excitation Energy Transfer and Charge Separation in the Isolated Photosystem II Reaction Center. *Photosyn. Res.* **1996,** *48*, 83-97.

205. Marcos Ramos, A.; Meskers, S. C. J.; Beckers, E. H. A.; Prince, R. B.; Brunsveld, L.; Janssen, R. A. J., Supramolecular Control over Donor−Acceptor Photoinduced Charge Separation. *J. Am. Chem. Soc.* **2004,** *126*, 9630-9644.

206. Lefler, K. M.; Co, D. T.; Wasielewski, M. R., Self-Assembly-Induced Ultrafast Photodriven Charge Separation in Perylene-3,4-dicarboximide-Based Hydrogen-Bonded Foldamers. *J. Phys. Chem. Let.* **2012,** *3*, 3798-3805.

207. Peeters, E.; van Hal, P. A.; Meskers, S. C. J.; Janssen, R. A. J.; Meijer, E. W., Photoinduced Electron Transfer in a Mesogenic Donor–Acceptor–Donor System. *Chem. Eur. J.* **2002,** *8* , 4470-4474.

208. Miller, N. C.; Cho, E.; Junk, M. J. N.; Gysel, R.; Risko, C.; Kim, D.; Sweetnam, S.; Miller, C. E.; Richter, L. J.; Kline, R. J.; Heeney, M.; McCulloch, I.; Amassian, A.; Acevedo-Feliz, D.; Knox, C.; Hansen, M. R.; Dudenko, D.; Chmelka, B. F.; Toney, M. F.; Brédas, J.-L.; McGehee, M. D., Use of X-Ray Diffraction, Molecular Simulations, and Spectroscopy to Determine the Molecular Packing in a Polymer-Fullerene Bimolecular Crystal. *Adv. Mater.* **2012,** *24*, 6071-6079.

209. Kang, S. J.; Kim, J. B.; Chiu, C.-Y.; Ahn, S.; Schiros, T.; Lee, S. S.; Yager, K. G.; Toney, M. F.; Loo, Y.-L.; Nuckolls, C., A Supramolecular Complex in Small-Molecule Solar Cells based on Contorted Aromatic Molecules. *Angew. Chem. Int. Ed.* **2012,** *51*, 8594-8597.

210. Shaller, A. D.; Wang, W.; Gan, H.; Li, A. D. Q., Tunable Molecular Assembly Codes Direct Reaction Pathways. *Angew. Chem. Int. Ed.* **2008,** *47*, 7705-7709.

211. Shoaee, S.; Clarke, T. M.; Huang, C.; Barlow, S.; Marder, S. R.; Heeney, M.; McCulloch, I.; Durrant, J. R., Acceptor Energy Level Control of Charge Photogeneration in Organic Donor/Acceptor Blends. *J. Amer. Chem. Soc.* **2010,** *132*, 12919-12926.

212. Chen, P.-Y.; McKittrick, J.; Meyers, M. A., Biological Materials: Functional Adaptations and Bioinspired Designs. *Prog. Mater. Sci.* **2012,** *57* , 1492-1704.

213. England, G.; Kolle, M.; Kim, P.; Khan, M.; Munoz, P.; Mazur, E.; Aizenberg, J., Bioinspired Micrograting Arrays Mimicking the Reverse Color Diffraction Elements Evolved by the Butterfly Pierella Luna. *Proc. Natl. Acad. Sci. U S A* **2014,** *111*, 15630-15634.

214. Waite, J. H.; Lichtenegger, H. C.; Stucky, G. D.; Hansma, P., Exploring Molecular and Mechanical Gradients in Structural Bioscaffolds. *Biochem.* **2004,** *43*, 7653-7662.

215. Zhang, X.; Richter, L. J.; DeLongchamp, D. M.; Kline, R. J.; Hammond, M. R.; McCulloch, I.; Heeney, M.; Ashraf, R. S.; Smith, J. N.; Anthopoulos, T. D.; Schroeder, B.; Geerts, Y. H.; Fischer, D. A.; Toney, M. F., Molecular Packing of High-Mobility Diketo Pyrrolo-Pyrrole Polymer Semiconductors with Branched Alkyl Side Chains. *J. Amer. Chem. Soc.* **2011,** *133*, 15073-15084.

216. Schmidt, R.; Oh, J. H.; Sun, Y.-S.; Deppisch, M.; Krause, A.-M.; Radacki, K.; Braunschweig, H.; Könemann, M.; Erk, P.; Bao, Z.; Würthner, F., High-Performance Air-Stable n-Channel Organic Thin Film Transistors Based on Halogenated Perylene Bisimide Semiconductors. *J. Amer. Chem. Soc.* **2009,** *131*, 6215-6228.

217. Eaton, S. W.; Shoer, L. E.; Karlen, S. D.; Dyar, S. M.; Margulies, E. A.; Veldkamp, B. S.; Ramanan, C.; Hartzler, D. A.; Savikhin, S.; Marks, T. J.; Wasielewski, M. R., Singlet Exciton Fission in Polycrystalline Thin Films of a Slip-Stacked Perylenediimide. *J. Amer. Chem. Soc.* **2013,** *135*, 14701-14712.

218. Gélinas, S.; Rao, A.; Kumar, A.; Smith, S. L.; Chin, A. W.; Clark, J.; van der Poll, T. S.; Bazan, G. C.; Friend, R. H., Ultrafast Long-Range Charge Separation in Organic Semiconductor Photovoltaic Diodes. *Science* **2014,** *343*, 512-516.

219. Beckers, E. H. A.; Chen, Z.; Meskers, S. C. J.; Jonkheijm, P.; Schenning, A. P. H. J.; Li, X.-Q.; Osswald, P.; Würthner, F.; Janssen, R. A. J., The Importance of Nanoscopic Ordering on the Kinetics of Photoinduced Charge Transfer in Aggregated π-Conjugated Hydrogen-Bonded Donor−Acceptor Systems. *J. Phys. Chem. B* **2006,** *110*, 16967-16978.

220. Gregg, B. A., Entropy of Charge Separation in Organic Photovoltaic Cells: The Benefit of Higher Dimensionality. *J. Phys. Chem. Lett.* **2011,** *2*, 3013-3015.

221. Yassar, A.; Demanze, F.; Jaafari, A.; El Idrissi, M.; Coupry, C., Cyano-Substituted Oligothiophenes: A New Approach to n-Type Organic Semiconductors. *Adv. Funct. Mater.* **2002,** *12*, 699-708.

222. Clot, O.; Selmarten, D.; McNevin, M. J., Synthesis and Characterization of Amino-Capped Oligothiophene-Based Hole-Transport Materials. *J. Mater. Chem.* **2005,** *15* , 4934-4942.

223. Tamayo, A. B.; Walker, B.; Nguyen*, T.-Q., A Low Band Gap, Solution Processable Oligothiophene with a Diketopyrrolopyrrole Core for Use in Organic Solar Cells. *J. Phys. Chem. C* **2008,** *112* , 11545-11551.

224. Schueppel, R.; Schmidt, K.; Uhrich, C.; Schulze, K.; Wynands, D.; Brédas, J. L.; Brier, E.; Reinold, E.; Bu, H. B.; Baeuerle, P.; Maennig, B.; Pfeiffer, M.; Leo, K., Optimizing Organic Photovoltaics using Tailored Heterojunctions: A Photoinduced Absorption Study of Oligothiophenes with Low Band Gaps. *Phys. Rev, B* **2008,** *77*, 085311.

225. Zhou, R.; Li, Q.-D.; Li, X.-C.; Lu, S.-M.; Wang, L.-P.; Zhang, C.-H.; Huang, J.; Chen, P.; Li, F.; Zhu, X.-H.; Choy, W. C. H.; Peng, J.; Cao, Y.; Gong, X., A Solution-Processable Diketopyrrolopyrrole Dye Molecule with (fluoronaphthyl)thienyl Endgroups for Organic Solar Cells. *Dyes and Pigments* **2014,** *101*, 51-57.

226. Peurifoy, S. R.; Guzman, C. X.; Braunschweig, A. B., Topology, Assembly, and Electronics: Three Pillars for Designing Supramolecular Polymers with Emergent Optoelectronic Behavior. *Polymer Chem.* **2015,** *6* , 5529-5539.

227. Guzman, C. X.; Calderon, R. M. K.; Li, Z.; Yamazaki, S.; Peurifoy, S. R.; Guo, C.; Davidowski, S. K.; Mazza, M. M. A.; Han, X.; Holland, G.; Scott, A. M.; Braunschweig, A. B., Extended Charge Carrier Lifetimes in Hierarchical Donor–Acceptor Supramolecular Polymer Films. *J. Phys. Chem. C* **2015,** *119* (34), 19584-19589.

228. Zhong, H.; Smith, J.; Rossbauer, S.; White, A. J. P.; Anthopoulos, T. D.; Heeney, M., Air-Stable and High-Mobility n-Channel Organic Transistors Based on Small-Molecule/Polymer Semiconducting Blends. *Adv. Mater.* **2012,** *24*, 3205-3211.

229. Chen, M. S.; Lee, O. P.; Niskala, J. R.; Yiu, A. T.; Tassone, C. J.; Schmidt, K.; Beaujuge, P. M.; Onishi, S. S.; Toney, M. F.; Zettl, A.; Fréchet, J. M. J., Enhanced Solid-State Order and Field-Effect Hole Mobility through Control of Nanoscale Polymer Aggregation. *J. Amer. Chem. Soc.* **2013,** *135*, 19229-19236.

230. Liu, F.; Gu, Y.; Wang, C.; Zhao, W.; Chen, D.; Briseno, A. L.; Russell, T. P., Efficient Polymer Solar Cells Based on a Low Bandgap Semi-crystalline DPP Polymer-PCBM Blends. *Adv. Mater.* **2012,** *24*, 3947-3951.

231. Lehn, J.-M., Perspectives in Supramolecular Chemistry—From Molecular Recognition towards Molecular Information Processing and Self-Organization. *Angew. Chem. Int. Ed.* **1990,** *29* , 1304-1319.

232. Balzani, V.; Scandola, F., *Supramolecular Photochemistry*. Chichester, 1994.

233. Lehn, J. M., *Supramolecular Chemistry : Concepts and Perspectives : a Personal Account built upon the George Fisher Baker lectures in chemistry at Cornell University and the Lezione Lincee, Accademia nazionale dei Lincei, Rome*. p x, 271 pages.

234. Balzani, V.; Scandola, F., *Comprehensive Supramolecular Chemistry*. Atwood, JL, 1996; Vol. 10.

235. Cram, D. J., The Design of Molecular Hosts, Guests, and Their Complexes (Nobel Lecture). *Angew. Chem. Int. Ed.* **1988,** *27* , 1009-1020.

236. Boulas, P. L.; Gómez-Kaifer, M.; Echegoyen, L., Electrochemistry of Supramolecular Systems. *Angew. Chem. Int. Ed..* **1998,** *37* (3), 216-247.

237. Balzani, V.; Credi, A.; Raymo, F. M.; Stoddart, J. F., Artificial Molecular Machines. *Angew. Chem. Int. Ed..* **2000,** *39* , 3348-3391.

238. Steed, J. W.; Atwood, J. L., *Supramolecular Chemistry*. Chichester, UK 2013.

239. Pedersen, C. J., The Discovery of Crown Ethers (Noble Lecture). *Angew. Chem. Int. Ed.* **1988,** *27*, 1021-1027.

240. Pedersen, C. J., Macrocyclic Polyether Sulfides. *J. Org. Chem.* **1971,** *36*, 254-257.

241. Pedersen, C. J., Cyclic Polyethers and their Complexes with Metal Salts. *J. Amer. Chem. Soc.* **1967,** *89* , 7017-7036.

242. Newcomb, M.; Moore, S. S.; Cram, D. J., Host-Guest Complexation. 5. Convergent Functional Groups in Macrocyclic Polyethers. *J. Amer. Chem. Soc.* **1977,** *99*, 6405-6410.

243. Cram, D. J.; Cram, J. M., Host-Guest Chemistry. *Complexes Between Organic Compounds Simulate the Substrate Selectivity of Enzymes* **1974,** *183* , 803-809.

244. Cram, D. J.; Cram, J. M., Design of Complexes Between Synthetic Hosts and Organic Guests. *Acc. Chem. Res.* **1978,** *11* , 8-14.

245. Cram, D. J.; Cram, J. M., *Container Molecules and their Guests*. Cambridge, UK, 1997.

246. ten Eikelder, H. M. M.; Markvoort, A. J.; de Greef, T. F. A.; Hilbers, P. A. J., An Equilibrium Model for Chiral Amplification in Supramolecular Polymers. *J. Phys. Chem. B* **2012,** *116*, 5291-5301.

247. Eakins, G. L.; Gallaher, J. K.; Keyzers, R. A.; Falber, A.; Webb, J. E. A.; Laos, A.; Tidhar, Y.; Weissman, H.; Rybtchinski, B.; Thordarson, P.; Hodgkiss, J. M., Thermodynamic Factors Impacting the Peptide-Driven Self-Assembly of Perylene Diimide Nanofibers. *J. Phys. Chem. B* **2014,** *118*, 8642-8651.

248.   Olson, M. A.; Braunschweig, A. B.; Ikeda, T.; Fang, L.; Trabolsi, A.; Slawin, A. M. Z.; Khan, S. I.; Stoddart, J. F., Thermodynamic forecasting of mechanically interlocked switches. *Org. Biomol. Chem.* **2009,** *7*, 4391-4405.

249.   Choi, J. W.; Flood, A. H.; Steuerman, D. W.; Nygaard, S.; Braunschweig, A. B.; Moonen, N. N. P.; Laursen, B. W.; Luo, Y.; DeIonno, E.; Peters, A. J.; Jeppesen, J. O.; Xu, K.; Stoddart, J. F.; Heath, J. R., Ground-State Equilibrium Thermodynamics and Switching Kinetics of Bistable [2]Rotaxanes Switched in Solution, Polymer Gels, and Molecular Electronic Devices. *Chem. Eur. J.* **2006,** *12*, 261-279.

250.   Bell, N. C.; Doyle, S. J.; Battistelli, G.; LeGuyader, C. L. M.; Thompson, M. P.; Poe, A. M.; Rheingold, A.; Moore, C.; Montalti, M.; Thayumanavan, S.; Tauber, M. J.; Gianneschi, N. C., Dye Encapsulation in Polynorbornene Micelles. *Langmuir* **2015,** *31*, 9707-9717.

251.   Ahrens, M. J.; Sinks, L. E.; Rybtchinski, B.; Liu, W.; Jones, B. A.; Giaimo, J. M.; Gusev, A. V.; Goshe, A. J.; Tiede, D. M.; Wasielewski, M. R., Self-Assembly of Supramolecular Light-Harvesting Arrays from Covalent Multi-Chromophore Perylene-3,4:9,10-bis(dicarboximide) Building Blocks. *J. Am. Chem. Soc.* **2004,** *126*, 8284-8294.

252.   Spek, A., Structure Validation in Chemical Crystallography. *Acta Crystallographica Section D* **2009,** *65* (2), 148-155.

253.   Spek, A. PLATON: A Multipurpose Crystallographic Tool Version 1.15. 2008.

254.   Sheppard, S. E., III.-The Optical and Sensitising Properties of the Isocyanine Dyes. *Journal of the Chemical Society, Transactions* **1909,** *95*, 15-19.

255.   Jelley, E. E., Spectral Absorption and Fluorescence of Dyes in the Molecular State. *Nature* **1936,** *138*, 1009-1010.

256.   Möbius, D., Scheibe Aggregates. *Adv. Mater.* **1995,** *7*, 437-444.

257.   Fink, R. F.; Seibt, J.; Engel, V.; Renz, M.; Kaupp, M.; Lochbrunner, S.; Zhao, H.-M.; Pfister, J.; Würthner, F.; Engels, B., Exciton Trapping in π-Conjugated Materials: A Quantum-Chemistry-Based Protocol Applied to Perylene Bisimide Dye Aggregates. *J. Am. Chem. Soc.* **2008,** *130* , 12858-12859.

258.   Beckers, E. H. A.; Meskers, S. C. J.; Schenning, A. P. H. J.; Chen, Z.; Würthner, F.; Marsal, P.; Beljonne, D.; Cornil, J.; Janssen, R. A. J., Influence of Intermolecular Orientation on the Photoinduced Charge Transfer Kinetics in Self-Assembled Aggregates of Donor−Acceptor Arrays. *J. Am. Chem. Soc.* **2006,** *128*, 649-657.

259. Anthony, J. E.; Brooks, J. S.; Eaton, D. L.; Parkin, S. R., Functionalized Pentacene: Improved Electronic Properties from Control of Solid-State Order. *J. Am. Chem. Soc.* **2001,** *123*, 9482-9483.

260. Anthony, J. E., Functionalized Acenes and Heteroacenes for Organic Electronics. *Chem. Rev.* **2006,** *106* , 5028-5048.

261. Chen, J.; Tee, C. K.; Shtein, M.; Martin, D. C.; Anthony, J., Controlled Solution Deposition and Systematic Study of Charge-Transport Anisotropy in Single Crystal and Single-Crystal Textured TIPS Pentacene Thin Films. *Org. Electron.* **2009,** *10*, 696-703.

262. Sele, C. W.; Kjellander, B. K. C.; Niesen, B.; Thornton, M. J.; van der Putten, J. B. P. H.; Myny, K.; Wondergem, H. J.; Moser, A.; Resel, R.; van Breemen, A. J. J. M.; van Aerle, N.; Heremans, P.; Anthony, J. E.; Gelinck, G. H., Controlled Deposition of Highly Ordered Soluble Acene Thin Films: Effect of Morphology and Crystal Orientation on Transistor Performance. *Adv. Mater.* **2009,** *21*, 4926-4931.

263. Anthony, J. E., Small-Molecule, Nonfullerene Acceptors for Polymer Bulk Heterojunction Organic Photovoltaics. *Chem. Mater.* **2011,** *23*, 583-590.

264. Ercolani, G., Assessment of Cooperativity in Self-Assembly. *J. Am. Chem. Soc.* **2003,** *125*, 16097-16103.

265. Smulders, M. M. J.; Schenning, A. P. H. J.; Meijer, E. W., Insight into the Mechanisms of Cooperative Self-Assembly: The "Sergeants-and-Soldiers" Principle of Chiral and Achiral C3-Symmetrical Discotic Triamides. *J. Am. Chem. Soc.* **2008,** *130*, 606-611.

266. Connors, K. A., *Binding Constants: the Measurement of Molecular Complex Stability*. Hoboken, NJ 1987.

267. Liu, L.; Guo, Q.-X., Isokinetic Relationship, Isoequilibrium Relationship, and Enthalpy−Entropy Compensation. *Chem. Rev.* **2001,** *101*, 673-696.

268. Gardlik, M.; Yan, Z.; Xia, S.; Rieth, S.; Gallucci, J.; Hadad, C. M.; Badjić, J. D., A Close Inspection of Ag(I) Coordination to Molecular Baskets: A Study of Solvation and Guest Encapsulation in Solution and the Solid State. *Tetrahedron* **2009,** *65*, 7213-7219.

269. Percec, V.; Imam, M. R.; Peterca, M.; Wilson, D. A.; Heiney, P. A., Self-Assembly of Dendritic Crowns into Chiral Supramolecular Spheres. *J. Am. Chem. Soc.* **2009,** *131*, 1294-1304.

270. Veld, M. A. J.; Haveman, D.; Palmans, A. R. A.; Meijer*, E. W., Sterically Demanding benzene-1,3,5-tricarboxamides: Tuning the Mechanisms of Supramolecular Polymerization and Chiral Amplification. *Soft Mater.* **2011,** *7*, 524-531.

271. Peterca, M.; Imam, M. R.; Ahn, C.-H.; Balagurusamy, V. S. K.; Wilson, D. A.; Rosen, B. M.; Percec, V., Transfer, Amplification, and Inversion of Helical Chirality Mediated by Concerted Interactions of C3-Supramolecular Dendrimers. *J. Am. Chem. Soc.* **2011,** *133*, 2311-2328.

272. Schrödinger, E., *What is Life?: With Mind and Matter and Autobiographical Sketches*. Cambridge University Press: Cambridge, 1992.

273. Bauer, P.; Wietasch, H.; Lindner, S. M.; Thelakkat, M., Synthesis and Characterization of Donor−Bridge−Acceptor Molecule Containing Tetraphenylbenzidine and Perylene Bisimide. *Chem. Mater.* **2007,** *19* , 88-94.

274. Thelakkat, M.; Schmidt, H.-W., Synthesis and Properties of Novel Derivatives of 1,3,5-Tris(diarylamino)benzenes for Electroluminescent Devices. *Adv. Mater.* **1998,** *10*, 219-223.

275. Socrates, G., *Infrared and Raman Characteristic Group Frequencies: Tables and Charts*. 3 ed.; 2001.

276. Version, A., 2.2-0 and SAINT+ Version 7.46 A; Bruker Analytical X-ray System. *Inc., Madison, Wisconsin, USA* **2007**.

277. Sheldrick, G., SHELXTL, version 6.10; Bruker AXS. *Inc., Madison, Wisconsin, USA* **2000**.

278. Sheldrick, G., Foundations of crystallography. *Acta Crystallographica A* **2008,** *64*, 112-122.

279. Rieth, S.; Li, Z.; Hinkle, C. E.; Guzman, C. X.; Lee, J. J.; Nehme, S. I.; Braunschweig, A. B., Superstructures of Diketopyrrolopyrrole Donors and Perylenediimide Acceptors Formed by Hydrogen-Bonding and pi-pi Stacking. *J Phy.s Chem. C* **2013,** *117*, 11347-11356.

280. Hanson, R. M.; Prilusky, J.; Renjian, Z.; Nakane, T.; Sussman, J. L., JSmol and the Next-Generation Web-Based Representation of 3D Molecular Structure as Applied to Proteopedia. *Isr. J. Chem.* **2013,** *53*, 207-216.

281. Macrae, C. F.; Edgington, P. R.; McCabe, P.; Pidcock, E.; Shields, G. P.; Taylor, R.; Towler, M.; Streek, J. v. d., Mercury: Visualization and Analysis of Crystal Structures. *J. Appl. Crystallogr.* **2006,** *39* 453-457.

282. Hanwell, M. D.; Curtis, D. E.; Lonie, D. C.; Vandermeersch, T.; Zurek, E.; Hutchison, G. R., Avogadro: An Advanced Semantic Chemical Editor, Visualization, and Analysis Platform. *J. Cheminformatics* **2012,** *4* , 17.